COATING AND FILLING OF NANOMETER-SCALE STRUCTURES USING CHEMICAL VAPOR DEPOSITION

BY

TUSHAR KANTI TALUKDAR

DISSERTATION

Submitted in partial fulfillment of the requirements
for the degree of Doctor of Philosophy in Mechanical Engineering
in the Graduate College of the
University of Illinois at Urbana-Champaign, 2018

Urbana, Illinois

Doctoral Committee:

Associate Professor Elif Ertekin, Chair
Professor John R. Abelson, Director of Research
Professor Gregory S. Girolami
Assistant Professor Sameh H. Tawfick

ABSTRACT

Void-free filling of high aspect ratio (AR = 3 to 10) structures, such as trenches or vias, is necessary in nanoscale device fabrication. Examples include shallow trench isolation, metallization, and reverse tone patterning in integrated circuits and optical waveguides in photonic devices. Gas-phase coating methods such as chemical vapor deposition (CVD) and atomic layer deposition (ALD) can be operated in a regime that is kinetically limited by the surface reaction rate rather than by the precursor transport rate. In that regime, the precursor diffuses everywhere within the structure, which affords a nearly uniform coating thickness. However, complete filling of a deep structure is ultimately sensitive to the geometry. In a trench with parallel sidewalls, the width of the opening along the centerline decreases as film builds up on the sidewalls, and the rate of precursor transport by molecular diffusion declines until it becomes reaction rate limiting. As the supply of precursor deep within the structure dwindles, a residual void (seam) is left along the centerline. This seam is unacceptable in many applications because it leads to a degradation of performance, including thermal, mechanical, or electrical properties, or to a higher etch rate during surface planarization processes.

In this dissertation, I report a newly discovered superconformal CVD method that affords bottom-up filling of trenches with oxide: the film growth rate increases with depth such that the profile of material develops a "V" shape that fills in along the centerline without a seam of low density material. The method utilizes low pressures of a metal precursor plus a forward-directed, lower-pressure flux of co-reactant (water). Under these conditions, many of the co-reactant molecules travel ballistically to the trench bottom where a fraction of them reflect. This scattering, which creates a virtual source of co-reactant from the trench bottom, leads to a superconformal growth process whose rate is highest at the bottom and declines towards the opening. Simultaneous with this superconformal component is the typical subconformal growth process due to the portion of the co-reactant flux that enters the trench opening isotropically; with a sufficiently large forward-directed flux, however, the overall profile is superconformal.

I demonstrate this approach for filling trenches with HfO_2 using 0.09 mTorr tetrakis-(dimethylamido)hafnium (TDMA-Hf) precursor and 0.009 mTorr H_2O co-reactant. Precursor-rich growth conditions at a substrate temperature $\leq$ 270 °C are used to assure that the growth rate is kinetically limited (determined) by the H_2O flux and is nearly independent of the TDMA-Hf flux. Under these conditions, the growth rate in a trench with an AR of 3.5 increases from 0.6 nm/min at the top to 1.0 nm/min at the bottom sidewalls (step coverage = 1.6).

I simulate the precursor transport-reaction problem within the trench using a Markov chain model to account for both the forward-directed and isotropic reactant fluxes, including the multiple re-emission events within the trench, as a function of the surface sticking probability. The model predicts the fraction of the total incident flux that must be forward-directed in order to afford seam-free filling as a function of the sticking probability and the starting AR.

Experimentally, I find that the opening of the trench accumulates a slightly greater thickness (a 'bread-loaf' profile) that tends to pinch off the trench just before complete filling. To eliminate this effect, I use a molecular growth inhibitor, H(hfac) or H(acac), to reduce the growth rate near to the opening. The result is seam-free filling of trenches with HfO_2 up to an AR of 10.

I also report CVD of highly conformal MgO film at a high growth rate (up to 300 nm/min) and a low substrate temperature (≤ 350 °C) using $Mg(DMADB)_2$ precursor plus H_2O co-reactant. The film stress is low enough, and the adhesion to the Si substrate is strong enough, to grow 2 μm thick MgO film at 350 °C. Conformal growth in microtrenches is demonstrated by controlling the precursor sticking probability: using a precursor-rich condition at 270 °C, a step coverage of 98 % is obtained in a trench of AR 9 at a growth rate of 7.5 nm/min. Films grown at a very high rate (> 90 nm/min) incorporate boron as B_2O_3, but those grown at a moderately high rate (7-25 nm/min) have a very low (~ 1 at. %) boron incorporation. The refractive indices are lower than bulk MgO due to a reduced physical density (~ 85 % of that of bulk). The measured electrical dielectric constant (9.5) and breakdown strength (6 MV/cm) agree well with literature values for MgO thin films.

This dissertation also reports extremely conformal HfB_2 coating in carbon nanotube (CNT) forests with height of ≤ 1.7 mm by employing static (unpumped) chemical vapor deposition (SCVD), utilizing a high pressure of $Hf(BH_4)_4$ precursor up to its full vapor pressure. When the substrate temperature is kept low (≤ 200 °C), the growth saturation occurs at a pressure that is orders of magnitude lower than the maximum precursor pressure limit, thereby affording a high degree of conformality in the forests. A step coverage of 92 % is achieved when the forest height is 80 μm.

In addition to high conformality, HfB_2 coating creates strong joints wherever the neighboring CNTs touch each other; this converts the CNT forest with van der Waals interactions into a mesoscale composite foam with greatly enhanced mechanical performance. Flat punch nanoindentation measurements of HfB_2-CNT composites with different HfB_2 coating thicknesses show that the modulus and compressive strength follow a power law relationship with density ($\sim \rho^n$) where the exponent n = 3 and 3.4, respectively.

To my parents and my wife

ACKNOWLEDGEMENTS

I take this opportunity to express my sincere gratitude to my advisor Professor John R. Abelson. I greatly enjoyed working with him. His critical thinking and meticulous analysis of results helped me to advance my projects toward successful completion. Professor Abelson gave me a lot of freedom in research within the framework of projects' goals; this encouraged me to enhance my independent creative thinking skills, which in turn made me a confident and independent researcher ready to move forward to the next step of my career goal. I also learned many soft skills from Professor Abelson, such as collaboration, communication and research presentation, during my Ph.D. years. As of today, I have developed a professional mindset which is largely modeled after him.

It has been a wonderful experience to have Professor Gregory S. Girolami as a collaborator and mentor. Professor Girolami's expertise in chemistry, combined with his critical and in-depth thinking, helped me to overcome many road-blocks during my dissertation research. When it comes to chemistry, I would like to especially thank my chemistry colleague and friend Sumeng Liu. Besides being an insightful researcher, Sumeng has been ready, even including weekends and nights, to supply me the chemical precursors. I also appreciate my other chemistry colleagues, Brian Trinh, Frank Schwandt, and Nels Anderson, for their help with supplying precursors.

I would like to acknowledge my mentors from Intel Corporation, Dr. Scott Clendenning and Dr. Jeff Bielefeld. Their comments and suggestions, based on their vast industrial research experiences, have been of great assistance in identifying the problems and possible steps toward achieving solutions in my main dissertation project. I would also like to thank my committee members, Professor Elif Ertekin and Professor Sameh Tawfick, for their constructive inputs. Special thanks go to Professor Tawfick and Carly Sandin for their efforts in mechanical testing and study of thin films.

I am especially thankful to my past and current colleagues in the Abelson research group – Andrew Cloud, Shaista Babar, Wenjiao Wang, Pengyi Zhang, Elham Mohimi, Zhejun Zhang, Xiaoqing Chu, and Kinsey Canova – for their assistance in lab work and cheerful discussions on topics that extend outside research.

I have received immense help from the staff members at the Frederick Seitz Materials Research Laboratory; special thanks to Dr. Richard Haasch, Douglas Jeffers, Dr. Scott MacLaren, Dr. Kathy Walsh, Dr. Julio Soares, Dr. Timothy Spila, Dr. Honghui Zhou, and Ernest Northen.

I will forever be indebted to my family to reach where I am now. My parents never had the opportunity of higher education, but they instilled the dream in me at an early age to pursue the highest possible academic education. My sister, Purabi Talukdar, has been a constant supporter of my potential to reach that goal. Words cannot fully express the contribution of my wife (and best friend) Shejuti Guha; without her continuous support, trust and compassion, I would not be able to reach this stage of my academic career.

TABLE OF CONTENTS

LIST OF TABLES

LIST OF FIGURES

CHAPTER 1

OVERVIEW

1.1 Introduction

Many nanoscale devices require the fabrication of a 3-dimensional structure based on two or more materials that achieve the function of interest based on their contrasting optical, electronic, thermal or other properties [1]. There exist powerful methods to *remove* material, such as reactive ion etching [2], as well as methods to *assemble* small units, such as colloidal crystals [3]. However, the *coating* and *filling* of high aspect ratio features with a desired material remains a challenging problem. An innovative solution would enable significant progress in the design, demonstration, and fabrication of advanced devices that require filling. The solution should apply to a palette of materials with dielectric, metallic or refractory properties.

Filling of a high aspect ratio feature involves strongly coupled kinetic processes. The deposition precursor must pass through the opening on the sample surface, be transported to the required depth, and react on surfaces to deposit film. In addition, the reaction byproducts must be transported out of the feature without decomposing, which otherwise would add impurities to the deposited material. When the deposition rate increases monotonically with the flux of species impinging on the surface, then the transport-reaction kinetics (typically, the solution to the diffusion-reaction equation) affords a greater deposited thickness near to the opening, tapering to a smaller or even no coating at depth. When carried to completion under these conditions, the opening ultimately closes (pinches) off, leaving an unfilled void space or "seam" along the centerline of feature.

The coating nonuniformity in a deep structure can be partially mitigated if the deposition is carried out under conditions of very low surface reaction rate with respect to the transport rate. This regime is routinely achieved using atomic layer deposition (ALD) or chemical vapor deposition (CVD) in the high-pressure limit, where the deposition rate is fully saturated [4-7]. However, for technologically demanding applications, such as making lightweight composite foam materials, it is still a challenge for these techniques to achieve extremely conformal coating

(i.e., step coverage ≈ 1) in a 3-dimensional geometry with very high aspect ratio and high surface area.

While conformal coating is a challenge, perfect filling is nearly impossible by the above-mentioned conformal approaches. To achieve seamless fill in a variety of features, a potential solution is superconformal growth processes in which the film growth rate is larger at the bottom of feature than that at near the opening. Such a superconformal process will produce a "V" shape coating profile in a deep feature and gradually enlarge the V angle, thereby eliminating the seam formation. Wang, Abelson *et al.* developed a superconformal CVD process for MgO that utilizes competitive kinetic adsorption of precursor and water [8, 9]. But no single method may work for varied materials systems because different precursors have significantly different kinetic behavior on the film growth surface, including adsorption, desorption, and reaction rates.

In addition to the desired kinetics for coating and filling, the deposition processes needs to operate at low substrate temperature, due to the restrictive 'thermal budget' in the fabrication process. Because of the continuous shrinkage in device dimensions, interlayer diffusional mixing of chemical elements, which significantly degrades electrical performance of devices, is less tolerable; this becomes more crucial in the back-end (metallization) of the microelectronic device fabrication. Consequently, there is a high demand for low temperature film growth processes, which can be in conflict with requirements for near-bulk composition and properties. Low temperature processes are also useful in applications requiring the use of substrates with low melting point or tempering temperature, such as polymers.

1.2 Motivation

1.2.1 Bottom-up fill in deep trenches

A well-recognized, pressing need for bottom-up filling of features exists in the fabrication of integrated circuits (IC) in microelectronic devices. As characteristic dimensions are progressively scaled down, future designs call for higher aspect ratio trenches and vias in the device isolation [10], 'back end' metallization [11], and reverse tone patterning [12] in ICs. The International Technology Roadmap for Semiconductors specifies filling as "challenging,

especially for low-k dual damascence metal structures and DRAM at nano-dimensions" [13]. In addition to ICs, filling trenches with specific material is essential in MEMS [14] and photonic [15, 16] device manufacturing.

Filling defects include residual void space or formation of a low-density seam along the centerline [17]. This seam is unacceptable in many applications because it leads to a degradation of performance, including thermal or mechanical properties [18, 19], or electrical conductivity [20-22], or to a higher etch rate during surface planarization processes [23].

1.2.2 Reported filling methods

Four available filling methods in the literature – iodine-catalyzed CVD of Cu and Mn [24-26], electrodeposition using curvature enhanced accelerator coverage [1, 27-31], high density plasma CVD for AR ~ 2 to 4 [32, 33], and atomic layer deposition via highly conformal coating [16, 34-39] – were summarized in a previous publication by our group [8]. In addition to discussing these reported filling methods, that report introduced a new superconformal method for MgO by two-reactant CVD of $Mg(DMADB)_2$ precursor and water co-reactant [8]. In general, the use of a filling method depends on the kinetic behavior of the deposition precursor, and via those kinetics, on the geometry of the feature to be filled. For example, the superconformal process for MgO film growth depends on the combination of (i) a competition for surface adsorption sites between precursor and water co-reactant, and (ii) a large ratio in molecular diffusivity between the high-mass precursor and low-mass water. The underlying requirements of a filling method are not necessarily achievable with available precursor molecules.

1.2.3 This dissertation: New superconformal CVD method

In this dissertation, I report a newly discovered superconformal CVD method that affords bottom-up filling of trenches with oxide using a precursor that is otherwise not ideal – no surface competition and high reactivity. The film growth rate increases with depth such that the profile of material develops a "V" shape that fills in along the centerline without a seam of low density material. The method utilizes low pressures of a metal precursor plus a forward-directed, lower-pressure flux of co-reactant (water). Under these conditions, many of the co-reactant molecules

travel ballistically to the trench bottom where a fraction of them reflect. This scattering, which *creates a virtual source of co-reactant from the trench bottom*, leads to a superconformal growth process whose rate is highest at the bottom and declines towards the opening. Simultaneous with this superconformal component is the typical subconformal growth process due to the portion of the co-reactant flux that enters the trench opening isotropically; with a sufficiently large forward-directed flux, however, the overall profile is superconformal.

1.2.4 Conformal coating of complex 3-dimensional structures

It has long been a goal in the materials research and development community to create lightweight composite materials with enhanced mechanical, thermal or electrical properties. One such realization is described by Prof. Michael F. Ashby in terms of modulus–density relationship in hybrid materials (Figure 1.1) [40]. As pointed out by a green arrow in Figure 1.1, there is an empty space in the top left corner of Ashby's modulus–density chart, indicating the vector for new materials development. A new process route to access that empty space is to make hybrid foam materials by conformally coating (uniform thickness) a porous template, such as a carbon nanotube (CNT) forest, with a second material.

CNT forests have a linearly-aligned structure with low-density, high porosity, and weak (van der Waals) links at internal crossing points [41, 42]. A 3-dimensional composite (hybrid) material can be created by conformal (uniform) coating of a thin film onto the CNTs, i.e., the forest serves as a growth scaffold. The mechanical, thermal and electrical behaviors of the hybrid can be engineered with the appropriate choices of coating material, coating thickness and design (shape factor) of the scaffold. For mechanical applications in extreme environments, HfB_2 is an excellent candidate as a coating material: HfB_2 is a refractory metallic ceramic with a high melting temperature (3250 °C), high bulk hardness (29 GPa) and a metallic resistivity of 8-15 μΩ-cm [43, 44]. For applications that require a dielectric, conformal coating of CNTs with HfO_2 (high-K) is an attractive option; examples include: field effect transistors [45], and metal-insulator-metal capacitors for energy storage [46],

1.3 Experimental Systems

All film growth experiments in this dissertation, except for HfB_2 and SiN_x, are conducted in a thermal cold-wall CVD system with a base pressure of ~ 10^{-8} Torr (Figure 1.2), equipped with *in situ* spectroscopic ellipsometry (SE) (J. A. Woollam M-88). This system has been described in the Ph.D. dissertations of former group members Dr. Brent A. Sperling [47] and Dr. Wenjiao Wang [48]. The deposition precursor and water co-reactant are injected to the reactor using two sets of parallel tubes. One set points towards the reactor inside walls, so that the reactant molecules experience multiple scattering events before they reach the substrate; under these conditions the partial pressures above the substrate are equal to the average values measured by the capacitance manometer elsewhere on the chamber. This set of inlets are used for isotropic (uniform) fluxes of reactants. The other set of tubes are pointed perpendicularly at the substrate and is 7 cm away from the substrate holder surface; this set of inlets is used for forward-directed fluxes of reactants. In situ SE is used to monitor real time film growth on planar substrates, which is then fitted with Cauchy optical models for different film materials [49].

HfB_2 film growth is performed in a hot-wall static (unpumped) CVD system; details of this system are described in Chapter 6. SiN_x film growth is done in a Pyrex tube hot-wall CVD reactor, evacuated with a roughing vacuum pump with a base pressure of ~ 10^{-2} Torr (Figure 1.3).

Ex situ analyses of film morphology, composition, crystallinity, and optical properties are done in the Center for Microanalysis of Materials, Material Research Laboratory at University of Illinois.

1.4 Chapter Summaries

Chapter 2: Superconformal coating and filling of deep trenches by CVD with forward-directed fluxes.

A new superconformal CVD method is experimentally demonstrate for filling trenches with HfO_2 using 0.09 mTorr tetrakis(dimethylamido)hafnium (TDMA-Hf) precursor and 0.009 mTorr H_2O co-reactant. Precursor-rich growth conditions at a substrate temperature $\leq$ 270 °C are used to assure that the growth rate is kinetically limited (determined) by the H_2O flux

and is nearly independent of the TDMA-Hf flux. Forward-directed flux of water directly impinges at the trench bottom, where they partially reflect; this creates a virtual source of water at the bottom. Since the film growth rate is proportional to the water flux, the virtual source creates a coating profile that is thickest at the bottom, i.e., V-shaped, as needed for trench filling. Under these conditions, the growth rate in a trench with an aspect ratio of 3.5 increases from 0.6 nm/min at the top to 1.0 nm/min at the bottom sidewalls (step coverage = 1.6).

- "Superconformal coating and filling of deep trenches by chemical vapor deposition with forward-directed fluxes", T. K. Talukdar, W. B. Wang, G. S. Girolami, and J. R. Abelson, *ready for submission (waiting for patent disclosure).*

Chapter 3: Modeling of superconformal CVD in deep trenches with forward-directed fluxes.

A kinetic model is developed to simulate superconformal CVD with forward-directed fluxes. The model employs Markov chain calculations for the ballistic transport of water from the isotropic source outside the trench and the virtual source created by the impinging forward-directed flux. We investigate the range of parameters that afford, in the model output, trench profiles similar to experiment. These results are then extended to a rectangular trench with AR of 10 and V-shaped trenches with different sidewall taper angles (1 to 5°) with respect to the trench axis. The model provides quantitative information, such as the critical V angle for complete fill when a rectangular trench covert to a V-shaped one and the dependence of the superconformal process (aspect ratio) on the water sticking probability and the fraction of forward-directed water flux

- "Superconformal coating and filling of deep trenches by chemical vapor deposition with forward-directed fluxes", T. K. Talukdar, W. B. Wang, G. S. Girolami, and J. R. Abelson, *ready for submission (waiting for patent disclosure).*

Chapter 4: Seamless fill of deep trenches by CVD: Use of a molecular growth inhibitor to eliminate pinch-off.

We demonstrate that an isotropic co-flow of a neutral inhibitor molecule during the superconformal growth of HfO_2 in trenches, using TDMA-Hf and forward-directed water flux, can suppress bread-loaf formation at the trench opening. Consequently, the pinch-off of the trench opening is eliminated, which affords a complete and seam-free fill of HfO_2 in trenches with aspect

ratio of ≤ 10. The effect of inhibitor sticking probability on film grown at the trench sidewalls near the opening is obtained by simulating the inhibitor flux distribution using a Markov chain ballistic transport model; an inhibitor with a high sticking probability and a low desorption rate is ideal to eliminate the pinch-off at the trench opening.

- "Seamless fill of deep trenches by chemical vapor deposition: Use of a molecular growth inhibitor to eliminate pinch-off", T. K. Talukdar, G. S. Girolami, and J. R. Abelson, *in preparation.*

Chapter 5: High quality MgO film grown at high rate by low temperature conformal CVD.

MgO thin films are deposited at a substrate temperature of 270-350 °C using magnesium N,N-dimethylaminodiboranate precursor, $Mg(DMADB)_2$, and H_2O co-reactant. A growth rate of up to 200 nm/min is obtained with optimized deposition conditions. Highly conformal coating with 98 % step coverage in trenches of aspect ratio 9 is obtained at a substrate temperature of 270 °C and a growth rate of 7.5 nm/min. Most of the films have dense and column-free microstructures with low surface roughness; the film density, measured by a combination of RBS and SEM, is 82 – 86 % of bulk. Films grown on Si substrates have good adhesion and low coefficient of friction (~ 0.1) in nanoscratch measurements. The refractive indices of the films are slightly lower than those of bulk MgO, consistent with the reduced physical densities. Depending on the growth conditions, the C content in the films varies between 0.7 – 6.0 at. %, and the B content ranges from 1 – 16 at. %. B in the film is present in the B_2O_3 chemical state; after subtracting the O content in B_2O_3, the O/Mg ratio ~ 1.02 in the MgO matrix. A film grown at a temperature of 270 °C and a growth rate of 6 nm/min has an electrical dielectric constant of 9.5 and a breakdown strength of 6 MV/cm.

- "High Quality MgO Film Grown at High Rate by Low Temperature Conformal CVD", T. K. Talukdar, S. Liu, Z. Zhang, F. Harwath, G. S. Girolami, and J. R. Abelson, *in preparation.*

Chapter 6: Conformal coating of carbon nanotube forests by low temperature CVD.

We demonstrate conformal HfB_2 coating in CNT forests with height of ≤ 1.7 mm by employing static (unpumped) chemical vapor deposition (SCVD), utilizing a high pressure of the $Hf(BH_4)_4$ precursor, up to its full vapor pressure. When the substrate temperature is kept low (≤ 200 °C in present experiments), the growth saturation occurs at a pressure that is orders of magnitude lower than the maximum precursor pressure limit, thereby affording a high degree of conformality in the forests. A step coverage of 92 % is achieved when the forest height is 80 μm. In addition to high conformality, HfB_2 coating creates strong joints wherever the neighboring CNTs touch each other; this converts the CNT forest with van der Waals interactions into a mesoscale composite foam with greatly enhanced mechanical performance.

We also demonstrate a case of two-reactant conventional pumped CVD using HfO_2 growth from TDMA-Hf precursor and water co-reactant, in which the kinetics do not afford simultaneous growth saturation for both the reactants. In this case, we deliver the reactants as forward-directed fluxes (ballistic transport) to achieve conformal HfO_2 coating within a forest. The forward-directed flux method is especially useful for CVD precursors for which the growth saturation is not observed within the limit of vapor pressure.

- "Conformal coating of carbon nanotube forests by low temperature chemical vapor deposition", T. K. Talukdar, S. Liu, C. Sandin, S. Tawfick, G. S. Girolami, and J. R. Abelson, *in preparation.*

Chapter 7: Stiffness and strength of conformal HfB_2 coated carbon nanotube forests.

We demonstrate the fabrication of HfB_2-CNT composite structures. The CVD of CNTs allows the fabrication of a scaffold having very low weight density and large open pores that represent an ideal substrate for subsequent coating and functionalization. Using an optimized SCVD process, the CNT scaffolds are then conformally coated with different HfB_2 film thicknesses to effectively increase the strength and modulus of the structures. Owing to the large surface area of the CNTs, a HfB_2 coating thickness of 45 nm in a 25 μm thick composite structure, has ~ 36 % HfB_2 content. The properties are analyzed in light of the mechanics of porous materials; the modulus and compressive strength follow a power law relationship with respect to the density ($\sim \rho^n$) with exponents n = 3 and 3.4, respectively. We show that this scaling can be

mathematically predicted using a minimalistic model, considering that the compressive response of the composite structures results from the bending of the coated CNTs. The nearly unity step coverage of the HfB_2 coating allows the implementation of this simple model. These results are useful steps towards the realization of low density thermal protection system using ultra-high temperature ceramics, which are otherwise extremely difficult to process.

- "Synthesis and mechanical behavior of ultra-high temperature resistant coatings (UHTC) using boride-coated carbon nanotube scaffolds", C. Sandin, T. K. Talukdar, S. Tawfick, and J. R. Abelson, *in preparation.*

Chapter 8: Future possibilities and preliminary results.

Based on the works reported this dissertation, I discuss promising future possibilities and present proof-of-concept results.

1.5 References

1. Kim, H., H.B.R. Lee, and W.J. Maeng, *Applications of atomic layer deposition to nanofabrication and emerging nanodevices.* Thin Solid Films, 2009. **517**(8): p. 2563-2580.

2. Lang, W., *Silicon microstructuring technology.* Materials Science & Engineering R-Reports, 1996. **17**(1): p. 1-55.

3. Murray, C.B., C.R. Kagan, and M.G. Bawendi, *Synthesis and characterization of monodisperse nanocrystals and close-packed nanocrystal assemblies.* Annual Review of Materials Science, 2000. **30**: p. 545-610.

4. George, S.M., *Atomic Layer Deposition: An Overview.* Chemical Reviews, 2010. **110**(1): p. 111-131.

5. Leskela, M. and M. Ritala, *Atomic layer deposition (ALD): from precursors to thin film structures.* Thin Solid Films, 2002. **409**(1): p. 138-146.

6. Kim, H., *Atomic layer deposition of metal and nitride thin films: Current research efforts and applications for semiconductor device processing.* Journal of Vacuum Science & Technology B, 2003. **21**(6): p. 2231-2261.

7. Yanguas-Gil, A., Y. Yang, N. Kumar, and J.R. Abelson, *Highly conformal film growth by chemical vapor deposition. I. A conformal zone diagram based on kinetics.* Journal of Vacuum Science & Technology A, 2009. **27**(5): p. 1235-1243.

8. Wang, W.J.B., N.N. Chang, T.A. Codding, G.S. Girolami, and J.R. Abelson, *Superconformal chemical vapor deposition of thin films in deep features.* Journal of Vacuum Science & Technology A, 2014. **32**(5): p. 051512.

9. Wang, W.B. and J.R. Abelson, *Filling high aspect ratio trenches by superconformal chemical vapor deposition: Predictive modeling and experiment.* Journal of Applied Physics, 2014. **116**(19): p. 194508.

10. Nandakumar, M., A. Chatterjee, S. Sridhar, K. Joyner, M. Rodder, and I.C. Chen. *Shallow trench isolation for advanced ULSI CMOS technologies*. in *International Electron Devices Meeting 1998. Technical Digest (Cat. No.98CH36217)*. 1998.

11. Ireland, P.J., *High aspect ratio contacts: A review of the current tungsten plug process.* Thin Solid Films, 1997. **304**(1-2): p. 1-12.

12. *Private communication with Applied Materials, Inc.* 2015.

13. *International Technology Roadmap for Semiconductors*. 2015.

14. Ayazi, F. and K. Najafi, *High aspect-ratio combined poly and single-crystal silicon (HARPSS) MEMS technology.* Journal of Microelectromechanical Systems, 2000. **9**(3): p. 288-294.

15. Jordana, E., J.M. Fedeli, P. Lyan, J.P. Colonna, P. Gautier, N. Daldosso, L. Pavesi, Y. Lebour, P. Pellegrino, B. Garrido, J. Blasco, F. Cuesta-Soto, and P. Sanchis. *Deep-UV Lithography Fabrication of Slot Waveguides and Sandwiched Waveguides for Nonlinear Applications*. in *2007 4th IEEE International Conference on Group IV Photonics*. 2007.

16. Saynatjoki, A., T. Alasaarela, A. Khanna, L. Karvonen, P. Stenberg, M. Kuittinen, A. Tervonen, and S. Honkanen, *Angled sidewalls in silicon slot waveguides: conformal filling and mode properties.* Optics Express, 2009. **17**(23): p. 21066-21076.

17. Kim, B., C. Sharbono, T. Ritzdorf, and D. Schmauch, *Factors affecting copper filling process within high aspect ratio deep vias for 3D chip stacking.* 56th Electronic Components & Technology Conference 2006, Vol 1 and 2, Proceedings, 2006: p. 838-+.

18. Abdolvand, R., H. Johari, G.K. Ho, A. Erbil, and F. Ayazi, *Quality factor in trench-refilled polysilicon beam resonators.* Journal of Microelectromechanical Systems, 2006. **15**(3): p. 471-478.

19. Schenk, H., P. Durr, D. Kunze, H. Lakner, and H. Kuck, *A resonantly excited 2D-micro-scanning-mirror with large deflection.* Sensors and Actuators a-Physical, 2001. **89**(1-2): p. 104-111.

20. Chen, C.C., I.C. Kao, H.C. Kuo, and H.J. Chien, *Studying of physical characteristics and optimizing of gap filling for tungsten.* Materials Science in Semiconductor Processing, 2011. **14**(3-4): p. 235-240.

21. Kubo, A., T. Homma, and Y. Murao, *An SiO2 film deposition technology using tetraethylorthosilicate and ozone for interlayer metal dielectrics.* Journal of the Electrochemical Society, 1996. **143**(5): p. 1769-1773.

22. Lin, X.F., X. Ma, and J.J. He, *Void-Filling and Loss Reduction in PECVD Silica Waveguide Devices Using Boron-Germanium Codoped Upper Cladding.* Ieee Photonics Technology Letters, 2010. **22**(20): p. 1491-1493.

23. *Private communication with Intel Corporation*. 2016.

24. Au, Y., Y.B. Lin, and R.G. Gordon, *Filling Narrow Trenches by Iodine-Catalyzed CVD of Copper and Manganese on Manganese Nitride Barrier/Adhesion Layers.* Journal of the Electrochemical Society, 2011. **158**(5): p. D248-D253.

25. Josell, D., S. Kim, D. Wheeler, T.P. Moffat, and S.G. Pyo, *Interconnect fabrication by superconformal iodine- catalyzed chemical vapor deposition of copper.* Journal of the Electrochemical Society, 2003. **150**(5): p. C368-C373.

26. Pyo, S.G., S. Kim, D. Wheeler, T.P. Moffat, and D. Josell, *Seam-free fabrication of submicrometer copper interconnects by iodine-catalyzed chemical vapor deposition.* Journal of Applied Physics, 2003. **93**(2): p. 1257-1261.

27. Moffat, T.P., J.E. Bonevich, W.H. Huber, A. Stanishevsky, D.R. Kelly, G.R. Stafford, and D. Josell, *Superconformal electrodeposition of copper in 500-90 nm features.* Journal of the Electrochemical Society, 2000. **147**(12): p. 4524-4535.

28. Baker, B.C., C. Witt, D. Wheeler, D. Josell, and T.P. Moffat, *Superconformal silver deposition using KSeCN derivatized substrates.* Electrochemical and Solid State Letters, 2003. **6**(5): p. C67-C69.

29. Josell, D., C. Burkhard, Y. Li, Y.W. Cheng, R.R. Keller, C.A. Witt, D.R. Kelley, J.E. Bonevich, B.C. Baker, and T.P. Moffat, *Electrical properties of superfilled sub-micrometer silver metallizations.* Journal of Applied Physics, 2004. **96**(1): p. 759-768.

30. Josell, D., D. Wheeler, and T.P. Moffat, *Gold superfill in submicrometer trenches: Experiment and prediction.* Journal of the Electrochemical Society, 2006. **153**(1): p. C11-C18.

31. Moffat, T.P., D. Wheeler, M.D. Edelstein, and D. Josell, *Superconformal film growth: Mechanism and quantification.* Ibm Journal of Research and Development, 2005. **49**(1): p. 19-36.

32. Cote, D.R., S.V. Nguyen, A.K. Stamper, D.S. Armbrust, D. Tobben, R.A. Conti, and G.Y. Lee, *Plasma-assisted chemical vapor deposition of dielectric thin films for ULSI semiconductor circuits.* Ibm Journal of Research and Development, 1999. **43**(1-2): p. 5-38.

33. Nishimura, H., S. Takagi, M. Fujino, and N. Nishi, *Gap-fill process of shallow trench isolation for 0.13 um technologies.* Japanese Journal of Applied Physics Part 1-Regular Papers Short Notes & Review Papers, 2002. **41**(5A): p. 2886-2893.

34. Choi, K.K., J. Kee, S.H. Kim, M.S. Park, C.G. Park, and D.K. Kim, *Filling performance and electrical characteristics of Al2O3 films deposited by atomic layer deposition for through-silicon via applications.* Thin Solid Films, 2014. **556**: p. 560-565.

35. Graugnard, E., V. Chawla, D. Lorang, and C.J. Summers, *High filling fraction gallium phosphide inverse opals by atomic layer deposition.* Applied Physics Letters, 2006. **89**(21).

36. Karuturi, S.K., L.J. Liu, L.T. Su, Y. Zhao, H.J. Fan, X.C. Ge, S.L. He, and A.T.I. Yoong, *Kinetics of Stop-Flow Atomic Layer Deposition for High Aspect Ratio Template Filling through Photonic Band Gap Measurements.* Journal of Physical Chemistry C, 2010. **114**(35): p. 14843-14848.

37. Lee, J.S., B. Min, K. Cho, S. Kim, J. Park, Y.T. Lee, N.S. Kim, M.S. Lee, S.O. Park, and J.T. Moon, *Al2O3 nanotubes and nanorods fabricated by coating and filling of carbon nanotubes with atomic-layer deposition.* Journal of Crystal Growth, 2003. **254**(3-4): p. 443-448.

38. Wang, J.J., X.G. Deng, R. Varghese, A. Nikolov, P. Sciortino, F. Liu, L. Chen, and X.M. Liu, *Filling high aspect-ratio nano-structures by atomic layer deposition and its applications in nano-optic devices and integrations.* Journal of Vacuum Science & Technology B, 2005. **23**(6): p. 3209-3213.

39. Hausmann, D., J. Becker, S.L. Wang, and R.G. Gordon, *Rapid vapor deposition of highly conformal silica nanolaminates.* Science, 2002. **298**(5592): p. 402-406.

40. Ashby, M.F., *Materials Selection in Mechanical Design*. 5th ed. 2016: Elsevier Science.

41. Saito, R., G. Dresselhaus, and M.S. Dresselhaus, *Physical Properties of Carbon Nanotubes*. 1998: Imperial College Press.

42. Huang, Z.P., J.W. Wu, Z.F. Ren, J.H. Wang, M.P. Siegal, and P.N. Provencio, *Growth of highly oriented carbon nanotubes by plasma-enhanced hot filament chemical vapor deposition.* Applied Physics Letters, 1998. **73**(26): p. 3845-3847.

43. Fahrenholtz, W.G., G.E. Hilmas, I.G. Talmy, and J.A. Zaykoski, *Refractory diborides of zirconium and hafnium.* Journal of the American Ceramic Society, 2007. **90**(5): p. 1347-1364.

44. Juretschke, H.J. and R. Steinitz, *Hall Effect and Electrical Conductivity of Transition-Metal Diborides.* Journal of Physics and Chemistry of Solids, 1958. **4**(1-2): p. 118-127.

45. Willinger, M.G., G. Neri, A. Bonavita, G. Micali, E. Rauwel, T. Herntrich, and N. Pinna, *The controlled deposition of metal oxides onto carbon nanotubes by atomic layer deposition: examples and a case study on the application of V2O4 coated nanotubes in gas sensing.* Physical Chemistry Chemical Physics, 2009. **11**(19): p. 3615-3622.

46. Sohn, J.I., Y.S. Kim, C. Nam, B.K. Cho, T.Y. Seong, and S. Lee, *Fabrication of high-density arrays of individually isolated nanocapacitors using anodic aluminum oxide templates and carbon nanotubes.* Applied Physics Letters, 2005. **87**(12).

47. Sperling, B.A., *Kinetic Roughening during Hot-Wire Chemical Vapor Deposition of Hydrogenated Amorphous Silicon*, in *Materials Science and Engineering*. 2006, University of Illinois at Urbana-Champaign.

48. Wang, W., *Super-Conformal Coating and Filling of High Aspect Ratio Recessed Structures by Two-Molecule CVD*, in *Materials Science and Engineering*. 2014, University of Illinois at Urbana-Champaign.

49. Jenkins, F.A. and H.E. White, *Fundamentals of Optics*. 3rd ed. 1957, New York: McGraw-Hill.

1.6 Figures

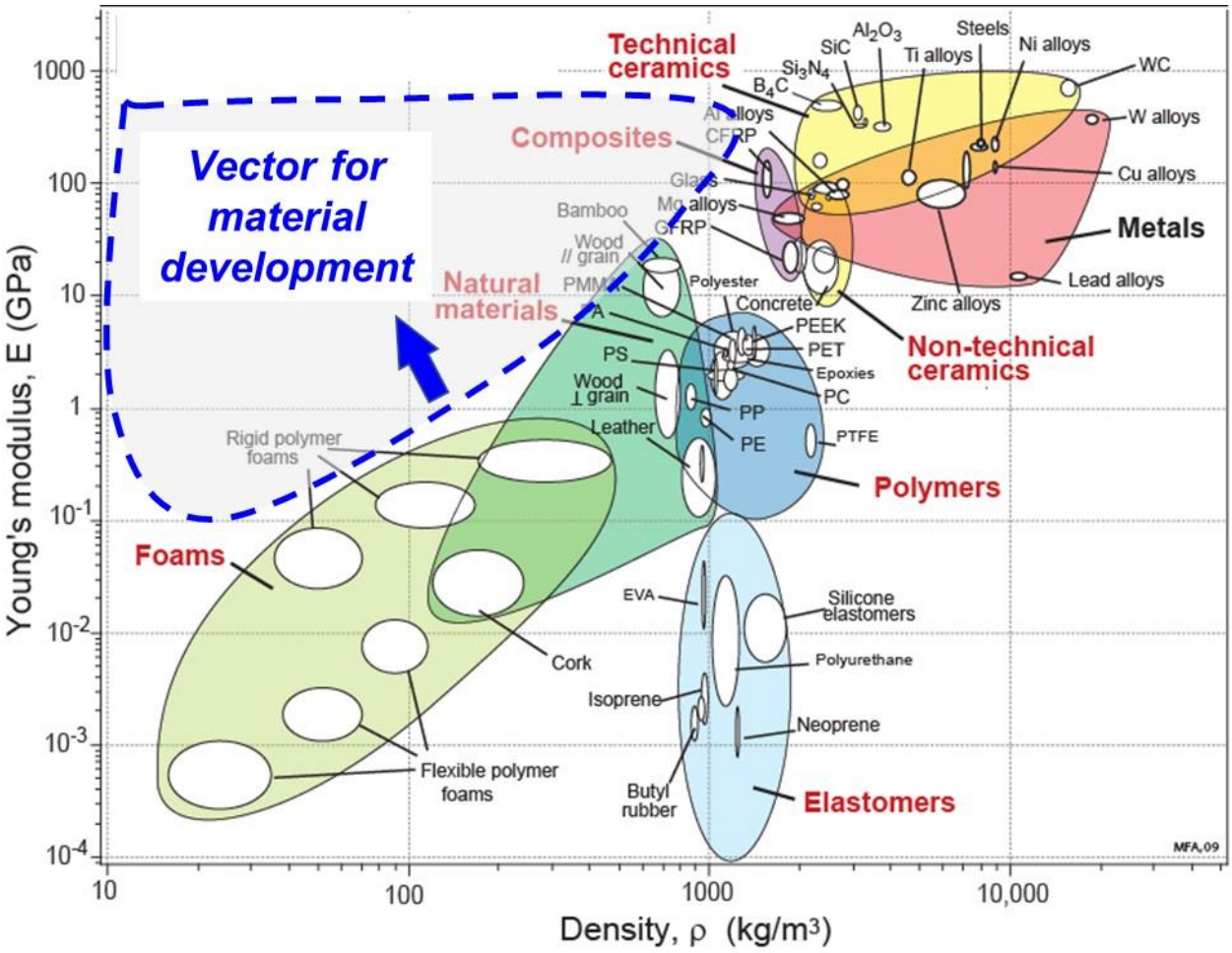

Figure 1.1. Ashby chart showing Young's modulus vs. density for selected materials. Reproduced from reference [40].

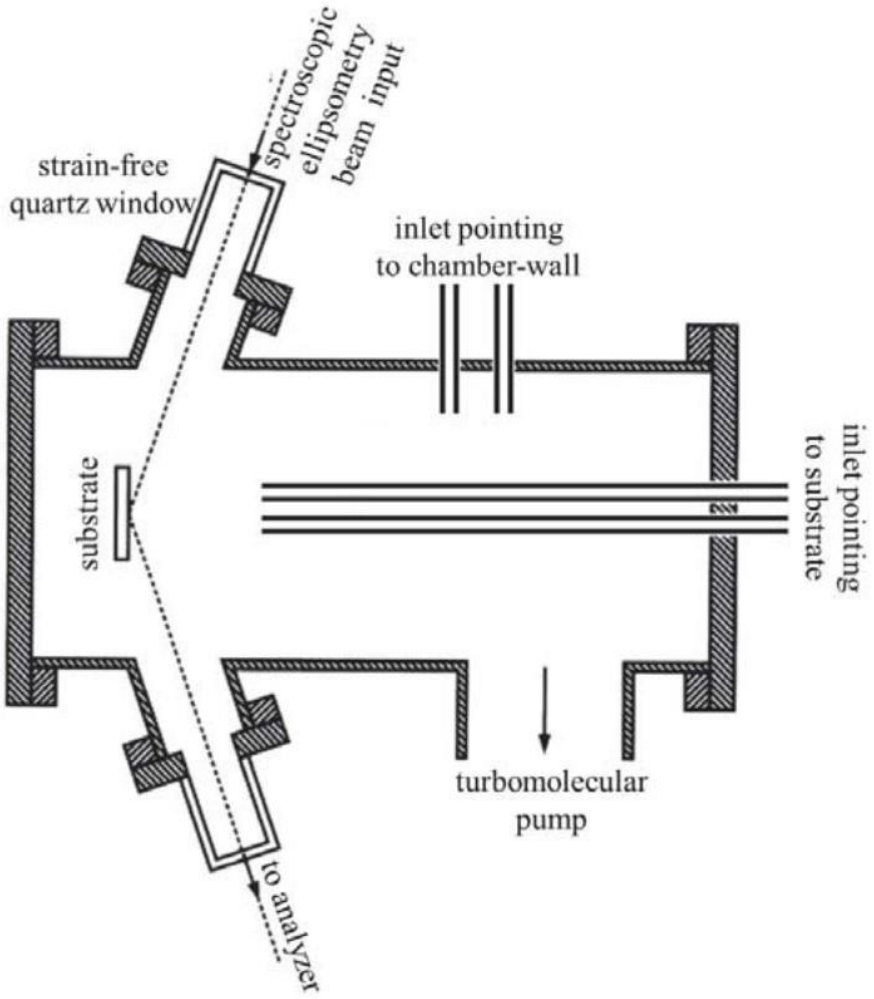

Figure 1.2. Schematic of the cold-wall CVD reactor used for HfO_2 and MgO films growth.

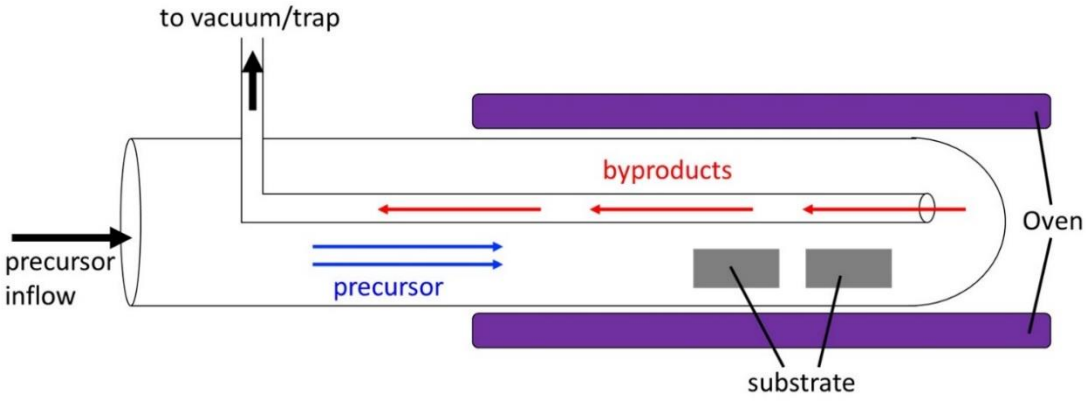

Figure 1.3. Schematic of the Pyrex tube hot-wall CVD reactor used for SiN_x film growth

CHAPTER 2

SUPERCONFORMAL COATING AND FILLING OF DEEP TRENCHES BY CVD WITH FORWARD-DIRECTED FLUXES

2.1 Introduction

2.1.1 Background

Void-free filling of high aspect ratio (AR = 3:1 to 10:1) structures, such as trenches or vias, is necessary in nanoscale device fabrication. Examples include shallow trench isolation in integrated circuits [1] and optical waveguides in photonic devices [2, 3]. Gas-phase coating methods such as chemical vapor deposition (CVD) and atomic layer deposition (ALD) can be operated in a regime that is kinetically limited by the surface reaction rate rather than by the precursor transport rate. In that regime, the precursor diffuses everywhere within the structure, which affords a nearly uniform coating thickness. However, complete filling of a deep structure is ultimately sensitive to the geometry. In a trench with parallel sidewalls, the width of the opening along the centerline decreases as film builds up on the sidewalls, and the rate of precursor transport by molecular diffusion declines until it becomes rate limiting. As the supply of precursor deep within the structure dwindles, a residual void (seam) is left along the centerline. This seam is unacceptable in many applications because it leads to a degradation of performance, including thermal or mechanical properties [4, 5], or electrical conductivity [6-8], or to a higher etch rate during surface planarization processes [9].

We have previously shown, using both molecular diffusion and ballistic transport models, that a V-shape with an outwards taper is required for conformal growth to afford seam-free filling of a trench [10]. The use of a taper, however, places constraints on the device architecture and stringent demands on the trench fabrication process. A possible solution is to develop a coating method with *superconformal* kinetics such that the growth rate is faster at the bottom of the structure, which progressively creates a V-shaped taper in the fill material. In principle, such a method could even fill structures that originally have a slightly inwards (re-entrant) taper. We

previously demonstrated such a superconformal process [11] for MgO based on the combination of (i) a competition for surface adsorption sites between precursor and water co-reactant, and (ii) a large ratio in molecular diffusivity between the high-mass precursor and low-mass water.

2.1.2 Approach

Here, we develop superconformal growth of HfO_2 from tetrakis(dimethylamido)hafnium (TDMA-Hf), $Hf(NMe_2)_4$. We choose the TDMA-Hf precursor because it reacts with water under ALD conditions to afford excellent quality HfO_2 for gate dielectrics [12-17]. However, the reaction kinetics of this molecule differ strongly from those which are the basis for superconformal MgO deposition: as we show below, the growth rate, instead of being limited by an adsorption competition at the growth surface, is nearly independent of the flux of the Hf precursor and increases approximately linearly with the flux of water. The lack of competition for surface sites causes CVD growth of HfO_2 from TDMA-Hf and water to be subconformal.

To achieve superconformal CVD growth from TDMA-Hf, we introduce a new approach that utilizes a forward-directed (ballistic) transport of water. The forward-directed flux is established by injecting water vapor through a small diameter delivery tube aligned with the axis of the trench; rapid expansion of this vapor into the partial vacuum of the chamber affords a flux with a small cone angle, similar to that from a Knudsen evaporation cell with a long chimney. The sticking probability of water molecules upon impact with the film growth surface is less than unity (0.02–0.20 in the present experiments). Therefore, water molecules that arrive forward-directed at the trench bottom mostly reflect, *which creates a virtual source of this reactant at the trench bottom*. The virtual source creates a coating profile that is thickest at the bottom, i.e., V-shaped, as needed for trench filling. In addition to the forward-directed flux, some water arrives at the trench opening in an isotropic distribution from the partial pressure of water in the chamber background. For the present conditions, the net growth profile is superconformal when the virtual source due to the forward-directed flux is at least equal to that from the background, and when the aspect ratio is not too high. In addition, we show that premature pinch-off, which occurs near the end of the filling process, can be eliminated by injecting an inhibitor molecule that reduces the film growth rate near the trench opening. The use of the inhibitor is potentially advantageous, as

it does not cause undesirable damage to the substrate structures, compared with the use of periodic etch-back to keep the trench open [9, 18].

2.2 Experimental

The film growth experiments are conducted in a turbo-pumped cold-wall CVD system described elsewhere [19]. The base pressure is 5×10^{-8} Torr, most of which is H_2 [20]; the substrate is heated radiatively by a tungsten wire mounted behind the substrate holder; the temperature is varied in the range of 180-270 °C. The TDMA-Hf precursor (≥ 99.99 %) is obtained from Sigma-Aldrich and kept in a Pyrex container adapted to a stainless-steel fitting. There is no flow regulation device; the mass flow is controlled by heating the source container to temperatures of 25 to 50 °C; the delivery tube is heated to 80 °C (slightly below precursor decomposition temperature of 90 °C [12]) to avoid condensation on its sidewalls; no carrier gas is used for the precursor. Deionized (DI) water at room temperature is used as the co-reactant; the water partial pressure is controlled with a needle valve. Precursor and water are supplied through separate stainless-steel tubes (4 mm i.d.). The precursor and water delivery tubes can be pointed directly at the substrate (they terminate 7 cm away from the substrate surface) or at the chamber sidewall; the configuration will be specified for each experiment below. The partial pressures reported here are the average values inside the reactor, which were measured with only precursor or only water flowing before the growth experiments. During film deposition, a slow rate of reaction in the gas phase or on the room-temperature chamber sidewalls will consume a portion of the molecules, hence, the partial pressures reaching the substrate during growth are smaller than those measured above. Growth rate measurements are done on 1.5 × 1.0 cm planar Si wafers covered with native oxide, which are cleaned with standard solvents (in the order of acetone, isopropyl alcohol, DI water, isopropyl alcohol, and then dried in a N_2 stream) that do not etch the native oxide. For conformal coating and filling studies, lithographically defined microtrenches with SiN sidewalls are used.

Film microstructure and thickness are determined by cross-sectional scanning electron microscopy (SEM). The refractive indices of HfO_2 films are derived from *ex situ* spectroscopic ellipsometry data acquired at incident angles of 50°, 60°, and 70° and fit to the Cauchy equation

[21]. The film thickness during growth is determined from *in situ* spectroscopic ellipsometry (SE) data using the derived indices and a multilayer optical model; surface and interfacial roughness layers are not included because AFM data indicate that the rms surface roughness is < 1 nm. In calibration experiments, the film thickness measured by ellipsometry is within ± 5 % of that determined from SEM cross-sectional images. The reported film growth rate is the final thickness divided by the duration of growth; this calculation assumes that there is no significant nucleation delay, which we verified by real-time SE in the growth chamber. Chemical composition and bonding are determined by X-ray photoelectron spectroscopy (XPS), and surface roughness is measured by atomic force microscopy (AFM). Rutherford backscattering spectrometry (RBS) is used to measure the areal density of Hf atoms; this value is divided by the film thickness as measured by SEM to give the density of the Hf sublattice, which is 86 % that of bulk HfO_2.

The sticking probability of water per sidewall collision is calculated as follows. Measurement of the growth rate over a large area planar substrate reveals that most of the growth from the forward-directed flux occurs in a circle of radius ~ 18 mm (7 cm away from the outlet of the tube), with a linear variation in rate from the center to the edge of the circle (Figure 2.1). This distribution is very similar to that predicted by the cone approximation for a nozzle-jet evaporation source [22]. The total mass flow of water through the doser tube is calculated from the steady-state partial pressure and the measured chamber pumping speed of ~ 50.5 *l*/s for water. Comparison of the impinging water flux on the circular area (radius ~ 18 mm) to the film growth rate (expressed as a flux, for 86 % bulk density) indicates that the water sticking probability β is ~ 0.02 under the conditions used for the data of Figures 2.6 – 2.10.

Conformality is reported as step coverage, which is conventionally defined as the ratio of film thickness on the sidewall at the bottom of the trench divided by the thickness just below the opening. In some of the present experiments, the film thickness falls to a minimum partway down the trench sidewall rather than at the bottom; we take this minimum thickness to compute the step coverage.

2.3 Growth Results and Discussion

The goal of the present study is to achieve the bottom-up filling of trenches with HfO_2 by CVD. For this purpose, we have investigated the well-studied combination of precursors tetrakis-(dimethylamido)hafnium (TDMA-Hf) and water [12-17]. Our earlier work demonstrated that conformal CVD of many kinds of thin films can be achieved by saturating the growth surface with precursor, and that superconformal CVD can often be achieved by starving the surface of a low molecular weight co-reactant [11, 23, 24]. One way to achieve such conditions is to use relatively high partial pressures of the metal precursor and low partial pressures of the co-reactant, and we therefore began our study in this process regime. The following sections will focus initially on ways to effect film conformality and then later will turn to evaluations of the film composition, morphology, and physical properties.

2.3.1 High-pressure experiments to grow HfO_2 with isotropic precursor fluxes

Initial experiments at relatively high partial pressures of TDMA-Hf (> 1 mTorr) were obtained by throttling of the pumping port; the gases were injected towards the chamber sidewall to afford isotropic fluxes in the chamber. It is known that TDMA-Hf reacts readily with hydroxylated surfaces and with water [12]; to reduce the reactivity, we maintained the partial pressure of water (P_{H2O}) below that of the TDMA-Hf precursor ($P_{TDMA\text{-}Hf}$). At 270 °C with 5 mTorr TDMA-Hf and 3 mTorr water pressures, the growth rate is relatively high (4 nm/min), but the microstructure is columnar and the step coverage (the ratio of film thickness at bottom sidewall to that at top sidewall) is poor (Figure 2.2).

When P_{H2O} is reduced to 1 mTorr, with the other parameters unchanged, the growth rate drops by a factor of 10 to 0.36 nm/min and the film is smooth, dense, and conformal, and the step coverage is very good (~ 90 %) in a trench with an aspect ratio of 6.5 (Figure 2.3). The results indicate that we can get reasonably conformal films, but only by going to water-starved conditions, at which the growth rate is very slow.

In an attempt to obtain a higher growth rate while preserving good conformality, the precursor and water pressures were increased to 24 and 3 mTorr, respectively; this ratio of partial pressures, 8:1, is even more water-starved than for the film of Figure 2.3. We also reduced the

temperature from 270 to 220 °C in order to decrease the rate of desorption from the growth surface. These conditions afford films with good conformality at growth rates of 1.6 nm/min on the external (top) surface and 1 nm/min on the upper sidewall of the trench (Figure 2.4). In comparison with Figure 2.3, use of higher reactant pressures and lower substrate temperature affords conformal coverage at a higher growth rate, provided that the precursor to water partial pressure ratio remains approximately ≥ 5 (the ratio in Figure 2.3). However, the larger growth rate on the exposed surfaces leads to a "bread-loaf" profile that will ultimately pinch off the trench opening before complete filling. A similar bread-loaf profile was reported for the CVD of HfO_2 from the closely related tetrakis(diethylamido)hafnium precursor and O_2, a system in which the reactivity with the oxidant is also high [25].

2.3.2 Determination of the rate law for HfO_2 growth

The results above give no indication of a superconformal regime under water-starved conditions, in sharp contrast with our prior results for MgO [11]. We therefore decided to carry out a more comprehensive investigation of the dependence of HfO_2 growth rates on the partial pressures of the two co-reactants. To a first approximation, the growth rate depends weakly on TDMA-Hf at high pressures but increases almost linearly with H_2O pressure (Figure 2.5). As noted in the Experiment section, the partial pressures are measured for each species in the absence of reaction. The loss of molecules due to chamber sidewall or gas phase reactions is probably responsible for the drop in growth rate at higher precursor pressure (Figure 2.5a). Nonetheless, the data are sufficient to illustrate that growth is dominated by the water flux (1^{st} order) and is approximately independent of precursor flux (0^{th} order) above a minimum value.

It is not possible from macroscopic data to determine the surface reaction mechanism(s) on a microscopic scale. However, the data are consistent with an Eley-Rideal mechanism in which, for a bimolecular reaction ($A + B \rightarrow product$), A adsorbs to saturation on the growth surface and impinging B reacts directly with adsorbed A without the need to compete for an available surface site (A reacts upon collision with B). In the present experiments, A is TDMA-Hf and B is H_2O. Several other bimolecular deposition reactions are thought to obey the Eley-Rideal mechanism, including TiN from TDMA-Ti and NH_3 [26], and Al_2O_3 from $AlCl_4$ and H_2O [27].

These results show that the rate law that governs the growth rate of HfO_2 has a very different functional dependence on the partial pressures of the two co-reactants than that seen in the MgO system: in the HfO_2 system, the rate law is sensitive to the H_2O partial pressure but largely independent of the Hf precursor partial pressure. In contrast, in the MgO system, the growth rate is more or less equally sensitive to the fluxes of both precursor and water; and in fact this second order kinetic dependence is the key to obtaining superconformal growth. We therefore considered whether there is a different strategy for obtaining superconformal HfO_2 films.

2.3.3 Low pressure experiments with directed flux

To obtain superconformal growth and filling using the TDMA-Hf precursor, we explored a new kinetic option that essentially entails taking a subconformal growth profile and turning it upside down in the trench. In this approach, *we deliver a significant portion of the H_2O flux directly to the trench bottom by aligning the H_2O delivery tube with the trench axis*, such that most of the water molecules travel in a forward-directed manner down the trench. When these water molecules reach the bottom of the trench, a fraction of them will reflect and create a virtual source of co-reactant located at the trench bottom. The reaction of these scattered molecules with the Hf precursor, which is delivered non-forward-directed, should result in a growth process whose rate is highest near the source and that declines towards the opening. In other words, the growth is subconformal when viewed as a function of distance from the trench bottom, but superconformal when viewed as a function of distance from the trench opening. To obtain forward-directed (molecular flow) transport between the delivery tube and the substrate, we use reduced pressures (< 0.2 mTorr), obtained by evacuating the chamber without throttling; the use of molecular flow nearly eliminates the consumption of precursor by gas phase reaction.

In initial experiments, we studied how the HfO_2 growth rate depends on the presence vs. the absence of a forward directed flux of water. To do this, a substrate that includes both steps and trenches is tilted such that the centerline of the trenches is 30° away from the axis of the H_2O delivery tube. This tilting will create two regions on the surface: those that are exposed to the forward-directed flux, and those that are shielded from this flux by being in the shadow of a surface relief feature. The growth condition is, as before, precursor rich and water starved (0.18 mTorr TDMA-Hf and 0.023 mTorr H_2O at 200 °C for 70 min) to assure that the growth rate depends

mainly on the water flux (Figure 2.6a). Because the sticking probability is much less than unity, much of the incident flux reflects from the substrate and establishes a partial pressure in the chamber; this isotropic flux also contributes to growth.

For this tilted substrate, we find that the coating thickness is larger for surfaces in line-of-sight with the source and smaller on surfaces that are shadowed (Figure 2.6b); the growth rates are 2.0 and 0.9 nm/min, respectively. The coating thickness near the bottom of trench, which is completely shadowed from the forward-directed flux, is nearly conformal before the opening is pinched-off. There is a remarkably sharp edge to the left side of the step, marked with a black rectangle in Figure 2.6b, which indicates the transition from shadowed growth (exposed to isotropic flux only) to un-shadowed growth (exposed to both isotropic and forward-directed flux). The relative film thicknesses in these two regions indicate that, under our conditions, the total flux is about 60 % directional and 40 % isotropic.

We then reoriented the substrate so that its surface normal is aligned with the axis of the H_2O delivery tube (Figure 2.7a). In this experiment, the TDMA-Hf delivery tube also points normal to the substrate, but it is displaced by 1.5 cm from the H_2O tube, so the forward-directed flux of precursor is not aligned down the axis of the trench, i.e., precursor must be transported into the trenches largely by molecular diffusion. With this configuration, the resulting film profile is remarkable: using 0.09 mTorr TDMA-Hf plus 0.009 mTorr H_2O at 200 °C for 60 min, the coating thickness on the trench sidewalls is *higher* at the bottom, with a gradual decrease in thickness toward the trench opening (Figure 2.7b). The step coverage is 1.6, i.e., *superconformal growth is achieved using a forward-directed flux*.

As mentioned above, we interpret that the forward-directed flux impinges on the trench bottom and the lower sidewalls and, because the sticking probability is < 1, creates a virtual source of reactants that originates at the trench bottom. The scattered flux of H_2O from this virtual source is thus largest at the trench bottom and decreases toward the aperture; because the film growth rate tracks the H_2O flux linearly (as we showed above), the result is that the film thickness is *greatest* at the bottom.

To prove conclusively that the superconformal effect is controlled by the forward-directed transport of H_2O, we conducted experiments in which one delivery tube is pointed down the axis

of the trench to afford forward-directed transport plus isotropic flux, and the other towards the chamber sidewall to afford isotropic flux only. Experimentally, this is done by switching the gas connections external to the chamber, leaving the tubes inside unchanged. With only water delivered in the forward-directed position, using 0.18 mTorr TDMA-Hf plus 0.023 mTorr H_2O at 200 °C for 60 min, the coating profile inside the trench is superconformal with a step coverage of 1.4 (Figure 2.8). Thus, a forward-directed flux of TDMA-Hf is not necessary to achieve superconformal growth inside the trench; instead, a forward-directed flux of H_2O is sufficient.

With only TDMA-Hf delivered in the forward-directed position (Figure 2.9a), using 0.09 mTorr TDMA-Hf plus 0.014 mTorr H_2O at 200 °C for 30 min, the coating profile reverts to subconformal with a step coverage < 1 (Figure 2.9b). This behavior is consistent with the coating profiles in Figures 2.3 and 2.4, for which H_2O is delivered isotropically. Thus, a forward-directed flux of TDMA-Hf is not sufficient for superconformal growth inside the trench, but a forward-directed flux of H_2O is necessary.

To recap, superconformal growth is obtained when the flux of water, which dominates the growth kinetics, is delivered forward-directed down the axis of the trench; superconformal growth does not require that the metal precursor be delivered forward-directed. However, pointing the metal precursor tube towards the substrate affords a higher flux at the growth surface than would be the case for an isotropic precursor flux (at the same total injection rate into the chamber), which enhances the growth rate and help to maintain kinetics that are essentially independent of the flux of precursor (Figure 2.5).

This approach can be generalized to other precursor–coreactant systems for which a kinetic regime exits such that growth is dominated by the flux of one species and coating is reasonably conformal. In preliminary screening experiments, we found that HfO_2 growth using hafnium tetra-*tert*-butoxide (HTB), $Hf(OC_4H_9)_4$, and H_2O exhibits such a kinetic regime. For a HTB pressure > 0.05 mTorr, a H_2O pressure < 0.5 mTorr, and a substrate temperature of 220 °C, the growth rate (measured on planar substrate) is limited by the H_2O flux and almost independent of the HTB flux (Figure 2.10). By choosing appropriate growth conditions (0.13 mTorr HTB and 0.163 mTorr H_2O at 220 °C for 40 min) along with a forward-directed H_2O flux, a superconformal HfO_2 coating with a step coverage of 1.3 is obtained in a trench with an aspect ratio of 3 (Figure 2.11).

2.3.4 Avoiding pinch-off

A limitation of this forward-directed flux method is that rapid film growth occurs on the exposed top surfaces and creates a 'bread-loaf' profile near the top of trench that narrows the opening. An example of this effect is seen for growth of an HfO_2 film in a trench with 3.5 aspect ratio, using 0.09 mTorr TDMA-Hf and 0.014 mTorr H_2O at 200 °C for 60 min (Figure 2.12a). At a longer growth time of 90 min, pinch-off occurs prior to complete fill (Figure 2.12b). Complete seam-free filling is possible (using the same conditions as in Figure 2.12a or 2.12b) if the trench has a slightly higher width at the opening (Figure 2.12c) or a tapered sidewall (Figure 2.12d), either of which compensates for the bread-loaf profile. However, to enable the forward-directed method to fill rectangular trenches, formation of a bread-loaf profile at the trench opening must be suppressed.

We have developed a solution to the bread-loaf problem that involves adding a growth inhibitor to the process gasses. The inhibitor must have the following characteristics: (i) it has a high probability to react with the growth surface, such that it will not reflect multiple times from the trench sidewalls and be transported deep within the trench; and (ii) it reduces the film growth rate by a suitable fraction. We find that the addition of 0.27 mTorr of hexafluoroacetylacetone to the process gasses completely suppresses the bread-loaf formation and enables complete trench fill on structures with nearly parallel sidewalls (Figure 2.11). Similar results are obtained by adding the halogen-free analog acetylacetone (the details of using molecular inhibitors will be discussed in Chapter 4).

2.3.5 HfO_2 properties

Oxide growth is typically carried out with an excess of the oxygen-source in order to achieve phase stoichiometry. Here, our films are grown under water-starved conditions, so it is important to determine whether these conditions afford films with useful solid-state properties. A film was deposited using 3.5 mTorr TDMA-Hf and 1.0 mTorr H_2O at 180 °C, in which both dosing tubes were pointed at the substrate; this configuration leads to greater water starvation (due to the higher precursor flux) than the configuration in which only the H_2O dosing tube is pointed at the surface.

XPS data were acquired after 2 min of argon sputtering to remove surface C (Figure 2.14a); after subtraction of the signal due to adsorbed –OH groups [28], the concentrations of Hf, O, and N in the film are 33, 65 and 2 at. %, respectively, which corresponds to an O / Hf ratio of 1.97. This ratio is stoichiometric within the error of XPS, and consistent with high quality films that can be grown from these same two precursors by ALD at 200 °C [12, 14]. The films are quite smooth: for the 140 nm thick film of Figure 2.14b, the rms roughness from tapping-mode AFM is 1.0 nm. A low roughness indicates that the areal density of nuclei on the substrate was large [29]. A high areal density occurs when the barrier to nucleation is small; *in situ* SE data indicated prompt nucleation when the gas flows were turned on, consistent with this interpretation.

The refractive index of the same HfO_2 film, as measured by *ex situ* variable angle SE as a function of wavelength (Figure 2.14c), is lower than bulk HfO_2 by ~ 10% [30]. The best fit result from the Cauchy model has no absorption (the extinction coefficient is zero) within the wavelength range of 300 to 1700 nm, which implies that there is a low density of defects across the bandgap. Using an effective medium approximation [30] in the model, we find that the average film density is ~ 84% that of bulk. A reduced physical density is typical for films grown at relatively low temperatures [31]. For a separate film grown using 0.18 mTorr TDMA-Hf and 0.023 mTorr H_2O at 200 °C (conditions used for superconformal coating in Figure 2.8), the density of the metal sublattice evaluated by RBS and SEM is ~ 86 % of that of bulk HfO_2. The wavelength-dependent refractive index of films grown at other partial pressures (0.015 to 24 mTorr TDMA-Hf and 0.009 to 3 mTorr H_2O) and temperatures (180 to 270 °C) is essentially identical to that shown in Figure 2.14c.

2.4 Conclusion

We demonstrate a new mode of low temperature CVD that affords superconformal growth and filling of deep trenches with HfO_2 using the TDMA-Hf precursor with H_2O as a co-reactant at 200 °C. The approach is based on the simultaneous use of two kinetic regimes. First, CVD is conducted with a small ratio of water to precursor, for which the growth reaction is controlled by the water flux and is approximately independent of the precursor flux. Under these conditions, the effective sticking probability (sticking coefficient) of water is about 0.02, which affords partially

conformal growth. Second, water is supplied to the growth surface from a doser tube with a low total pressure in the chamber (< 1 mTorr).

This dosing protocol creates a very forward-directed molecular flux, similar to the output of a nozzle-jet evaporation source. To achieve forward-directed flux on a large-area substrate, the method would involve the use of a showerhead of nozzles for H_2O delivery, in combination with fast pumping to minimize the isotropic background. Within each trench, a significant fraction of the forward-directed water flux makes its first impact at the bottom of the trench. But because the sticking probability for deposition is low, the majority of the water flux scatters, which creates a *virtual source of water at the trench bottom*. The virtual source affords a growth rate profile that is largest at the trench bottom and tapers towards the opening, i.e., the trench fill is V-shaped. The isotropic water flux also contributes, but the net growth rate is superconformal. Continued deposition then moves the apex of the V towards the opening until trench fill is complete. We also show that premature pinch-off near the opening can be eliminated by adding a third reactant that serves as a growth inhibitor on upper surfaces.

We propose that this approach can be applied to a wide range of precursor–coreactant combinations, provided that a regime exists in which the coating is reasonably conformal and the growth kinetics are dominated by the flux of one species.

2.5 References

1. Nandakumar, M., et al. *Shallow trench isolation for advanced ULSI CMOS technologies*. in *International Electron Devices Meeting 1998. Technical Digest (Cat. No.98CH36217)*. 1998.

2. Jordana, E., et al. *Deep-UV Lithography Fabrication of Slot Waveguides and Sandwiched Waveguides for Nonlinear Applications*. in *2007 4th IEEE International Conference on Group IV Photonics*. 2007.

3. Saynatjoki, A., et al., *Angled sidewalls in silicon slot waveguides: conformal filling and mode properties.* Optics Express, 2009. **17**(23): p. 21066-21076.

4. Abdolvand, R., et al., *Quality factor in trench-refilled polysilicon beam resonators.* Journal of Microelectromechanical Systems, 2006. **15**(3): p. 471-478.

5. Schenk, H., et al., *A resonantly excited 2D-micro-scanning-mirror with large deflection.* Sensors and Actuators a-Physical, 2001. **89**(1-2): p. 104-111.

6. Chen, C.C., et al., *Studying of physical characteristics and optimizing of gap filling for tungsten.* Materials Science in Semiconductor Processing, 2011. **14**(3-4): p. 235-240.

7. Kubo, A., T. Homma, and Y. Murao, *An SiO2 film deposition technology using tetraethylorthosilicate and ozone for interlayer metal dielectrics.* Journal of the Electrochemical Society, 1996. **143**(5): p. 1769-1773.

8. Lin, X.F., X. Ma, and J.J. He, *Void-Filling and Loss Reduction in PECVD Silica Waveguide Devices Using Boron-Germanium Codoped Upper Cladding.* Ieee Photonics Technology Letters, 2010. **22**(20): p. 1491-1493.

9. *Private communication with Intel Corporation*. 2016.

10. Wang, W.B. and J.R. Abelson, *Filling high aspect ratio trenches by superconformal chemical vapor deposition: Predictive modeling and experiment.* Journal of Applied Physics, 2014. **116**(19): p. 194508.

11. Wang, W.B., et al., *Superconformal chemical vapor deposition of thin films in deep features.* Journal of Vacuum Science & Technology A: Vacuum, Surfaces, and Films, 2014. **32**(5): p. 051512.

12. Hausmann, D.M., et al., *Atomic layer deposition of hafnium and zirconium oxides using metal amide precursors.* Chemistry of Materials, 2002. **14**(10): p. 4350-4358.

13. Cho, M.J., et al., *Comparison between atomic-layer-deposited HfO2 films using O-3 or H2O oxidant and Hf[N(CH3)(2)](4) precursor.* Applied Physics Letters, 2004. **85**(24): p. 5953-5955.

14. Kukli, K., et al., *Atomic layer deposition of hafnium dioxide thin films from hafnium tetrakis(dimethylamide) and water.* Thin Solid Films, 2005. **491**(1-2): p. 328-338.

15. Hausmann, D.M. and R.G. Gordon, *Surface morphology and crystallinity control in the atomic layer deposition (ALD) of hafnium and zirconium oxide thin films.* Journal of Crystal Growth, 2003. **249**(1-2): p. 251-261.

16. Suri, R., D.J. Lichtenwalner, and V. Misra, *Interfacial self cleaning during atomic layer deposition and annealing of HfO2 films on native (100)-GaAs substrates.* Applied Physics Letters, 2010. **96**(11): p. 112905 1-3.

17. McDonnell, S., et al., *Scaling of HfO2 dielectric on CVD graphene.* Applied Surface Science, 2014. **294**: p. 95-99.

18. Cote, D.R., et al., *Plasma-assisted chemical vapor deposition of dielectric thin films for ULSI semiconductor circuits.* Ibm Journal of Research and Development, 1999. **43**(1-2): p. 5-38.

19. Sperling, B.A., *Kinetic Roughening during Hot-Wire Chemical Vapor Deposition of Hydrogenated Amorphous Silicon*, in *Materials Science and Engineering*. 2006, University of Illinois at Urbana-Champaign.

20. Hoffman, D., B. Singh, and J.H. Thomas, *Handbook of Vacuum Science and Technology*. 1997: Elsevier Science.

21. Jenkins, F.A. and H.E. White, *Fundamentals of Optics*. 3rd ed. 1957, New York: McGraw-Hill.

22. Mahan, J.E., *Physical Vapor Deposition of Thin Films*. 2000: Wiley.

23. Yanguas-Gil, A., et al., *Highly conformal film growth by chemical vapor deposition. I. A conformal zone diagram based on kinetics.* Journal of Vacuum Science & Technology A, 2009. **27**(5): p. 1235-1243.

24. Jayaraman, S., et al., *Hafnium diboride thin films by chemical vapor deposition from a single source precursor.* Journal of Vacuum Science & Technology A, 2005. **23**(6): p. 1619-1625.

25. Ohshita, Y., et al., *Effects of deposition conditions on step-coverage quality in low-pressure chemical vapor deposition of HfO2.* Journal of Crystal Growth, 2002. **235**(1-4): p. 365-370.

26. Lim, J.W., H.S. Park, and S.W. Kang, *Kinetic modeling of film growth rate in atomic layer deposition.* Journal of the Electrochemical Society, 2001. **148**(6): p. C403-C408.

27. Pauleau, Y., *Chemical Physics of Thin Film Deposition Processes for Micro- and Nano-Technologies*. 2012: Springer Netherlands.

28. McCafferty, E. and J.P. Wightman, *Determination of the concentration of surface hydroxyl groups on metal oxide films by a quantitative XPS method.* Surface and Interface Analysis, 1998. **26**(8): p. 549-564.

29. Babar, S., et al., *Growth Inhibitor To Homogenize Nucleation and Obtain Smooth HfB_2 Thin Films by Chemical Vapor Deposition.* Chemistry of Materials, 2013. **25**(5): p. 662-667.

30. *WVASE® Spectroscopic Ellipsometry Data Acquisition and Analysis Software*. 2012, J. A. Woollam Co., Inc.: Lincoln, NE 68508, USA.

31. Aarik, J., et al., *Influence of substrate temperature on atomic layer growth and properties of HfO2 thin films.* Thin Solid Films, 1999. **340**(1-2): p. 110-116.

32. Yanguas-Gil, A., et al., *Highly conformal film growth by chemical vapor deposition. II. Conformality enhancement through growth inhibition.* Journal of Vacuum Science & Technology A, 2009. **27**(5): p. 1244-1248.

33. Nuruddin, A., J.R. Doyle, and J.R. Abelson, *Surface-Reaction Probability in Hydrogenated Amorphous-Silicon Growth.* Journal of Applied Physics, 1994. **76**(5): p. 3123-3129.

2.6 Figures

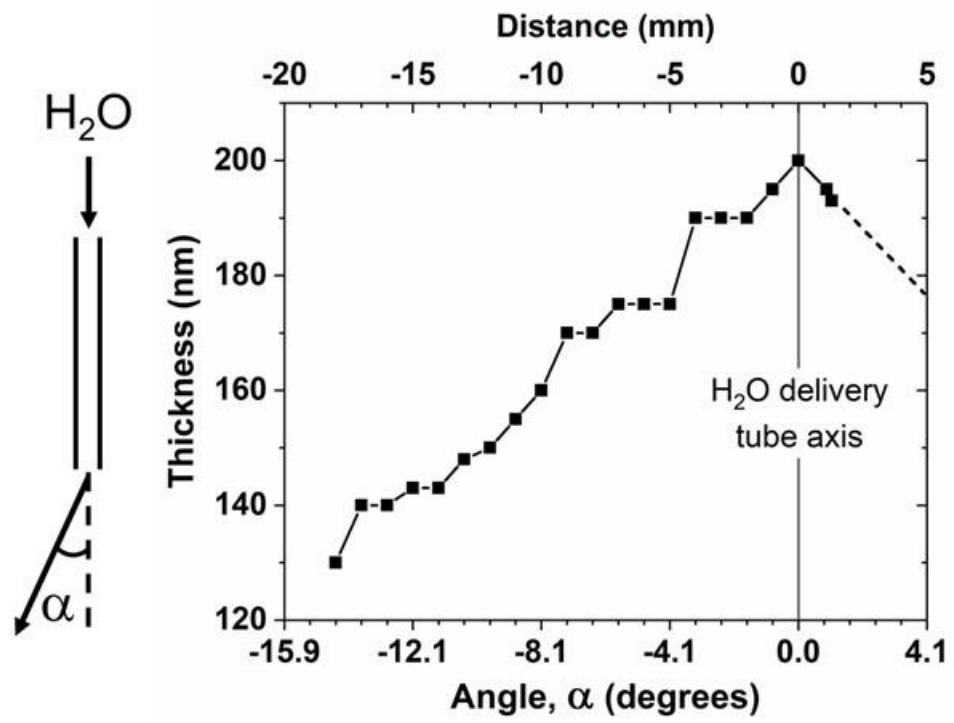

Figure 2.1. Thickness variation on planar Si substrate as a function of linear cone angle, which is used to identify an area on the substrate where most of the forward-directed H_2O flux impinges. The dashed line for visualization only. This area and H_2O throughput from source container are used to calculate an approximate value of sticking probability (β).

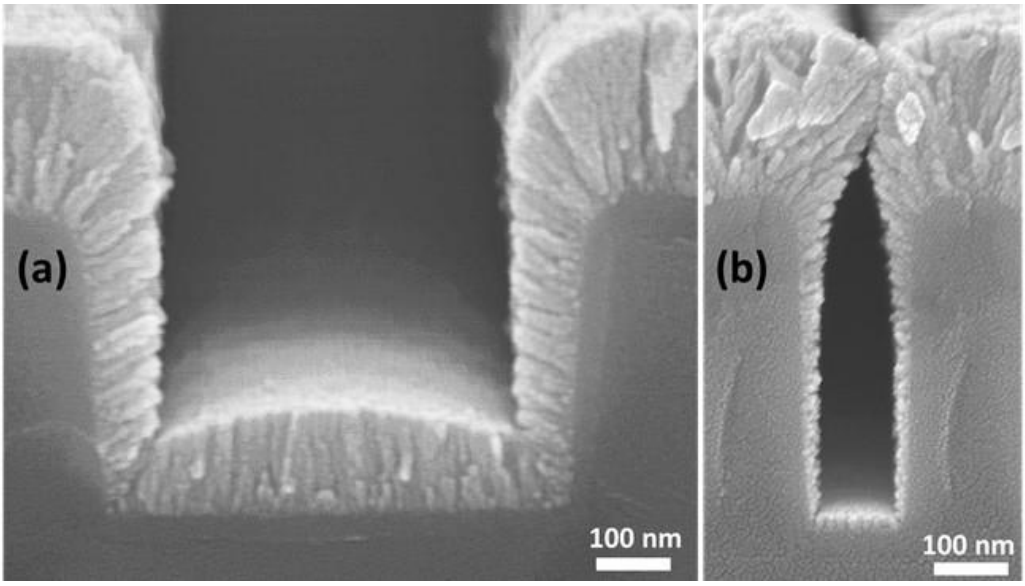

Figure 2.2. PVD-like poor step coverage in trenches of aspect ratio 0.7 (a) and 3 (b) under water-rich conditions: 5 mTorr TDMA-Hf precursor and 3 mTorr H_2O are co-flowed for 60 min at a substrate temperature of 270 °C. The film growth rate at the top surfaces is 4 nm/min.

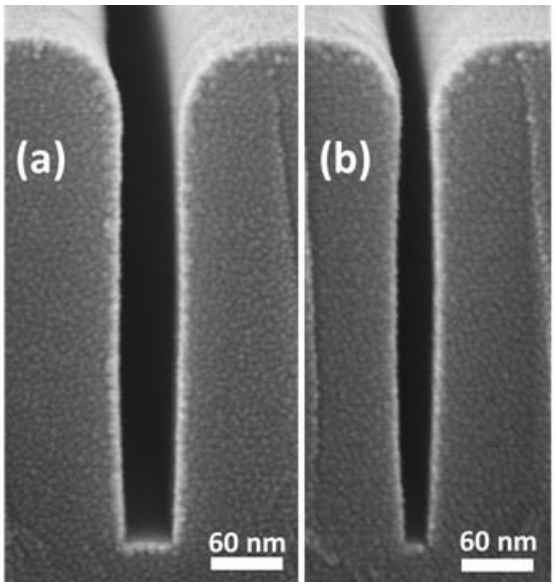

Figure 2.3. Excellent step coverage in trenches of aspect ratio 6.5 (a) and 11 (b) under precursor-rich conditions: the H_2O pressure is reduced to 1 mTorr while other conditions are kept the same as in Figure 2.2. The growth rate at the trench top is 0.36 nm/min.

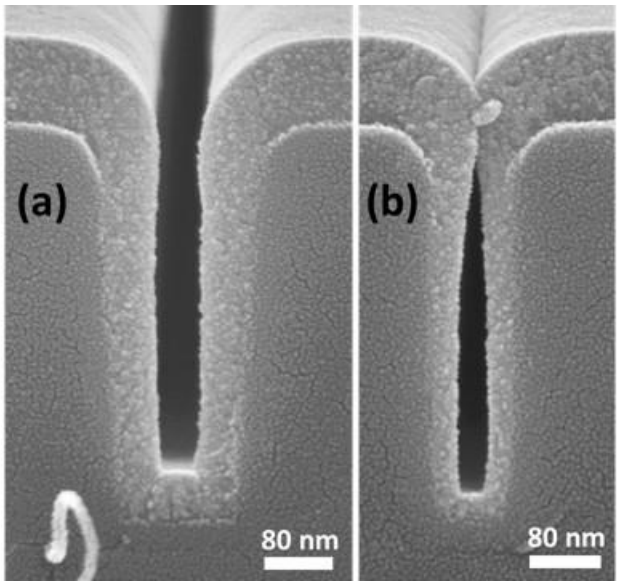

Figure 2.4. Coating profile in trenches of aspect ratio 3 (a) and 5 (b) for 24 mTorr TDMA-Hf and 3 mTorr H_2O at 220 °C for 60 min. The film growth rate at the trench top is 1.6 nm/min.

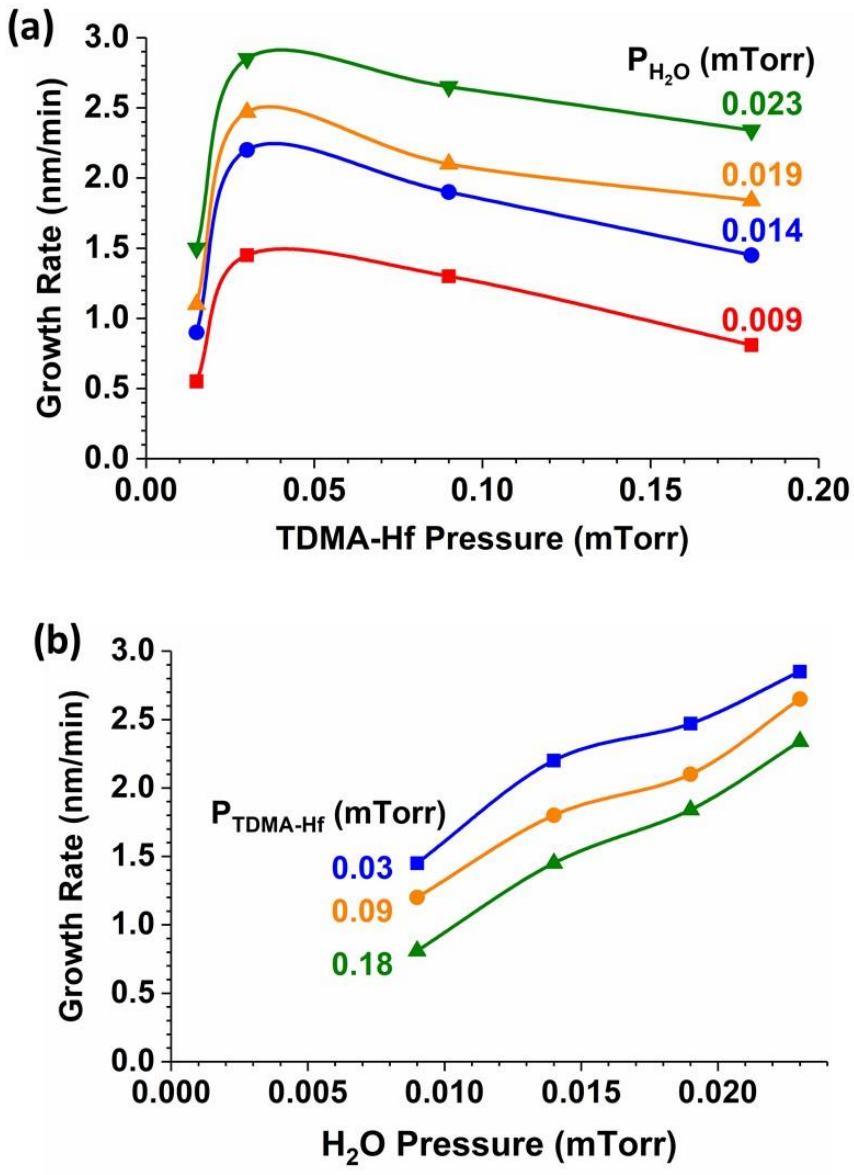

Figure 2.5. Film growth rates on planar Si (100) substrates at 220 °C measured by spectroscopic ellipsometry as a function of (a) TDMA-Hf precursor and (b) H_2O partial pressures. Lines through data points are a guide for the eye only.

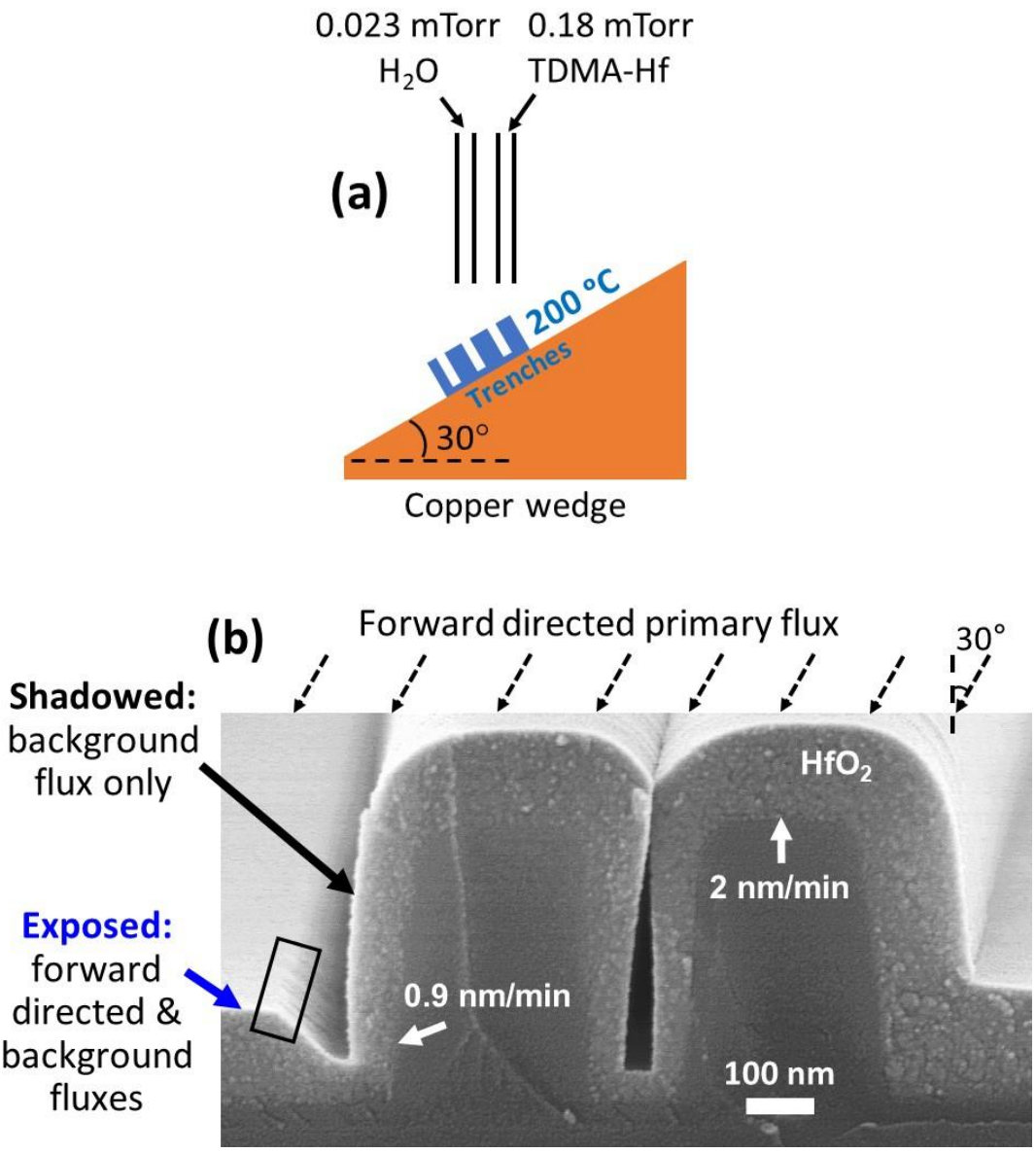

Figure 2.6. Film thickness profile obtained by tilting a trench substrate such that the surface normal is 30° away from the axis of the delivery tube: a) schematic diagram of the setup and growth conditions (growth time = 70 min), and b) cross-sectional SEM image of a trench located approximately below the water delivery tube. The sharp edge on the left side of the image is marked with a black rectangle.

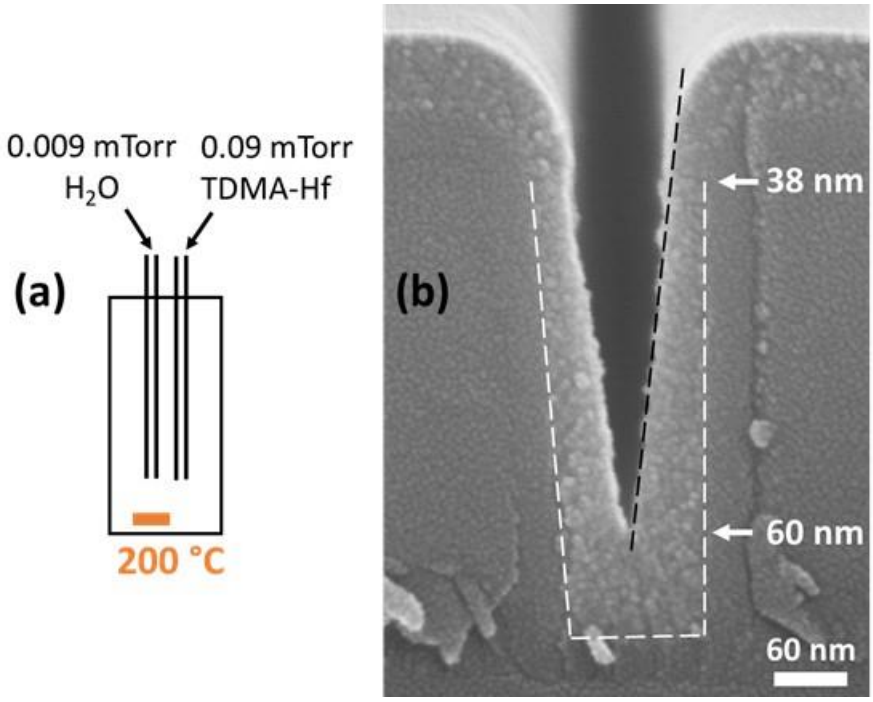

Figure 2.7. a) Growth conditions and orientation of delivery tubes inside the CVD chamber for forward-directed flux. b) SEM image of superconformal HfO_2 coating (step coverage = 1.6) in a trench of aspect ratio 3.5. Growth time = 60 min. A black dashed line is added to show the formation of bread-loaf shape at the trench opening.

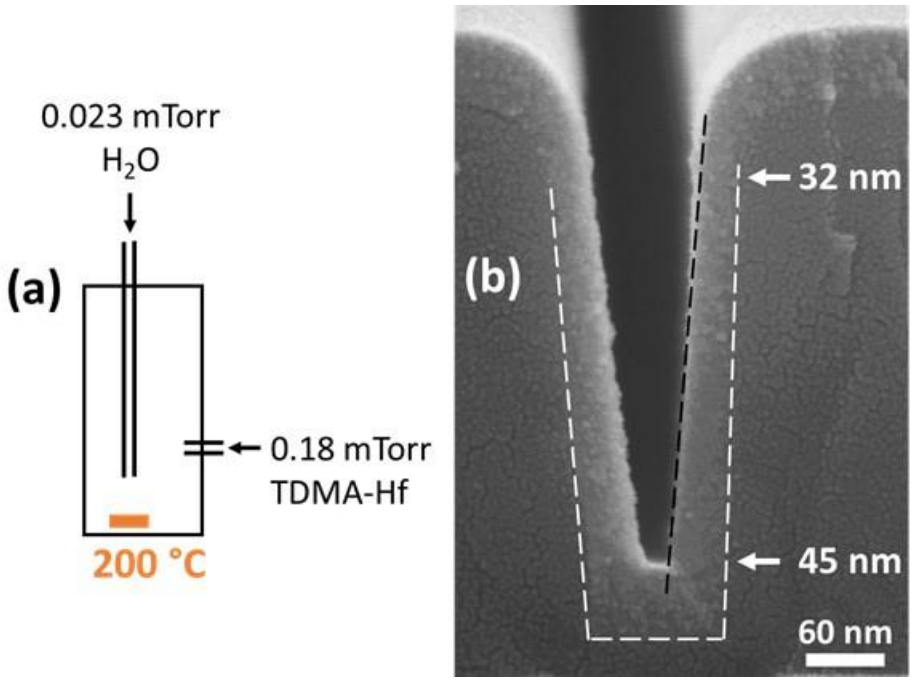

Figure 2.8. a) TDMA-Hf is supplied through a side port so that the substrate receives TDMA-Hf flux from the isotropic background only. b) SEM image (growth time = 40 min) showing that coating inside trench (aspect ratio = 3.5) is superconformal with a step coverage of 1.4. A black dashed line is added to show the formation of bread-loaf shape at the trench opening.

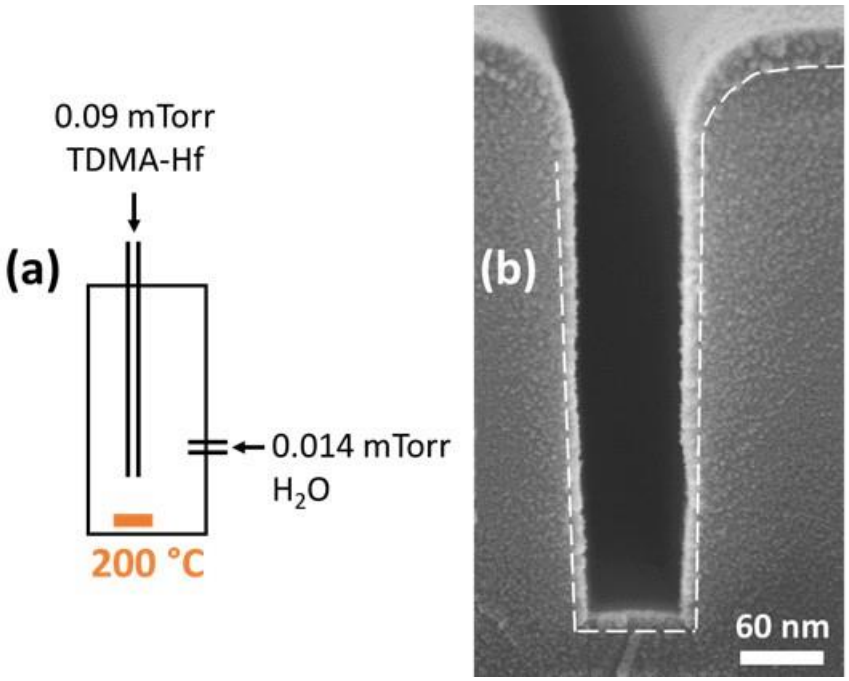

Figure 2.9. a) The TDMA-Hf flux is forward-directed and H_2O is from the isotropic background only. b) Growth inside trench (AR = 4.2) is somewhat conformal but not superconformal (growth time = 30 min).

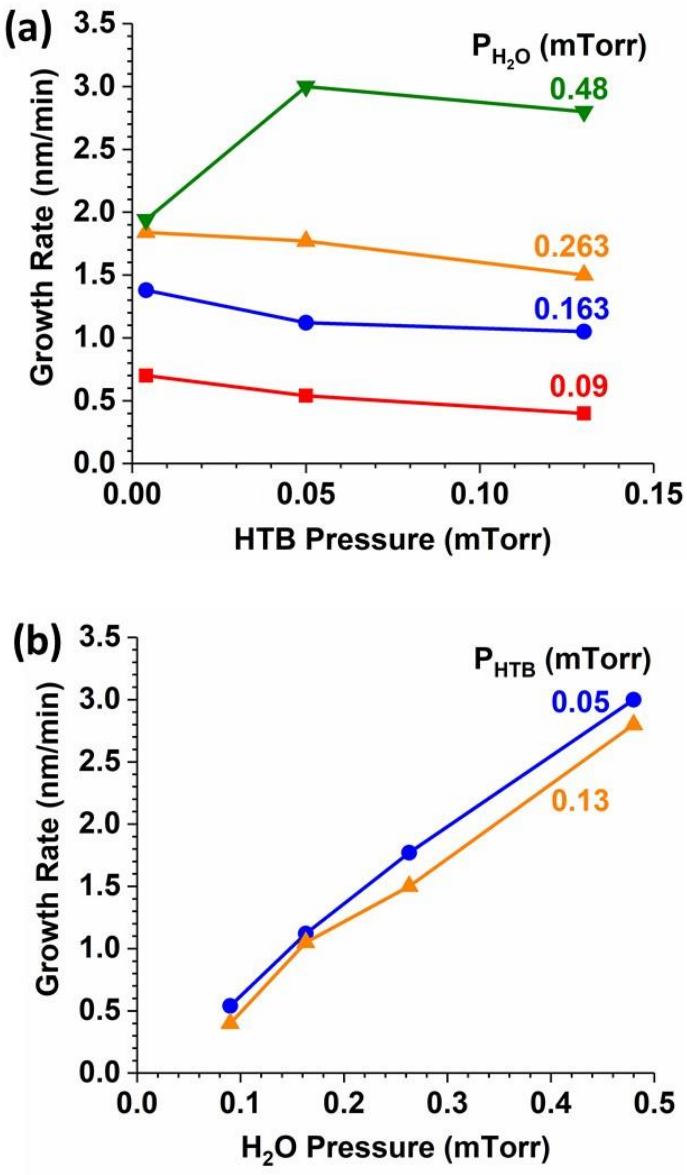

Figure 2.10. Film growth rates on planar Si (100) substrates at 220 °C measured by spectroscopic ellipsometry as a function of (a) hafnium-tetra-tert-butoxide (HTB) precursor and (b) H_2O partial pressures. To a first approximation, the growth rate depends weakly on HTB at high pressures (> 0.05 mTorr) but increases almost linearly with H_2O pressure.

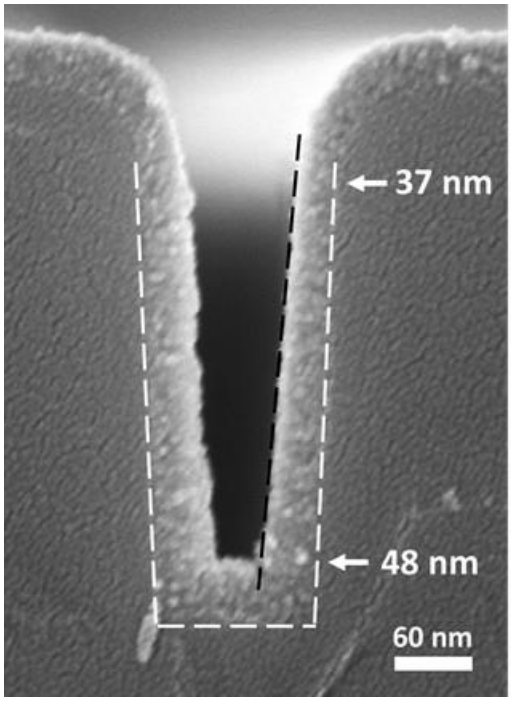

Figure 2.11. Cross-sectional SEM image of superconformal HfO_2 coating (step coverage = 1.3) in a trench of aspect ratio 3. Growth conditions: 0.13 mTorr HTB and 0.163 mTorr H_2O at 220 °C for 40 min.

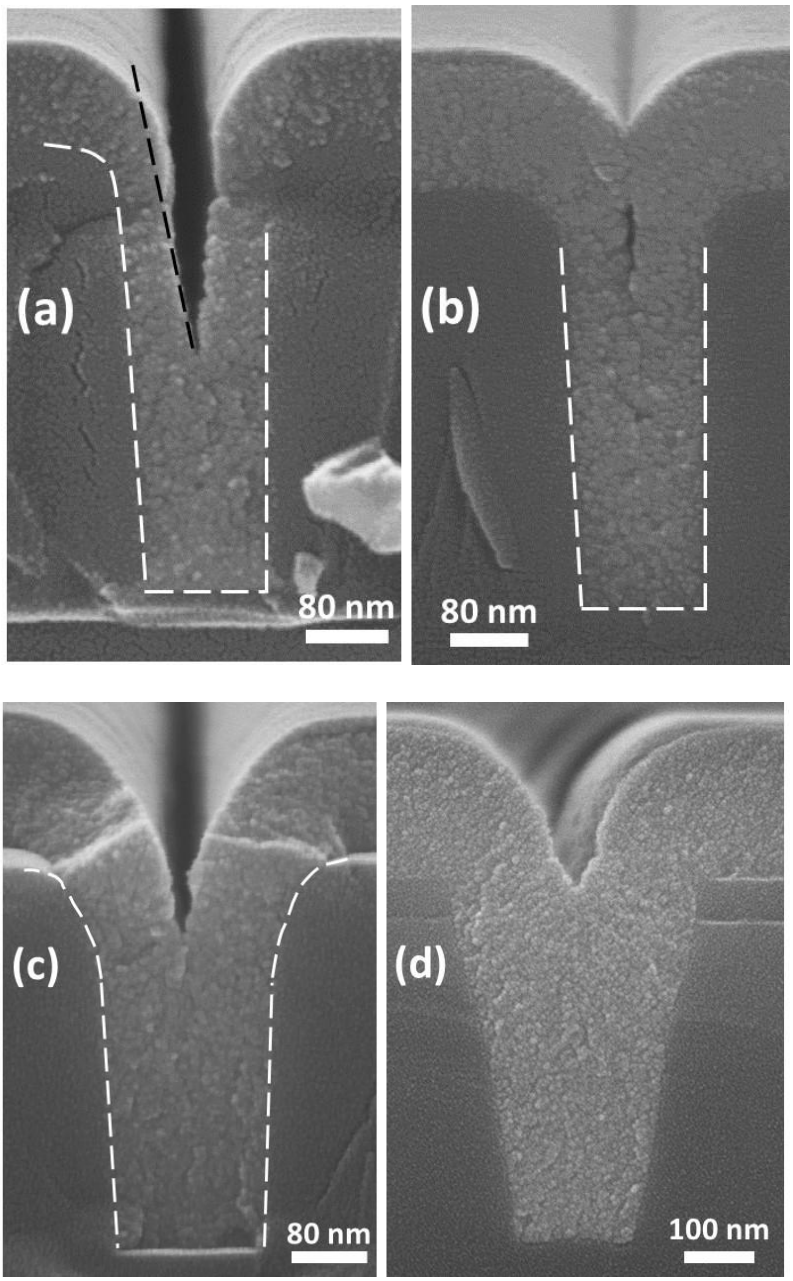

Figure 2.12. Growth on microtrench substrate at 200 °C with 0.09 mTorr TDMA-Hf and 0.014 mTorr H_2O. a) After 60 min: bottom-up growth with "bread-loaf" profile near the trench opening (AR = 3.5). A black dashed line is added to show the bread-loaf shape at the trench opening. b) After 90 min: pinch-off prior to complete fill that leaves a short seam near to the trench opening (AR = 3.5). c) Bread-loaf can be avoided to achieve seam-free complete filling if the trench opening is slightly wider than the depth of trench (AR = 2.4). d) Seam-free complete filling in a trench (AR = 2) with tapered sidewalls.

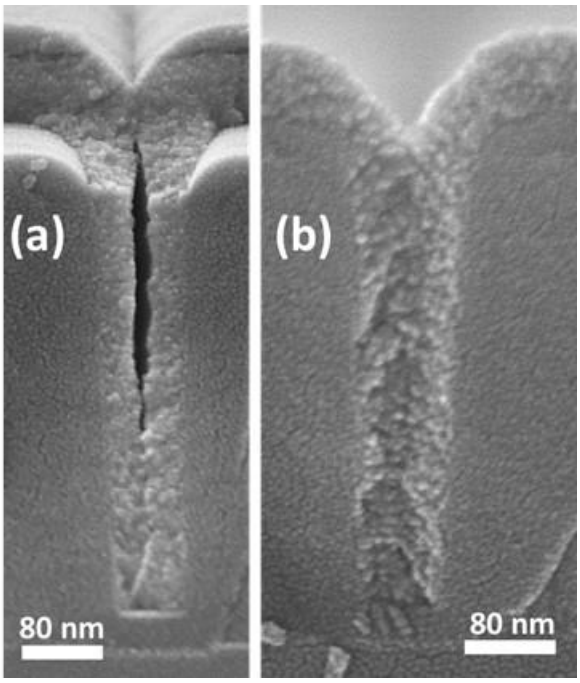

Figure 2.13. Growth in trenches (AR = 6) with nearly parallel sidewalls using 0.09 mTorr TDMA-Hf and 0.014 mTorr H_2O at 200 °C for 60 min. a) Without inhibitor: pinch-off with a large void in the center. b) With a co-flow of 0.27 mTorr H(hfac) inhibitor that suppresses bread-loaf formation to afford complete fill.

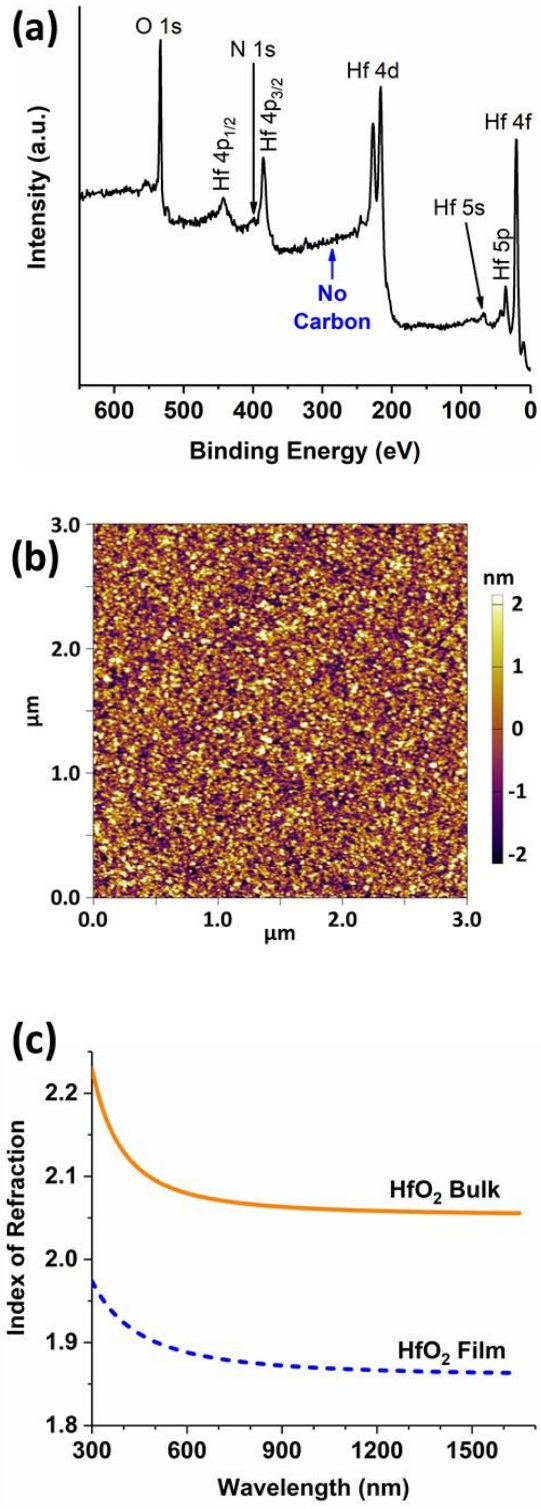

Figure 2.14. Characterization of 140 nm HfO_2 film grown using 3.5 mTorr TDMA-Hf and 1.0 mTorr H_2O at 180 °C. (a) XPS survey after argon sputtering for 2 min; (b) AFM image of the same film; (c) refraction index of the same film, as derived from the Cauchy model.

2.7 Supplementary Materials

Film conformality and morphology are known to be a strong function of the probability that a precursor species will react with the film growth surface (REF). When the reaction involves a kinetic competition for available surface sites, then the probability (reaction rate constant) is a complex function of the fluxes and temperature [32], and consequently varies with depth inside a deep feature. However, insight can be gained by assuming that the sticking probability (β) is a constant and calculating its value for different growth conditions. Below, we show that is assumption is valid under the conditions of interest in this work.

An analytical method to estimate β is to model the trench as a blackbody cavity in which precursor species either react with the sidewall or escape out through the opening; the trench aspect ratio then sets the ratio between the interior surface area and the area of the opening [33]. (This method was originally applied to trenches of ~ 0.1 mm width such that the film thickness of < 0.1 μm was negligible, i.e., the geometry remained constant. Here the trenches are narrower, so the effective aspect ratio increases as film build up on the sidewalls. We neglect this effect in order to obtain a first estimate.) The calculated values of β are approximately 1.0 and 0.03 for the trenches in Figure 2.2(a) and Figure 2.3(a), respectively. The striking difference in β indicates that surface reactivity can be sharply reduced by making the growth conditions water starved, which provides better conformality at the expense of a lower growth rate.

CHAPTER 3

MODELING OF SUPERCONFORMAL CVD IN DEEP TRENCHES WITH FORWARD-DIRECTED FLUXES

3.1 Introduction

In chapter 2, a new superconformal CVD process has been experimentally demonstrated for rectangular trenches with nearly parallel sidewalls. Filling is a dynamic process in which the feature shape and aspect ratio (AR) continuously evolve. A coating condition that affords super-conformal growth for the *initial* feature geometry is not guaranteed to afford the same behavior all the way through the filling process. As a feature fills with coating material, the width along the centerline continuously decreases, so the aspect ratio increases; this is also the case during the formation of a V-shape. This reduces the particle transport rate and the probability that a given area of the surface will receive flux that has been scattered (re-emitted) from other areas of the surface. In that regard, mathematical modeling of the coating process inside the trenches is invaluable because it affords limits on allowable geometries according to the performance of super-conformal coating processes.

Previously, a theoretical model for a different superconformal method was developed by a former group member, Dr. Wenjiao Wang [1]. In that model, both molecular diffusion and ballistic transport of reactants from an isotropic (uniform) source outside the trench were considered. The diffusion model was shown to underestimate the precursor fluxes at large depth in high AR features; the experimental results were better that could be accounted for by diffusion [1]. The main reason behind this underestimation is that the Knudsen diffusion coefficient assumes a single mean free path between wall collisions [2], whereas in reality, molecules that are emitted at glancing angles to the centerline of the feature will travel long distances without collision. On the other hand, the mathematical results obtained from the ballistic model agreed well with the experimental results. It was, therefore, concluded that a ballistic transport model is necessary to obtain an accurate prediction of the coating behavior inside deep features.

The superconformal CVD method for HfO_2 growth in the present work (Chapter 2) is obtained by utilizing a relatively high pressure of TDMA-Hf precursor, such that the growth rate due to precursor is almost in saturation, and a forward-directed flux of water co-reactant controls the growth rate. Water transport occurs from two sources: an isotropic (uniform) flux distribution enters the trench through the opening, and a virtual water source at the trench bottom is created by the forward-directed flux (Figure 3.1). The experimental data given in Chapter 2 provide strong support for the latter, which leads to superconformal filling.

In this study, we perform computational modeling using ballistic transport of water from the isotropic and forward-directed sources. We investigate the range of parameters that afford, in the model output, trench profiles similar to experiment. These results are then extended to a rectangular trench with AR of 10 and V-shaped trenches with different sidewall taper angles (1 to 5°) with respect to the trench axis. The model provides quantitative information, such as the critical V angle for complete fill when a rectangular trench coverts to a V-shaped one, and the dependence of the superconformal step coverage on the water sticking probability and the fraction of forward-directed water flux.

3.2 Model Assumptions

To make the computations tractable, we make several assumptions that are consistent with the experimental data in Chapter 2:

i. Under precursor-rich conditions, the growth rate is independent of the precursor pressure and varies linearly with water flux via an effective sticking probability (β).

ii. The growth rate at any one location within the trench is controlled by the flux of water from the sum of the two sources, the isotropic flux due to its partial pressure in the chamber and the forward-directed flux from the doser tube (Figures 3.1 and 3.2).

iii. The re-emission of flux from trench wall follows cosine law. There is a report showing that when the adsorption surface has roughness or even micro-structures, the re-emission of adsorbed molecules follows a cosine law [3].

iv. The flux from the doser tube is parallel with the trench axis, and of constant intensity across the width of the trench.

The last of these four assumptions is not strictly true, because molecules exit a doser tube with trajectories having a range of angles. Nevertheless, this assumption is not too badly violated, and it serves to illustrate the ideal case of perfect collimation. In addition, it simplifies calculations of the dependence of the coating profile on the tilt angle of the trench with respect to the forward-directed flux and on the taper angle of the sidewalls with respect to parallel.

3.3 Ballistic Transport

An efficient method to calculate ballistic particle transport within a re-entrant structure was proposed by Cale *et al*. [4]. The transmission probability between each area on the surface and all other areas is calculated from the angular emission probability with respect to the local normal, the solid angle, and the tilt of the receiving surface. These probabilities are coded into a square matrix. The incident flux on all surfaces is calculated using Markov chain model and coded into a column matrix. For a constant sticking probability, a matrix inversion (which accounts for the multiple internal reflections and loss out the opening) then affords the net sticking on all surfaces, i.e., the film growth rate. We previously implemented this method to investigate the conditions necessary to fill a V-shaped profile without producing a seam along the centerline [1]. We showed that ballistic transport into the apex of the V plays a very strong role in filling, one that is not modeled correctly under the approximation of molecular (Knudsen) diffusion with a mean displacement between sidewall collisions.

The text in the below subsections – model description, impingement flux from isotropic source outside the trench, re-emitted flux, and matrix notation for constant sticking probability – is adapted from reference [5]. It is reproduced here to provide the necessary details that underpin for the present work.

3.3.1 Model description

The particle transport is calculated in three dimensions and the results are projected onto a two-dimensional cross-section. This is valid when the trench is very long compared with its width

W_0 and depth L_0 such that it can be considered semi-infinite (Figure 3.3). For an arbitrary position *i* inside the trench, the total receiving flux is the sum of impingement flux from outside the trench and the re-emitted flux from all other positions inside the trench that falls onto this position:

$$f_{total,i} = f_{impinge,i} + f_{r,i} \tag{3.1}$$

The impingement flux $f_{impinge,i}$ depends on the position *i*, and is a constant for a defined trench shape, given that the flux distribution outside the trench is uniform (stable), and the forward-directed flux is parallel to the trench axis. The re-emitted flux $f_{r,i}$ approaches steady state after many cycles of wall collisions and re-emission. To calculate the impingment and re-emitted flux that falls onto position *i*, the contributions from every small area at the trench opening, and from every other position on the trench walls need to be summed up. Below, for the derivation of f_{ik}, $f_{r,i}$, and q_{ik}, we adopt the formulae and notation by Cale [4].

3.3.2 Impingement flux from isotropic source outside the trench

For the impingement flux, the gas (water) outside the trench is regarded as a uniform and isotropic source at the trench opening; the emission across the plane of the opening follows a cosine law [6]. From an arbitrary position *k* in the trench opening (Figure 3.3), the flux that falls onto position *i* obeys:

$$f_{ik} = e_k \cos(\Omega_{ki}) K_{ik} \frac{1}{\pi} \frac{\cos(\Omega_{ik})}{S_{ik}^2} \tag{3.2}$$

where e_k is the total equivalent emission flux from position *k*. Ω_{ki} is the angle between connection of *ki* and area *k*'s normal. K_{ik} stands for visibility between the two positions, which equals 1 if *k* and *i* are visible to each other, otherwise 0. In this study, for filling of V-shape trench, K_{ik} is constantly 1. Similarly, Ω_{ik} is the angle between connection of *ki* and area *i*'s normal, and S_{ik} stands for the length of connection of *ik*. So, the last term gives the solid angle of unit area at position *i* to position *k*, and $1/\pi$ is the normalization factor. The total impingement flux to position *i* is then:

$$f_{impinge,i} = \sum_k f_{ik} \tag{3.3}$$

As the source is uniform, the emission flux e_k is the same for all other opening positions. If we define the term q_{ik} as

$$q_{ik} = K_{ik} \frac{1}{\pi} \frac{\cos(\Omega_{ik})\cos(\Omega_{ki})}{S_{ik}^2} \tag{3.4}$$

Then, this q_{ik} term gives the fraction of emission flux from position *k* that hits position *i*. For isotropic source outside the trench, the total impingement flux to position *i* is an integration over all such positions on the trench opening surface:

$$f_{impinge,i} = \iint (e * q_{ik})\, dA_k \tag{3.5}$$

Setting the origin at the center of the trench opening, we derived the formula for the impingement flux to position *i* (y_i, z_i):

$$f_{impinge,i} = \frac{1}{2} e \times (z_0 - z_i)\left\{\left[-y_i \cos(\alpha_i) + (z_0 - z_i)\sin(\alpha_i)\right] \times M + \cos(\alpha_i)(N + y_i \times M)\right\} \tag{3.6}$$

where

$$M = \frac{y_0 - y_i}{(z_o - z_i)^2 \sqrt{(y_0 - y_i)^2 + (z_o - z_i)^2}} + \frac{y_0 + y_i}{(z_o - z_i)^2 \sqrt{(y_0 + y_i)^2 + (z_o - z_i)^2}}$$

$$N = \frac{1}{\sqrt{(y_0 + y_i)^2 + (z_o - z_i)^2}} - \frac{1}{\sqrt{(y_0 - y_i)^2 + (z_o - z_i)^2}}$$

Here α_i is the angle between position *i*'s normal and the y-axis (equals zero for a rectangular trench), z_0 is the z coordinate for the opening surface (equals zero before deposition), and y_0 is the y coordinate for the trench edge at the opening.

3.3.3 Forward-directed impingement flux from doser tube

The water flux from doser tube reaching the trench is regarded to be parallel to the trench axis (Figure 3.2b), and so the forward-directed impingement flux at a position *i* in the trench is simply the projection of the flux from doser tube onto the position *i*, given as:

$$f_{impinge,i} = f_{dose} \sin(\alpha_i) \tag{3.7}$$

where f_{dose} is the flux emanating from the doser tube.

3.3.4 Re-emitted flux

The re-emission from an arbitrary position *j* inside the trench also follows a cosine distribution with respect to the local normal, as confirmed by numerical simulation for re-emission after multiple reflections in surface micro-structures [3]. The total reemitted flux to position *i* is:

$$f_{r,i} = \iint (e_j * q_{ij})\, dA_j \tag{3.8}$$

where A_j is a small area at arbitrary position *j* located on the trench sidewall or bottom. However, as the re-emitting flux e_j varies with position and would change as it approaches steady-state after multiple cycles of collision and re-emission, the calculation has to discretize the positions inside trench to a series of nodes.

As the trench is symmetric along the x axis, the results can be projected onto the y-z plane [6]. Then, discretizing the positions along the cross-sectional shape of the trench, the re-emitting flux that hits position *i* follows:

$$f_{r,i} = \sum\nolimits_{j \neq i} e_j * q'_{ij} * l_j \tag{3.9}$$

where q'_{ij} is integration of q_{ij} over the *x* axis, and l_j is the length of section *j*.

Some fraction of the total flux impinging on position *i* is consumed by surface reaction to form film, and the rest is re-emitted:

$$e_i = f_{total,i} - r_i \tag{3.10}$$

3.3.5 Matrix notation and calculation for steady-state distribution

Based on the model described above, we develop a computationally efficient approach, which is to group the impingement and re-emitted fluxes for all nodes of the trench into vectors, and use a matrix to represent the transport probability between every pair of nodes:

$$F = E * Q + F_{impinge} \tag{3.11}$$

$$E = F - R \tag{3.12}$$

where F is a vector of receiving flux for all nodes; E is a vector of product of emission flux and node length, $e*l$; Q is the matrix of the transmission probability, q'_{ij}; $F_{impinge}$ is a vector of impingement flux; and R is the vector for the reaction rate, which can be a function of receiving flux.

The initial conditions for the model are:

$$\begin{cases} F_{t0} = F_{impinge} \\ E_{t0} = 0 \\ R_{t0} = f\left(F_{t0}\right) \end{cases} \tag{3.13}$$

where F_{t0} is the initial receiving flux vector (Equation 3.6); E_{t0} is the initial emitting flux vector; and R_{t0} the initial reaction vector calculated based on F_{t0}. Afterwards, E and F can be re-calculated with each other according to Equations 3.11 and 3.12, until a self-consistent solution is found. When this group of equations achieves steady-state, the stable flux distribution is represented by F.

In the limit of low pressure (low flux) reaction conditions, the flux and reaction rate are related by a constant sticking probability, which is the case for water flux in HfO_2 growth. The reaction rate is given by:

$$R = F * S \tag{3.14}$$

where S is a vector of constant sticking probability (β).

The following self-consistent equation represents the steady-state:

$$F = F * (1 - S) * Q + F_{impinge} \tag{3.15}$$

Solving this equation – which implicitly contains the infinite series of internal reemissions – we obtain:

$$F = \frac{F_{impinge}}{\left[1 - (1 - S).Q\right]} \tag{3.16}$$

Thus, *in the case of constant sticking probability, the stable flux distribution can be derived from a single equation*.

3.4 Ballistic Modeling Results and Discussion

3.4.1 Fraction of Forward-directed Flux

As a test of the ballistic transport model with constant sticking probability, we consider the experimental result in the trench of Figure 3.4a. The trench has an aspect ratio of 3.5 and an outwards taper angle of 1.1°; the tapered sidewalls will intercept a portion of the parallel flux. The isotropic flux is calculated from the partial pressure in the chamber using the ideal gas law [7]. The initial impingement of water on the trench sidewalls depends on the source: for the isotropic component it falls rapidly with depth; for the forward directed flux it has a constant small value due to the tilt angle (Figure 3.4b). We treat the ratio of isotropic to forward-directed fluxes as a free parameter in the model because it is difficult to measure precisely; this parameter scales the growth rates from each source (Figure 3.5). The constant sticking probability (β) for the growth conditions of Figure 3a is calculated to be 0.021 (Chapter 2). A water flux that is 40 % directional and 60 % isotropic, with β = 0.021, predicts growth rates of 0.6 nm/min at the top of the sidewall and 1.0 nm/min at the bottom of the sidewall. The predicted step coverage of 1.0/0.6 = 1.6 agrees very well with the experimental thickness profile (Figure 3.4a) and supports the hypothesis that the superconformal growth is due to the existence of a virtual source of water at the bottom of the trench, which is created by scattering of the forward-directed flux.

3.4.2 Critical V angle for Complete Fill

As the superconformal growth continues, the rectangular trench converts into a V-shaped trench (inset of Figure 3.6a). Inside a V-shaped trench the growth rate for both isotropic and forward-directed fluxes at any one time will depend on the instantaneous tilt angle θ of the sidewall with respect to the centerline (axis) of the trench. Figure 3.6a shows the calculated growth rate profiles for four values of the tilt angle (θ = 1, 2, 3, and 5°) in the two limiting cases for the water flux: 100 % isotropic or 100 % forward-directed. For a flux that is 100 % forward-directed (solid lines), the growth profile inside the trench is superconformal for all $\theta \geq 2°$; for a smaller tilt angle, θ = 1°, the growth profile is superconformal near to the trench opening and conformal at depth/width > 20. Geometrically, the tilt angle defines a nominal aspect ratio, equal to $0.5/\tan(\theta)$. Once a V shape is formed, complete filling can be achieved using a process that is merely conformal [1].

In contrast to the above results, for a flux that is 100% isotropic (dashed lines in Figure 3.6a), *growth is subconformal for all the sidewall tilt angles considered*. We do not calculate cases intermediate between a rectangle and a V shape (meaning a V with a broad bottom) because a V shape will be the most challenging situation in which to achieve superconformal growth. Thus, if a V shape is superconformal, then intermediate cases will also be. This approach does not cover the possibility that complete fill could result from a situation in which the step coverage transits between superconformal and merely conformal as the V is formed. We suggest that for the filling process to be robust, it is best to maintain superconformal growth through the creation of the V shape, to avoid the possibility of subconformal coating due to process variations.

Experimentally, creating a 100% forward-directed flux inside the trench is not realistic; we therefore explore the growth rates (Figure 3.6b) for a linear combination of 40% directional plus 60% isotropic fluxes, which is the best fit to the experimental data for our system in Figure 3.5. In this case, the growth is subconformal for θ < 2°, essentially perfectly conformal at 2°, and superconformal for larger sidewall tilt angles. In our earlier simulations for a V-shaped trench, we showed that the effective aspect ratio rises very sharply as the angle diminishes [1]. As a consequence, it is difficult for the growth kinetics of [1] or the kinetics of the present process to fill V shapes with θ < 2°. However, improved reactor geometry, i.e., fast pumping to lower the

isotropic flux, could increase the contribution of forward-directed flux, and thus the fill in cases of small θ.

For the 100% forward-directed flux, the first impingement on the sloped sidewalls is constant with depth, but perhaps surprisingly, the water flux (film growth rate) increases with depth (Figure 3.7a). This result can be understood as a consequence of a reduced particle loss probability: with increasing depth, water molecules see a smaller solid angle to the trench opening, hence, have a higher probability of making internal reflections and ultimately contributing to deposition, i.e., they mostly get trapped.

3.4.3 Step coverage, sticking probability and fraction of forward-directed flux

To investigate the dependence of step coverage on the water sticking probability and fraction of forward-directed water flux, we consider a rectangular trench with an aspect ratio of 10 (Figure 3.8a) and a V-shaped trench with $\theta = 3°$ (Figure 3.8b). Note that sticking probability depends on the surface chemistry of the reactant molecules and the growth conditions (substrate temperature and reactant partial pressure), whereas the fraction of forward-directed flux depends on the reactor design (engineering). The required minimum step coverage to convert a rectangular trench to a V-shaped one with a certain angle will depend on the time evolution of the coating profile inside the trench. For example, step coverage of ≥ 3 is needed to convert a rectangular trench with aspect ratio of 10 to a V-shaped trench with $\theta \geq 2°$. Knowing the required minimum step coverage, Figure 3.8a can be used to determine a maximum sticking probability and a minimum fraction of forward-directed flux. Figure 3.8b then indicates whether the chosen sticking probability and fraction of forward-direct flux can also maintain step coverage of ≥ 1 during continued filling of the V shape.

3.5 Distribution of TDMA-Hf Precursor Pressure in Trenches

The model developed in this chapter assume that the partial pressure of the TDMA-Hf precursor is high enough, compared to the water partial pressure, to afford growth rate saturation at all depths in a trench. Since the Hf precursor transport typically occurs from the isotropic flux distribution outside the trench (experiments in Chapter 2), its partial pressure drops along the depth

of the trench, due to the coupled kinetics of precursor transport and consumption as film at the sidewall. Therefore, it is important to assure that we have a high enough flux at the bottom of the trench.

From the ballistic model above, we already know the film growth rate as a function of trench depth, which can be used to calculate the Hf precursor pressure distribution in the trench. To use the ballistic transport model for the Hf precursor flux, we need to know the sticking probability of the Hf precursor. In a high-pressure saturation regime, the sticking probability of the Hf precursor becomes a function of both substrate temperature and its partial pressure [8]; this is not the case for water pressure as we operate in a low flux, reaction rate limited regime for water. The pressure dependence of the Hf precursor sticking probability causes it to vary with trench depth, and an accurate determination of this variation requires surface kinetic information beyond the available experimental data in Chapter 2.

In contrast, a diffusion-reaction model can approximate the Hf precursor pressure drop in a trench based on the available experimental and ballistic model data. A theoretical model for the diffusion-reaction in trenches, taking the sidewall taper angle (θ) in a V-shaped trench into account, was developed in [1].

Here, we use the above-mentioned diffusion-reaction model to calculate the TDMA-Hf pressure as a function of depth in a rectangular trench and a V-shaped trench with $\theta = 2°$ (Figure 3.9). For growth saturation, the minimum threshold pressure of the Hf precursor is ~ 0.03 mTorr (from experimental data in Chapter 2). The result in Figure 3.9 suggest that an isotropic Hf precursor pressure of 0.1 mTorr outside a rectangular trench with aspect ratio ≤ 12 is sufficient to achieve precursor saturation kinetics at the bottom. However, for the same isotropic pressure of 0.1 mTorr outside a V-shaped trenches with $\theta = 2°$ (nominal aspect ratio = 14), the precursor pressure drops below 0.03 mTorr at a depth/width = 8. Note that, as discussed before, the diffusion model underestimates the precursor pressure at a large depth in high aspect ratio trenches, which becomes more severe at the apex of a V-shaped trench [1]. Nonetheless, this result predicts that, to achieve a growth saturation for the Hf precursor when a rectangular trench converts to a V-shaped one with $\theta \leq 2°$, the Hf precursor pressure in the reactor needs to be > 0.1 mTorr.

3.6 Conceptual Reactor Design for Forward-directed Flux

From the ballistic modeling results, the dependence of superconformal step coverage on the fraction of forward-directed water flux is predicted in Figure 3.8; a higher fraction of forward-directed water flux provides a higher step coverage for the same water sticking probability. Also, the present experimental results in Chapter 2 are obtained using a single nozzle for the water injection into the reactor. To accommodate the superconformal CVD method with forward-directed fluxes for large-area substrates, an engineering solution is to use a showerhead of nozzles for the rate limiting reactant (water in the case of HfO_2). In addition to the thickness uniformity on large area substrates, such a showerhead needs to produce the necessary fraction of forward-directed flux to afford the minimum required step coverage (discussed above). Note that the surface saturating reactant (TDMA-Hf precursor in the case of HfO_2) can be injected into the reactor isotropically and, hence, does not need a showerhead for large area substrates.

Shower head of nozzles is common in plasma CVD process; however, the conventional design of showerhead mainly consider the thickness uniformity on large area substrates [9]. Such a design typically includes a plate with array of nozzles (Figure 3.9a), which will create a large fraction of isotropic flux over the substrate due to the reflected fluxes; this conflicts with the requirement of the superconformal step coverage in the present study. We propose an alternative design (conceptual) for a showerhead (and reactor) to deliver water into the reactor (i) using a lattice of tubing for the nozzles with gaps between the tubes, and (ii) installing the turbo pump just above the shower head for fast pumping of the background flux (Figure 3.9b). The idea behind this new design is to reduce the isotropic (uniform) flux of water above the substrate, thereby, increase the ratio of forward-directed to isotropic water fluxes, which is necessary to increase the superconformal step coverage.

3.7 Conclusion

A kinetic model based on Markov chain calculations is developed to simulate the ballistic transport of water from the isotropic source outside the trench and the virtual source created by the impinging forward-directed flux. The model predicts that, in the present experimental setup, we get about 40 % forward-directed flux and 60 % isotropic flux in a trench with aspect ratio

of 3.5. This information is then used with the ballistic transport model to identify the range of parameters – step coverage, sticking probability, fraction of forward-directed flux, and V angle – that afford complete filling.

3.8 References

1. Wang, W.B. and J.R. Abelson, *Filling high aspect ratio trenches by superconformal chemical vapor deposition: Predictive modeling and experiment.* Journal of Applied Physics, 2014. **116**(19): p. 194508.

2. Welty, J., G.L. Rorrer, and D.G. Foster, *Fundamentals of Momentum, Heat and Mass Transfer, 6th Edition*. 2014: Wiley.

3. Feres, R. and G. Yablonsky, *Knudsen's cosine law and random billiards.* Chemical Engineering Science, 2004. **59**(7): p. 1541-1556.

4. Cale, T.S. and G.B. Raupp, *A Unified Line-of-Sight Model of Deposition in Rectangular Trenches.* Journal of Vacuum Science & Technology B, 1990. **8**(6): p. 1242-1248.

5. Wang, W., *Super-Conformal Coating and Filling of High Aspect Ratio Recessed Structures by Two-Molecule CVD*, in *Materials Science and Engineering*. 2014, University of Illinois at Urbana-Champaign.

6. Maissel, L.I. and R. Glang, *Handbook of Thin Film Technology*. 1970: McGraw-Hill.

7. Venables, J.A., *Introduction to Surface and Thin Film Processes*. 2000: Cambridge University Press.

8. Yanguas-Gil, A., et al., *Highly conformal film growth by chemical vapor deposition. I. A conformal zone diagram based on kinetics.* Journal of Vacuum Science & Technology A, 2009. **27**(5): p. 1235-1243.

9. Armaou, A. and P.D. Christofides, *Plasma enhanced chemical vapor deposition: Modeling and control.* Chemical Engineering Science, 1999. **54**(15-16): p. 3305-3314.

3.9 Figures

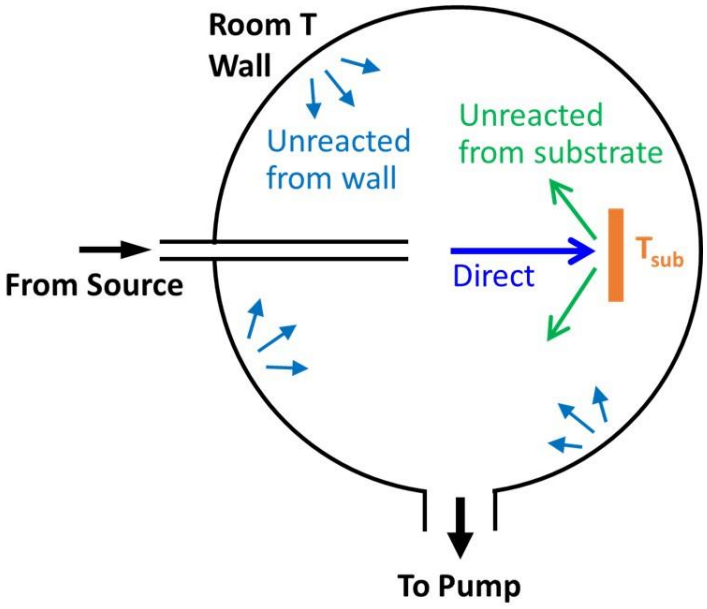

Figure 3.1. Schematic of the flux components inside a cold-wall CVD reactor. The gas emanating from the doser tube directly impinges on the substrate, creating a forward-directed flux component. The unreacted flux from the substrate then hits the room temperature reactor wall, where it partially reacts and partially reflects. The latter component creates an isotropic flux in the chamber that reaches the substrate.

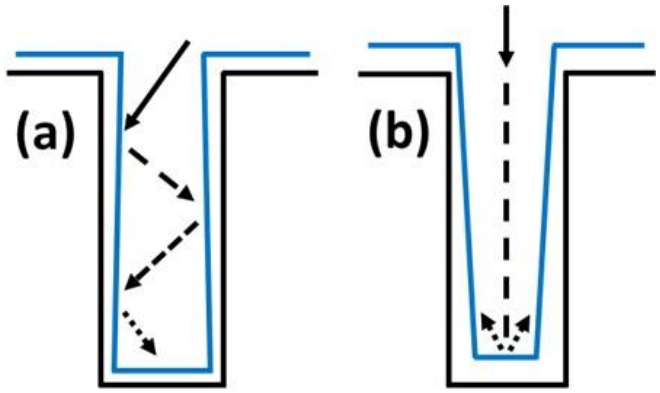

Figure 3.2. Schematic of coating processes considered for modeling: (a) slightly subconformal coating by isotropic background flux, and (b) superconformal coating by forward-directed ballistic H_2O flux.

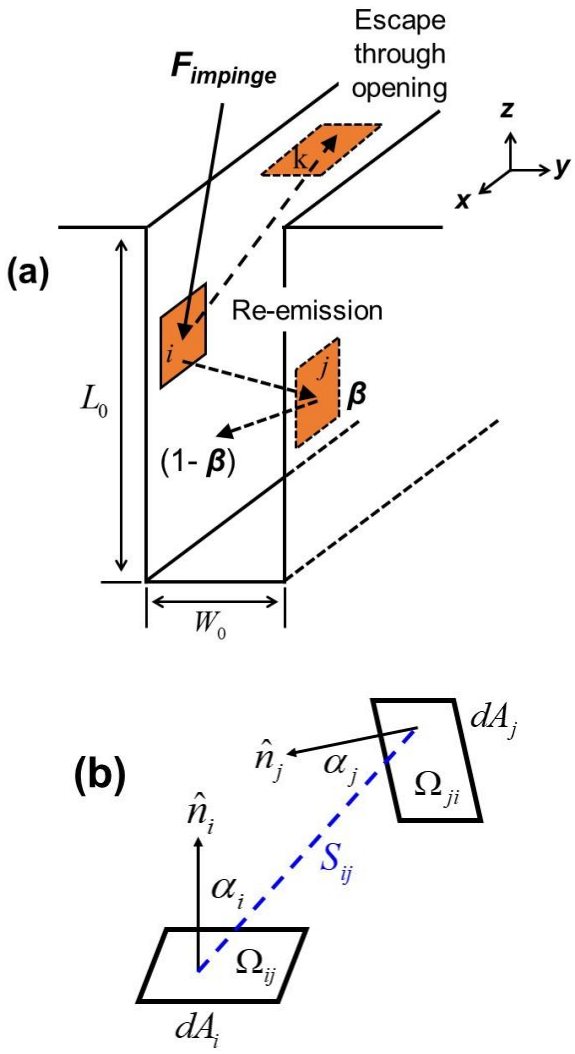

Figure 3.3. a) Schematic of a rectangular trench showing trench width W_0, depth L_0, and infinite length in *x*-direction. Three-dimensional fluxes are projected onto a two-dimensional cross-section (*y*-*z* plane). Representative small areas on the sidewalls and trench opening are labeled as *i*, *j*, and *k*. The flux falling on any position is found by integration over all elements connected to it via a solid angle. b) Schematic of two representative small areas, dA_i and dA_j. α_i is the angle between surface normal of *i* (labeled as $\hat{n}_i$) and the connecting line between *i* and *j*. The solid angle between *i* and *j* at position *i* is given by: $\Omega_{ij} \sim \frac{\cos(\alpha_i)}{S_{ij}^2}$, where S_{ij} is the length of the connection between *i* and *j*.

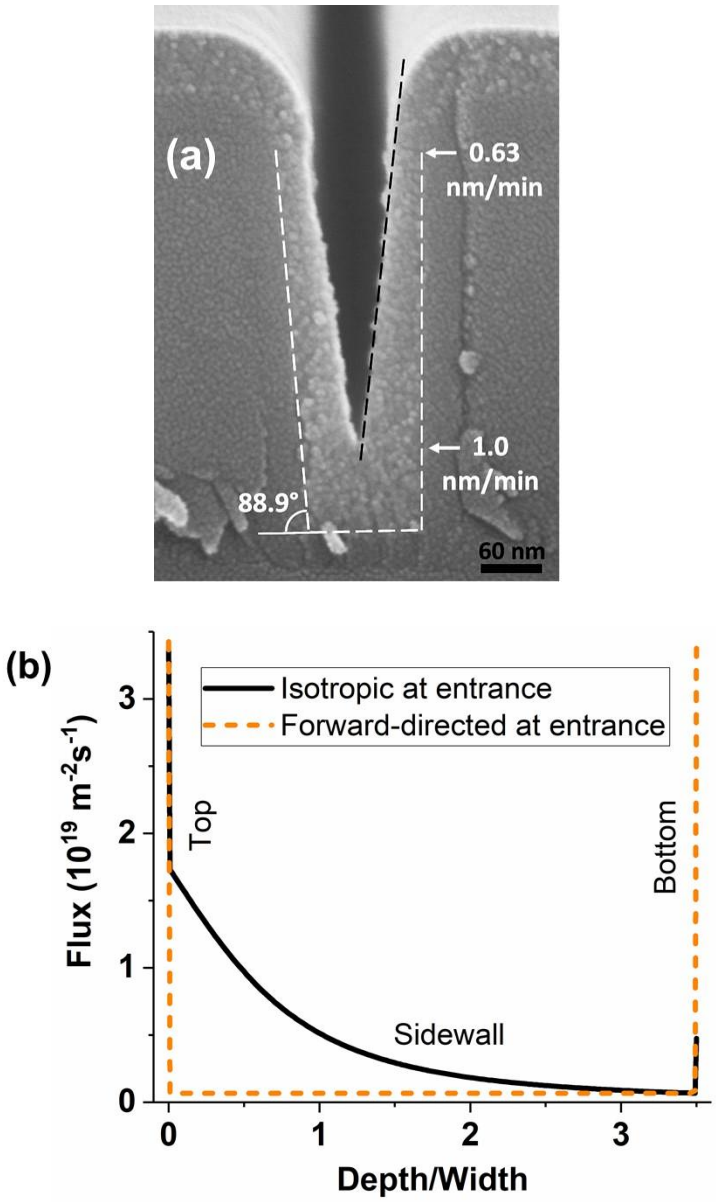

Figure 3.4. a) SEM image of superconformal HfO_2 coating (step coverage = 1.6) in a trench of aspect ratio 3.5, coated using 0.09 mTorr TDMA-Hf and 0.009 mTorr H_2O (forward-directed) at 200 °C for 60 min. b) Calculated Initial water flux distributions on the trench sidewall for the forward-directed and isotropic components. The trench sidewall has an outwards taper of 1.1°, so it intercepts some of the forward-directed flux. Note the large magnitude of the directed flux at the trench bottom.

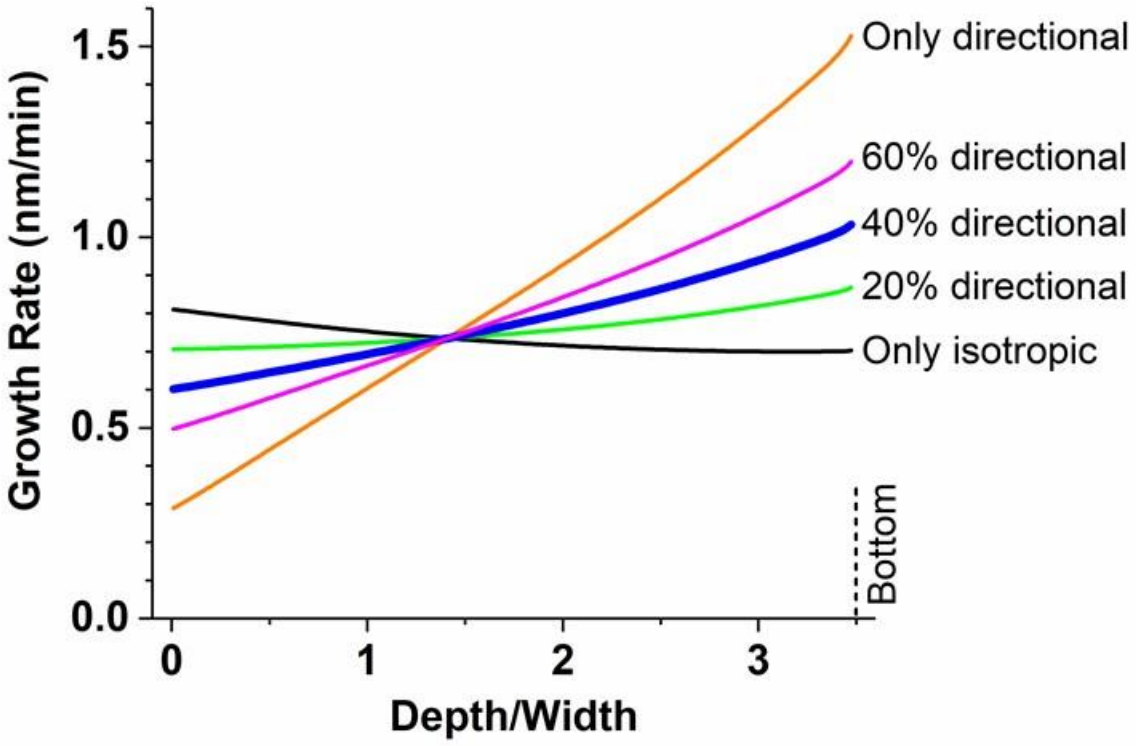

Figure 3.5. Calculated growth rates (with $\beta = 0.021$) for isotropic and directional fluxes along with different linear combinations of the two. The blue curve (40% directional + 60% isotropic fluxes) gives the best fit to the experimental results of Figure 3.4a.

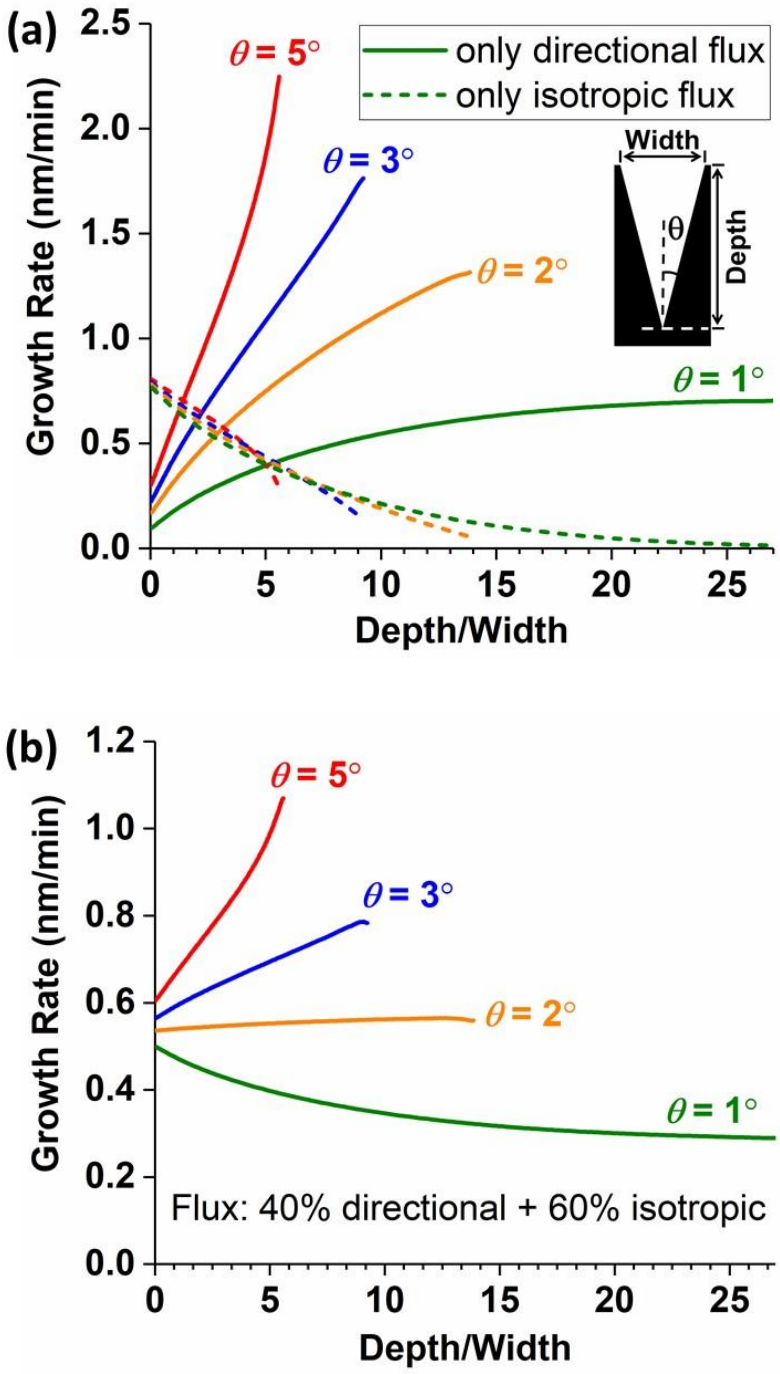

Figure 3.6. a) Calculated growth rates for V-shaped trenches with θ = 1, 2, 3 and 5°. Inset: schematic of a V-shaped trench showing trench width, depth, and sidewall tilt angle θ. b) Growth rates for the same tilt angles using 40% directional plus 60% isotropic fluxes (the best fit linear combination in Figure 3.5).

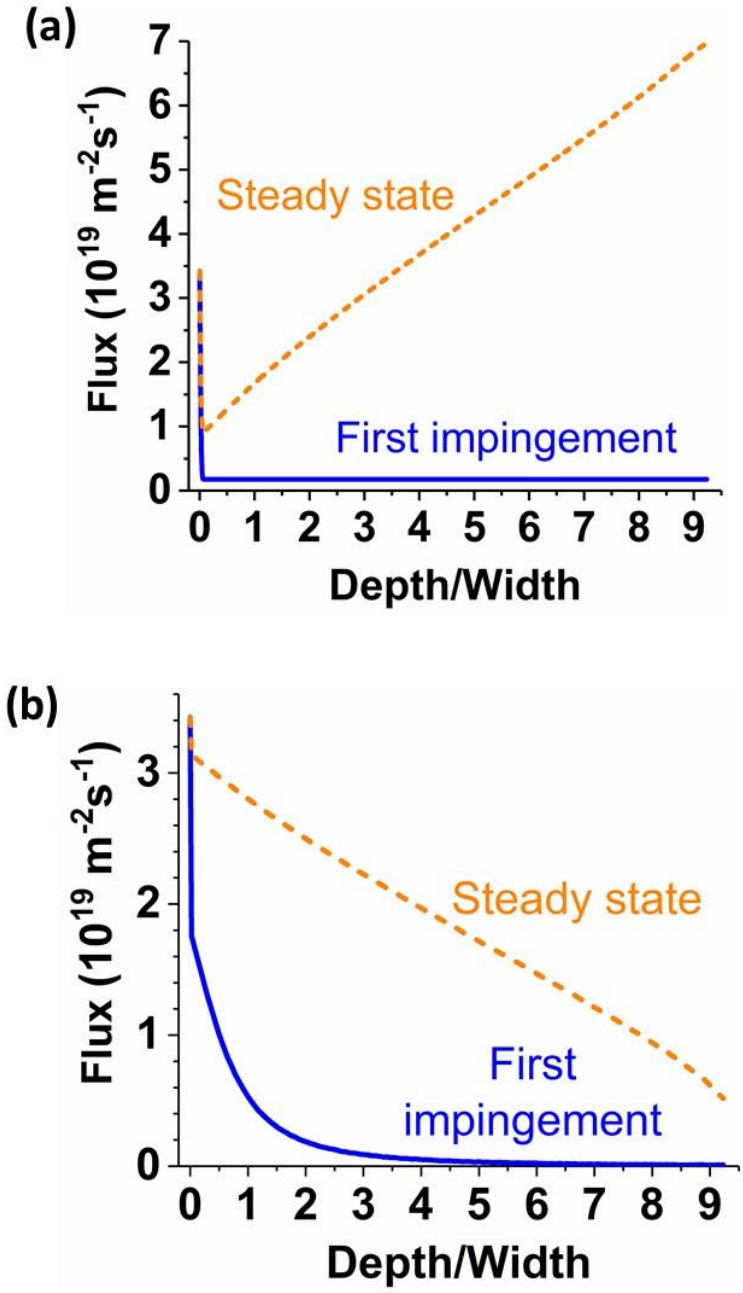

Figure 3.7. First impingement and steady state (calculated using ballistic transport method) flux distributions inside a V-shaped trench with $\theta = 3°$ for forward-directed (a) and isotropic fluxes (b). In both cases steady state flux inside the trench is higher than the first impingement flux. Once molecules reach a depth inside the trench they have less probability to escape out though the trench opening. Consequently, they have higher probability of multiple internal reflections inside the trench until consumed as film by sticking on trench sidewall (growth).

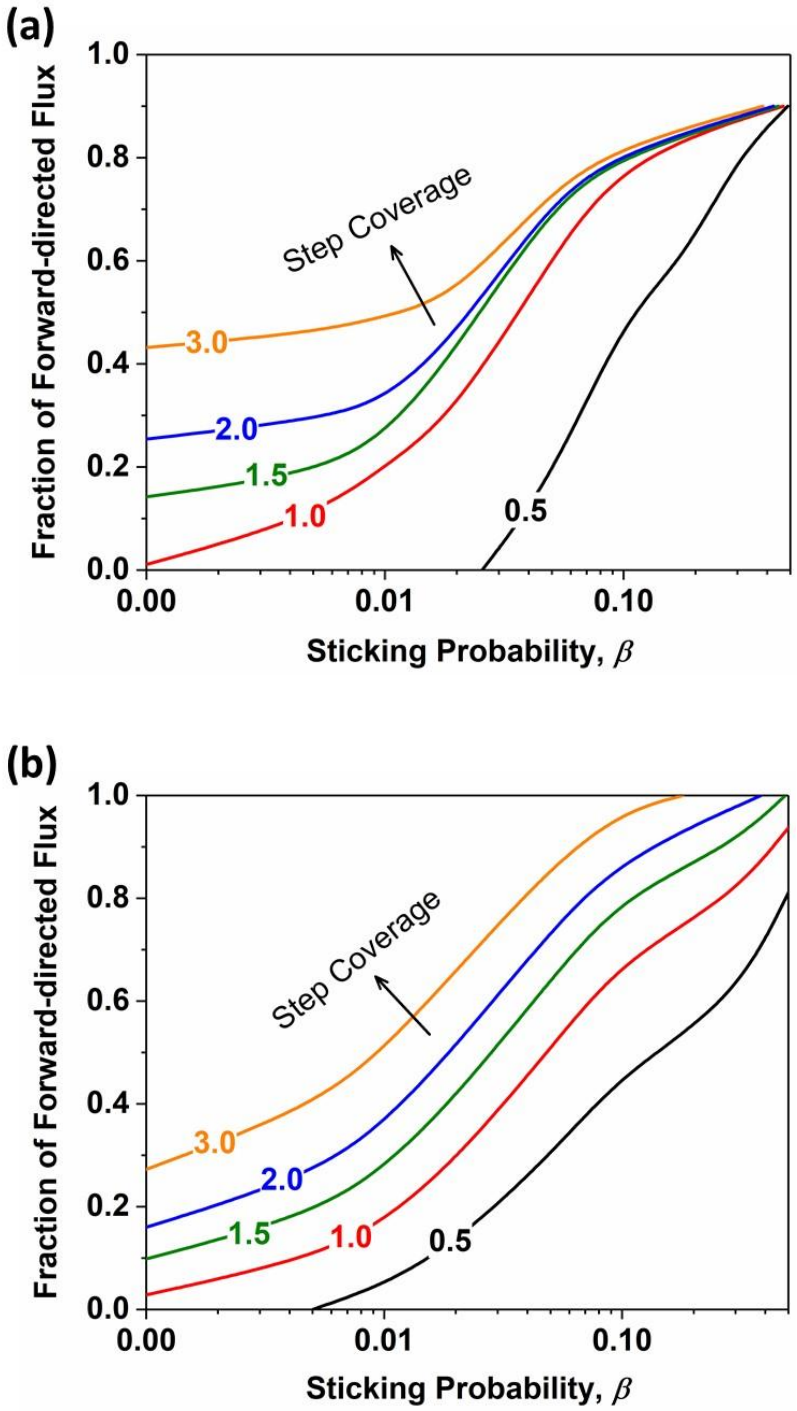

Figure 3.8. Contour plots of step coverage as a function of water sticking probability and fraction of forward-directed water flux. a) Rectangular trench with an aspect ratio of 10. b) V-shaped trench with $\theta = 3°$ (nominal aspect ratio = 9.5).

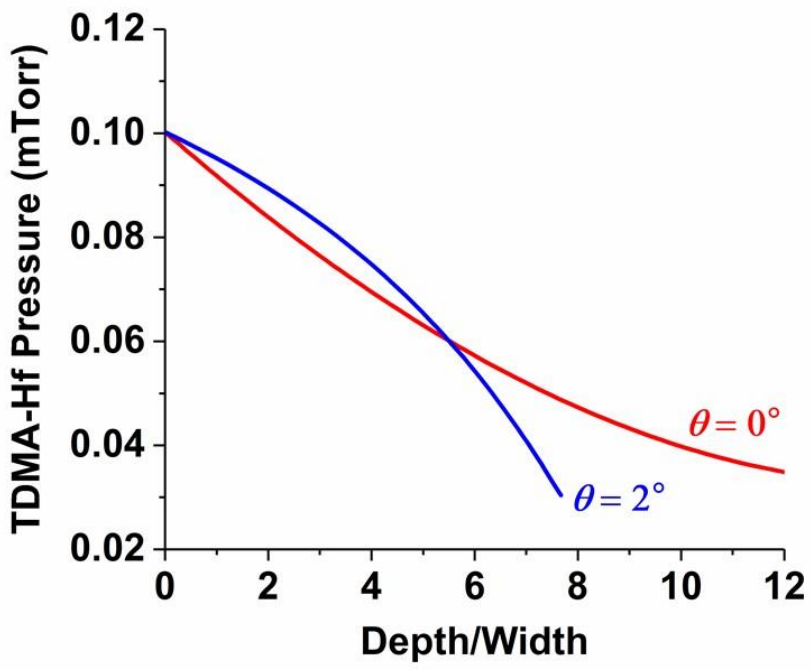

Figure 3.9. Diffusion-reaction calculation of the TDMA-Hf precursor pressure as a function of depth in a rectangular trench (θ = 0°) and a V-shaped trench with θ = 2° (nominal aspect ratio = 14). A substrate temperature of 200 °C is considered in the calculation.

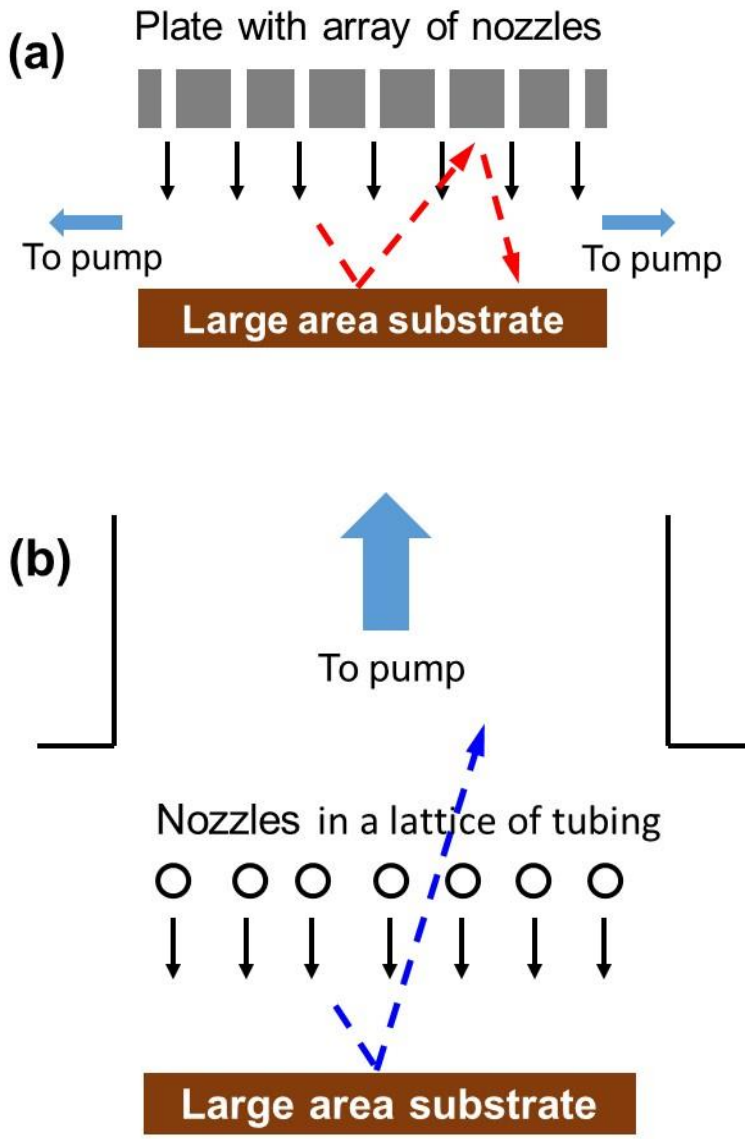

Figure 3.10. Schematics of showerhead: a) conventional showerhead design used for thickness uniformity on large area substrates, and b) a new conceptual design to increase the fraction of forward-directed water flux, in addition to achieving thickness uniformity.

CHAPTER 4

SEAMLESS FILL OF DEEP TRENCHES BY CVD: USE OF A MOLECULAR GROWTH INHIBITOR TO ELIMINATE PINCH-OFF

4.1 Introduction

4.1.1 Background

Complete filling of deep trenches or vias with a second material, without leaving a void or seam inside, is of high demand for the fabrication of advanced microelectronic and photonic devices [1-5]. As the device size shrinks, the effective aspect ratio of these structures increases [6], which makes the filling process more difficult to achieve. One major challenge in filling these structures is the formation of a thickness overhang near to the opening, called a 'bread-loaf' coating profile [7], which pinches off the opening prior to complete filling. Cyclic chemical vapor deposition (CVD) with periodic plasma etch-back can be used to prevent bread-loaf formation [7]. However, plasma etch step sometime causes irrecoverable damage to the underlying substrate [8-11], which is undesirable for the above applications.

We present an alternative solution in which an additional reactant species, which serves as a growth *inhibitor*, is added continuously during the CVD process. The adsorption and reaction properties of the inhibitor are critical. One category of inhibitor we term *non-consumable* (Figure 4.1a), meaning that the molecule adsorbs reversibly on the growth surface and reduces the film growth rate, but ultimately desorbs without dissociation [12]. Due to the reversibility, a non-consumable inhibitor will reach an equilibrium partial pressure everywhere inside the trench and thus reduce the growth rate on all the surfaces. This enhances conformality but does not differentially eliminate the bread-loaf problem. We previously reported three cases of non-consumable inhibition, the use of NH_3 during HfB_2 growth from $Hf(BH_4)_4$ [12], the use of dimethyoxyethane (dme) during TiB_2 growth from $Ti(BH_4)_3$(dme) [13], and the use of vinyl tri-methyl silane (VTMS) during Cu growth from Cu(hfac)VTMS [14]. In the first case of NH_3,

inhibition is due to site blocking. Whereas in the latter two cases, the inhibitor appears to stimulate the associative desorption of the precursor fragment, $Ti(BH_4)_3$ or Cu(hfac), from the growth surface; site blocking may occur, but is not required to explain the reduced growth rate. Note that since the initial precursor adsorption step releases dme or VTMS, respectively, the net reaction conserves inhibitor molecules, i.e., they are non-consumable.

A second category of inhibitor we term *consumable* (Figure 1b), meaning that it adsorbs on the growth surface and tends to dissociate rather than to desorb intact (the adsorption is irreversible). The dissociation products then incorporate into the film, or associate and desorb. The film growth rate is reduced either by site blocking due to adsorbed inhibitor or its reaction products, or by a reduction in the reactivity of sites that are not site-blocked, but which contain heteroatoms from the inhibitor. To eliminate bread-loaf formation, it is important that (i) the consumable inhibitor have a high rate of adsorption and dissociation relative to desorption (i.e. a high adsorption constant, defined by the ratio of adsorption to desorption rates), and (ii) any products released from the surface are not capable of causing inhibition. These requirements assure that the inhibitor effect takes place on the surfaces directly exposed to the inhibitor flux, i.e., near to the trench opening. By contrast, a low rate of adsorption or dissociation, or an inhibition effect from byproducts, creates an inhibition effect that penetrates deeper into the trench, similar to the effect of a non-consumable inhibitor.

In steady-state, the probability for an incident species to adsorb onto the surface depends on the availability of vacant sites, and on a competition between all incident species for adsorption on those sites. We described the mathematics of this situation in an earlier publication [15]. A crucial point is that, with increasing partial pressure, the surface will become fully covered with adsorbates, which sharply reduces the adsorption rate of subsequently arriving molecules. If the partial pressure of inhibitor is made large enough to saturate the surface (together with the coverage of adsorbed precursor), then its adsorption rate will decline, and it will diffuse deep into the structure rather than inhibiting growth where it collided with the sidewalls for the first or second time. Thus, when the partial pressure of a non-consumable inhibitor is large enough to induce growth rate inhibition, but not so large as to fully saturate the surface, it can eliminate bread-loaf shaped coating; whereas at a higher partial pressure, the same inhibitor may diffuse deeper into the structure and cause an overall growth rate reduction, but without differentially eliminating the

bread-loaf. Thus, optimization of the partial pressures of inhibitor and reactants is expected to be important.

We next consider the role of the inhibitor in two kinetic situations.

4.1.2 The film growth process, by itself, is conformal (or subconformal).

The use of an inhibitor creates a superconformal profile (i.e. the step coverage > 1) inside trenches by reducing the growth rate mostly at the upper surfaces. We previously reported the use of H atoms as an inhibitor for CrB_2 film growth from the $Cr(B_3H_8)_2$ precursor [16]. H atoms, generated from a remote H_2 plasma source, have a high sticking probability and reduce the CrB_2 growth rates at the trench opening by > 50 %, thereby produces a coating profile with increasing film thickness toward the bottom of the trench (superconformal). An intrinsic part of the growth kinetics is the removal of excess H from the surface. The additional H atoms supplied by the plasma take part in this kinetics, i.e., they are ultimately removed from the surface rather than being incorporated in to the film.

In addition to H atoms, we have explored other atomic species and neutral molecules as consumable inhibitors (Table 1). For HfB_2 film growth from the $Hf(BH_4)_4$ precursor, N atoms and H(hfac) are able to significantly decrease growth rate (by > 80 %); $Pd(hfac)_2$ is able to completely stop the film growth. However, these inhibitors incorporate heteroatoms into the film; and in the case of $Pd(hfac)_2$, when the inhibitor is turned off, growth needs to re-nucleate on the relatively unreactive surface, which induces a high surface roughness.

4.1.3 The film growth process, by itself, is superconformal.

a. **<u>An inhibitor is used to enhance the superconformal effect inside a trench</u>**, i.e., to increase the ratio of growth rate at the bottom sidewall to that at the top sidewall, which is already > 1. We previously demonstrated superconformal growth of MgO using competitive surface reaction kinetics [17]; this process can completely fill trenches of aspect ratio up to 9. In this case we predict that a suitable inhibitor can be used to enhance the step converge for higher aspect ratio (> 10) trenches. When the rectangular trench is converted to a V-shaped trench, the transport of reactant is very difficult when the angle between the side wall and trench axis

is equal or less than a value of ~ 3° [18]; the added inhibitor can assist in creating and maintaining an angle greater than this.

b. **<u>An inhibitor is used to suppress the bread-loaf formation at the trench opening</u>**, thereby eliminating pinch-off to afford seamless fill. We recently demonstrated a superconformal CVD growth process for HfO_2 from tetrakis(dimethylamino)hafnium, abbreviated as TDMA-Hf, and H_2O using forward-directed flux of rate limiting reactant, which is H_2O [19]. This approach creates a virtual source of water at the bottom of a trench structure. Because the underlying growth kinetics afford a slightly subconformal process, the creation of a virtual water source at the trench bottom creates a coating profile that decreases in thickness from the bottom to top sidewalls, i.e., it is superconformal from the top. However, since the forward-directed water flux also impinges on the top surface, the coating on the flat surface outside the trench is thicker and eventually forms a bread-loaf profile at the trench opening and pinches-off before complete fill. The time evolution of a bread-loaf shape and the ultimate failure due to pinch-off in a trench with aspect ratio of 3 is demonstrated in Figure 4.2a-c.

4.1.4 'Bread-loaf ratio'

The geometry of a bread-loaf shape at the trench opening can be described by the ratio of maximum film thickness at the trench opening (t_0) to that at just below the opening where the bread-loaf shape has minimum thickness (t_{min}) (Figure 4.2d); we refer to this, t_0/t_{min}, as the 'bread-loaf ratio'. To avoid pinch-off at the trench opening, the bread-loaf ratio must be ≤ 1.0 – *an important criterion for complete fill*. The trench in Figure 4.2a has a bread-loaf ratio of ~ 2; this number is similar for the other HfO_2 film growth conditions used in the present experiments and in our previous report [19]. To reduce the bread-loaf ratio to ≤ 1, a successful inhibitor for complete fill should reduce the growth at the top surface of a trench by at least 50 %.

In addition to the bread-loaf ratio requirement, the underlying film growth kinetics needs to be either: (i) superconformal in a rectangular trench having the capability to form a V-shaped fill with sidewall tilt angle (θ) of $\geq 3°$ with respect to the trench axis, or (ii) at least conformal (step coverage ≤ 1) if a V shape with $\theta \geq 3°$ already exists [18, 19].

In this work, we explore different inhibitors for HfO_2 growth from the TDMA-Hf precursor and water co-reactant (Table 1); for the inhibitors H(hfac) and H(acac), we demonstrate the elimination of pinch-off at the trench opening and achieve complete seamless fill in trenches with aspect ratio up to 10. We also use a Markov chain model for ballistic transport-reaction within the trench to calculate the inhibitor flux (and consumption rate) for different values of the inhibitor sticking probability; the simulation results provide upper and lower bounds on the reaction kinetics that inhibitor should exhibit for the present purpose.

4.2 Experiment

4.2.1 Film growth

The film growth experiments are conducted in a turbo-pumped cold-wall CVD system with a base pressure of 5×10^{-8} Torr, most of which is H_2. The substrate is radiatively heated to 200 °C by a tungsten wire mounted behind the substrate holder; the temperature is measured by a K type thermocouple probe clamped to a spot on the substrate holder plate. The TDMA-Hf precursor (≥ 99.99 %), and inhibitors (3DMAS, MOTMS, H(hfac) and H(acac)) are obtained from Sigma-Aldrich and kept in a Pyrex container adapted to a stainless-steel fitting. There is no flow regulation device for TDMA-Hf; the mass flow is controlled by heating the source container to temperatures of 25 to 50 °C; the delivery tube is heated to 80 °C (slightly below precursor decomposition temperature of 90 °C) to avoid condensation on its walls; no carrier gas is used for the precursor. For all four inhibitors, flow is controlled with needle (metering) valves. Deionized (DI) water at room temperature is used as the co-reactant; the water partial pressure is controlled with a needle valve. Precursor, water and inhibitor are supplied through separate stainless-steel tubes (4 mm i.d.). The precursor and water delivery tubes can be pointed normal to the substrate (they terminate 7 cm away from the substrate surface) or at the chamber sidewall. The water delivery tube is pointed at the substrate (forward-directed) unless otherwise stated. The inhibitor tube is always pointed at the reactor wall to obtain an isotropic flux distribution over the substrate surface. A TDMA-Hf pressure of 0.09 – 0.18 mTorr and a H_2O pressure of 0.009 – 0.023 mTorr are used in this work; these pressure ranges provide superconformal HfO_2 coating in trenches [19]. The inhibitor pressure is varied within a range of 0.01 – 2.6 mTorr. The partial pressures reported here

are the average values inside the reactor, which were measured with only precursor or only water or only inhibitor flowing before the growth experiments. The forward-directed fluxes on the growth surface are higher than those given by the isotropic pressures. During film deposition, a slow rate of reaction in the gas phase or on the room-temperature chamber walls will consume a portion of the molecules, hence, the partial pressures reaching the substrate during growth are smaller than those measured above. Growth rate measurements are done on 1.5 x 1.0 cm planar Si and 300 nm thermal SiO_2/Si wafers. The Si wafers are cleaned using standard solvents (in the order of acetone, isopropyl alcohol, DI water, isopropyl alcohol and dry N_2 blow), which do not etch the native oxide. For conformal coating and filling studies, lithographically defined microtrenches with SiN walls are used.

4.2.2 Film characterization

Film microstructure and thickness are determined using cross-sectional scanning electron microscopy (SEM). The refractive indices of HfO_2 films are derived from ex situ variable angle spectroscopic ellipsometry data acquired at incident angles of 50°, 60°, and 70° and fit to the Cauchy equation. The film thickness during growth is determined from in situ spectroscopic ellipsometry (SE) data using the derived indices and a multilayer optical model, consisting of Si substrate, native oxide on Si, and the deposited HfO_2 film. The film thickness measured by ellipsometry is found to be within ± 5 % of that determined from SEM cross-sectional images. The reported film growth rate is the final thickness divided by the duration of growth; this assumes the absence of a significant nucleation delay, which we verified by real-time SE in the growth chamber. Rutherford backscattering spectrometry (RBS) is used to measure the areal density of Hf atoms; this value is divided by the film thickness as measured by SEM to give the density of the Hf sublattice. Auger electron spectroscopy (AES) is used to identify the chemical elements in the film. Because of the charging effect on HfO_2 film surface and preferential erosion of lighter elements, AES data are interpreted qualitatively, instead of converting the intensities to atomic concentrations.

4.3 Results and Discussion

4.3.1 Ballistic model: inhibitor consumption in trenches

The microscopic surface reaction kinetics involving three reactants is inherently complex and cannot be fully determined from macroscopic film growth data. However, we show that the growth rate variation as a function of the inhibitor flux can be utilized to shift the growth conditions near the trench opening, while leaving the kinetics deeper in the trench relatively unchanged. By adopting a simple model, in which the inhibitor kinetics are represented by a sticking probability per wall collision, the inhibition effect as a function of depth in a trench can be modeled as a function of that sticking probability.

A ballistic transport-reaction model, fully described in reference [18], is used to calculate the net inhibitor flux distribution as a function of trench depth, which is then converted to a consumption rate by multiplying with the sticking probability, β (Figure 4.3). We consider three different values of β , 0.01, 0.1 and 0.9, referred to as low, medium and high, respectively. Note that the film growth rate inside the trench will be reduced by the largest fraction at a depth at which the inhibitor consumption is maximum. For low β, the inhibitor consumption rate is nearly uniform at all depths in a rectangular trench with aspect ratio 10 (Figure 4.3a), whereas for a medium or high β, the inhibitor consumption drops with depth into the trench. However, a small fraction of the isotropic flux from outside the trench directly impinges onto the trench bottom and is then redistributed on the sidewalls from the bottom towards the top. If β is medium or high, this flux redistribution creates a minimum consumption point at some depth above the bottom.

In a V-shaped trench with θ = 3°, however, the inhibitor consumption monotonically decreases with depth for all three (low, medium or high) values of β; the minimum is at the bottom of the trench for any β. (Figure 4.3b). This is because, in addition to the absence of a flat bottom, transport of molecules toward the apex of V is extremely difficult; here we consider θ = 3°, which we previously showed to be a minimum angle for superconformal growth of HfO_2 in a V-shaped trench.

For coating inside a rectangular trench with nearly parallel sidewalls, the above results predict that the most significant inhibition effect will occur when the trench bottom closes to form

a V. To sufficiently reduce the growth rate (by ≥ 50 % in present experiments) at the opening, while having a minimum effect on film growth at the lower sidewalls of the trench, an inhibitor with medium to high sticking probability will be the most suitable.

4.3.2 Experimental results

A. Tris(dimethylamino)silane (3DMAS), $[(CH_3)_2N)]_3SiH$

3DMAS is commonly used as an ALD precursor for SiO_2 growth, but reaction with H_2O requires a high substrate temperature (> 400 °C) [20]. Here we explore whether this molecule can, at lower temperature, be used as a non-consumable inhibitor. To rule out the possibility of forming a SiO_2 layer, we performed experiments with a co-flow of 0.25 mTorr 3DMAS plus 0.5 mTorr H_2O on a planar Si substrate at 300 °C, and on a SiO_2 substrate at 280 °C. For both cases, the 3DMAS partial pressure was increased to 2.3 mTorr after 10 min. The *in situ* SE data shows no change with time for either substrate, i.e., no film nucleation and growth (*Supplementary Materials*). These temperatures are well above our HfO_2 growth temperature of 200 °C, which further assures the absence of SiO_2 growth.

On a planar substrate, co-flowing 3DMAS at a pressure of 0.05 to 0.25 mTorr together with 0.18 mTorr TDMA-Hf and 0.019 mTorr H_2O at 200 °C, decreases the HfO_2 growth rate (Figure 4.4a). However, the rate of decrease with increasing P_{3DMAS} is low; for a 3DMAS pressure of 0.25 mTorr, the decrease in growth rate is only ~ 24 %, which is not enough to suppress the HfO_2 bread-loaf. A higher decrease in growth rate (~ 47 %), which still below the critical value of 50 % identified above, is observed when the 3DMAS pressure is increased to 2.1 mTorr; however, at high pressure the sticking probability of 3DMAS may decrease due to surface saturation effects [21], leading to similar inhibition on all surfaces.

In a trench with an aspect ratio of 6, a 3DMAS pressure of 0.25 mTorr is co-flowed with 0.18 mTorr TDMA-Hf and 0.023 mTorr H_2O at 200 °C (Figure 4.5b). The growth rate at the top surface is 1.4 nm/min and a minimum growth rate of 0.7 nm/min occurs at the sidewall near the mid-depth of the trench (Figure 4.5b); the resulting bread-loaf ratio is 2. Comparing this result with an identical trench, coated using the same conditions but without any inhibitor (Figure 4.5a),

shows that the growth decreases similarly at all surface (~ 30 %). These results indicate a low adsorption constant.

The refractive index of HfO_2 grown with or without 3DMAS almost overlaps (Figure 4.6), meaning that the incorporation of inhibitor into the film is very low or zero, which is the characteristic of a non-consumable inhibitor. While the weak inhibition effect of 3DMAS is not sufficient to suppress bread-loaf formation, it could be useful for applications that only need to enhance the conformal coating of HfO_2 (as opposed to filling) in very high aspect ratio (> 10) trenches.

B. Methoxytrimethylsilane (MOTMS), $CH_3OSi(CH_3)_3$

In the sol-gel literature, MOTMS is reported to modify the silica surface by converting surface –OH (hydroxyl) to $–OSi(CH_3)_3$ groups [22]; this motivated us to test MOTMS on the HfO_2 surface as a growth inhibitor. A decrease in growth rate, due to the steric bulk or the reduced reactivity of the $–OSi(CH_3)_3$ group, is observed on a planar substrate using 0.18 mTorr TDMA-Hf, 0.023 mTorr H_2O and a variable pressure (1.0 to 2.6 mTorr) of MOTMS at 200 °C (Figure 4.4b). Similar to 3DMAS (Figure 4.4a), the decrease in HfO_2 growth rate as function of MOTMS pressure has small slope; for example, with 2.6 mTorr of MOTMS the growth rate decreases by ~ 30 % (weak inhibition). Film grown using the same MOTMS pressure has slightly lower refractive index than that grown without any inhibitor (Figure 4.6); the decline in refractive index can be due to the incorporation of inhibitor atoms into the film or a reduced film density. The RBS measured density for the Hf sublattice is ~ 77% that of bulk, whereas a film grown without any inhibitor has a density ~ 86 % that of bulk. The weak inhibition, combined with the low incorporation, leads to a relatively uniform and small inhibition effect in a trench with aspect ratio of 7 (Figure 4.5c); the bread-loaf ratio remains unchanged (~ 2), similar to that for 3DMAS (Figure 4.5b).

C. Hexafluoroacetylacetone [H(hfac)], $CF_3COCH_2COCF_3$

We previously reported that H(hfac) strongly inhibits the growth of HfB_2 film from a single-source precursor, $Hf(BH_4)_4$, where the hfac ligand binds to surface sites and reduces precursor adsorption [16]. However, H(hfac) is an acid that can etch metal oxides to afford metal chelates and water as the byproducts [23]. For HfO_2, the etch products $Hf(hfac)_4$ or

$Hf_2(OH)_2(hfac)_6$ have low volatility at 200°C; thus, we expect that H(hfac) will have a very small (if any) etching effect on HfO_2. We expose a HfO_2 film to a H(hfac) pressure of 3 mTorr and measure the oxide thickness by SE. The observed HfO_2 etch rate is 0.005 nm/min; at a H(hfac) pressure of 40 mTorr, the etch rate increases slightly to 0.017 nm/min (Figure 4.7). These etch rates are two orders of magnitude lower than the decrease in growth rate obtained using H(hfac) at pressures less than 0.5 mTorr; hence, we attribute the kinetic effect of H(hfac) to inhibition rather than to etching (discussed further below).

Co-flow of H(hfac) during the HfO_2 film growth, with 0.09 mTorr TDMA-Hf and 0.014 mTorr H_2O at 200 °C, reduces the growth rate rapidly (up to 77 %) for a H(hfac) pressure of < 0.32 mTorr; at higher pressure the slope of growth rate decrease is lower (Figure 4.4c). To test if a small pressure of H(hfac) can afford a reduction in the bread-loaf ratio, we first start with a co-flow of 0.1 mTorr H(hfac) in a trench with aspect ratio of 7, while keeping the other conditions unchanged (Figure 4.8a). The resulting coating profile has a bread-loaf ratio of 1.4, which is an improvement in comparison with the ratio of 2 obtained for without any inhibitor (Figure 4.5a), but not good enough to avoid pinch-off.

We next increase the H(hfac) pressure to 0.27 mTorr, keeping other conditions the same. The coating result obtained in a trench with aspect ratio of 6 is remarkable; the obtained bread-loaf ratio is ~ 1, which is ideal for filling (Figure 4.8b). Moreover, the gradual increase in film growth rate on the lower sidewalls of the trench (Figure 4.5a) is preserved with the co-flow of 0.27 mTorr H(hfac). As expected, using the same growth conditions for a longer time affords complete fill in an identical trench without any seam inside. For comparison, another identical trench, coated using the same conditions but without any inhibitor for the same growth time, shows a large void inside due to the pinch-off at the bread-loaf edges (Figure 4.8d).

The refractive index decreases by ~ 13 % for 0.27 mTorr H(hfac) co-flowed with 0.09 mTorr TDMA-Hf and 0.014 mTorr H_2O at 200 °C (Figure 4.6). The reduction in refractive index can be due to F and C incorporation into the film, as verified by the AES depth profile (*Supplementary Materials*), plus a decrease in the film density. The RBS measured film density for the same sample is ~ 68 % that of bulk.

D. Acetylacetone [H(acac)], $CH_3COCH_2COCH_3$

H(acac) is a halogen free analog of H(hfac); it is a weaker acid and less volatile than H(hfac). It has recently been reported as an inhibitor for area selective ALD of SiO_2 deposition dielectric surfaces [24]. For growth with 0.09 mTorr TDMA-Hf and 0.014 mTorr H_2O at 200 °C, adding H(hfac) pressures up to 0.04 mTorr *increases* the growth rate; possible reasons for this behavior are discussed below. For pressures of 0.04 mTorr and above, H(acac) strongly inhibits HfO_2 growth (Figure 4.9). Similar to H(hfac) in Figure 4.4c, the slope of the growth rate reduction becomes low for H(acac) pressures > 0.08 mTorr, and high pressures of H(acac) do not completely stop the film growth. For a film grown on planar Si substrate using 0.09 mTorr TDMA-Hf, 0.014 mTorr H_2O and 0.06 mTorr H(acac) at 200 °C, the refractive index decreases by ~ 7 % at wavelength of 600 nm (Figure 4.6); this decrease can be caused by C incorporation into the film and a decrease in the film density to ~ 73 %.

To investigate the initial increase in growth rate when co-flowed with a H(acac) pressure of < 0.04 mTorr, we impinge the surface with H-atoms from a remote plasma source during the HfO_2 film growth from TDMA-Hf and H_2O; an instantaneous increase in film growth rate is observed for a small flux of H-atoms (not shown) due to a faster decomposition of the TDMA-Hf precursor by the H-atoms. Similarly, H(acac) can increase the film growth by providing H+ that help to decompose the TDMA-Hf. However, when H(acac) surface coverage, which is a function the H(acac) pressure, reaches a certain limit, the inhibition effect starts to dominate and any further increase in the H(acac) pressure reduces the growth rate. For the purpose of the present study (to suppress bread-loaf at the trench opening), we focus only on the inhibition effect of the H(acac) molecules.

<u>Complete fill in trenches with nearly parallel sidewalls:</u>

We next investigate film growth in trenches with 0.09 mTorr TDMA-Hf and 0.014 mTorr H2O at 200 °C, plus a co-flow of H(acac) at a pressure of ≥ 0.06 mTorr, for which the inhibition effect is significant (Figure 4.9). For a H(acac) pressure of 0.06 mTorr, complete fill is achieved in a trench with aspect ratio of ≤ 5 for a growth time of 60 min (Figure 4.10a). A slight increase of the H(acac) pressure to 0.07 mTorr affords complete fill in trenches with aspect ratio of ≤ 9

(Figure 4.10b). Further increase of the H(acac) pressure to 0.09 mTorr significantly improves the fill in trenches with aspect ratio ≤ 11.5 (Figure 4.10c).

To scrutinize the fill quality, we use cross-sectional TEM for the growth conditions of Figure 4.10b. The bright field TEM image of a trench with aspect ratio of 7 reveals a subtle low-density seam at near the bottom, whereas the fill is dense and free of any seam at the top half of the trench (Figure 4.11a). We previously reported that to convert a rectangular trench to a V-shaped one, such that the V angle is higher than the critical value of 2°, the required minimum step coverage has a strong dependence on the fraction of the forward-direct water flux. In the present experimental setup, the fraction of the forward-direct and isotropic water fluxes is 40 % and 60 %, respectively. The presence of a subtle seam in Figure 4.11a suggests that an increase in the fraction of the forward-directed flux, which is possible in a faster pumped reactor, is necessary to afford HfO_2 fill without any seam at all.

The EDS element map obtained in the TEM shows low concentrations of N (Figure 4.11b) and C (Figure 4.11c) incorporation in the same coated trench sample; this is consistent with the small decrease in the film refractive index for a co-flow of H(acac) (Figure 4.6). Note that the trench sidewall material is SiN_x, so a bright N signal is observed at the sidewalls. The brightness of the C signal in the fill inside the trench is less than that in the film outside the trench; this is consistent with a large decrease in the inhibitor consumption when the inhibitor sticking probability is high (Figure 4.3). I.e., for the H(acac) pressure of 0.07 mTorr, the inhibitor flux significantly drops inside the trench and acts mostly on the upper sidewalls of the trench.

The inhibitor reaches a saturation regime at high pressure:

To investigate if we can further improve the fill in trenches with aspect ratio of > 10, a higher inhibitor pressure is used. The idea is to shift the growth conditions up to a depth that extends beyond the bread-loaf at the opening, thereby enhancing the V angle when the rectangular trench converts to a V-shaped trench. Interestingly, when the H(acac) pressure is increased to 0.12 mTorr, keeping the other conditions the same as in the Figure 4.10, the growth rate decreases similarly at all surfaces (Figure 4.12a) and the bread-loaf ratio reverts back to that obtained without co-flowing any inhibitor (Figure 4.5a). A similar result is obtained for a 0.32 mTorr of H(hfac) pressure, with other conditions the same as in Figure 4.12a, in a trench with aspect ratio of 8

(Figure 4.12b). In both these cases, the inhibitor pressure is high enough to create a saturated surface coverage, and thus a lower sticking rate, that leads to a nearly constant inhibitor pressure at all depths in the trench. Nonetheless, the inhibitor significantly decreases the effective water sticking probability, which is ideal to afford highly conformal film growth kinetics, at a reduced growth rate, in recessed structures with very high aspect ratio.

Coating in trenches with a re-entrant geometry:

In a re-entrant trench, the width is minimum at the opening and increases with depth (Figure 4.13a). Conformal coating in such a trench is extremely difficult because of the low conductance of the reactant molecules due to the narrow opening; and complete fill using a highly conformal process is simply impossible due to the pinch-off at the narrow opening. To fill such a geometry requires either (i) a true bottom-up process that selectively grows film only from the bottom surface, or (ii) a superconformal process with a step coverage large enough to compensate for the decreasing width from the top to bottom.

In preliminary attempts to fill re-entrant trenches, we test our superconformal process using forward-directed water flux along with a co-flow of H(hfac) inhibitor to suppress bread-loaf at the opening. Note that to afford complete fill in a re-entrant trench, the bread-loaf ratio needs to be $\leq$ 1; consequently, in addition to the requirement of a high step coverage of the superconformal growth process, the inhibition effect of the inhibitor needs to be very strong. For a co-flow of 0.063 mTorr H(acac) with 0.09 mTorr TDMA-Hf, 0.014 mTorr H_2O at 200 °C, the observed inhibition effect in a re-entrant trench with aspect ratio of 8 is not strong enough to keep the trench opening from pinching-off, which leaves a large void inside (Figure 4.13b). However, when the H(acac) pressure is increased to 0.09 mTorr, keeping other conditions unchanged, the void width significantly decreases, and approaches a line seam. Given the enormous challenge of filling these structures, we consider the coating profile obtained in the Figure 4.13c as a remarkable result. Since we already observed saturation of the H(acac) inhibitor at high pressure (Figure 4.12a), we did not perform experiments with a further increased H(acac) pressure. The presence of a seam inside the trench in Figure 4.13c may be a limitation of the underlying superconformal process itself, as opposed to a limitation of the inhibitor; enhancing the fraction of forward-directed water flux would likely improve the filling.

Coating in trenches using isotropic water flux:

Until now all the experiments were done with a forward-directed water flux so that the growth process in a trench, by itself, is superconformal; inhibitors are co-flowed to suppress the bread-loaf at the opening. As discussed in the Introduction, we previously used inhibitors to convert conformal HfB_2 growth kinetics from a single-source precursor, $Hf(BH_4)_4$, into a superconformal process inside trenches. To identify whether the H(acac) inhibitor can afford a similar effect on the HfO_2 growth process, we conduct an experiment in which water is delivered isotopically, by pointing the water delivery tube towards an inside wall of the reactor. This creates a subconformal HfO_2 coating profile with a bread-loaf ratio of ≥ 2. To convert such a process to a superconformal one, the inhibitor needs not only to suppress the bread-loaf at the opening, but also to reduce growth rate all the way to the trench bottom with strongest inhibition at the trench opening.

For a 0.08 mTorr H(acac) pressure, co-flowed with 0.09 mTorr TDMA-Hf and 0.014 mTorr H_2O (isotropic) at 200 °C for 90 min, a superconformal effect is not observed in trenches (Figure 4.14). The bread-loaf ratio remains unchanged (for example, ~ 2 in the trench with aspect ratio of 4.5 in Figure 4.14a), and the inhibition effect is same on all surfaces; these results suggest an inhibitor saturation, although we did not obtain such a saturation when the water is supplied in a forward-directed way at a slightly higher H(acac) pressure of 0.09 mTorr (Figure 4.10c). When three reactants are co-flowed, the film growth kinetics at the surface is interdependent, and we did not perform detailed analysis of the growth rate dependence on the H(acac) inhibitor pressure when the water is supplied isotopically (at lower flux). Therefore, the results obtained in the Figure 4.14 are not sufficient to conclude whether or not H(acac) can convert the subconformal HfO_2 growth in trenches when water flux is isotropic.

4.4 Conclusion

We demonstrate that an isotropic co-flow of a neutral inhibitor molecule during the superconformal growth of HfO_2 in trenches, using TDMA-Hf and forward-directed water flux, can suppress bread-loaf formation at the trench opening. Consequently, the pinch-off of the trench opening is eliminated, which affords a complete and seam-free fill of HfO_2. The effect of inhibitor

sticking probability on film grown at the trench sidewalls near the opening is obtained by simulating the inhibitor flux distribution using a Markov chain ballistic transport model; an inhibitor with a high sticking probability and a low desorption rate is ideal to eliminate the pinch-off at the trench opening.

We show that the sticking probability of the inhibitor can fall dramatically at higher inhibitor pressure, presumably due to a saturation of the possible surface coverage. Therefore, we require an inhibitor that can suppress bread-loaf using a relatively low flux. From coating experiments using different inhibitors, we identified that H(hfac) and H(acac) inhibitors can afford complete fill in trenches with aspect ratio of ≤ 10. The halogen free H(acac) is more desirable because it does not incorporate F into the film. They both incorporate C into the film; however, C-doped oxide is acceptable and presently in use in the semiconductor industry.

We also demonstrate that the use of an inhibitor coupled with a superconformal film growth process can be used to fill re-entrant shaped trenches, i.e., the trench opening has the minimum width, provided that the growth process affords a large superconformal step coverage.

4.5 References

1. Ayazi, F. and K. Najafi, *High aspect-ratio combined poly and single-crystal silicon (HARPSS) MEMS technology.* Journal of Microelectromechanical Systems, 2000. **9**(3): p. 288-294.

2. Ireland, P.J., *High aspect ratio contacts: A review of the current tungsten plug process.* Thin Solid Films, 1997. **304**(1-2): p. 1-12.

3. Nandakumar, M., A. Chatterjee, S. Sridhar, K. Joyner, M. Rodder, and I.C. Chen. *Shallow trench isolation for advanced ULSI CMOS technologies*. in *International Electron Devices Meeting 1998. Technical Digest (Cat. No.98CH36217)*. 1998.

4. Jordana, E., J.M. Fedeli, P. Lyan, J.P. Colonna, P. Gautier, N. Daldosso, L. Pavesi, Y. Lebour, P. Pellegrino, B. Garrido, J. Blasco, F. Cuesta-Soto, and P. Sanchis. *Deep-UV Lithography Fabrication of Slot Waveguides and Sandwiched Waveguides for Nonlinear Applications*. in *2007 4th IEEE International Conference on Group IV Photonics*. 2007.

5. Saynatjoki, A., T. Alasaarela, A. Khanna, L. Karvonen, P. Stenberg, M. Kuittinen, A. Tervonen, and S. Honkanen, *Angled sidewalls in silicon slot waveguides: conformal filling and mode properties.* Opt Express, 2009. **17**(23): p. 21066-76.

6. *International Technology Roadmap for Semiconductors*. 2015.

7. Cote, D.R., S.V. Nguyen, A.K. Stamper, D.S. Armbrust, D. Tobben, R.A. Conti, and G.Y. Lee, *Plasma-assisted chemical vapor deposition of dielectric thin films for ULSI semiconductor circuits.* Ibm Journal of Research and Development, 1999. **43**(1-2): p. 5-38.

8. Stamper, A.K., J.B. Lasky, and J.W. Adkisson, *Plasma-Induced Gate-Oxide Charging Issues for Sub-0.5 Mu-M Complementary Metal-Oxide-Semiconductor Technologies.* Journal of Vacuum Science & Technology a-Vacuum Surfaces and Films, 1995. **13**(3): p. 905-911.

9. Cote, D., S. Nguyen, V. McGahay, C. Waskiewicz, S. Chang, A. Stamper, P. Weigand, N. Shoda, and T. Matsuda, *Process-induced gate oxide damage issues in advanced plasma chemical vapor deposition processes.* 1996 1st International Symposium on Plasma Process-Induced Damage, 1996: p. 61-66.

10. Cote, D.R., S.V. Nguyen, W.J. Cote, S.L. Pennington, A.K. Stamper, and D.V. Podlesnik, *Low-Temperature Chemical-Vapor-Deposition Processes and Dielectrics for Microelectronic Circuit Manufacturing at Ibm.* Ibm Journal of Research and Development, 1995. **39**(4): p. 437-464.

11. *Private communication with Intel Corporation*. 2016.

12. Babar, S., N. Kumar, P. Zhang, and J.R. Abelson, *Growth Inhibitor To Homogenize Nucleation and Obtain Smooth HfB2 Thin Films by Chemical Vapor Deposition.* Chemistry of Materials, 2013. **25**(5): p. 662-667.

13. Kumar, N., A. Yanguas-Gil, S.R. Daly, G.S. Girolami, and J.R. Abelson, *Growth Inhibition to Enhance Conformal Coverage in Thin Film Chemical Vapor Deposition.* Journal of the American Chemical Society, 2008. **130**(52): p. 17660-+.

14. Babar, S., E. Mohimi, B. Trinh, G.S. Girolami, and J.R. Abelson, *Surface-Selective Chemical Vapor Deposition of Copper Films through the Use of a Molecular Inhibitor.* Ecs Journal of Solid State Science and Technology, 2015. **4**(7): p. N60-N63.

15. Yanguas-Gil, A., N. Kumar, Y. Yang, and J.R. Abelson, *Highly conformal film growth by chemical vapor deposition. II. Conformality enhancement through growth inhibition.* Journal of Vacuum Science & Technology A, 2009. **27**(5): p. 1244-1248.

16. Yang, Y., *Chemical vapor deposition of metal diboride and metal oxide thin films from borohydride-bonded precursors*, in *Materials Science and Engineering*. 2007, University of Illinois at Urbana-Champaign.

17. Wang, W.B., N.N. Chang, T.A. Codding, G.S. Girolami, and J.R. Abelson, *Superconformal chemical vapor deposition of thin films in deep features.* Journal of Vacuum Science & Technology A: Vacuum, Surfaces, and Films, 2014. **32**(5): p. 051512.

18. Wang, W.B. and J.R. Abelson, *Filling high aspect ratio trenches by superconformal chemical vapor deposition: Predictive modeling and experiment.* Journal of Applied Physics, 2014. **116**(19): p. 194508.

19. Talukdar, T.K., W.B. Wang, G.S. Girolami, and J.R. Abelson, *Superconformal Coating and Filling of Deep Trenches by Chemical Vapor Deposition with Forward-Directed Fluxes.* Manuscript in preparation, 2018.

20. Burton, B.B., S.W. Kang, S.W. Rhee, and S.M. George, *SiO2 Atomic Layer Deposition Using Tris(dimethylamino)silane and Hydrogen Peroxide Studied by in Situ Transmission FTIR Spectroscopy.* Journal of Physical Chemistry C, 2009. **113**(19): p. 8249-8257.

21. Yanguas-Gil, A., Y. Yang, N. Kumar, and J.R. Abelson, *Highly conformal film growth by chemical vapor deposition. I. A conformal zone diagram based on kinetics.* Journal of Vacuum Science & Technology A, 2009. **27**(5): p. 1235-1243.

22. Sen Wei, H., C.C. Kuo, C.C. Jaing, Y.C. Chang, and C.C. Lee, *Highly transparent superhydrophobic thin film with low refractive index prepared by one-step coating of modified silica nanoparticles.* Journal of Sol-Gel Science and Technology, 2014. **71**(1): p. 168-175.

23. Mehrotra, R.C., R. Bohra, and D.P. Gaur, *Metal B-diketonates and allied derivatives*. 1978: Academic Press.

24. Mameli, A., M.J.M. Merkx, B. Karasulu, F. Roozeboom, W.M.M. Kessels, and A.J.M. Mackus, *Area-Selective Atomic Layer Deposition of SiO2 Using Acetylacetone as a Chemoselective Inhibitor in an ABC-Type Cycle.* Acs Nano, 2017. **11**(9): p. 9303-9311.

25. Venables, J.A., *Introduction to Surface and Thin Film Processes*. 2000: Cambridge University Press.

4.6 Tables and Figures

Table 4.1. List of inhibitors explored by our group based on their sticking probability and incorporation into film.

Inhibitor	Film Material	Inhibitor Sticking Probably	Inhibitor Incorporation	Hetero-atom (Impurity)	Reference
H-atom	CrB_2	High	Low	None	[16]
N-atom	HfB_2	High	High	N	[16]
H(hfac)	HfB_2	High	High	C, F	[16]
Pd(hfac)	HfB_2	Very High (re-nucleates)	High	Pd, C, F	[16]
3DMAS	HfO_2	Low	Low	None	this work
MOTMS	HfO_2	Low	Low	C	this work
H(hfac)	HfO_2	High	High	C, F	this work
H(acac)	HfO_2	High	High	C	this work

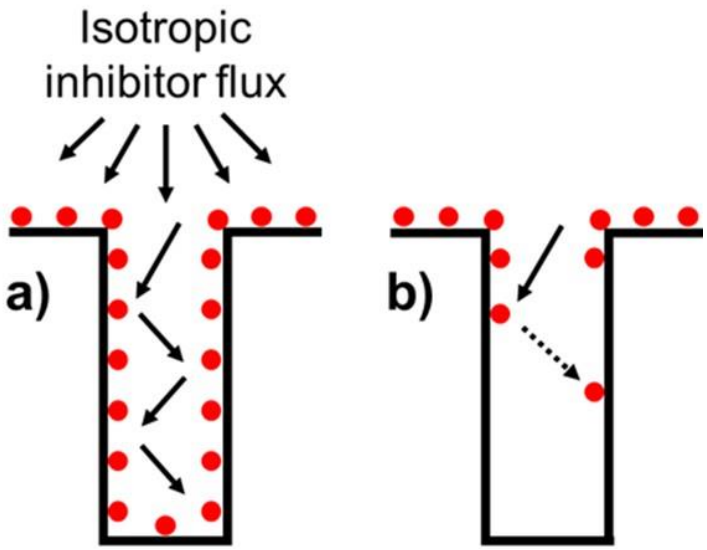

Figure 4.1. Schematic of the steady-state distribution of inhibitor molecules inside narrow trenches. a) Non-consumable inhibitor in adsorption equilibrium affords the same inhibition on all surfaces; b) consumable inhibitor with high adsorption constant affords inhibition only on upper surfaces. In both cases, the inhibitor has an isotropic (uniform) flux distribution outside the trench.

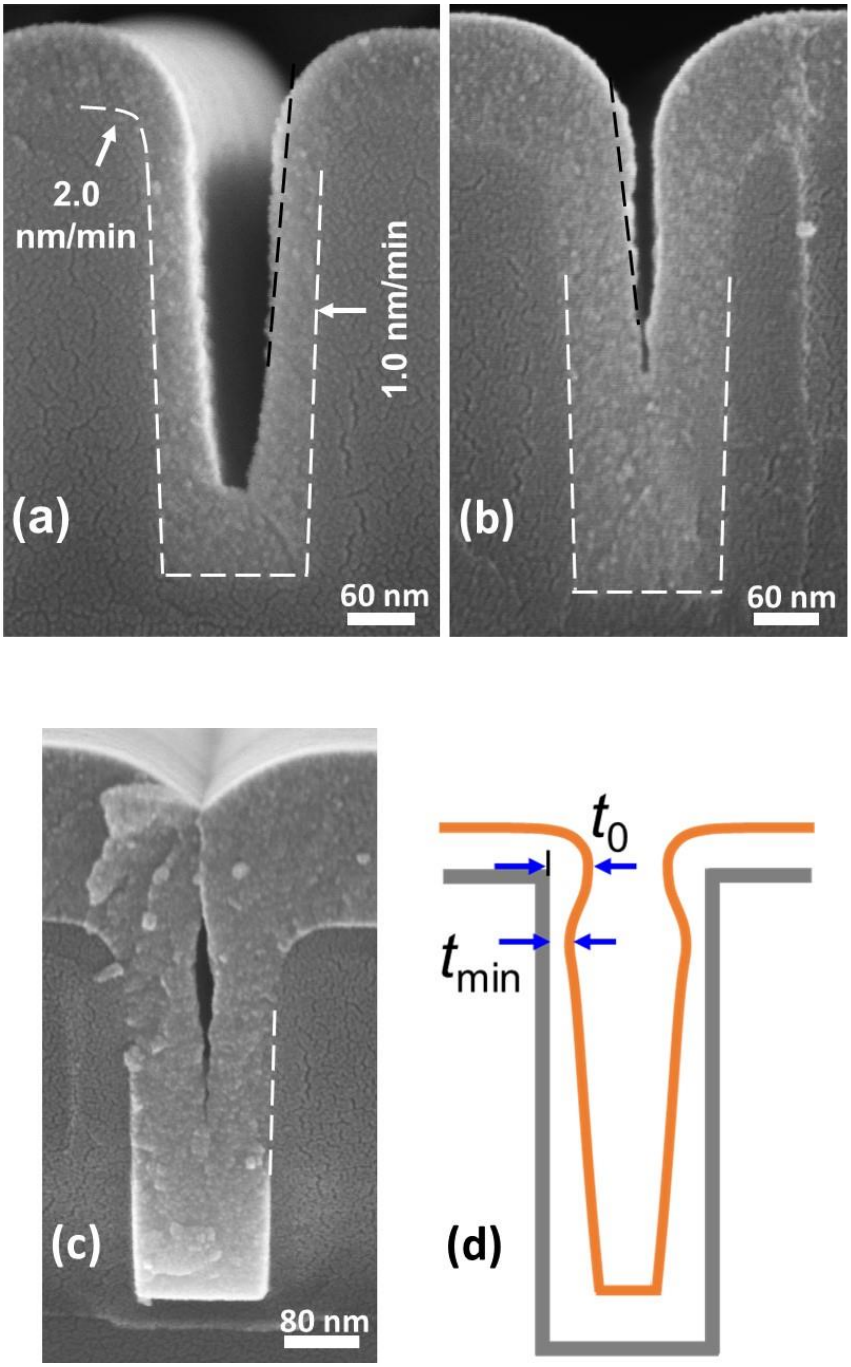

Figure 4.2. a-c) Cross-sectional SEM image of trenches with aspect ratio of 3, coated with 0.18 mTorr TDMA-Hf and 0.023 mTorr H_2O at 200 °C for: a) 40 min, b) 60 min, and c) 90 min. A black dashed line is added to highlight the bread-loaf shape at the trench opening. d) Schematic of a coating profile inside a rectangular trench describing the bread-loaf ratio, t_0/t_{min}, at the trench opening.

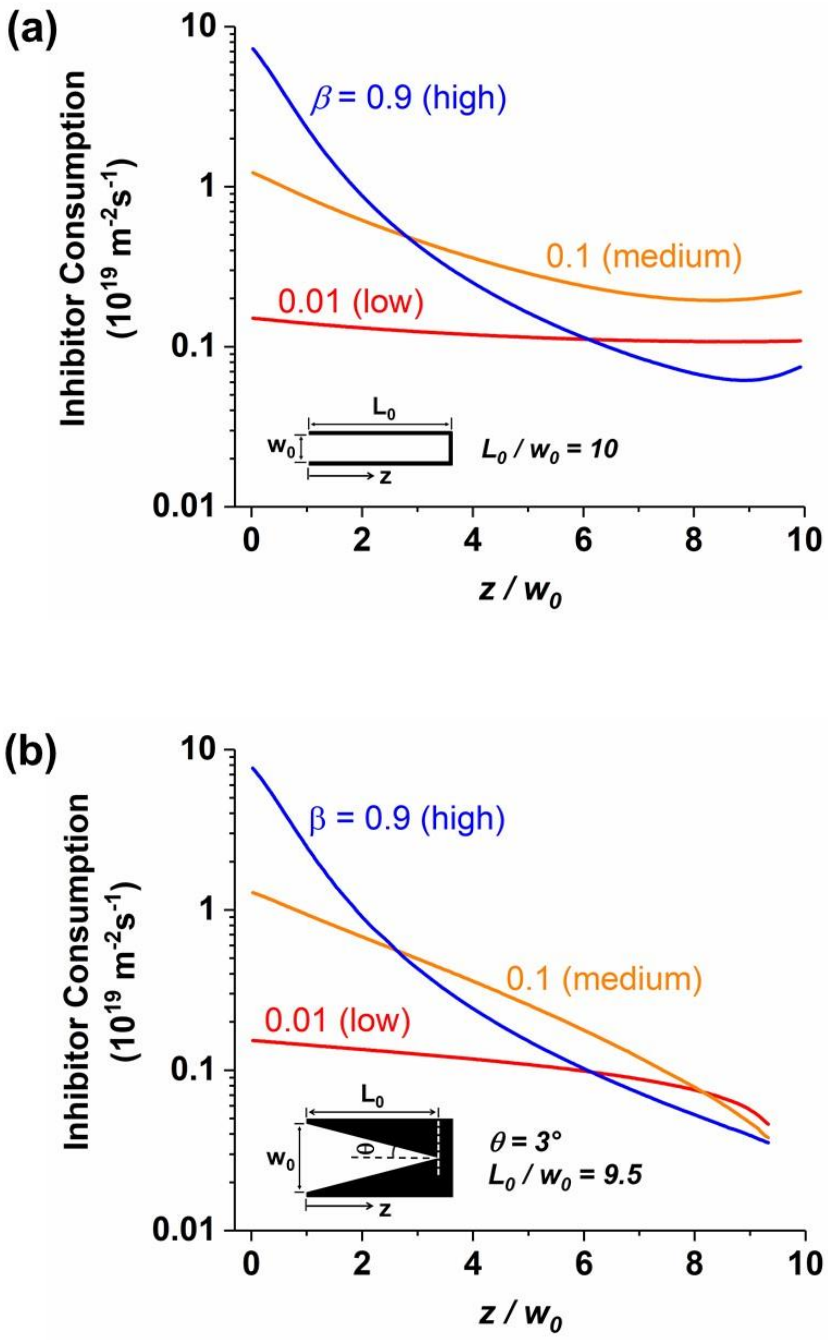

Figure 4.3. H(acac) inhibitor consumption rate (in flux units) inside trenches as a function of normalized depth; three different sticking probability values, 0.01, 0.1 and 0.9, are considered. a) Rectangular trench with aspect ratio of 10. Inset: Geometry of a rectangular trench showing the nominal aspect ratio (L_0/W_0). b) V-shaped trench with sidewall tilt angle of 3° with respect to the trench axis. Inset: Geometry of a V-shaped trench; for $\theta = 3°$, the nominal aspect ratio ($0.5/\tan\theta$) is 9.5. The uniform H(acac) pressure outside the trench is 0.1 mTorr which is converted to an isotropic flux using the ideal gas law [25].

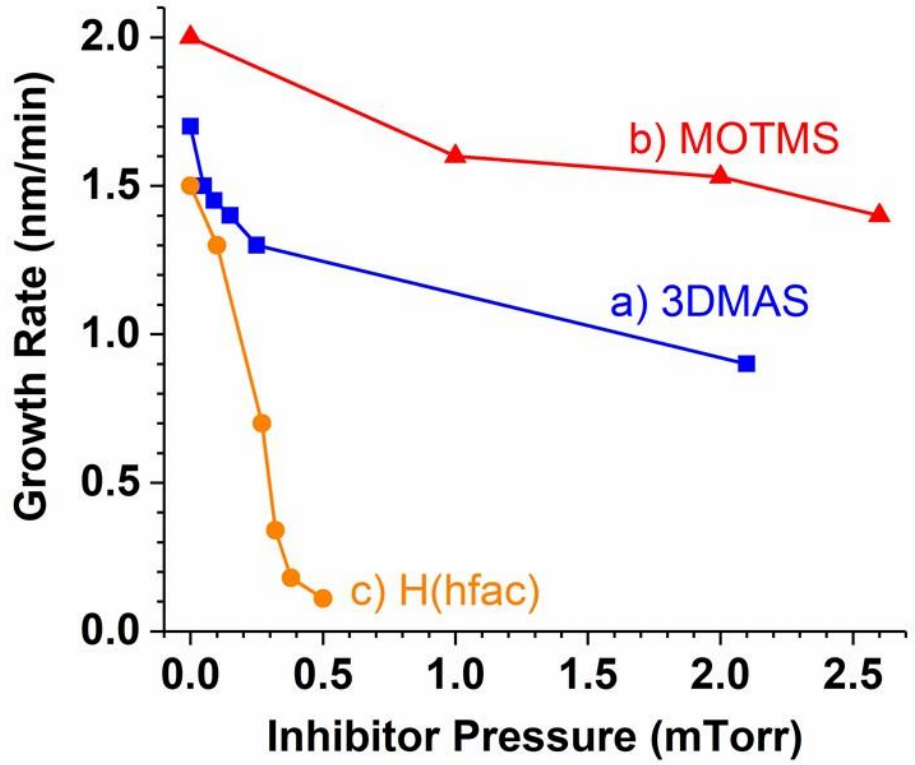

Figure 4.4. HfO_2 growth rates on planar Si (100) substrates at 200 °C measured by spectroscopic ellipsometry as a function of the inhibitor partial pressure. a) 3DMAS inhibitor co-flowed with 0.18 mTorr TDMA-Hf and 0.019 mTorr H_2O. b) MOTMS inhibitor co-flowed with 0.18 mTorr TDMA-Hf and 0.023 mTorr H_2O. c) H(hfac) inhibitor co-flowed with 0.09 mTorr TDMA-Hf and 0.014 mTorr H_2O. Lines through data points are a guide for the eye only.

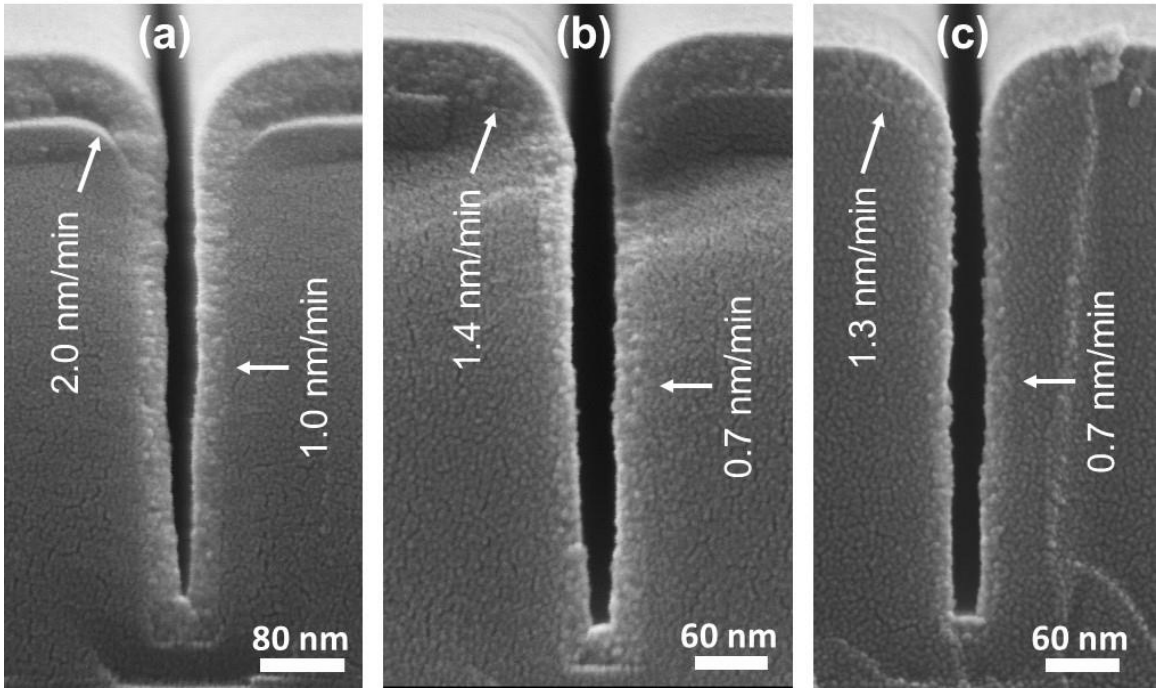

Figure 4.5. Cross-sectional SEM images of trenches, coated using 0.18 mTorr HfO_2 and 0.023 mTorr H_2O at 200 °C for 30 min. a) Without inhibitor (AR = 6). b) With 0.25 mTorr 3DMAS (AR = 6). c) With 2.6 mTorr MOTMS (AR = 7). In both b) and c), the growth rate is reduced by ~ 30 % both at the top surface and at sidewall near the middle of the trenches; however, the bread-loaf ratio (~ 2) is unaffected by these inhibitors in the present experiments.

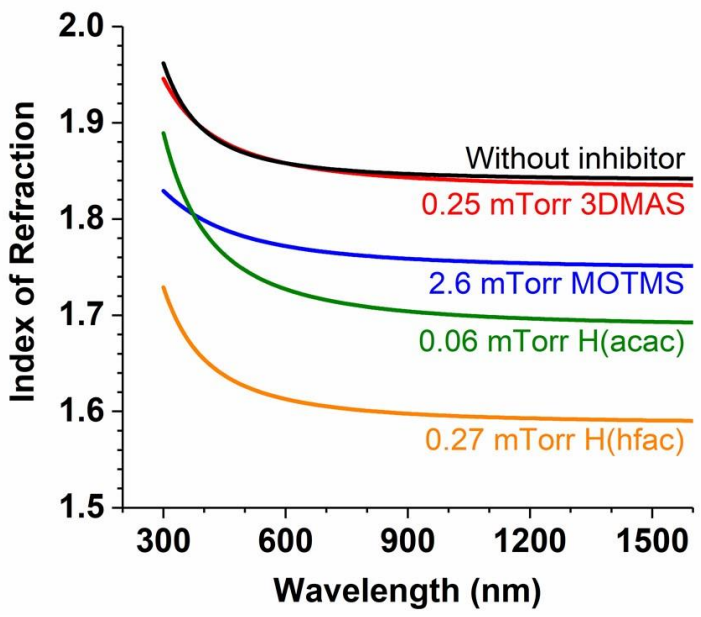

Figure 4.6. Refractive index of HfO_2 film grown without any inhibitor or with co-flow of different inhibitor molecules.

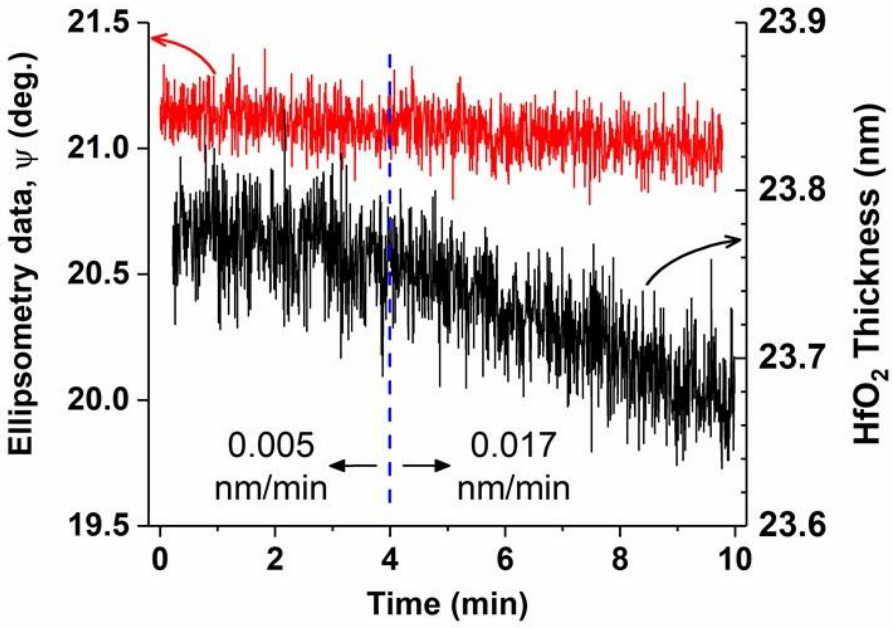

Figure 4.7. Ellipsometry data for possible etching of a HfO_2 film deposited with 0.09 mTorr TDMA-Hf and 0.014 mTorr H_2O at 200 °C: in situ SE data (red curve) and the corresponding HfO_2 thickness (black curve) at 200 °C with a H(hfac) flow of 3 mTorr for the first 4 min (etch rate = 0.005 nm/min) and 40 mTorr for the next 6 min (etch rate = 0.017 nm/min).

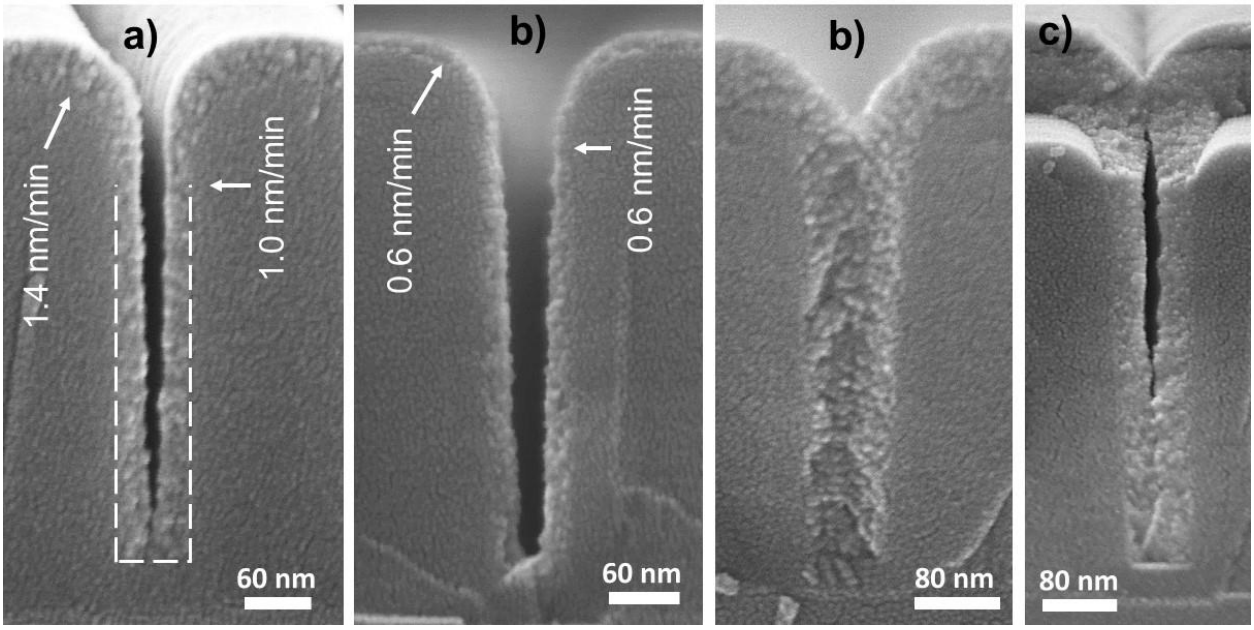

Figure 4.8. Cross-sectional SEM images of trenches, coated with 0.09 mTorr TDMA-Hf, 0.014 mTorr H_2O and variable H(hfac) pressure at 200 °C. a) 0.1 mTorr H(hfac) for 30 min (AR = 7); the bread loaf ratio is ~ 1.4. b) 0.27 mTorr H(hfac) for 30 min (AR = 6); the bread-loaf ratio is ~ 1. c) Complete fill in a trench: same conditions as in b) for 60 min. d) Void formation: conditions as in c) but without co-flowing H(hfac).

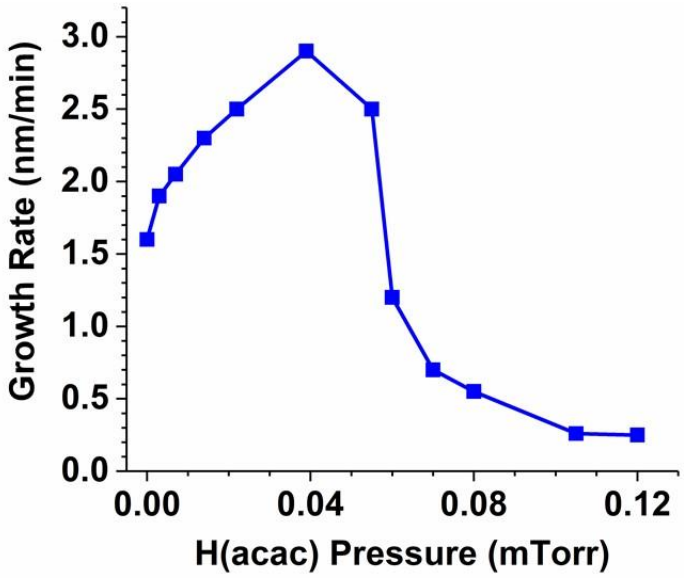

Figure 4.9. Film growth rates on a planar Si substrate as a function of H(acac) pressure that is co-flowed with 0.09 mTorr TDMA-Hf plus 0.014 mTorr H_2O at 200 °C. The line through the data points is a guide for the eye only.

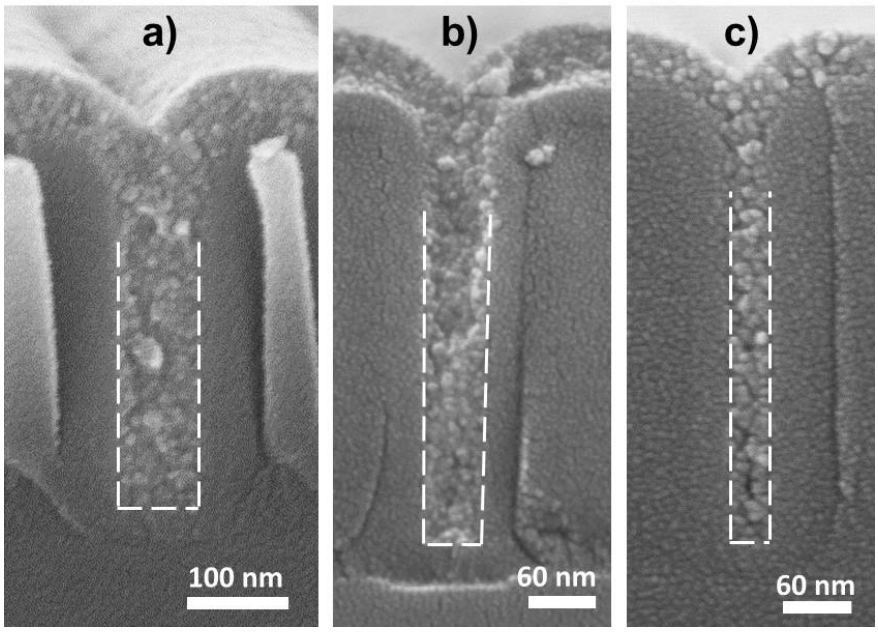

Figure 4.10. Complete fill in trenches with different aspect ratio (AR), coated using 0.09 mTorr TDMA-Hf, 0.014 mTorr H_2O and variable H(acac) pressure at 200 °C. a) 0.06 mTorr H(acac) for 60 min (AR = 5). b) 0.07 mTorr H(acac) for 60 min (AR = 9). c) 0.09 mTorr H(acac) for 75 min (AR = 11.5).

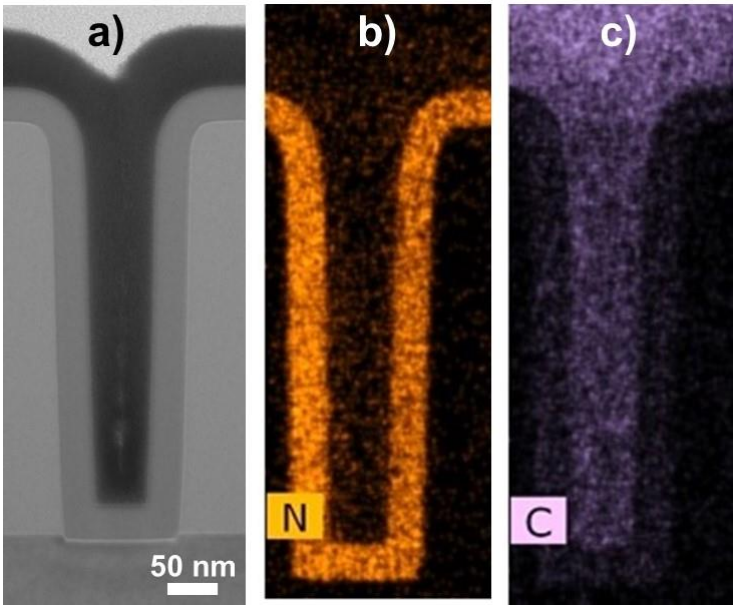

Figure 4.11. a) Bright field TEM image of a trench with AR = 7 from the same sample as in Figure 4.9b; there is a subtle low-density seam near the bottom of the trench. b and c) TEM-EDS elemental maps of N (b) and C (c) for the same sample as in a).

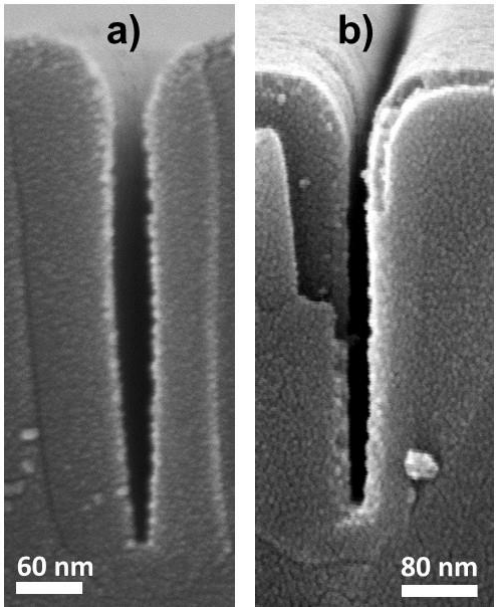

Figure 4.12. Cross-sectional SEM image of trenches, coated by coflowing inhibitors with 0.09 mTorr TDMA-Hf and 0.014 mTorr H_2O at 200 °C for 80 min: a) 0.12 mTorr H(acac) in a trench with AR = 11.5; and b) 0.32 mTorr H(hfac) in a trench with AR = 8.

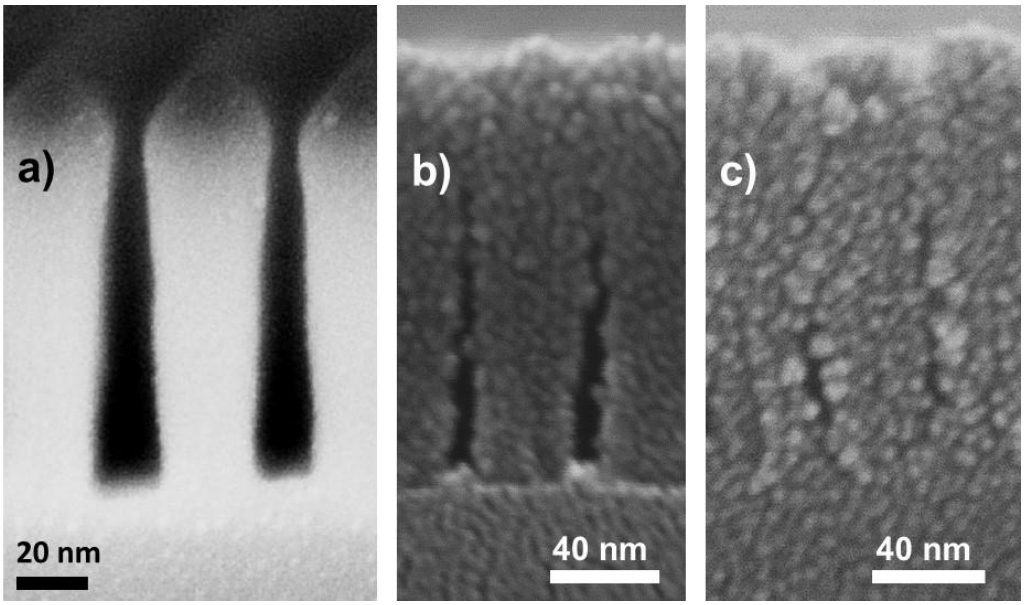

Figure 4.13. SEM image of re-entrant shaped trenches of aspect ratio 8. a) before coating. b) coated using 0.09 mTorr TDMA-Hf, 0.014 mTorr H_2O and 0.063 mTorr H(acac) at 200 °C for 20 min. c) coated using the same growth conditions as in b) but with 0.09 mTorr of H(acac) for 45 min.

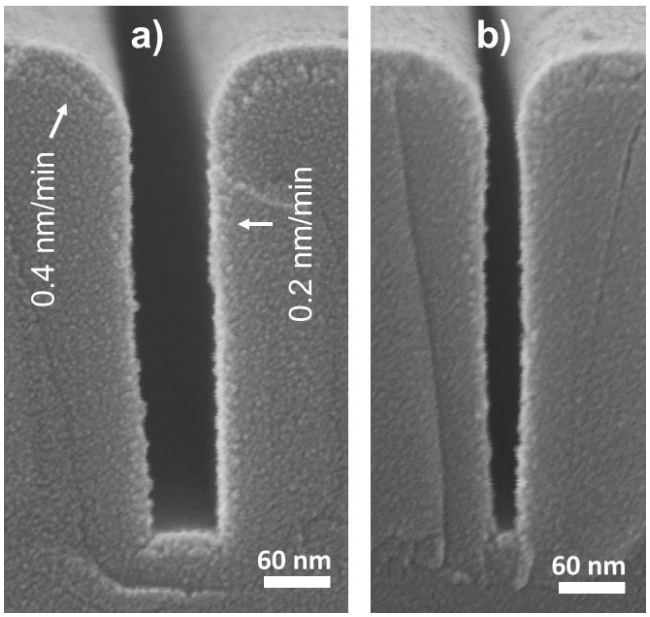

Figure 4.14. Coating profile in trenches with aspect ratio of 4.5 (a) and 8 (b) when 0.014 mTorr H_2O is supplied *isotropically* along with 0.09 mTorr TDMA-Hf precursor and 0.08 mTorr H(acac) inhibitor at 200 °C for 90 min. The bread-loaf ratio in these trenches is ~ 2.

4.7 Supplementary Material

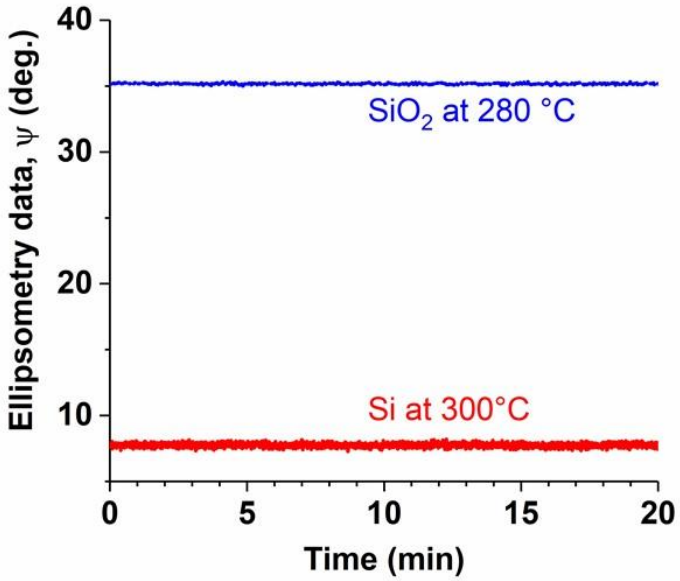

Figure S1. In situ SE data, Ψ, at 504.3 nm wavelength collected on substrates Si (at 300 °C) and SiO2 (at 280 °C) with 0.5 mTorr H2O, plus 0.25 mTorr 3DMAS for the first 10 min and 2.3 mTorr for the next 10 min. No dynamic change in Ψ (flat) indicates that nothing is grown on the surfaces.

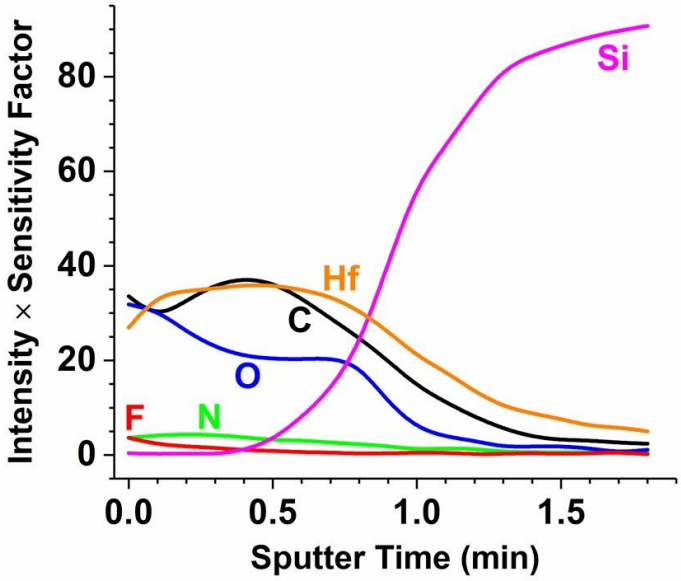

Figure S2. AES depth profile for film grown on planar Si substrate using 0.09 mTorr TDMA-Hf, 0.014 mTorr H_2O and 0.27 mTorr H(hfac) at 200 °C. Because of the charging effect on HfO_2 film surface and preferential erosion of lighter elements, AES data can be interpreted only qualitatively.

CHAPTER 5

HIGH QUALITY MgO FILM GROWN AT HIGH RATE BY LOW TEMPERATURE CONFORMAL CVD

5.1 Introduction

MgO is an attractive insulating material with a wide band gap (7.7 eV) [1], high dielectric constant (9.9) [2] and good thermal stability (melting point 2825 °C) [3]. These properties make MgO a suitable dielectric for capacitors in ICs and DRAMs, and for capacitive coupling of cables in wireless network towers [4]. MgO is also suitable as a plasma wall material [5], e.g., in plasma display panels, which require a film thickness ≥ 0.5 μm [6]. Optical waveguide applications require a film thickness in the micron range, determined by the wavelength being used [7]. To be manufacturable, these applications require that high quality films be deposited at a rate ~ 10s of nm/min or higher. In some of these applications the substrate has a complex geometry, which further requires that the coating be conformal (of uniform thickness) on all surfaces. In addition, the growth temperature must be < 400 °C to avoid exceeding the thermal budget of the substrate components.

Gas phase methods, such as chemical vapor deposition (CVD) or atomic layer deposition (ALD), are suitable for conformal coating of complex or recessed structures: when growth is limited by the surface reaction rate, the deposition precursor can be delivered to all surfaces, both external and internal. However, no report of MgO film growth by CVD or ALD (Table 1 and references therein) documents the simultaneous achievement of high growth rate, high conformality, low substrate temperature and good solid-state properties. Sputter deposition can afford MgO film growth at ≤ 300 nm/min, but the conformality has not been reported (and is expected to be poor) [8].

We recently demonstrated the CVD of MgO using a novel precursor, magnesium N,N-dimethylaminodiboranate, $Mg(H_3BNMe_2BH_3)_2$, abbreviated as $Mg(DMADB)_2$ [9-11]. This molecule has the highest volatility (vapor pressure ~ 0.8 Torr at 25 °C) of any known Mg-

containing molecule [12], hence, it can be delivered to the growth reactor without the aid of a carrier gas. It exhibits a unique regime of low temperature reactivity in which the competition between precursor and water for surface adsorption sites affords film growth in trenches that can be made perfectly conformal or even superconformal, i.e., growth is faster at depth than near to the opening [10]. In this report, we utilize this precursor in a different regime, such as higher substrate temperature and water flux, to obtain very high rate growth of MgO films with good optical, electrical, and mechanical properties and good step coverage (conformality) in deep trenches.

5.2 Experimental

Film growth is conducted in a turbo-pumped, cold-wall CVD system with a base pressure of 5×10^{-8} Torr, most of which is H_2. The substrate is radiatively heated by a tungsten wire mounted behind the substrate; the temperature is in the range of 270 – 350 °C, measured by a K type thermocouple mounted on the substrate holder. The $Mg(DMADB)_2$ precursor is synthesized by G.S.G. [12] and kept in a Pyrex container adapted to a stainless-steel fitting. The mass flow of precursor is controlled by heating the source container to various temperatures up to 40 °C; Ar carrier gas is used in selected experiments as noted below. The precursor delivery tube is heated to 70 °C to avoid condensation on tube walls. In selected experiments the gate valve to the turbo pump is throttled to maintain a higher process pressure inside the reactor. Deionized water at room temperature is used as the co-reactant; the water injection rate (partial pressure) is controlled using a needle valve. Precursor and water are supplied through separate stainless-steel tubes (4 mm i.d.) that point towards the substrate holder and terminate at 7 cm away from the substrate surface. The partial pressures of $Mg(DMADB)_2$ and H_2O are the average values inside the reactor measured before the growth experiments with only precursor or only water flowing. Within the pressure range used in the present experiments (< 100 mTorr), the Mg precursor does not react with water on the room temperature reactor walls, hence, the only consumption of reactants should take place on hot surfaces of the substrate holder. Growth rate measurements are done on 1.5 x 1.0 cm planar Si wafers that are cleaned using standard solvents (acetone and isopropyl alcohol) without removing the native oxide. For conformal coating studies, lithographically defined microtrenches

with SiN walls are used. The step coverage (degree of conformality) of MgO coating in trenches is calculated as the ratio of film thickness at the bottom sidewall to that at the top sidewall.

Film microstructure and thickness are determined using cross-sectional scanning electron microscopy (SEM). The refractive indices are derived from ex situ variable angle spectroscopic ellipsometry (VASE) data acquired at incident angles of 50°, 60°, and 70°, and fit to the Cauchy equation [13]. The film thickness during growth is determined from in situ spectroscopic ellipsometry (SE) data using the derived indices and a multilayer optical model consisting of Si substrate, native oxide on Si, and the deposited MgO film; surface and interfacial roughness layers are not included in the optical model. In calibration experiments, the film thickness measured by ellipsometry is within ± 5 % of that determined from SEM cross-sectional images. The reported film growth rate is the final thickness divided by the duration of growth; this assumes the absence of a significant nucleation delay, which we verified by real-time SE in the growth chamber. X-ray photoelectron spectroscopy (XPS) is used to identify the chemical state and elemental composition in the film. Rutherford backscattering spectrometry (RBS) is used to measure the areal density of Hf atoms; this value is divided by the SEM thickness to afford the density of the Hf sublattice. Films grown at ≤ 350 °C appear amorphous in X-ray diffraction.

Film adhesion is studied using nanoscratch measurements with a conospherical diamond tip of radius 1 μm. The applied normal load is 10 mN with a ramp rate of 0.33 mN/s; the lateral displacement (scratch) rate is 8.3 μm/s.

Electrical characterization is performed using metal-insulator-metal (MIM) capacitors (Figure 5.1) prepared as follows. First, 200 nm of Au is deposited by e-beam evaporation onto the SiO_2/Si substrate. Then 200 nm of MgO film is deposited using 3 mTorr $Mg(DMADB)_2$ and 8.8 mTorr H_2O at 270 °C for 10 min (growth rate = 6 nm/min). A portion of the underlying Au layer is masked during MgO deposition so that it can later be contacted. Finally, circular areas of Au (diameter = 1 mm, area = 7.9×10^{-3} cm^2) are deposited as the top contact by e-beam evaporation through a shadow mask with circular holes. C-V and I-V measurements of the MIM capacitors are performed using a probe station equipped with micromanipulators, a semiconductor parameter analyzer (Agilient 4155C) and an LCR meter (Agilient 4284A).

5.3 Results and Discussion

5.3.1 Growth rate

For very high growth rate of MgO deposition (90 – 300 nm/min), a relatively high substrate temperature (300-350 °C) is used and the $Mg(DMADB)_2$ precursor flux is enhanced using Ar carrier gas (Table 2). Films A, B and C are smooth, dense, and free of any columnar microstructure (Figure 5.2). To compensate the charging effect in SEM, films cross-sections are sputter coated with a Au-Pd alloy, which shows up as nodules on the film cross-section (Figures 5.2a and 5.2c).

Film A, with an Ar flow rate of 4 sccm, has a thickness of 0.9 μm at a growth rate of 90 nm/min (Figure 5.2a). Film B, with an Ar flow rate of 8 sccm, has a thickness of 0.4 μm at a growth rate of 200 nm/min (Figure 5.2b). Repeating the conditions of film B for longer time affords higher film thickness; however, the films delaminate for thickness > 0.7 μm (not shown).

5.3.2 Stress state

Film delamination can result from growth (intrinsic) stress or thermal (cooling) stress [14]. We do not perform any stress measurement in the present work, but the literature values of thermal coefficient of expansion for Si (2.6×10^{-6} /°C [15]) and MgO (12.6×10^{-6} /°C [16]) can be used to calculate the thermal stress. When the film is cooled down from the growth temperature (300 °C) to room temperature (23 °C), the thermal mismatch strain is large, 0.27 %, with the film in tensile strain. Above a film thickness of 0.7 μm, the net stress in films of type B evidently exceeds the adhesion strength of film to substrate, causing delamination.

The intrinsic growth stress in films depends (in an unknown way) on the substrate temperature and may change from tensile to compressive at a higher temperature [17]. To study empirically whether the state of film growth stress can be altered at a different growth conditions, the substrate temperature is increased to 350 °C and the $Mg(DMADB)_2$ flux is increased by increasing the carrier gas flow rate to 12 sccm. The resulting film (C) has a growth rate of 133 nm/min and a thickness of 2.0 μm without any delamination (Figure 5.2c). (We did not grow an even thicker film in an attempt to observe delamination.) Thus, these growth conditions modified the growth stress such that, in combination with the stresses due to thermal contraction,

delamination was avoided. It is also possible that the strength of the bond with the substrate was enhanced. The rough cross-section of the film C is due to the physical breaking of the thick (2 µm) sample.

5.3.3 Nanoscratch tests

Nanoscratch measurements on film C exhibit a smoothly increasing lateral force with increasing normal load through the maximum indentation depth of 660 nm (Figure 5.3). The absence of any force discontinuities is significant: the typical nanoscratch failure of hard materials, the onset of failure occurs by film delamination with large cracks or peel-off and a corresponding jump in the lateral force [18]. However, at around 50 s (black arrow in Figure 5.3b) the lateral force becomes noisy which is probably the point of delamination. The corresponding normal load is ~ 3 mN, which is therefore identified as the critical load for failure. We previously reported a critical load of 84 mN for HfB_2, which is a very hard material, using a conospherical diamond tip of 5 µm radius [19]. The diamond tip used in the present experiments has a radius of 1 µm, which makes the local pressure distribution higher than that in reference [19]. Converting the critical load into the corresponding approximate Hertzian contact pressure –by considering literature values of Poisson's ratio and elastic modulus for diamond, HfB_2 film [20, 21] and bulk MgO [22] – shows that the critical contact pressure for HfB_2 film is ~ 1.2 times of that for MgO film, which is an excellent result for the MgO film.

In addition to the good adhesion, the rate of increase in lateral force up to the point of delamination failure is quite low. This is interpreted as a low coefficient of friction, given by the ratio of lateral to normal force. For a normal load of 1.5 mN (around 45 s in Figure 5.3a), the coefficient of friction is ~ 0.1; this is comparable with as deposited HfB_2 films and slightly lower than that of a TiN film (a benchmark material) [20]. The nanoscratch results suggest that the MgO films are highly promising for applications that require a sliding contact, such as capacitive couplers that undergo mechanical assembly.

5.3.4 Conformality

We grew films without using any Ar carrier gas in order to quantitatively determine how conformality varies with the partial pressure of the $Mg(DMADB)_2$ precursor. We previously reported that a precursor-rich growth condition is ideal for conformal growth because the reaction probability of the precursor can be made very low [10, 23, 24]. We also modeled the step coverage in a high aspect ratio trench: we calculated the net rate of precursor adsorption and reaction on the growth surface, and embedded that solution into a diffusion-reaction calculation along the axis of the trench [25, 26].

The growth conditions and corresponding growth rates (7.5 – 25 nm/min) are listed in Table 2. Film D, in which the water partial pressure is higher than the precursor partial pressure (a water rich condition), affords a step coverage of only 70 % in a trench with a low aspect ratio of 2.5 (Figure 5.4a). By contrast, film E, grown with lower water partial pressure (a precursor rich condition), has a step coverage of 94 % and 85 % in trenches with aspect ratios of 2.5 and 3.5, respectively (Figure 5.4b). To obtain a near unity step coverage in higher aspect ratio trenches, the water to Mg partial pressure is further reduced in film F, which affords a step coverage of 98 % in a trench with aspect ratios of 9 (Figure 5.4c). The latter occurs at a relatively high film growth rate of 7.5 nm/min.

There is an additional factor, not recognized at the time these experiments were conducted, that can contribute to high conformality. We recently demonstrated that oxides in trenches can be made perfectly conformal or even superconformal by injecting the rate-limiting flux in a forward directed manner such that a significant fraction of it impinges at the bottom of the trench; this creates a virtual source which affords bottom-up filling [23]. In the present work, both precursor and water are injected through doser tubes pointing towards the substrate in order to maximize the delivered flux. The trench sample is offset by ~ 1 cm from the point where the axis of the delivery tubes meets the substrate holder, so the incident flux is not well aligned with the axis of the trenches. Nonetheless, the trenches shown in Figure 5.4 likely received a fraction of forward-directed flux that contributed to the nearly perfect conformality (Figure 5.4c). The contribution of the forward-directed flux becomes even more significant when the trench opening narrows, because it contributes a transport rate significantly above that predicted by Knudsen diffusion. With nearly parallel sidewalls it is not possible to avoid the formation of a low density seam along

the centerline [11, 23]; however, with slightly tapered trench sidewalls (the case in Figure 5.4c) the filling can be void-free.

5.3.5 Composition

XPS analyses for selected films are listed in Table 4; the O contribution from surface hydroxyl groups is subtracted to determine the O content in the bulk of the film [27]. Films A, B and C are grown at higher substrate temperatures (300-350 °C) than film D (270°C); the former have higher boron content (13-16 at. %) than film D (1 at. %). This is attributed to the decomposition of the DMADB ligand on the surface at the higher temperature; in addition, the higher total pressure used in films A, B and C increases the scattering of byproduct molecules (HDMADB) back onto the surface. The carbon content in film A is very low (< 1 at. %) and in film D is relatively low (3 at. %) compared to films B and C.

The MgO matrix appears to be essentially stoichiometric, as follows. The wide scan XPS spectra for film D, after 3 min of sputtering to remove surface carbon contamination, shows peaks of C 1s and B 1s; the N 1s in the noise level (Figure 5.5a, inset: N 1s high-resolution peak). The high-resolution O 1s peak at the film surface is deconvoluted into two peaks (Figure 5.5b): O 1s in MgO (530.5 eV) and O 1s in B_2O_3 plus -OH groups (532.2 eV); the latter cannot be distinguished because of the binding energy overlap. However, the high-resolution B 1s peak has a binding energy of 192.4 eV, which corresponds to the B_2O_3 chemical state (Figure 5.5c). B 1s peak is used to scale the O content in B_2O_3; after subtracting this O contribution, the O/Mg ratio (=1.02) in film D is stoichiometric within the error limits.

5.3.6 Optical properties

The refractive indices of films B, D, G and F are compared with those of bulk MgO [28] (Figure 5.6). Films B and G have lower refractive index than films D and F. This is attributed to a lower density in films B and G: using an effective medium approximation consisting of bulk MgO plus void [29], the best fit density is ~ 84 % of bulk in films B and G and ~ 90% of bulk in films D and F. The RBS measured density for film B is 82 % of bulk, in good agreement with the optical

fit. The 2.0 μm thick film (C) grown at a rate of 133 nm/min has an RBS density of 86 % of bulk; the refractive index for this film is expected to be in between the results obtained for films B and D.

5.3.7 Electrical properties

The growth conditions used for the MgO film in the MIM capacitor (Figure 5.1) are the same as those in film G (Figure 5.7); the film growth rate is 6 nm/min. The surface of film G is less smooth than films A, B or C (Figure 5.2), and the refractive index of film G is similar to film B (Figure 5.6). The C-V measurements for two MIM capacitor dots (labeled as 1 and 2), at a frequency of 1 MHz, afford relative dielectric constants of 9.5 and 9.0, and breakdown fields of 6.0 and 4.4 MV/cm, respectively (Figure 5.8). The lower values for dot 2 are attributed to the surface roughness of the MgO film, which introduces locally thinner regions. In addition, deposition of the top Au contact pad on the rough surface may create downward pointing Au tips of nanometer-scale radius, which increase the local electric field strength and reduce the measured dielectric constant and breakdown strength. Nonetheless, the values compare well with literature values for MgO films grown by ALD (Table 1).

5.4 Conclusion

Highly conformal MgO is deposited at a high growth rate (up to 300 nm/min) and a low substrate temperature (≤ 350 °C) using the Mg precursor, $Mg(DMADB)_2$, plus H_2O as the oxidant. The film stress is low enough, and the adhesion to the Si substrate is strong enough, to grow MgO film 2 μm thick at 350 °C. Conformal growth on microtrenches is demonstrated by controlling the precursor sticking probability: using a precursor-rich condition at 270 °C, a step coverage of 98 % is obtained in a trench of aspect ratio 9 at a growth rate of 7.5 nm/min. Films grown at a very high rate (> 90 nm/min) incorporate boron as B_2O_3, but those grown at a moderately high rate (7-25 nm/min) have a very low (~ 1 at. %) boron incorporation. The refractive indices are lower than bulk MgO due to a physical density ~ 85 % that of bulk. The dielectric constant and electrical breakdown strength agree well with literature values for MgO thin films. The results obtained in this work suggest that MgO can be deposited by CVD in applications that require rapid growth of conformal, thick films of high quality on complex substrate shapes.

5.5 References

1. Roessler, D.M. and W.C. Walker, *Electronic Spectrum and Ultraviolet Optical Properties of Crystalline MgO.* Physical Review, 1967. **159**(3): p. 733.

2. Subramanian, M.A., et al., *Dielectric-Constants of BeO, MgO, and CaO Using the 2-Terminal Method.* Physics and Chemistry of Minerals, 1989. **16**(8): p. 741-746.

3. Haynes, W.M., *CRC Handbook of Chemistry and Physics, 92nd Edition*. 2011: CRC Press.

4. *Private communication with CommScope*. 2014.

5. Seehase, H., *Plasma Display Panel Mgo Thin-Film Properties and Their Modification by Low-Energy Ion-Bombardment.* Displays, 1985. **6**(1): p. 21-34.

6. Park, C.H., et al., *Effects of MgO thin film thickness and deposition rate on the lifetime of ac plasma display panel.* Surface & Coatings Technology, 2005. **197**(2-3): p. 223-228.

7. Marcatili, E.A., *Dielectric Rectangular Waveguide and Directional Coupler for Integrated Optics.* Bell System Technical Journal, 1969. **48**(7): p. 2071.

8. Terauchi, M., et al., *High-performance MgO thin films for PDPs with a high-rate sputtering-deposition process.* Journal of the Society for Information Display, 2008. **16**(12): p. 1195-1201.

9. Wang, W.B., et al., *Highly conformal magnesium oxide thin films by low-temperature chemical vapor deposition from Mg(H3BNMe2BH3)(2) and water.* Applied Physics Letters, 2013. **102**(10).

10. Wang, W.B., et al., *Superconformal chemical vapor deposition of thin films in deep features.* Journal of Vacuum Science & Technology A, 2014. **32**(5).

11. Wang, W.B. and J.R. Abelson, *Filling high aspect ratio trenches by superconformal chemical vapor deposition: Predictive modeling and experiment.* Journal of Applied Physics, 2014. **116**(19).

12. Kim, D.Y. and G.S. Girolami, *Highly Volatile Magnesium Complexes with the Aminodiboranate Anion, a New Chelating Borohydride. Synthesis and Characterization of Mg(H3BNMe2BH3)(2) and Related Compounds.* Inorganic Chemistry, 2010. **49**(11): p. 4942-4948.

13. Jenkins, F.A. and H.E. White, *Fundamentals of Optics*. 3rd ed. 1957, New York: McGraw-Hill.

14. Koch, R., *The Intrinsic Stress of Polycrystalline and Epitaxial Thin Metal-Films.* Journal of Physics-Condensed Matter, 1994. **6**(45): p. 9519-9550.

15. Okada, Y. and Y. Tokumaru, *Precise Determination of Lattice-Parameter and Thermal-Expansion Coefficient of Silicon between 300-K and 1500-K.* Journal of Applied Physics, 1984. **56**(2): p. 314-320.

16. Engberg, C.J. and E.H. Zehms, *Thermal Expansion of Al2o3, Beo, Mgo, B4c, Sic, and Tic above 1000-Degrees-C.* Journal of the American Ceramic Society, 1959. **42**(6): p. 300-305.

17. Abermann, R., *Measurements of the Intrinsic Stress in Thin Metal-Films.* Vacuum, 1990. **41**(4-6): p. 1279-1282.

18. Ye, J., et al., *Nanoscratch evaluation of adhesion and cohesion in SiC/low-k/Si stacked layers.* Journal of Applied Physics, 2004. **95**(7): p. 3704-3710.

19. Lee, J., et al., *Shear strength measurements of hafnium diboride thin solid films.* Wear, 2014. **318**(1-2): p. 168-176.

20. Chatterjee, A., et al., *Nanoscratch and nanofriction behavior of hafnium diboride thin films.* Wear, 2008. **265**(5-6): p. 921-929.

21. Jayaraman, S., et al., *HfB2 and Hf-B-N hard coatings by chemical vapor deposition.* Surface & Coatings Technology, 2006. **200**(22-23): p. 6629-6633.

22. *Magnesium oxide (MgO): Young's, shear and bulk moduli, Poisson's ratio*, in *II-VI and I-VII Compounds; Semimagnetic Compounds*, M. O., R. U., and S. M., Editors. 1999, Springer: Berlin, Heidelberg. p. 1-3.

23. Talukdar, T.K., et al., *Superconformal Coating and Filling of Deep Trenches by Chemical Vapor Deposition with Forward-Directed Fluxes.* Manuscript in preparation, 2018.

24. Talukdar, T.K., G.S. Girolami, and J.R. Abelson, *Seamless Fill of Deep Trenches by Chemical Vapor Deposition: Use of a Molecular Growth Inhibitor to Eliminate Pinch-off.* Manuscript in preparation, 2018.

25. Yanguas-Gil, A., et al., *Highly conformal film growth by chemical vapor deposition. I. A conformal zone diagram based on kinetics.* Journal of Vacuum Science & Technology A, 2009. **27**(5): p. 1235-1243.

26. Yanguas-Gil, A., et al., *Highly conformal film growth by chemical vapor deposition. II. Conformality enhancement through growth inhibition.* Journal of Vacuum Science & Technology A, 2009. **27**(5): p. 1244-1248.

27. Newberg, J.T., et al., *Formation of hydroxyl and water layers on MgO films studied with ambient pressure XPS.* Surface Science, 2011. **605**(1-2): p. 89-94.

28. Stephens, R.E. and I.H. Malitson, *Index of Refraction of Magnesium Oxide.* Journal of Research of the National Bureau of Standards, 1952. **49**(4): p. 249-252.

29. *WVASE® Spectroscopic Ellipsometry Data Acquisition and Analysis Software*. 2012, J. A. Woollam Co., Inc.: Lincoln, NE 68508, USA.

30. Carta, G., et al., *CVD of MgO thin films from bis(methylcyclopentadienyl) magnesium.* Chemical Vapor Deposition, 2007. **13**(4): p. 185-189.

31. Kwak, B.S., et al., *Metalorganic Chemical Vapor-Deposition of [100] Textured Mgo Thin-Films.* Applied Physics Letters, 1989. **54**(25): p. 2542-2544.

32. Zeng, J.M., et al., *Preparation and characterization of epitaxial MgO thin film by atmospheric-pressure metalorganic chemical vapor deposition.* Journal of Crystal Growth, 1996. **169**(3): p. 474-479.

33. Wang, L., et al., *Synthesis and characterization of low-melting, highly volatile magnesium MOCVD precursors and their implementation in MgO thin film growth.* Chemistry of Materials, 2005. **17**(23): p. 5697-5704.

34. Babcock, J.R., et al., *Polydentate amines as CVD precursor ancillary ligands. Epitaxial MgO thin-film growth using a highly volatile, thermally and air-stable magnesium precursor.* Chemical Vapor Deposition, 2000. **6**(4): p. 180-183.

35. Sung, M.M., et al., *Chemical beam deposition of MgO films on Si substrates using methylmagnesium tert-butoxide.* Chemistry of Materials, 2002. **14**(2): p. 826-831.

36. de Rouffignac, P., et al. *Atomic Layer Deposition and Characterization of MgO from Magnesium Bis(Di-secbutylacetamidinate) and Water*. in *AVS Atomic Layer Deposition*. 2009. Monterey, CA, USA.

37. Vangelista, S., et al., *Low-temperature atomic layer deposition of MgO thin films on Si.* Journal of Physics D-Applied Physics, 2013. **46**(48).

5.6 Tables and Figures

Table 5.1. Mg-containing CVD (or ALD) precursors, MgO growth rate and solid-state properties.

Precursor	**$T_{substrate}$ (°C)**	**Growth rate (nm/min)**	**Step coverage (aspect ratio)**	**Refractive index**	**Dielectric constant**	**Breakdown field (MV/cm)**	**Reference**
$Mg(CH_3\text{-}C_5H_4)_2$	400–550	20–50	…	…	…	…	[30]
$Mg(tmhd)_2$	650–740	1.7–8.3	…	1.71	…	…	[31]
$Mg(acac)_2$	480–680	30	…	…	…	…	[32]
$Mg(hfa)_2(TMEDA)$	550-675	1.4-1.6	…	…	…	…	[33]
$Mg(dpm)_2TMEDA$	600	1.2	…	…	…	…	[34]
$Mg_4Me_4(O^tBu)_4$	400–800	1.1–1.7	…	…	…	…	[35]
$Mg(^{sec}ButAMD)$	225-275	0.08 nm/cycle (ALD)	…	1.74	9.8	5	[36]
$Mg(C_5H_5)$	80–350	0.12 nm/cycle (ALD)	…	…	10.8	1.7-5.5	[37]
$Mg(DMADB)_2$	225–800	1–20	90 % (15:1) at 225 °C	1.72 at 600 nm	…	…	[11]
$Mg(DMADB)_2$	270–350	6–200	98 % (9:1) at 270 °C	1.67 at 600 nm	9.5	6	this work

Table 5.2. Growth conditions for films deposited at a very high rate using a carrier gas (Ar) for $Mg(DMADB)_2$ precursor.

MgO Film	$T_{precursor}$ (°C)	$T_{substrate}$ (°C)	Q_{Ar} (sccm)	P_{Ar} (mTorr)	P_{H_2O} (mTorr)	t_{growth} (min)	Growth rate (nm/min)
A	40	300	4	70	70	10	90
B	40	300	8	205	70	2	200
C	40	350	12	340	70	15	133

Table 5.3. Growth conditions for films deposited at moderately high rate without carrier gas.

MgO Film	$T_{precursor}$ (°C)	$T_{substrate}$ (°C)	$P_{Mg(DMADB)_2}$ (mTorr)	P_{H_2O} (mTorr)	t_{growth} (min)	Growth rate (nm/min)
D	35	270	12.5	19.2	4	25
E	35	270	12.5	10	6	16
F	35	270	12.5	7.1	15	7.5
G	23	270	3	8.8	10	6

Table 5.4. XPS atomic concentrations (at. %) in selected films; the O contribution from surface hydroxyl groups is subtracted to determine the O content in the bulk of the film.

Film	Mg	O	C	B
A	33	53	0.7	13
B	29	53	4.0	14
C	28	50	5.7	16
D	46	49	3.4	1.4

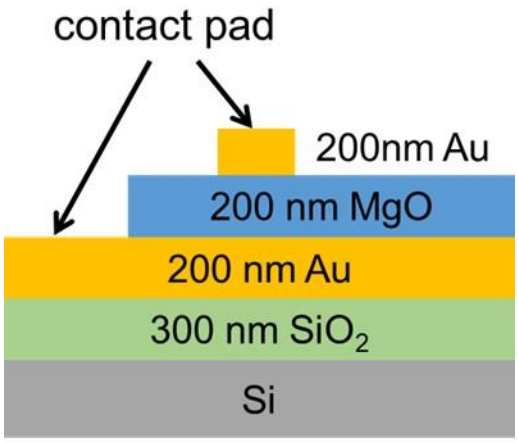

Figure 5.1. Schematic of MIM capacitor fabricated using MgO film and Au contact pads.

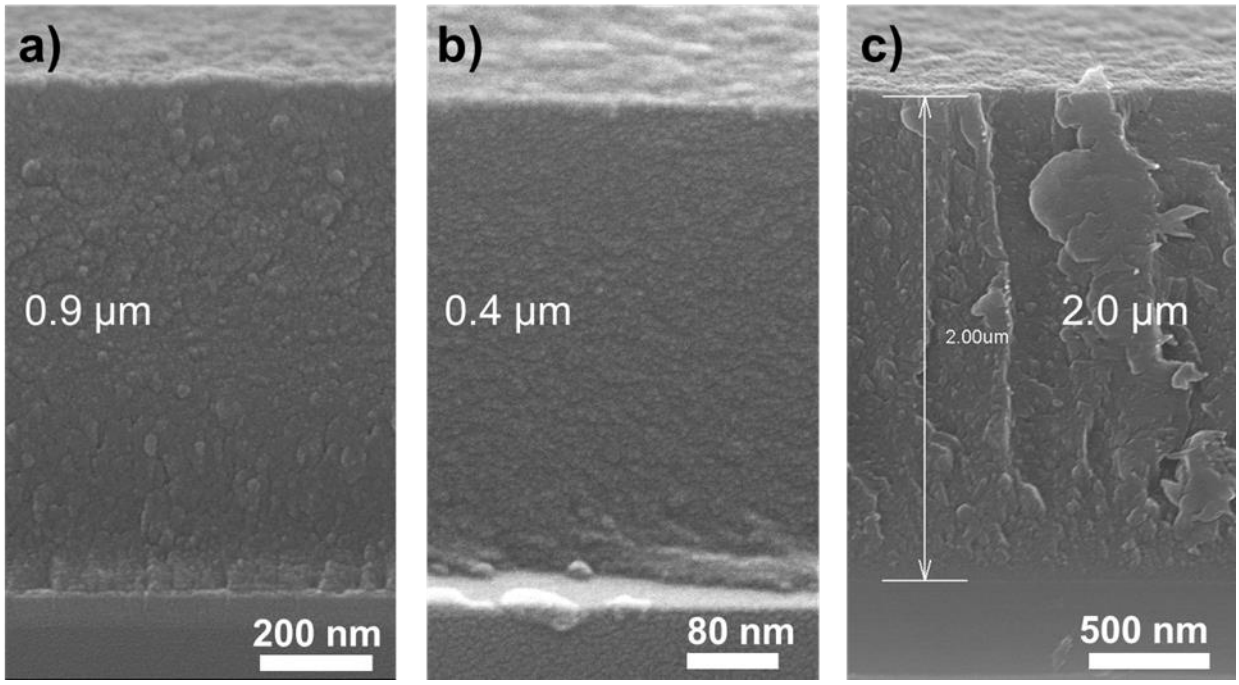

Figure 5.2. Cross-sectional SEM images of the films A (a), B (b), and C (c).

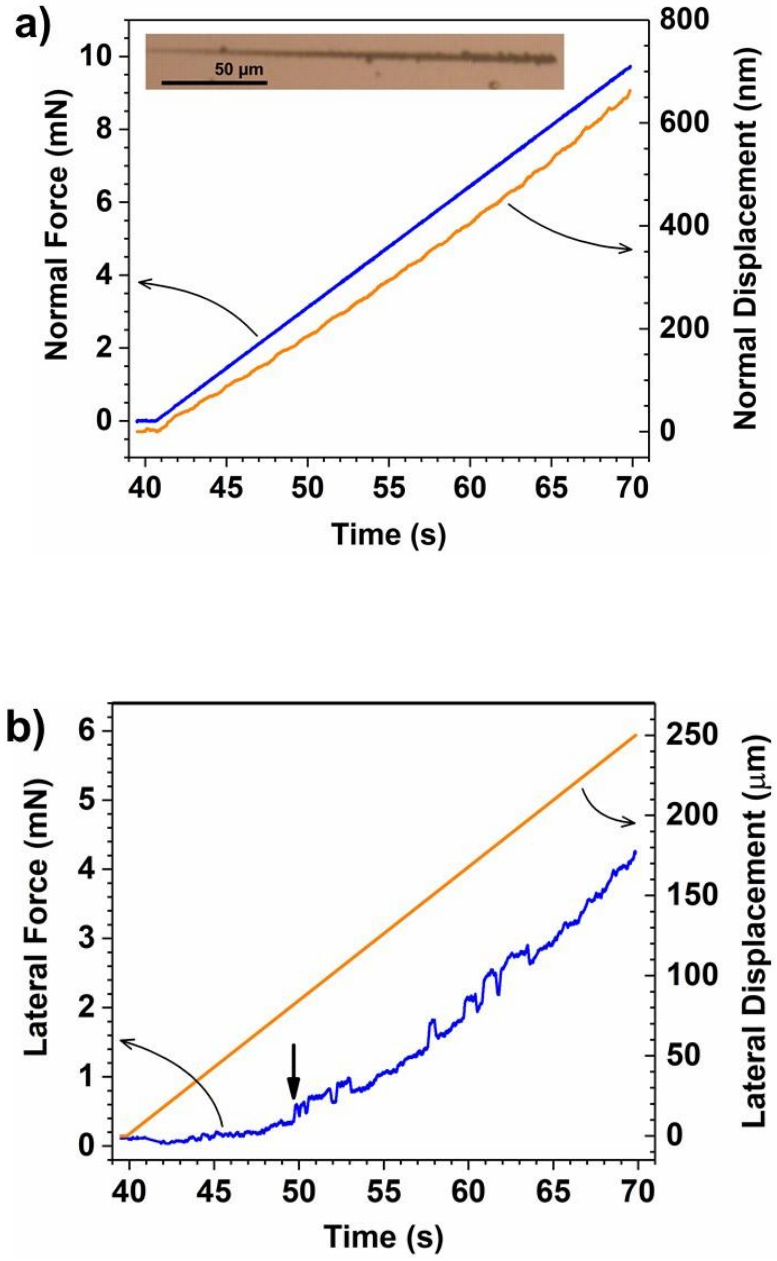

Figure 5.3. Nanoscratch test on film C. a) Normal force and normal displacement for a maximum load of 10 mN. Inset: optical microscope image of the scratch mark. b) Corresponding lateral force and lateral displacement.

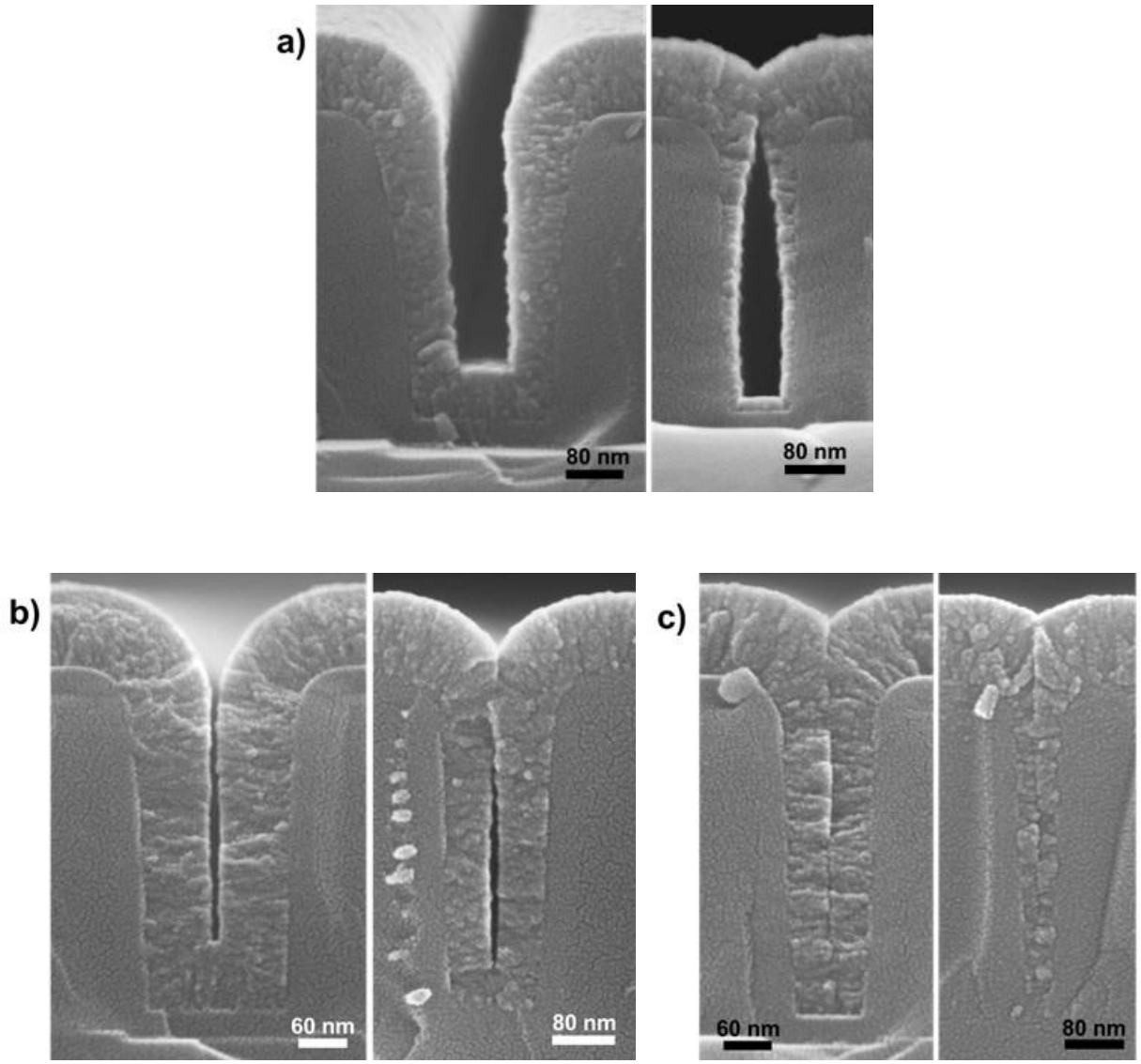

Figure 5.4. Cross-sectional SEM images of the coating profile inside trenches. a) Aspect ratio 2.5 (left) and 5 (right) using the growth conditions of film D. b) Aspect ratio 2.5 (left) and 3.5 (right) using the growth conditions of film E. c) Aspect ratio 4.5 (left) and 9 (right) using the growth conditions of film F.

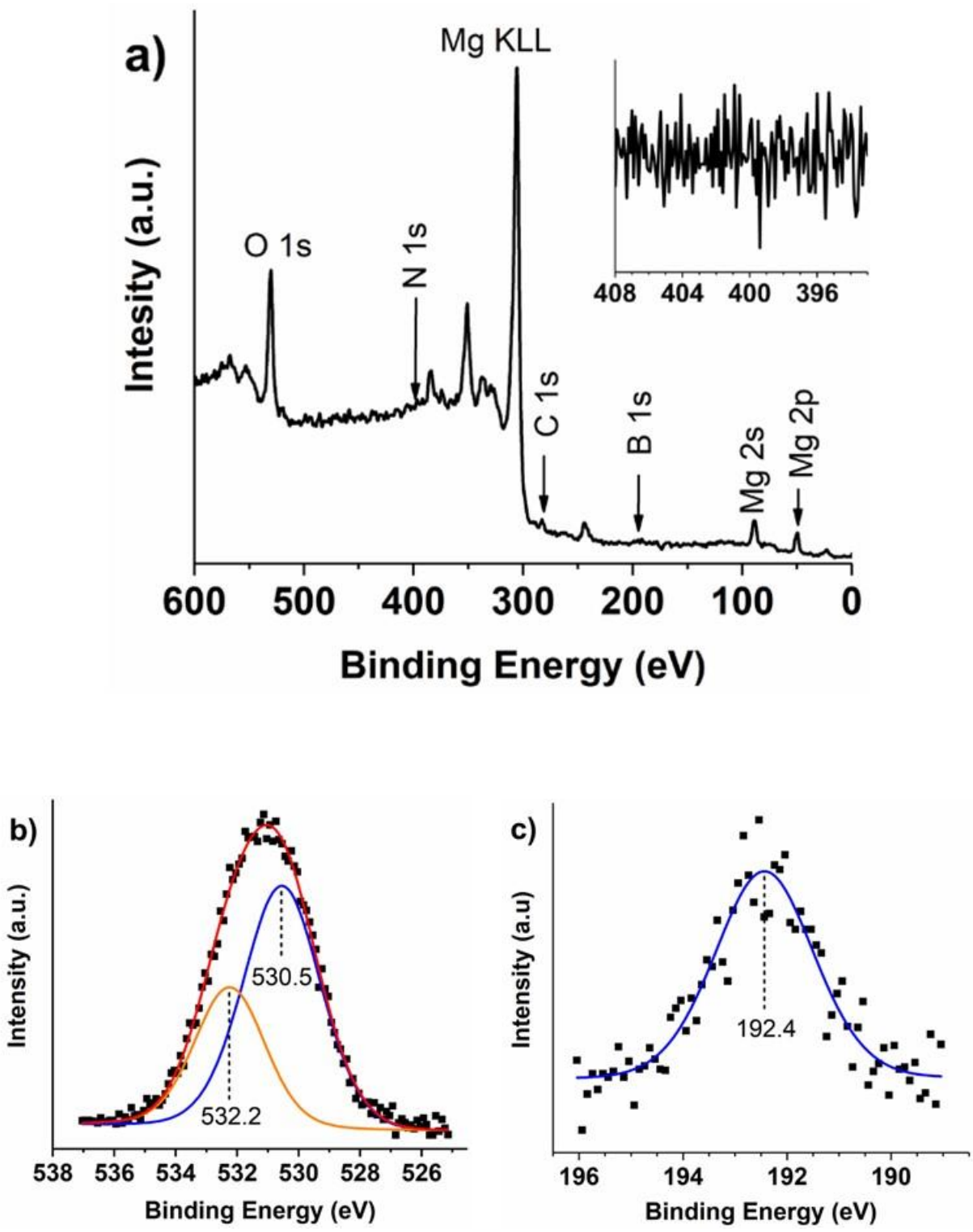

Figure 5.5. a) XPS wide scan spectra of the MgO film D, after argon sputtering for 6 min. Inset: N 1s high-resolution peak. b) O 1s high-resolution peak at the film surface. Black squares are experimental data and the solid lines are fitted data. c) B 1s high-resolution peak at the film surface.

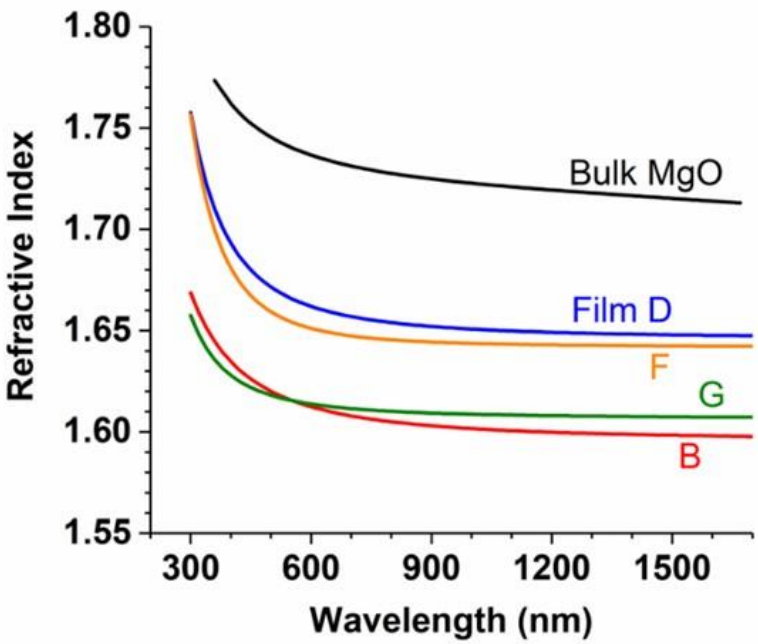

Figure 5.6. Refractive indices of films obtained using *ex situ* VASE.

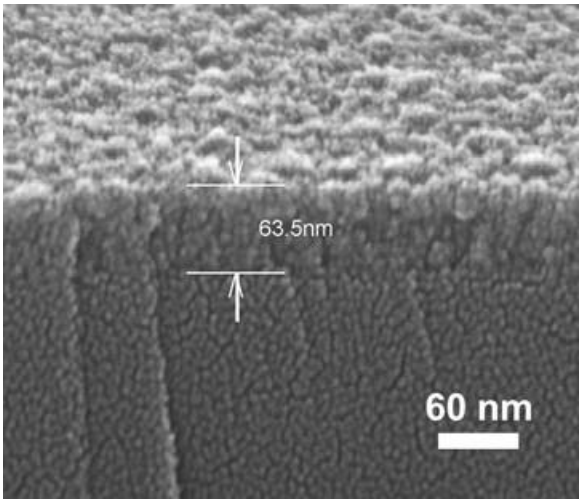

Figure 5.7. SEM image of film G (the same growth conditions used to make the MIM capacitor).

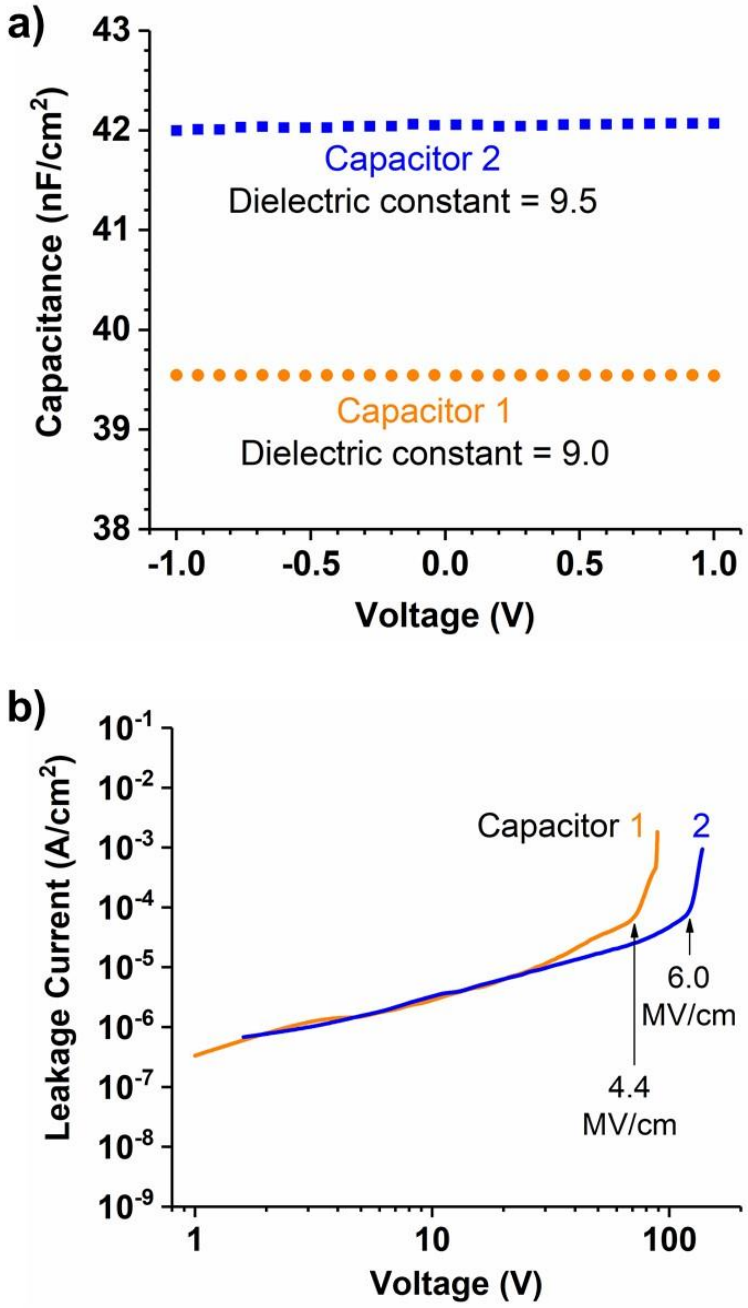

Figure 5.8. Electrical measurements of a 200 nm thick MgO film grown using the same conditions as film G (growth rate = 6 nm/min). a) Capacitance as a function of applied voltage at a frequency of 1 MHz. b) Leakage current as function of applied voltage

CHAPTER 6

CONFORMAL COATING OF CARBON NANOTUBE FORESTS BY LOW TEMPERATURE CVD

6.1 Introduction

Carbon nanotube (CNT) forests have a linearly-aligned structure with low-density, high porosity, and weak (van der Waals) links at internal crossing points [1, 2]. A three-dimensional composite (hybrid) material can be created by conformal (uniform) coating of a thin film onto the CNTs, i.e., the forest serves as a growth scaffold. The mechanical, thermal and electrical behaviors of the hybrid can be engineered with the appropriate choices of coating material, coating thickness and design (shape factor) of the scaffold. For mechanical applications in extreme environments, HfB_2 is an excellent candidate as a coating material: HfB_2 is a refractory metallic ceramic with a high melting temperature (3250 °C), high bulk hardness (29 GPa) and a metallic resistivity of 8-15 μΩ-cm [3, 4]. For applications that require a dielectric, conformal coating of CNTs with HfO_2 (high-K) is an attractive option; examples include: field effect transistors [5], and metal-insulator-metal capacitors for energy storage [6],

Gas phase coating methods, such as atomic layer deposition (ALD) or chemical vapor deposition (CVD), are uniquely applicable for coating CNT forests or other high aspect ratio structures because they can deliver deposition precursor (reactant) molecules to all internal surfaces. The reactant molecules must pass through the opening on the sample surface, be transported to the required depth, and react on surfaces to deposit film. In addition, the reaction byproducts must be transported out of the feature without decomposing, which otherwise would add its constituents (which are often heteroatoms) to the deposited material. Uniformly coating a CNT forest presents two major challenges: (i) the internal surface area is very large per surface area, and (ii) gas phase transport is reduced by internal scattering. Both of these issues are amplified as coating builds up on the CNT walls.

This situation can be partially mitigated using ALD, in which the alternation of two self-limiting surface reactions allows the theoretical step coverage (SC) to approach unity. However, for ALD within deep features, the time required to execute a dosing cycle (dose-pump-purge) is proportional to AR^2 [7], hence the growth rate is essentially proportional to AR^{-2}. In contrast, the film growth rate in CVD must be reduced in proportion to AR^{-1} [8]. To achieve a useful growth rate in ALD the dosing times must be limited, which affords a SC slightly below unity [9], similar to the present results for CVD. The significant difference between these two techniques occurs for high AR: when the AR is ~ 100 the techniques can afford similar growth rates. However, for higher AR – which is the case within the CNT forest in the present work – CVD is the faster of the two and does not involve any gas cycling. In practice, the choice of a growth method also hinges on the availability of an excellent precursor. In our earlier work, we obtained highly conformal HfB_2 growth from a single-source CVD precursor, $Hf(BH_4)_4$ [10, 11], which has a (huge) high vapor pressure of ~ 15 Torr at room temperature [12], which makes it highly suitable for the coating of mesoscale foams by CVD. By contrast, there are no ALD precursors for HfB_2 and few ALD precursors for the transition metals [13].

We recently demonstrated that low-pressure CVD processes can afford ALD-like conformality with useful growth rates [10, 11, 14-16]. CVD of a thin film in a high AR structure, such as a trench or via, is well described by the diffusion-reaction equation (Fick's second law) in steady state, where the film growth rate defines the consumption rate of precursor on the surfaces [11]. The challenge is that, due to wall consumption, the partial pressure (flux) of the precursor falls continuously with depth away from the opening. If the growth rate is monotonically dependent on the pressure, then the coating thickness must decline with depth. The only means to obtain perfectly conformal (uniform thickness) growth is to operate under conditions such that the growth rate is essentially saturated (pressure independent) all the way down to the lowest pressure, which occurs at the bottom of the trench. Saturation is observed experimentally when the precursor can be delivered at a high enough pressure, and growth conducted at a low enough temperature, for site blocking effects on the film surface to dominate the growth kinetics [8]. In our previous research, we have utilized these conditions to obtain remarkably uniform coatings in high AR features, and we have developed a first-order theory to predict the possible regimes of conformal CVD in the form of a conformal zone diagram [8]. In a recent development, former group member Dr. Yanguas-Gil has extended the conformal theory to porous (or fibrous) and high surface area

materials, which accounts for the reduced Knudsen diffusion coefficient and enhanced internal surface area [17].

There are several challenges when applying the CVD method to this problem. First, to optimize the growth conditions, the effective diffusion coefficient in the convoluted structure must be estimated to within a factor of ~ 2 (discussed further below). Furthermore, the diffusivity declines with increasing coating thickness because the open space in the structure is progressively reduced. Second, the precursor chosen must exhibit a strong saturation effect in its growth rate vs. pressure, but also react to afford film at a suitable rate. Third, the apparatus must be capable of establishing enough vapor pressure above the sample surface to attain rate saturation. The typical embodiment of CVD uses a dynamically pumped vacuum system, which limits the maximum attainable precursor pressure to a value that is orders of magnitude below its vapor pressure. This greatly reduces the conformality of the film or the AR that can be covered [8]. In addition, due to the very low sticking coefficient of the precursor, only a tiny fraction of molecules reacts to form film; with dynamic pumping, the vast majority of the (expensive) precursor molecules is pumped away and wasted.

In this work, we implement static (unpumped) chemical vapor deposition (SCVD) to achieve maximum precursor pressure, and thus, extremely conformal coating in CNT forests with height of ≤ 1.7 mm. A simple tube reactor is evacuated, filled with the precursor molecule up to its full vapor pressure, then slow ramped to a desired temperature for film growth. In our earlier work, we had obtained highly conformal HfB_2 growth at a precursor pressure of 10 mTorr in a pumped system [11]; in SCVD, we use a pressure that is *three orders of magnitude* larger. Due to the absence of pumping the precursor utilization efficiency is high, 0.25 - 0.85 [18]; and SCVD can be implemented as a batch process to simultaneously coat a large area of substrates. SCVD has been employed previously in the photonics literature for growth of semiconductor materials [19-25], and for Cu metallization in ICs [26]. We previously demonstrated HfB_2 infilling in a colloidal crystal by SCVD [18].

However, an important requirement for SCVD is that the reaction byproducts, which build up in the tube as the precursor is consumed, must not decompose on the film surface, because that would introduce the elements contained in the byproducts and/or change the film stoichiometry. The need for byproduct removal is one of the motivations for the use of dynamic pumping in

conventional CVD, which emphasizes higher growth temperature to maximize growth rate and fast gas flow to minimize boundary layer effects and byproduct concentrations. For the present HfB_2 film growth experiments from $Hf(BH_4)_4$, the temperature is kept low ($\leq 200°C$); we have found no evidence for significant byproduct decomposition during film growth. SCVD grown HfB_2 films are essentially stoichiometric and do not exhibit O or C within the Auger detection limit of ~ 1 at. % [18].

We apply the conformal theory to map out the minimum required precursor pressure to coat a CNT forest to a desired SC as a function of the film thickness, forest height and area density of CNTs (which stand normal to the substrate). For that purpose, we calculate the Knudsen diffusion coefficient in a CNT forest using two different approaches: (i) by solving the diffusion-transport reaction for a forest with a measured MgO coating thickness that tapers to zero at a certain depth (a boundary condition of zero precursor flux); and (ii) by adopting the average inter-CNT spacing in a forest as the average scattering length in the Knudsen diffusivity for the precursor molecules. In the approach (i), MgO film growth is carried out in a pumped CVD system from $Mg(DMADB)_2$ precursor and water co-reactant [14].

We also investigate a special case of two-reactant CVD, in which the kinetics do not afford growth saturation for one of the reactants; for example, HfO_2 film growth from TDMA-Hf precursor and H_2O co-reactant, in which the film growth rate saturates vs. precursor pressure but is linearly proportional to water pressure within the optimized kinetic regime [27, 28]. In this case, we overcome the diffusion limitation of reactant transport by delivering the reactants in a forward-directed way into the CNT forest, thereby achieving a conformal HfO_2 coating in the forest.

6.2 Experimental

6.2.1 HfB_2 film growth in static CVD

Conformal HfB_2 coating of CNT forests is performed in a hot wall SCVD system (Figure 6.1). The reactor is constructed from a Pyrex tube (23 mm i.d.) with one end sealed; the tube is enclosed by a single zone box furnace. The other end is adapted to a stainless-steel fitting and connected to a turbo pump with the option of either flowing or static conditions. The base

pressure in this setup is ~ 10^{-7} Torr, which is essential for eliminating unwanted impurities in the film. Hafnium borohydride, $Hf(BH_4)_4$, is synthesized by Girolami *et al.* [12] and used as a single-source precursor for HfB_2 film growth.

The experimental protocol for the SCVD is chosen based on the conformal theory (below) such that the precursor pressure is maximized, and the reaction rate is reduced via the use of a low substrate temperature. The usual procedure steps include loading a batch of samples in the glass tube and baking them at 350 °C under vacuum to remove moisture. The tube and samples are cooled down to room temperature (RT), and the gate valve near the open end of glass tube (Figure 6.1) is closed to switch the system to static (unpumped) mode. The tube is then dosed with the desired precursor pressure (2 to 12.5 mTorr in the present experiments), which is monitored by a high-accuracy capacitance manometer. The tube and samples are heated at a slow ramp rate, 1 °C/min, up to 200 °C. The temperature is kept constant at 200 °C for 2 hours to ensure that all precursor is reacted-out; the extent of reaction is indicated by in situ measurements of total pressure rise in the reactor. Afterward, the system is cooled down to RT and the samples are unloaded.

At high pressure $Hf(BH_4)_4$ precursor slowly starts to nucleate around 100°C (with a long nucleation delay of several minutes); meaning that a small fraction of final film thickness is deposited before the substrate temperature reaches to 200 °C.

Since in SCVD the precursor is not supplied continuously, its partial pressure inside the reactor depletes as the reaction progresses and eventually must below the minimum required for conformal growth. This low-pressure condition means that the final stages of coating have a lower step coverage, which is averaged into the measured overall step coverage. Thus, if the growth were stopped earlier, the measured step coverage would be slightly better than in the present experiments, where we do not attempt to stop the growth process before the precursor is exhausted.

The uncoated (pristine) CNT forest substrates are synthesized by Tawfick *et al.* [29]. The blanket of forests has a base area of ~ 1.5 × 1.5 cm; the forest thickness (height) ranges from 14 μm to 1.7 mm; and the average forest area density is ~ 1×10^{14} tubes/m^2. The outer and inner diameter of the uncoated CNTs are about 5 and 4 nm, respectively, with a wall thickness of about 1 nm; this means that the CNTs are multi-walled tubes.

6.2.2 MgO film growth in pumped CVD

For the deposition of MgO thin films from $Mg(DMADB)_2$ and deionized water, a cold-wall pumped CVD system is used; the details are described elsewhere [14]. A substrate temperature of 220 °C is used. $Mg(DMADB)_2$ precursor is synthesized by Girolami *at el.* [30] and kept at RT in a Pyrex container which is adapted to a stainless-steel fitting. The valve to the turbo pump is throttled to achieve a Mg precursor pressure of 2 mTorr; no carrier gas is used. Water is kept at RT and a partial pressure of 3 mTorr is supplied using a needle valve to regulate flow. Precursor and water are supplied through separate stainless-steel tubes (4 mm i.d.) that point to the inside wall of the reactor (away from the substrate), creating a uniform (isotropic) flux distribution above the substrate.

6.2.3 HfO_2 film growth in pumped CVD

For HfO_2 film growth, the same cold-wall pumped CVD system is used; the substrate is maintained at a temperature of 200 °C. TDMA-Hf precursor is obtained from Sigma-Aldrich and kept at 40 °C in a Pyrex container adapted to a stainless-steel fitting; the precursor delivery tube outside the reactor is heated to 80 °C to prevent condensing on the inside walls of the tube. The valve to the turbo pump is not throttled in this case; a 0.18 mTorr of TDMA-Hf and 0.023 mTorr of deionized water is used. Precursor and water are supplied through separate stainless-steel tubes (4 mm i.d.) that point towards the substrate and terminate at 7 cm away from the substrate surface, creating very forward-directed ballistic fluxes toward the sample [27].

6.2.4 Film characterization

Film microstructure and thickness are determined using scanning electron microscopy (SEM). For SEM, the substrates are cleaved (which also cleaves the forest) and cross-sectional images of the forest are taken from a position near to the center of the substrate. The coating (film) thickness is calculated by subtracting the radius of uncoated tubes from the average radius of coated tubes at that depth in the forest (measured from the top downwards). The *net* step coverage in the CNT forests is calculated as the ratio of the *final* film thickness at the bottom of the forest to that at the top.

Rutherford backscattering spectrometry (RBS) is used to measure the areal density of Hf or Mg atoms in corresponding films; this value is divided by the film thickness as measured by SEM to give the density of the Hf or Mg sublattice, respectively. For the growth conditions described above, the densities of the HfB_2 and MgO films are ~ 70 % of that of corresponding bulk material; and the density of the HfO_2 film is ~ 86 % of that of bulk HfO_2. Note that RBS measurements were done on companion films grown on planar Si substrates.

6.3 Theory of Conformal Coating

For CVD thin films from a single-source precursor, the functional dependence of the film growth rate (*GR*) on the precursor pressure (*P*) and the growth temperature (*T*) can be modeled using first order Langmuir kinetics as [8]:

$$GR(p,T) = \frac{K_1(T)P}{1+K_2(T)P} \tag{6.1}$$

where K_1 and K_2 are lumped rate coefficient that account for precursor adsorption, desorption and reaction at the growth surface. At low precursor pressure $K_2(T)P \ll 1$, and Equation 6.1 becomes $GR(P,T) \approx K_1 P$. In contrast, at high pressure $K_2(T)P \gg 1$, which results in a growth saturation with $GR_{sat}(T) \approx K_1/K_2$. Note that at high pressure the film growth rate becomes essentially independent of P, which is a critical condition for conformal coating in a high aspect ratio structure.

Using the above kinetic behavior, we previously developed an analytical model for the kinetic conditions that afford extremely conformal coating, i.e., where the surface reaction rate is nearly constant [8]. For a deep trench or via of given aspect ratio (AR), the required precursor pressure (P) is related to the film growth rate (GR) and the desired step coverage (SC) of the coating as:

$$P \geq \frac{GR.AR}{\sqrt{1-SC}} \sqrt{\frac{c\rho k_B T}{2D_0 K_1(T)}} \tag{6.2}$$

where D_0 is the pre-factor in the Knudsen diffusion coefficient (the feature width is accounted for

by the AR); ρ is the atomic density of the film; and c = 2, 4 for a trench or via, respectively. This result shows that (i) a high degree of step coverage (e.g., $SC = 0.9$) can be maintained in a high AR structure if the precursor pressure is high; and (ii) for a given SC and AR, the growth rate can be increased (via the substrate temperature) in proportion to the available precursor pressure. Note that GR has a unit of thickness per unit time in Equation 6.2.

The extension of the above theory to porous and high surface area materials is recently reported in the reference [17]. The pressure drop (ΔP) in a porous material is given by:

$$\Delta P = \frac{GR.\bar{S}L^2 k_B T}{D}\left(\frac{1}{2} + \frac{1}{S_e}\right) \tag{6.3}$$

where $\bar{S}$ is the surface area per unit volume; L is the thickness (depth); and S_e is the surface area enhancement defined as: $S_e = \bar{S}L$. For a porous material with a very high surface area and a large thickness, the term $1/S_e$ becomes negligible. In Equation 6.3, *GR* has the unit of atoms per unit area per unit time. The effective Knudsen diffusion coefficient (D) is defined as:

$$D = \frac{1}{3}\sqrt{\frac{8k_B T}{\pi m}}\,\bar{d}\,\frac{\varepsilon}{\tau} \tag{6.4}$$

where $\bar{d}$ is the average pore size; ε is the porosity of the material; and τ is the tortuosity factor for the Knudsen flow.

Equation 6.3 is then used to a develop an analytical expression, analogous to Equation 6.2, for the required precursor pressure (P) as a function of the step coverage (SC) and the rate coefficients (K_1 and K_2); the expression is given by [17]:

$$P^2 \geq \frac{1}{1-\mathrm{SC}}\frac{K_1(T)}{\left(K_2(T)\right)^2}\frac{\bar{S}L^2 k_B T}{D}\left(\frac{1}{2} + \frac{1}{S_e}\right) \tag{6.5}$$

with the same assumption that the pressure is high enough such that $K_2(T)P \gg 1$.

The lumped rate coefficients, $K_1(T)$ and $K_2(T)$, are ratios of microscopic surface reaction rate coefficients. However, to determine $K_1(T)$ and $K_2(T)$ at a given temperature, it is sufficient

to measure the macroscopic film growth rate on a planar substrate as a function of pressure, then fit the measured dependence to Equation 6.1.

6.4 Diffusion Coefficient in CNT Forest

While the Knudsen diffusion coefficient in a deep trench or via is determined by the characteristic trench width or via diameter, it is a great challenge to accurately estimate the diffusion coefficient in a CNT forest, largely due to the microscopic randomness in the alignment of the tubes. Below we consider two different approaches to estimate the diffusion coefficient in a CNT forest, one of which by design is a conservative underestimate. We then argue that a suitable working value is in-between the two estimates, and we use that value in precursor diffusion-reaction calculations within the forests.

6.4.1 Using MgO coating in a CNT forest

The diffusivity can be extracted directly from measurement of a film thickness profile and use of the continuity equation when the boundary conditions can be specified, as detailed below. We coated a CNT forest of height 17 μm using a water rich growth condition, 2 mTorr $Mg(DMADB)_2$ precursor and 3 mTorr H_2O co-reactant at 220 °C, such that the film growth rate is approximately proportional to the $Mg(DMADB)_2$ flux (local pressure) which decreases with the depth in forest (Figure 6.2a). From our previous work on MgO coating in deep trenches at 220 °C, the partial pressure of the $Mg(DMADB)_2$ precursor drops about 4.5 times more rapidly with depth than the water partial pressure [31]; this assures that water rich growth conditions are maintained at all depths in the forest and we need not consider the water pressure in the calculation. At a forest depth where the MgO film thickness reaches zero, we assume that the Mg precursor flux (pressure) is zero, establishing one of the necessary boundary conditions. Film thickness at three different forest depths are measured from the SEM images: 45 nm near the top of the forest (Figure 6.2b); 12 nm at a depth of 10 μm (Figure 6.2c); and zero at a depth of ~ 13.6 μm (Figure 6.2d).

To calculate the precursor pressure (flux) distributions in the forest, we solve the one-dimensional (1D) continuity equation in steady state [11], incorporating the above experimental thickness profile. This steady state differential equation is given by:

$$\frac{D}{k_B T}\frac{d^2 P}{dz^2} = \frac{\bar{S} t_0}{\tau}\left(1 - \frac{z}{L_c}\right) \tag{6.6}$$

where τ is the time duration of growth; t_0 is the film thickness at the opening ($z = 0$); and L_c is the depth at which the film thickness becomes zero. Here, we model the precursor transport only in the z-direction (along depth) of the forest, which is acceptable for the center of a forest with centimeter-scale in-plane dimensions (far away from edge effects).

Equation 6.6 is integrated twice, within an interval of z to L_c, to obtain an analytical solution for the precursor pressure (P) as a function of the forest depth (z), which is given by:

$$P(z) = \frac{\bar{S}\rho t_0 k_B T}{\tau D}\left(\frac{L_c^2}{6} - \frac{L_c}{2}z + \frac{1}{2}z^2 - \frac{1}{6L_c}z^3\right) \tag{6.7}$$

The surface area per unit volume ($\bar{S}$) in a CNT forest is calculated using the relationship:

$$\bar{S} = 2\pi\left(r_o + t_{avg}\right)N_{CNT} \tag{6.8}$$

where r_0 is the outer radius of a CNT; t_{avg} is the average film thickness in the forest; and N_{CNT} is the forest area density expressed as the number of tubes per unit area.

Using Equations 6.6 and 6.7, along with the known $Mg(DMADB)_2$ pressure (2 mTorr) at $z = 0$, the calculated effective diffusion coefficient (D) in the forest of Figure 6.2a is ~ 2.9×10^{-5} m^2/s.

6.4.2 Using an average in-plane spacing between the CNTs

Equation 6.4 can be used to calculate D in a porous material if the average scattering length ($\bar{d}$), the porosity (ε) and the tortuosity factor (τ) are known. For a CNT forest, a conservative approach to estimate $\bar{d}$ is to take the reciprocal of $\sqrt{N_{CNT}}$ that approximates an array of CNTs as a square box with inner edge length of $\bar{d}$ [32]. In case of coating a forest, this characteristic length decreases with film growth, giving an expression:

$$\bar{d} = \frac{1}{\sqrt{N_{\mathrm{CNT}}}} - 2\left(r_{\mathrm{o}} + 2t_{avg}\right) \tag{6.9}$$

Similarly, the porosity (ε) of the forest depends on the coating thickness and is given by:

$$\varepsilon = 1 - \pi \left(r_0 + t_{avg} \right)^2 N_{CNT} \tag{6.10}$$

Considering that the CNT forests have a statistical vertical alignment and that the precursor or co-reactant diffuses only in the z-direction, the tortuosity factor (τ) is assumed to be unity in the present calculations.

Using Equations 6.4 and 6.8–6.10, the effective diffusion coefficient (D) in the CNT forest of Figure 6.2a is calculated to be ~ 3.7×10^{-6} m^2 / s. This value is less than that obtained from the MgO thickness profile in the forest (Figure 6.2) by a factor of 8; we attribute this difference to the very conservative approximation of in-plane $\bar{d}$ in the CNT forest. In reality, there is a certain probability that a molecule can travel a much longer distance before colliding with a CNT, which is not accounted for in that estimation of $\bar{d}$. Nonetheless, approach (ii) is more suitable to calculate the diffusion coefficient in a large number of CNT forests with variable film thickness and forest area density, because it is not practical to repeat the experiment in Figure 6.2 for many CNT forests. In the rest of this work, we use approach (ii) to calculate the diffusion coefficient in the CNT forests, but we *multiply the value by a factor of 2* to modestly correct the overly conservative diffusion coefficient values. Note that an underestimate of the diffusion coefficient also underestimates the ability to obtain conformal coverage in a deep structure; the experimental results should therefore be more conformal than suggested by the model.

6.5 Conformal HfB_2 Coating

6.5.1 Experimental results

SCVD is used to conformally coat CNT forests with different heights using a starting pressure in the range (2.0 – 12.5 Torr) for the $Hf(BH_4)_4$ precursor and a nominal substrate temperature of 200 °C (Table 1). For sample A, a 12.5 Torr of precursor pressure is used in a CNT forest with height of 0.4 mm (Figure 6.3a). The coating thickness decreases from 11 nm at the top of forest (Figure 6.3b) to 9 nm at the bottom of forest (Figure 6.3c), giving a step coverage of ~ 82 %. Note that the available precursor partial pressure in the SCVD reactor decreases dynamically

(consumed as film); therefore, there is a sharp decrease in the step coverage near the end stage of film growth, when the precursor pressure in the reactor approaches zero. Consequently, the net step coverage of the coating becomes lower than the maximum achievable; this can be avoided by stopping the growth process before the complete depletion of precursor in the reactor.

A remarkable observation in Figures 6.3b and 3c is that the HfB_2 coating creates "welded" joints at locations where the neighboring CNTs touch each other (some of which are marked with white arrows in Figures 6.3b and 6.3c; such joints greatly modify the mechanical behavior of the foam structure. In an uncoated forest, the CNTs are in contact with each other by a weak van der Waals force, and so they slip under load. In contrast, the HfB_2 coating converts these weak contact points into strong joints, increasing the maximum load that the forest can withstand before failure [33]. In addition to creating strong joints in the CNT forest, the HfB_2 coating also greatly improves the adhesion of CNTs to the underlying Si substrate (the interface between the HfB_2 film and Si substrate is marked with a white dashed line in Figure 6.3c.

With a lower precursor pressure of 4 Torr and a similar forest, the same net step coverage is obtained in sample B (Table 1); this is due to the fact that the minimum precursor pressure for growth saturation (described below) is much lower than the pressures used for sample A or B. When a lower forest height of 80 μm is used for sample C, the net step coverage improves significantly to 92 %. To further test the conformality in a forest with much higher height of 1.7 mm (sample D), the precursor transport is enhanced by patterned cylindrical holes with diameter of 3 μm, which span the full height of the forest and are uniformly spaced at 20 μm. A step coverage of 63 % is obtained in this sample, which we consider to be very impressive, given the large forest height of 1.7 mm. The reason for the good conformality in such a tall forest is the rapid transport of precursor down the holes, then the lateral diffusion of precursor into the structure. The lateral diffusion distance in this structure (= 10 μm) is very short compared with the forest height.

The conformal theory in a trench (or via), described in Equation 6.2, predicts that a rectangular trench (parallel sidewalls) with aspect ratio of ≤ 200 can be conformally coated to a *step coverage of 99.9 %* (the theoretical limit is < 1 in Equation 6.2), for a precursor pressure of 2 Torr and a substrate temperature of 200 °C. To experimentally proof the high degree of HfB_2 film conformality in SCVD, a lithographically defined SiN_x walled microtrench with aspect ratio

of 5 is completely filled with HfB_2 by SCVD, using the above the growth conditions (Figure 6.4). Note that the trench width decreases dynamically as the film thickness on the sidewalls increases, thereby increasing the effective aspect ratio up to a very large number near the end of fill. A slight outward tapering at the trench opening (as observed in Figure 6.4), however, helps to avoid a pinch-off at that stage of fill.

6.5.2 Modeling results

To employ the conformal theory described in Equation 6.5, we first calculate the rate coefficients, K_1 and K_2 at temperatures of 200 and 250°C, for which data are available. Equation 6.1 is then used to calculate the film growth rate at any pressure up to the full vapor pressure of the precursor. For HfB_2 films grown from $Hf(BH_4)_4$ precursor, the growth rate essentially saturates at ~ 25 mTorr with a rate of 2.7 nm/min when the substrate temperature is 200 °C (Figure 6.5). In contrast, for a substrate temperature of 250 °C, the growth saturation occurs at ~ 100 mTorr with a rate of 22 nm/min. At a lower temperature the precursor reactivity is reduced, resulting in a lower film growth rate and a lower minimum pressure for growth saturation. The available precursor vapor pressure of 15 Torr is far higher than the minimum saturation pressure, even for a substrate temperature of 250 °C; therefore, higher temperature can be used to conformally coat porous material at a relatively fast rate by SCVD.

To estimate the pressure drop as a function of the forest depth, Equation 6.3 is used for a forest with area density of 1×10^{14} tubes/m^2 at 200 °C and film thicknesses of 5, 10, and 20 nm (Figure 6.6); the film growth is considered to be in saturation with a rate of 2.7 nm/min (Figure 6.5). The analytical solution for pressure drop, described by Equation 6.3, assumes constant growth rate throughout the depth of the forest (i.e., step coverage = 1). For a HfB_2 film thickness of 5 nm, a forest depth of ≤ 1 mm can be conformally coated (step coverage ≈ 1) using the full vapor pressure of the Hf precursor. Note that the minimum saturation pressure at 200 °C is ~ 15 mTorr (Figure 6.5); in the calculation of Figure 6.6, we let the pressure to drop up to 0.5 Torr. As expected, the maximum forest depth for conformal coating decreases with increasing film thickness; this is due to a combined effect of increased surface area and decreased scattering length ($\bar{d}$) for a higher film thickness. Figure 6.6 shows that forest depths of ≤ 0.75 mm and

0.45 mm can be conformally coated (underlying assumption of unity step coverage) for a film thickness of 10 nm and 20 nm, respectively.

For the CNT forest used in Figure 6.3, we employ Equation 6.5 to calculate the minimum required Hf precursor pressure, using step coverages of 80, 90 and 95 %, as a function of film thickness (Figure 6.7). For a given forest density, the maximum film thickness is limited by the average inter-CNT spacing ($\bar{d}$), as described in Equation 6.9. For the forest considered in Figure 6.7, the maximum film thickness is ~ 45 nm. When the film thickness approaches this maximum value, the diffusion in the forest becomes extremely difficult due to a very narrow spacing between the tubes. Consequently, the required precursor pressure rises very sharply. These results suggest that, to achieve a high degree of conformality in a CNT forest, the maximum film thickness must be limited to a value (for example, ~ 40 nm in Figure 6.7) somewhat less than half of the inter-CNT spacing. Of course, in a real CNT forest the packing of the tubes is somewhat irregular, so a small growth rate will persist in open channels beyond the value calculated here.

The dependence of the minimum required precursor pressure on the film thickness and forest density is calculated for the forest in Figure 6.3, at a step coverage of 90 % and a substrate temperature of 200 °C (Figure 6.8a) or 250 °C (Figure 6.8b). For given values of film thickness and forest density, the required pressure increases with temperature; this is due to the increased precursor reactivity at a higher temperature, leading to a faster precursor consumption rate in the forest. Figure 6.8 offers guidelines for choosing (trading off) the CNT forest density and HfB_2 coating thickness within the allowed pressure limit; the choices are related to the desired properties in an application (described more in Chapter 7). Since the precursor partial pressure in the SCVD reactor decreases with film growth, to maintain the desired step coverage, the growth process must be stopped when the local partial pressure at the bottom of forest is still above (or around) the saturation threshold. In that regard, the results in Figure 6.8 provide quantitative information about when to stop the growth process. Note that the precursor partial pressure can be determined from the total pressure in the SCVD reactor by accounting for the reaction stoichiometry: one B_2H_6 plus five H_2 molecules are generated per one precursor molecule consumed.

6.6 Conformal HfO_2 Coating with Low Pressures

Because of a high surface area and a low diffusion in CNT forests, a low partial pressure of the reactant molecules is unfavorable to achieve the necessary local surface saturation for conformal coating. Conformal coating becomes essentially impossible when the process is operated in a kinetic regime where growth rate is proportional to the reactant flux (pressure). We recently reported such a kinetic regime for HfO_2 growth from TDMA-Hf precursor and water co-reactant, in which growth rate saturates at high TDMA-Hf precursor pressure, but is rate controlled by, and linearly dependent on, the H_2O pressure [27]. However, we demonstrated that the diffusion transport limitation can be turned into an advantage by delivering water molecules forward-directed at the bottom of a deep trench, thereby creating a virtual source of water at the bottom. Since the local growth rate is proportional to the corresponding water flux, coating is thicker at the bottom and decreases toward the top of trench; such a superconformal profile affords complete fill in trenches without any void or seam. Experimentally, the forward-directed transport of H_2O molecules at the trench bottom was implemented by: (i) pointing the water delivery tube at the substrate (forward-directed flux), and (ii) keeping the total process pressure < 1 mTorr to minimize the gas phase scattering rate [27].

In this work, we test the same HfO_2 growth kinetics in a CNT forest with height of 14 μm by pumped CVD; the growth conditions are: 0.18 mTorr TDMA-Hf and 0.023 mTorr H_2O at 200 °C (Figure 6.9). In this experiment, both the precursor and water delivery tubes are pointed to the forest substrate, so that the local partial pressure of TDMA-Hf precursor is at near saturation at all depths in the forest. SEM image of the coated forest shows a bright region near the top, which sharply changes to a darker region at a forest depth of ~ 3 μm (Figure 6.9a). The measured coating thicknesses in the forest are: 12 nm at the top (Figure 6.9b); 6 nm at the mid-depth (Figure 6.9c); and 5 nm at the bottom of forest where coating on the underlying Si substrate is also observed (Figure 6.9d). Surprisingly, the coating is highly conformal in the bottom half of the forest with a step coverage of 5/6 or 83 %.

To better understand these experimental results, we use Equation 6.3 to calculate the H_2O pressure drop in the forest as a function of depth, considering an average film thickness of 5 nm (Figure 6.10). Since the steady state water partial pressure outside the forest is 0.023 mTorr, the result in Figure 6.10 predicts that water is completely depleted at a depth of ~ 2.5 μm, which is

strikingly close to the height of bright region in Figure 6.9a. Note that, our estimation of diffusion coefficient is slightly conservative as discussed before, which overestimates the pressure drop in a forest. According to Figure 6.10, the coating thickness in the forest should be zero after a depth of 2.5 μm, which is in a strong disagreement with the experimental results in Figure 6.9. Based on our previous experience with forward-directed fluxes [14, 27, 28], we attribute the experimental coating result in Figure 6.9 to the ballistic transport of precursor and water molecules in the depth of forest, affording a higher local flux than that estimated by diffusion transport (Figure 6.10). Since the top portion of the forest (first few microns from the top) receives both isotropic and forward-directed fluxes, the CNTs within that depth has a higher coating thickness; a similar behavior was observed in the HfO_2 coating of microtrenches (Chapter 2). After that depth, however, the isotropic flux diffusing from the outside of forest depletes to zero, and the forward-directed fluxes maintain a gas distribution in the depth of forest to afford conformal coating.

Considering the impressive HfO_2 coating result in a forest, we propose that the forward-directed fluxes can be used for conformal coating in CNT forests for two-reactant CVD process, in which the growth kinetics do not afford a simultaneous growth saturation for both the reactants. This approach can also be employed for a single-reactant CVD process, in which the vapor pressure of the reactant is too low to achieve complete growth saturation; this is the case for a large fraction of the available CVD precursors.

6.7 Conclusions

We demonstrate extremely conformal HfB_2 coating in CNT forests with height of ≤ 1.7 mm by employing static (unpumped) chemical vapor deposition (SCVD), utilizing a high pressure of the $Hf(BH_4)_4$ precursor, up to its full vapor pressure. When the substrate temperature is kept low (≤ 200 °C in present experiments), the growth saturation occurs at a pressure that is orders of magnitude lower than the maximum precursor pressure limit, thereby affording a high degree of conformality in the forests. A step coverage of 92 % is achieved when the forest height is 80 μm.

In addition to high conformality, HfB_2 coating creates strong joints wherever the neighboring CNTs touch each other; this converts the CNT forest with van der Waals interactions

into a mesoscale composite foam with greatly enhanced mechanical performance. We calculate and compare the Knudsen diffusion coefficient in a CNT forest using two different approaches, and then employ the theory of conformal CVD to predict the minimum required precursor pressure as a function of the coating thickness, forest height and the area density of CNTs. We propose that the SCVD method can be used for conformal coating with nearly unity step coverage for a single-source precursor, provided that: (i) a growth saturation is achievable within the limit of vapor pressure, and (ii) the reaction byproducts are stable enough not to decompose on the growth surface at temperature.

We also demonstrate a case of two-reactant conventional pumped CVD using HfO_2 growth from TDMA-Hf precursor and water co-reactant, in which the kinetics do not afford simultaneous growth saturation for both the reactants. In this case, we deliver the reactants as forward-directed fluxes (ballistic transport) to achieve conformal HfO_2 coating within a forest. The forward-directed flux method is especially useful for CVD precursors for which the growth saturation is not observed within the limit of vapor pressure.

6.8 References

1. Saito, R., G. Dresselhaus, and M.S. Dresselhaus, *Physical Properties of Carbon Nanotubes*. 1998: Imperial College Press.

2. Huang, Z.P., J.W. Wu, Z.F. Ren, J.H. Wang, M.P. Siegal, and P.N. Provencio, *Growth of highly oriented carbon nanotubes by plasma-enhanced hot filament chemical vapor deposition.* Applied Physics Letters, 1998. **73**(26): p. 3845-3847.

3. Fahrenholtz, W.G., G.E. Hilmas, I.G. Talmy, and J.A. Zaykoski, *Refractory diborides of zirconium and hafnium.* Journal of the American Ceramic Society, 2007. **90**(5): p. 1347-1364.

4. Juretschke, H.J. and R. Steinitz, *Hall Effect and Electrical Conductivity of Transition-Metal Diborides.* Journal of Physics and Chemistry of Solids, 1958. **4**(1-2): p. 118-127.

5. Willinger, M.G., G. Neri, A. Bonavita, G. Micali, E. Rauwel, T. Herntrich, and N. Pinna, *The controlled deposition of metal oxides onto carbon nanotubes by atomic layer deposition: examples and a case study on the application of V2O4 coated nanotubes in gas sensing.* Physical Chemistry Chemical Physics, 2009. **11**(19): p. 3615-3622.

6. Sohn, J.I., Y.S. Kim, C. Nam, B.K. Cho, T.Y. Seong, and S. Lee, *Fabrication of high-density arrays of individually isolated nanocapacitors using anodic aluminum oxide templates and carbon nanotubes.* Applied Physics Letters, 2005. **87**(12).

7. Gordon, R.G., D. Hausmann, E. Kim, and J. Shepard, *A kinetic model for step coverage by atomic layer deposition in narrow holes or trenches.* Chemical Vapor Deposition, 2003. **9**(2): p. 73-78.

8. Yanguas-Gil, A., Y. Yang, N. Kumar, and J.R. Abelson, *Highly conformal film growth by chemical vapor deposition. I. A conformal zone diagram based on kinetics.* Journal of Vacuum Science & Technology A, 2009. **27**(5): p. 1235-1243.

9. Niinisto, J., K. Kukli, M. Kariniemi, M. Ritala, M. Leskela, N. Blasco, A. Pinchart, C. Lachaud, N. Laaroussi, Z.Y. Wang, and C. Dussarrat, *Novel mixed alkylamido-cyclopentadienyl precursors for ALD of ZrO(2) thin films.* Journal of Materials Chemistry, 2008. **18**(43): p. 5243-5247.

10. Jayaraman, S., Y. Yang, D.Y. Kim, G.S. Girolami, and J.R. Abelson, *Hafnium diboride thin films by chemical vapor deposition from a single source precursor.* Journal of Vacuum Science & Technology A, 2005. **23**(6): p. 1619-1625.

11. Yang, Y., S. Jayaraman, D.Y. Kim, G.S. Girolami, and J.R. Abelson, *CVD growth kinetics of HfB2 thin films from the single-source precursor Hf(BH4)(4).* Chemistry of Materials, 2006. **18**(21): p. 5088-5096.

12. Jensen, J.A., J.E. Gozum, D.M. Pollina, and G.S. Girolami, *Titanium, Zirconium, and Hafnium Tetrahydroborates as Tailored Cvd Precursors for Metal Diboride Thin-Films.* Journal of the American Chemical Society, 1988. **110**(5): p. 1643-1644.

13. Knisley, T.J., L.C. Kalutarage, and C.H. Winter, *Precursors and chemistry for the atomic layer deposition of metallic first row transition metal films.* Coordination Chemistry Reviews, 2013. **257**(23-24): p. 3222-3231.

14. Talukdar, T.K., S. Liu, Z. Zhang, F. Harwath, G.S. Girolami, and J.R. Abelson, *High Quality MgO Film Grown at High Rate by Low Temperature Conformal CVD.* Manuscript in preparation, 2018.

15. Jayaraman, S., E.J. Klein, Y. Yang, D.Y. Kim, G.S. Girolami, and J.R. Abelson, *Chromium diboride thin films by low temperature chemical vapor deposition.* Journal of Vacuum Science & Technology A, 2005. **23**(4): p. 631-633.

16. Wang, W.J.B., Y. Yang, A. Yanguas-Gil, N.N. Chang, G.S. Girolami, and J.R. Abelson, *Highly conformal magnesium oxide thin films by low-temperature chemical vapor deposition from Mg(H3BNMe2BH3)(2) and water.* Applied Physics Letters, 2013. **102**(10).

17. Yanguas-Gil, A., *Growth and Transport in Nanostructured Materials: Reactive Transport in PVD, CVD, and ALD*. 2016: Springer International Publishing.

18. Cloud, A.N., *Ultraconformal chemical vpor deposition and synthesis of transition metal nitride films*, in *Materials Science and Engineering*. 2013, University of Illinois at Urbana-Champaign.

19. Blanco, A., E. Chomski, S. Grabtchak, M. Ibisate, S. John, S.W. Leonard, C. Lopez, F. Meseguer, H. Miguez, J.P. Mondia, G.A. Ozin, O. Toader, and H.M. van Driel, *Large-scale synthesis of a silicon photonic crystal with a complete three-dimensional bandgap near 1.5 micrometres.* Nature, 2000. **405**(6785): p. 437-440.

20. Garcia-Santamaria, F., M. Ibisate, I. Rodriguez, F. Meseguer, and C. Lopez, *Photonic band engineering in opals by growth of Si/Ge multilayer shells.* Advanced Materials, 2003. **15**(10): p. 788-+.

21. Miguez, H., S.M. Yang, N. Tetreault, and G.A. Ozin, *Oriented free-standing three-dimensional silicon inverted colloidal photonic crystal microribers.* Advanced Materials, 2002. **14**(24): p. 1805-1808.

22. Miguez, H., E. Chomski, F. Garcia-Santamaria, M. Ibisate, S. John, C. Lopez, F. Meseguer, J.P. Mondia, G.A. Ozin, O. Toader, and H.M. van Driel, *Photonic bandgap engineering in germanium inverse opals by chemical vapor deposition.* Advanced Materials, 2001. **13**(21): p. 1634-+.

23. Chomski, E., O. Dag, A. Kuperman, N. Coombs, and G.A. Ozin, *New forms of luminescent silicon: Silicon-silica composite mesostructures.* Chemical Vapor Deposition, 1996. **2**(1): p. 8-+.

24. Galisteo-Lopez, J.F., M. Ibisate, R. Sapienza, L.S. Froufe-Perez, A. Blanco, and C. Lopez, *Self-Assembled Photonic Structures.* Advanced Materials, 2011. **23**(1): p. 30-69.

25. Lopez, C., *Materials aspects of photonic crystals.* Advanced Materials, 2003. **15**(20): p. 1679-1704.

26. Doppelt, P. and T.H. Baum, *The chemical vapor deposition of copper and copper alloys.* Thin Solid Films, 1995. **270**(1-2): p. 480-482.

27. Talukdar, T.K., W.B. Wang, G.S. Girolami, and J.R. Abelson, *Superconformal Coating and Filling of Deep Trenches by Chemical Vapor Deposition with Forward-Directed Fluxes.* Manuscript in preparation, 2018.

28. Talukdar, T.K., G.S. Girolami, and J.R. Abelson, *Seamless Fill of Deep Trenches by Chemical Vapor Deposition: Use of a Molecular Growth Inhibitor to Eliminate Pinch-off.* Manuscript in preparation, 2018.

29. Sandin, C.R., *Synthesis and indentation of boride and carbide coated carbon nanotube composite microstructures*, in *Mechanical Science and Engineering*. 2016, University of Illinois at Urbana-Champaign.

30. Kim, D.Y. and G.S. Girolami, *Highly Volatile Magnesium Complexes with the Aminodiboranate Anion, a New Chelating Borohydride. Synthesis and Characterization of Mg(H3BNMe2BH3)(2) and Related Compounds.* Inorganic Chemistry, 2010. **49**(11): p. 4942-4948.

31. Wang, W.B., N.N. Chang, T.A. Codding, G.S. Girolami, and J.R. Abelson, *Superconformal chemical vapor deposition of thin films in deep features.* Journal of Vacuum Science & Technology A, 2014. **32**(5).

32. Futaba, D.N., K. Hata, T. Namai, T. Yamada, K. Mizuno, Y. Hayamizu, M. Yumura, and S. Iijima, *84% Catalyst activity of water-assisted growth of single walled carbon nanotube forest characterization by a statistical and macroscopic approach.* Journal of Physical Chemistry B, 2006. **110**(15): p. 8035-8038.

33. Sandin, C., T.K. Talukdar, J.R. Abelson, and S. Tawfick, *Synthesis and mechanical behavior of ultra-high temperature resistant coatings (UHTC) using boride-coated carbon nanotube scaffolds.* Manuscript in preparation, 2018.

6.9 Tables and Figures

Table 6.1. HfB_2 coated CNT forests at growth temperature of ≤ 200 °C. The inequality indicates that the film nucleation and growth start at a temperature lower than 200 °C during the temperature ramp in SCVD.

Sample	$Hf(BH_4)_4$ pressure (Torr)	Forest height (mm)	Film thickness (nm)		Net step coverage (%)
			Top	Bottom	
A	12.5	0.4	11	9	82
B	4	0.4	11	9	82
C	2	0.08	12	11	92
D*	5	1.7	16	10	63

* The CNT forest in sample D has patterned cylindrical holes (diameter of 3 μm and uniform spacing of 20 μm) that span the full height of the forest. These enhance precursor transport to the bottom.

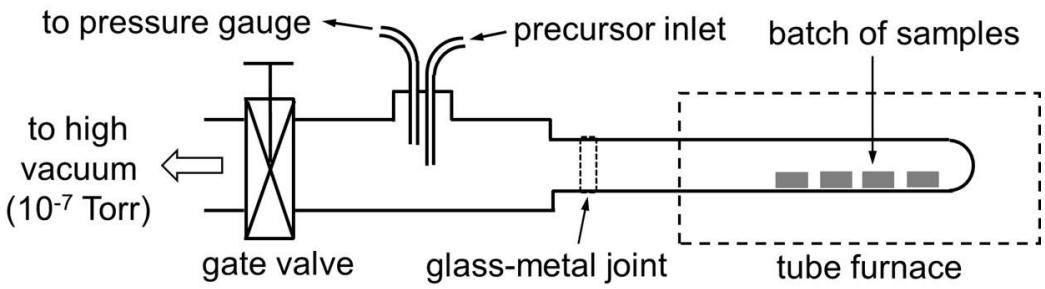

Figure 6.1. Schematic of the static CVD setup used for conformal HfB_2 coating in CNT forests.

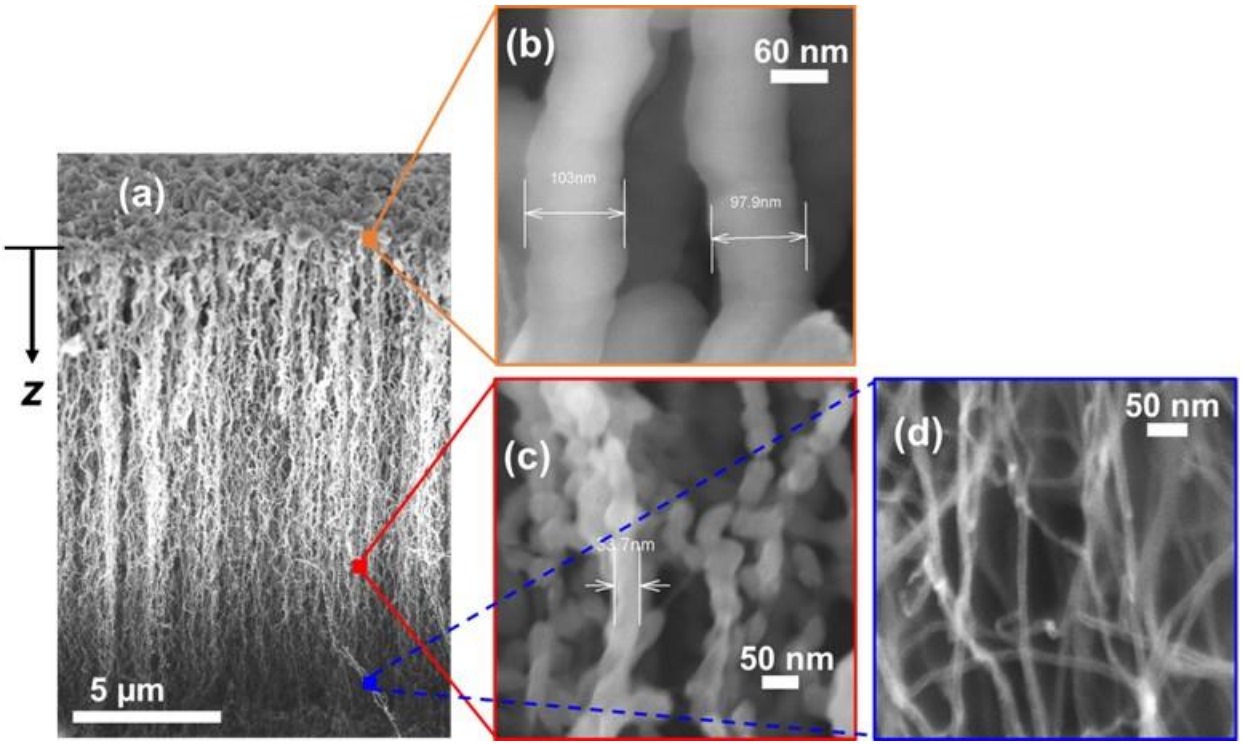

Figure 6.2. SEM images of MgO coating in a CNT forest of height 17 µm, coated using 2 mTorr $Mg(DMADB)_2$ and 3 mTorr H_2O at 220 °C for 60 min by pumped CVD. a) A top portion of the forest showing gradual decreases in contrast (brightness) with depth (*z*), meaning a decline in film thickness. b-d) Magnified images showing the film thickness: 45 nm at z = 0 (b); 12 nm at *z* = 10 µm (c); and zero at *z* = ~ 13.6 µm. The forest density in the plane of the substrate is ~ 1×10^{14} tubes/m^2.

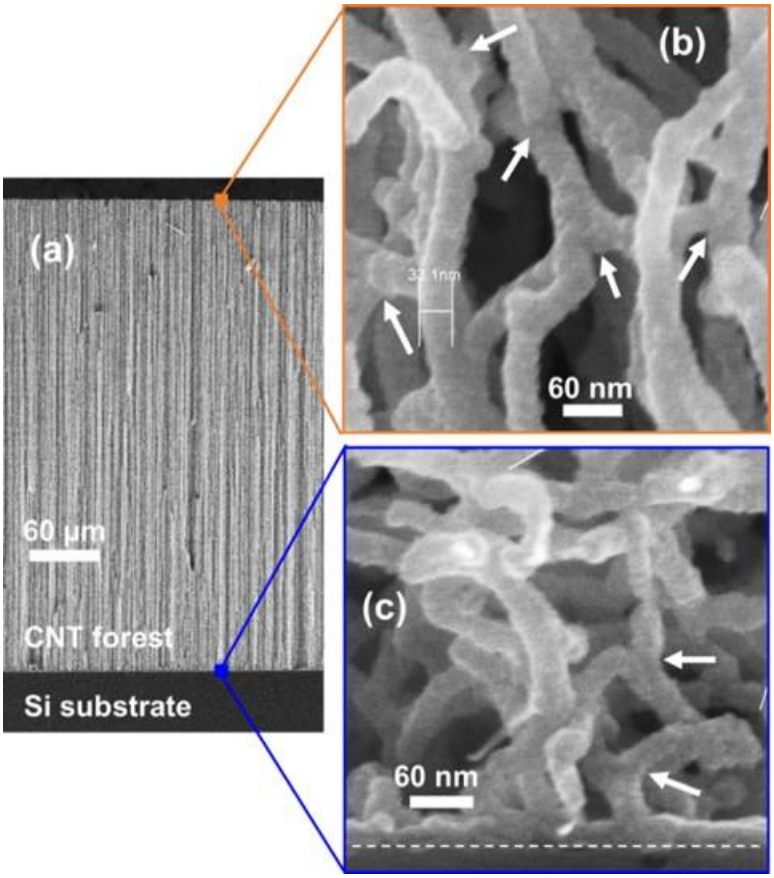

Figure 6.3. SEM images of HfB_2 coating in a CNT forest (sample A) of height 0.4 mm, coated using a 12.5 Torr of $Hf(BH_4)_4$ pressure at ≤ 200 °C by SCVD. a) Image at low magnification showing the full height of the CNT forest. b) Image at high magnification showing a film thickness of 11 nm at the top of forest, and c) a film thickness of 9 nm at the bottom of forest. The interface between the HfB_2 film at the bottom and the underlying Si substrate is marked with a white dashed line in c). The white arrows in b) and c) point to some of the 'welded' joints created by HfB_2 coating at locations where the CNTs touch each other.

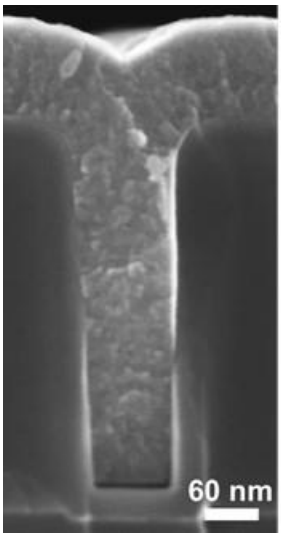

Figure 6.4. Cross-sectional SEM image of a HfB_2 *filled* trench with aspect ratio of 5, obtained with a 2 Torr of $Hf(BH_4)_4$ precursor at ≤ 200 °C by SCVD.

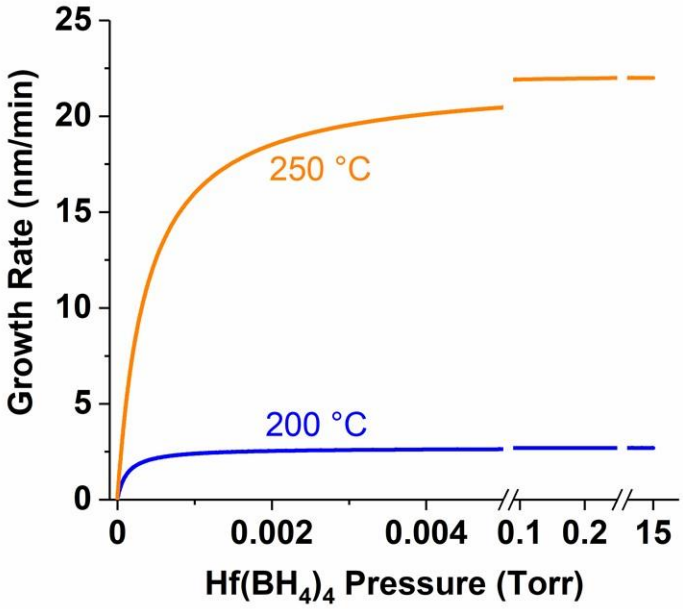

Figure 6.5. Calculated HfB_2 film growth rates at 200 and 250 °C as a function of $Hf(BH_4)_4$ precursor pressure, obtained using Equation 6.1 and experimental results in references [8, 10, 11]. Two breaks are used in the x-axis to show the rate up to the precursor vapor pressure (15 Torr at room temperature).

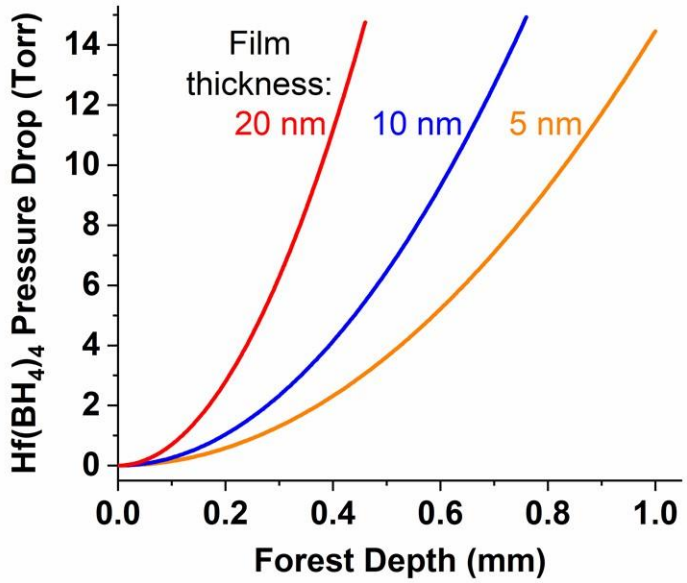

Figure 6.6. Calculated $Hf(BH_4)_4$ pressure drops for different HfB_2 coating thicknesses as a function of depth in a CNT forest at 200 °C; the area density of the forest is 1×10^{14} tubes/m^2. The underlying assumption in this calculation is that the film growth rate is constant throughout the depth of the forest, i.e., a step coverage of unity.

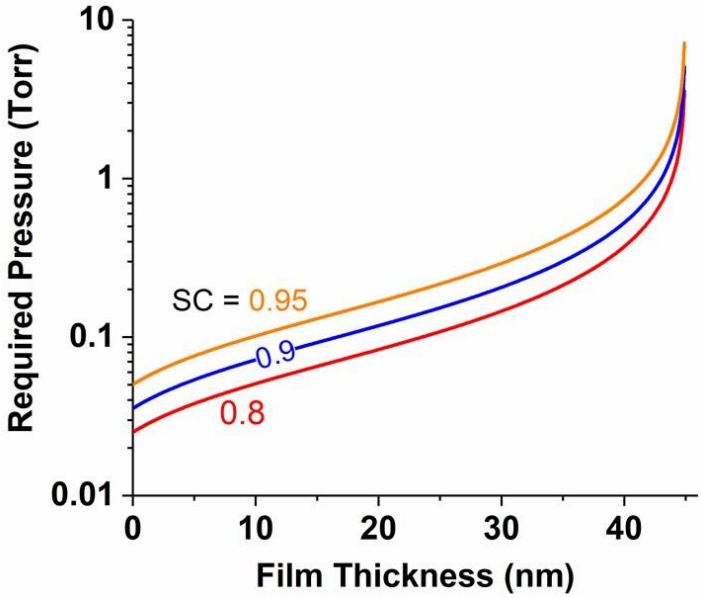

Figure 6.7. Calculated (Equation 6.5) minimum required $Hf(BH_4)_4$ pressure for step coverages of 80, 90 and 95 %, as a function of film thickness in a CNT forest at 200 °C. The forest shown in Figure 6.3a (height = 0.4 mm) is considered in these calculations.

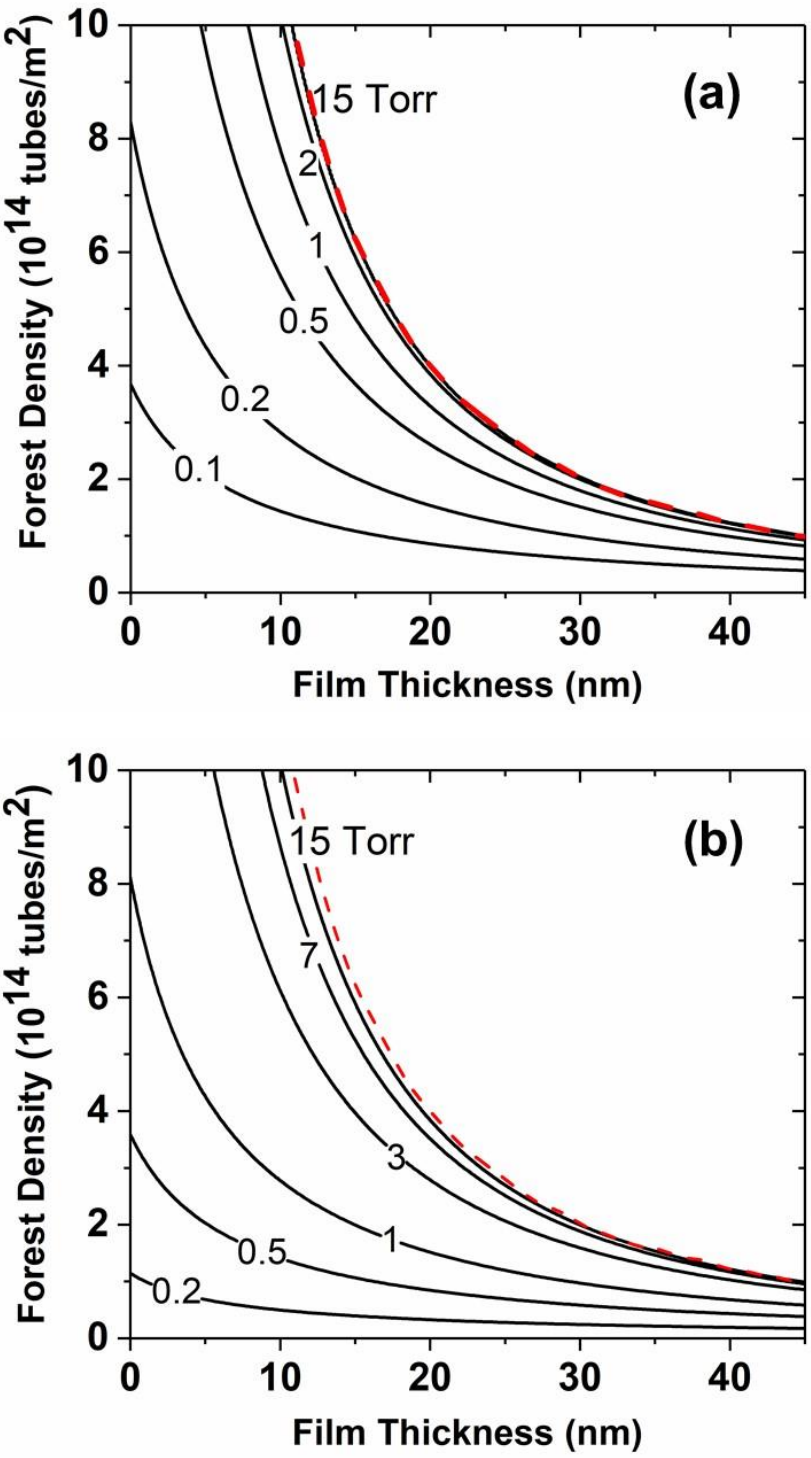

Figure 6.8. Contour plot of minimum required $Hf(BH_4)_4$ pressure for a step coverage of 90 % as a function of film thickness and CNT forest density, at a substrate temperature of 200 °C (a) and 250 °C (b). The forest shown in Figure 6.3a is considered in these calculations.

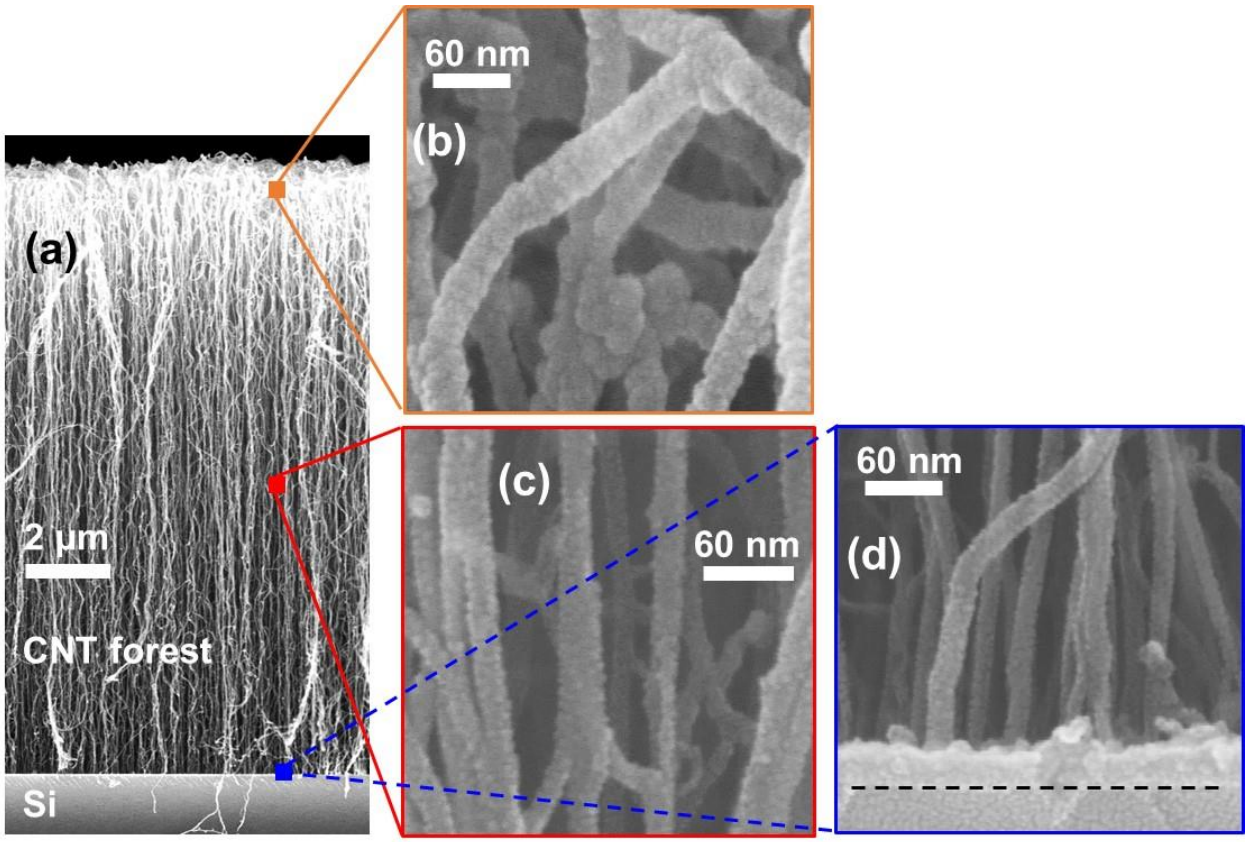

Figure 6.9. SEM images of HfO_2 coating in a CNT forest of height 14 µm, coated using 0.18 mTorr TDMA-Hf and 0.023 mTorr H_2O at 200 °C for 15 min by pumped CVD. The precursor and water delivery tubes are pointed to the forest to obtain forward-direct ballistic fluxes. a) Image at low magnification showing the full height of the CNT forest. b-d) Magnified images showing a film thickness of 12 nm at near the top of forest (b); 6 nm at the mid-depth of forest (c); and 5 nm at the bottom of forest. The forest density is ~ 1×10^{14} tubes/m^2.

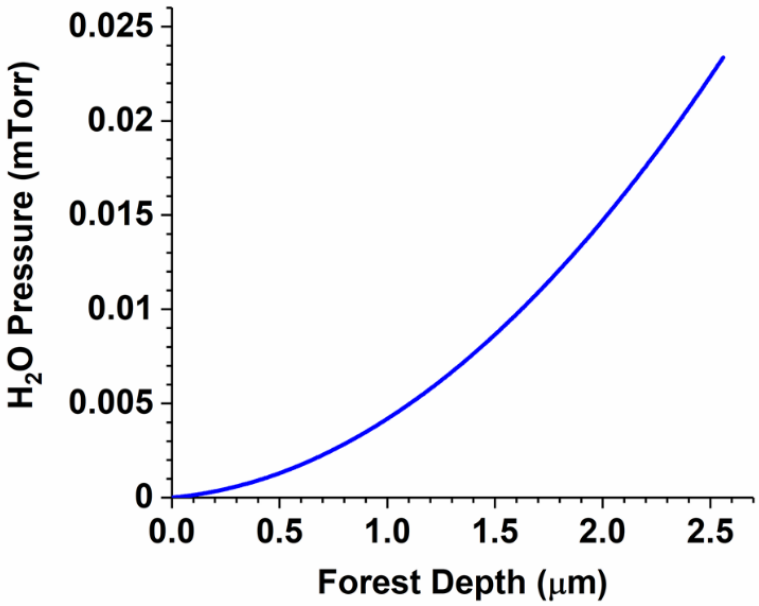

Figure 6.10. Calculated H_2O pressure drop for a HfO_2 coating thickness of 5 nm, as a function of depth in a CNT forest at 200 °C; the forest shown in Figure 6.9a is considered in this calculation

CHAPTER 7

STIFFNESS AND STRENGTH OF CONFORMAL HfB_2 COATED CARBON NANOTUBE FORESTS

In chapter 6 the conformal HfB_2 coating of carbon nanotube (CNT) forest using static chemical vapor deposition (SCVD) was discussed. This chapter briefly explores the modulus and compressive strength measurements of HfB_2 coated CNT forest, using flat punch nanoindentation technique.

This work is a highly collaborative effort between Prof. Sameh Tawfick, Prof. John R. Abelson, Ms. Carly Sandin, and myself. Prof. Tawfick and Ms. Sandin synthesized the CNT forests, and I coated them with HfB_2 thin films. Ms. Sandin then performed the mechanical measurements on the coated samples. Film thickness was measured by Ms. Sandin and myself.

The following text is adapted from a collaborative manuscript (*in preparation*) in which a HfB_2 coating of CNT forest section is written by Prof. Abelson and myself. Further details of the CNT forest synthesis and mechanical measurements can be found in Reference [1].

7.1 Introduction

Ultra-high temperature coatings (UHTC) are required to protect several parts of hypersonic vehicles such as sharp leading edges where the temperatures are expected to reach 2000 ºC [2]. Hafnium and zirconium borides are considered particularly strong candidates for these applications owing to their high melting temperatures combined with their high thermal conductivity [3]. This makes these alloys strong candidates for use in sharp wing leading edges and nose tips. They also exhibit extraordinary thermal stability due to their low thermal expansion coefficient and relatively high oxidation temperature. For example: the oxidation of HfB_2 takes place around 1200 ºC, which can be further enhanced by alloying with high melting temperature additives such as silicon carbide.

The processing routes to produce these materials are extremely severe. Hot pressing is the standard process to produce dense HfB_2 (or ZrB_2), in which a combination of very high process temperature (~ 1800 °C), inert gas environment and high pressure (~ 50 MPa) is necessary [4]. Another method to produce dense HfB_2 is the spark plasma sintering, which also requires an extremely high process temperature (~ 2100 ºC) and a pressure of ~ 30 MPa [4]. While these techniques are suitable for bulk-like HfB_2, the required process conditions render them impractical to create thin films coating with uniform thickness in a complex geometry, such as CNT forest.

In contrast, chemical vapor deposition (CVD) can be used to make highly conformal HfB_2 thin films with good properties; as deposited films have a hardness of 15 GPa, an elastic modulus of 320 GPa and a low coefficient of friction (~ 0.1) [5-7]. Upon thermal annealing at 700 °C, HfB_2 films transform into a nanocrystalline phase of grain size 5-8 nm. Annealing increases the hardness to 40 GPa with enhanced wear resistance [5, 6]. Alloying of HfB_2 films with nitrogen results in a ternary alloy that has a reduced elastic modulus and does not crystallize upon annealing to 700°C [8].

In this study, we present a new route for preparing UHTC of HfB_2 using aligned carbon nanotube (CNT) scaffolds. The process consists of two consecutive CVD steps: the first is to synthesize the CNT forests [1]; followed by the second CVD process to obtain a highly conformal HfB_2 coating on the CNTs (Chapter 6). This simple route enables the synthesis of millimeter-scale thick films with tunable porosity and mechanical behavior at temperatures lower than 800 °C. We believe that this process is amenable for scaling and could be implemented to coat meter-scale panels.

7.2 Experimental

CNT forests with 25 μm diameter and 30 μm height are synthesized on Si substrates [1]; this forest size is referred to as ‘CNT pillar’ to distinguish from those described in Chapter 6. The CNT pillars are conformally coated with HfB_2 films using $Hf(BH_4)_4$ precursor in SCVD (Figure 7.1); the details are described in Chapter 6. Different coating thicknesses in the range of 3 to 45 nm are obtained by using appropriate $Hf(BH_4)_4$ precursor pressure (0.1 to 5 Torr) at a growth

temperature of ≤ 200 °C (Figure 7.2); the coating thickness is measured by scanning electron microscope (SEM).

Stress-strain measurements of the HfB_2 coated CNT pillars are done by flat punch nanoindentation; the flat punch has a radius of 60 μm. The low aspect ratio of the CNT pillars forbids the failure by Euler's column buckling [9]. The stress is calculated as the applied load divided by the pillar area, and the engineering strain is defined as the displacement divided by the original length (height) of the pillar.

7.3 Results

The HfB_2-CNT composites exhibit a highly nonlinear compressive response reminiscent of open cell foams (Figure 7.3). In general, the behavior can be divided into three regimes: (I) the initial regime of pre-collective buckling loading; (II) the post-collective buckling plateau; and (III) the densification regime. Importantly, the material exhibits nonlinear inelastic response in all three regimes. For example, Figure 7.4 shows typical engineering stress-strain curve obtained for HfB_2 coating thickness of 3, 16, 20 and 50 nm in pre-buckling regime I. The response is clearly nonlinear during loading and unloading even in this regime. The loading curves show a hardening response, characterized by gradual increase in slope as discussed below. This inelastic response observed in regime I (Figure 7.4) is in contrast with the purely elastic response of open cell foams in the pre-buckling regime; this is explained as follows.

The uncoated CNT bundles are not perfectly straight after synthesis, which is maintained after the conformal HfB_2 coating. The coated CNTs intersect at many points where they are bonded by: (i) welding of the contact points by HfB_2 coating, and (ii) Van der Waal forces between coated CNTs in touch with each other. The total number of these nodes in HfB_2-CNT sample depends on the area density of CNTs (i.e., number to tubes per unit area) and the coating thickness; whereas the bonding strength of these nodes depends on the angle of intersection and the coating thickness. Note that the Van der Waals forces between touching CNTs are much weaker than the HfB_2 welded nodes (joints). Due to the random distribution of these nodes, the local bending stress distribution in the HfB_2-CNT composite is not uniform.

Upon compressive loading, the coated CNTs with weakly bonded nodes slip with respect to each other, even at the smallest applied load. This has two effects on the stress-strain response; first, the re-arrangement during loading (in regime I) results in a hardening behavior as observed in Figure 7.4. During the arrangements, the coated CNTs deforms (locks) into a more resistant configuration. Consequently, their load-resistance ability increases as demonstrated by the increase in slope (Figure 7.4). The second effect is observed by the large levels of hysteresis (~ few percent strain), which is a direct result of the HfB_2-CNT composite being locked in a new configuration.

For each coating thickness, we also compress pillars up to larger strains until they collapse and start to densify. The resulting stress-strain curves (Figure 7.3) allow us to identify the maximum load before the onset of buckling plateau (regime II in Figure 7.3); the corresponding stress is considered as the compressive strength. The peak stress before the plateau is associated with collective buckling of the CNTs across the cross section. For very thin coating (≤ 3 nm), the peak stress arises due to coordinated buckling of all CNTs across one plane (Figure 7.3a). This leads to the accordion-like buckling behavior observed by several groups for uncoated CNTs [9, 10], which is useful for applications requiring energy absorption by the foam structure [11].

From the stress-strain curves in pre-buckling regime I (Figure 7.4), the modulus of the HfB_2-CNT composites is calculated by measuring the unloading slope for the first 10% of the peak load. Note that, this slope is not constant for different peak loads used for different HfB_2 coating thickness. To better understand this response, we compress the micropillars with different maximum loads (within regime I) and measure the first 10 % of unloading slope in each case. When these unloading slopes are plotted against the corresponding maximum stress (normalized with buckling stress), we observe a trend that the unloading slope increases with the applied stress following a power law (Figure 7.5); this is true for all the HfB_2 coating thicknesses in the present experiments with a power $m = 0.56 - 0.6$. The power m is reminiscent of the strain hardening coefficient that describes the true stress-strain response in the post-yielding regime for ductile materials. To define and further clarify the physical significance of m, we can write an empirical constitutive relation in regime I as:

$$\sigma_I = MK^m \varepsilon^p \tag{7.1}$$

where σ_I is the unloading slope in regime I; M is the effective nonlinear modulus; K is the ratio of maximum stress to bucking stress, ε is the applied engineering strain; m and n are the reorganization and strain hardening coefficients, respectively. Our results indicate that $p = 0$ for all the tested HfB_2 coated CNT pillars, meaning that there is no consistent dependence of the unloading slope on the applied strain. Instead, a consistent trend is obvious in the dependence of the unloading slope on the applied stress (Figure 7.5). We believe that this constitutive law sheds a light on the stress-strain response of this new type of open cell foam. As the stress increases, the coated CNTs gradually reorganize themselves due to slip at the weak nodes. When the applied stress reaches the transition point between regime I and II (Figure 7.3), the slipping of the coated CNTs is no longer random to reorganize themselves. When the stress is increased beyond this locking point, the coated CNTs collectively buckle by forming folds that span across the cross-section of the pillars. Interestingly, the reorganization rate is similar for most of the HfB_2 coating thicknesses in the present study; we refer this as the reorganization hardening coefficient having the value $m \sim 0.55$. Based on this definition, m depends on the morphology of the CNT scaffold, characterized by the alignment and area density of the CNTs; the detail understanding of this dependence needs further investigation and beyond the scope of this work.

7.4 Discussion

The y-intercept in Figure 7.5 is simply M (modulus) in Equation 7.1 and has the unit of stress. It corresponds to the unloading slope at the onset of buckling ($K = 1$). We use the calculated values of M as the effective modulus of the material and use it to compare the elastic behavior of the HfB_2-CNT composites, as a function of the coating thickness (Figure 7.6a) and density (Figure 7.6b). The compressive strength of the pillars is plotted as a function of the coating thickness and density (Figure 7.7). The scaling of the modulus (and compressive strength) with the density of the material is highly relevant to aerospace composites and load bearing materials. For cellular materials, these properties usually change with density following a power law in the form: property $(M, S) \sim \rho^n$, where S is the compressive strength; and n ranges from 1 to 3 [13]. It is well known that $n = 1$ and 2 correspond to stretch and bending dominated microstructures, respectively [14]. We find that the modulus-density behavior of the HfB_2-CNT foams scales with $n = 3$, which agrees

well with our previous work on Al_2O_3 coated CNTs [11]. The scaling behavior of the compressive strength with the density have an exponent, $n = 3.37$. Scaling law exponents larger than 2 (e.g., 3) correspond to composite foam structures, in which the connectivity of the node morphology changes due to coating. More specifically, as the coating thickness increases, the CNTs are cross-linked (welded) at the intersection points, resulting in a significant strengthening of the structure and an exponent $n > 2$. Note that a lower exponent is usually advantageous if the goal is to construct an ultralight foam without sacrificing the mechanical behavior. On the other hand, when a low-density material, such as a CNT pillar, is used as the scaffold to construct a low porosity composite by conformal coating, a higher exponent indicates an efficient coating process and a rapid enhancement of properties with coating thickness.

7.5 Mechanics Model

The ability of SCVD to coat and penetrate the CNT scaffold is demonstrated by considering the CNTs with the highest coating thickness of 45 nm. The density of these coated sample is measured to be 3656 kg/m^3 which corresponds to 36 % of the bulk HfB_2 density. At this thickness, the modulus and strength of the coated micropillar is measured to be 107 GPa and 1.94 GPa respectively; the modulus corresponds to 33 % of the HfB_2 film modulus. We use a minimalistic mechanics model to gain more insights into this behavior. We consider the material to be CNT foam before coating, which transforms into a porous HfB_2-CNT composite after the HfB_2 coating. First, we analyze the mechanics of the CNT pillar before coating. We consider the difference between the known single MWNT modulus, size and density on one hand, and the measured CNT pillar modulus, geometry and density on the other hand. The CNT pillar properties measured by indentation result from the arrangement of the individual MWNT. Similar to the classical analysis of foams, the CNT forest is made from a combination of similar cubic unit cells (Figure 7.8a). The behavior of a unit cell is equivalent to the behavior of the CNT pillar. Inside each unit cell, the individual MWNT are subject to bending stresses when the CNT pillar is compressed. Because the CNTs are slender beam elements, the bending stresses within the unit cell can be computed using Euler-Bernoulli beam approximation of simply supported beams (Figure 7.8b). The supports in this case arise from the contact nodes between the CNTs. Based on this description; we can then calculate the Modulus (M) of a unit cell of the CNT pillar using

$$M = \frac{k_{CNT} l_{cell}}{A_{cell}} \tag{7.2}$$

where k_{CNT} is the stiffness of the CNT beams in the cell; l_{cell} is the length of the unit cell; and A_{cell} is the area of the unit cell. The stiffness of the CNT beams in a cell is given by:

$$k_{CNT} = \frac{3E_{CNT} I_{CNT}}{l_0^3} \tag{7.3}$$

Here E_{CNT} is taken to be 1 TPa, and $I_{CNT} = \pi/4\left(r_o^4 - r_i^4\right) = 427 \text{ nm}^4$. The length of the effective CNT beam (l_0) for pure CNT forest is taken to be equal to the size of the cubic cell, giving $l_0 = l_{CNT}$. The size of the unit cell is the unknown but can readily be determined by substituting the indentation measured value of modulus for uncoated CNTs, $M_{pillar} = 2.5 \text{ MPa}$. From this analysis, we calculate $l_0 = 150 \text{ nm}$, which agrees well with the intersection morphology of the CNTs observed in the SEM images.

Application of this minimalistic beam model to the HfB_2 coated CNTs provides useful insights into the mechanisms of modulus enhancement due to coating (Figure 7.8a). When the CNTs are coated, we expect the new modulus of rigidity as: $(EI)_{composite} = (EI)_{CNT} + (EI)_{HfB_2}$. We take $E_{HfB_2} = 320 \text{ GPa}$ and $I_{HfB_2} = \pi/4\left(r_{HfB_2}^4 - r_o^4\right)$, which varies with the coating thickness. First, we use these values to calculate the composite modulus $M_{composite}$ for each thickness, assuming that the unit cell does not change its size due to coating, i.e., $l_1 = l_0 = l_{cell}$. The results of this calculation, shown in Figure 7.7, indicate that $M_{composite}$ is under-estimated using the assumption of fixed cell size. Next, we assume that $l_1 = l_0 - 2\left(r_{HfB_2} - r_o\right)$, i.e., the cell size is reduced by the coating thickness (Figure 7.8b). $M_{composite}$ is then calculated using this variable cell size model, and the results are also shown in Figure 7.7. Clearly, this minimalistic model captures the modulus change due to thin coating. This also demonstrates the high degree of conformability (step coverage) of the coating obtained by SCVD, which is the essence of the mathematical model through the assumption made in the calculation of I_{HfB_2}. Notably, compared to previous similar model for the coating of aligned CNTs, this minimalistic model does not consider any variations in the coating thickness (gradients) across the length or the diameter. However, for the maximum deposition thickness of 45 nm, the

model overestimates the modulus, which indicates that the thickness of HfB_2 is not uniform across the height of the pillar when the coating thickness approaches this value of 45 nm.

7.6 Conclusion

We demonstrate the fabrication of HfB_2-CNT composite structures. The CVD of CNTs allows the fabrication of a scaffold having very low weight density and large open pores that represent an ideal substrate for subsequent coating and functionalization. Using an optimized SCVD process, the CNT scaffolds are then conformally coated with different HfB_2 film thicknesses to effectively increase the strength and modulus of the structures. Owing to the large surface area of the CNTs, a HfB_2 coating thickness of 45 nm in a 25 μm thick composite structure, has ~ 36 % HfB_2 content. The properties are analyzed in light of the mechanics of porous materials; the modulus and compressive strength follow a power law relationship with respect to the density ($\sim \rho^n$) with exponents n = 3 and 3.4, respectively. We show that this scaling can be mathematically predicted using a minimalistic model, considering that the compressive response of the composite structures results from the bending of the coated CNTs. The nearly unity step coverage of the HfB_2 coating allows the implementation of this simple model. These results are useful steps towards the realization of low density thermal protection system using ultra-high temperature ceramics, which are otherwise extremely difficult to process.

7.7 References

1. Sandin, C., *Synthesis and indentation of boride and carbide coated carbon nanotube composite microstructures*, in *Mechanical Science and Engineering*. 2016, University of Illinois at Urbana-Champaign.

2. Paul, A., et al., *UHTC composites for hypersonic applications.* 2012.

3. Fahrenholtz, W.G., et al., *Refractory diborides of zirconium and hafnium.* Journal of the American Ceramic Society, 2007. **90**(5): p. 1347-1364.

4. Gasch, M., et al., *Processing, properties and arc jet oxidation of hafnium diboride/silicon carbide ultra high temperature ceramics.* Journal of Materials Science, 2004. **39**(19): p. 5925-5937.

5. Chatterjee, A., et al., *Tribological behavior of hafnium diboride thin films.* Surface & Coatings Technology, 2006. **201**(7): p. 4317-4322.

6. Chatterjee, A., et al., *Nanoscratch and nanofriction behavior of hafnium diboride thin films.* Wear, 2008. **265**(5-6): p. 921-929.

7. Chatterjee, A., et al., *Nanowear of Hafnium Diboride Thin Films.* Tribology Transactions, 2010. **53**(5): p. 731-738.

8. Jayaraman, S., et al., *HfB2 and Hf-B-N hard coatings by chemical vapor deposition.* Surface & Coatings Technology, 2006. **200**(22-23): p. 6629-6633.

9. Maschmann, M., et al., *Continuum analysis of carbon nanotube array buckling enabled by anisotropic elastic measurements and modeling.* Carbon, 2014. **66**: p. 377-386.

10. Hutchens, S.B., L.J. Hall, and J.R. Greer, *In situ Mechanical Testing Reveals Periodic Buckle Nucleation and Propagation in Carbon Nanotube Bundles.* Advanced Functional Materials, 2010. **20**(14): p. 2338-2346.

11. Brieland-Shoultz, A., et al., *Scaling the Stiffness, Strength, and Toughness of Ceramic-Coated Nanotube Foams into the Structural Regime.* Advanced Functional Materials, 2014: p. n/a-n/a.

7.8 Figures

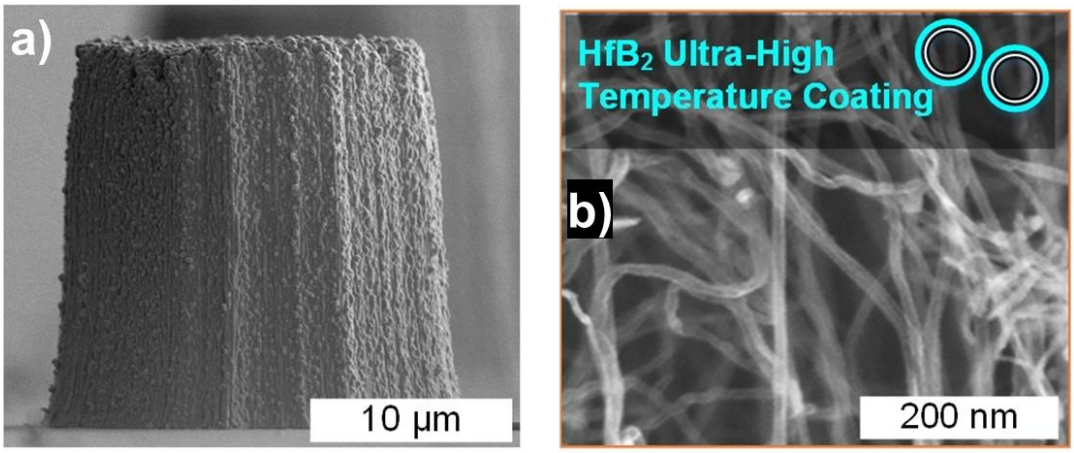

Figure 7.1. a) SEM image of a CNT pillar used for the flat punch nanoindentation. b) High resolution SEM image showing the details of the CNT network coated with HfB_2.

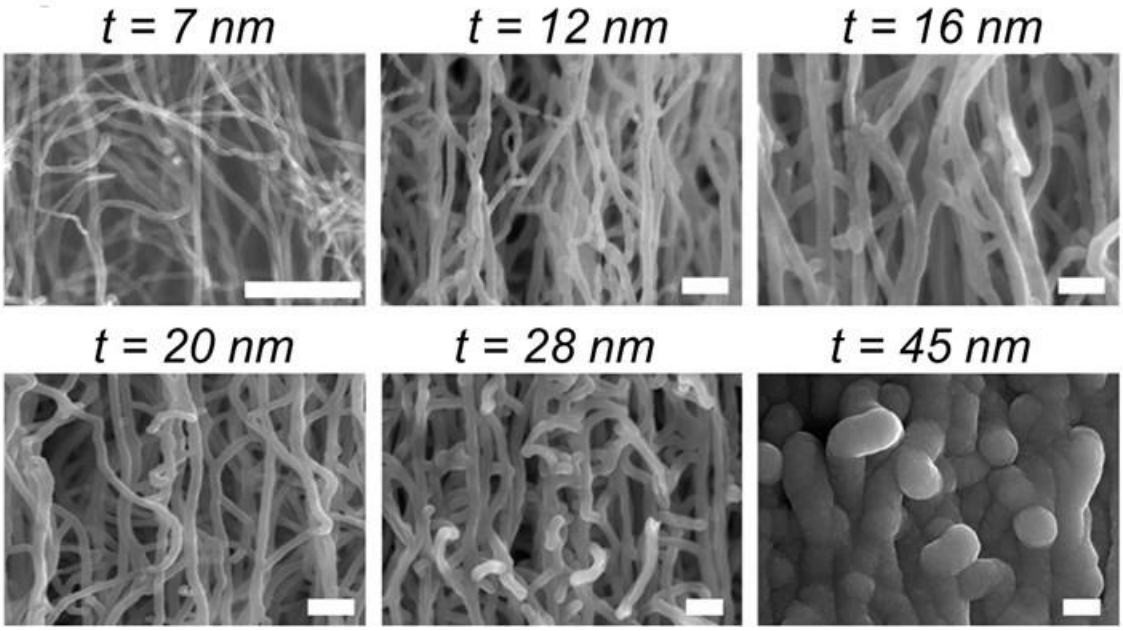

Figure 7.2. SEM images of the CNTs showing different HfB_2 coating thicknesses. Scale bar is 200 nm.

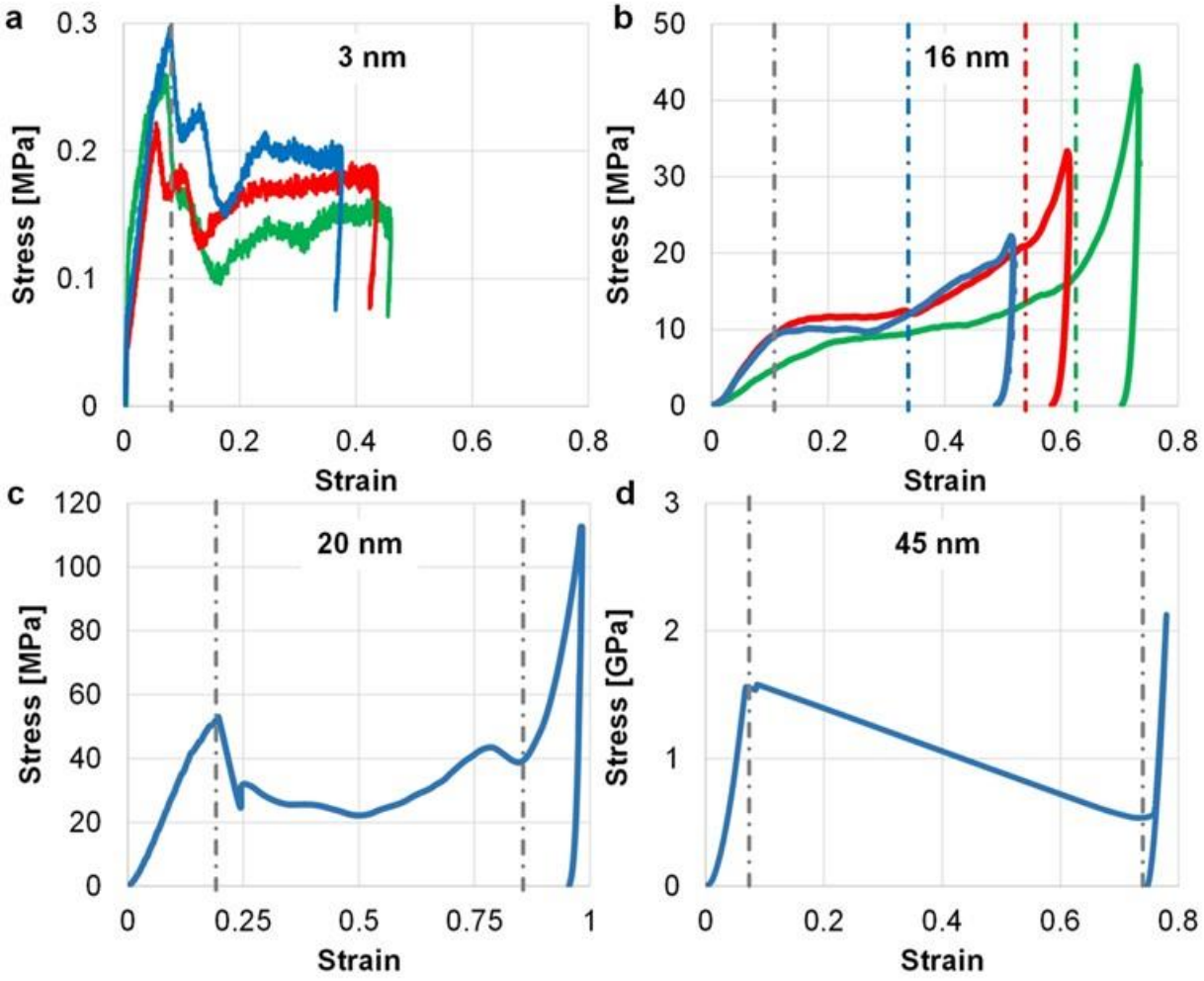

Figure 7.3. Measured stress-strain curves beyond the collapse of HfB_2 coated CNT pillars, for coating thickness of 3 (a), 16 (b), 20 (c), and 45 nm (d). The maximum value of the stress is taken as the compressive strength. The vertical dashed lines mark the transitions from stage I to II, and II to III. For the coating thickness of 3 nm in a): only the transition from stage I to II is identified, and the average stress at the transition is considered as the compressive strength. For the coating thickness of 16 nm in b): nanoindentation tests on identical pillars show that the transition from stage II to III occurs at different strain values; these are identified with the color-coded vertical dashed lines in b).

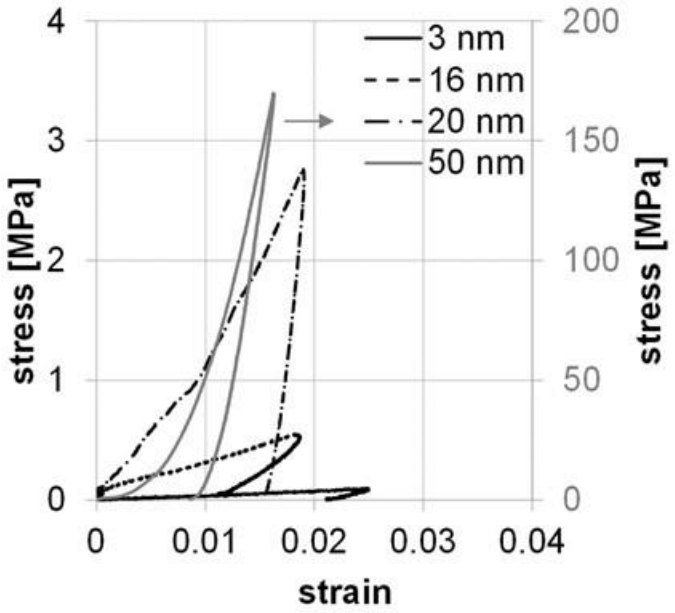

Figure 7.4. Measured stress-strain curves for HfB_2-CNT samples with different coating thicknesses; the maximum strain is limited to keep the stresses within the pre-buckling regime I, as identified in Figure 7.3. Note that the stress-strain curve for the 45 nm thick HfB_2 coating is shown on the right y-axis, to include the full span of the measured stresses on that sample.

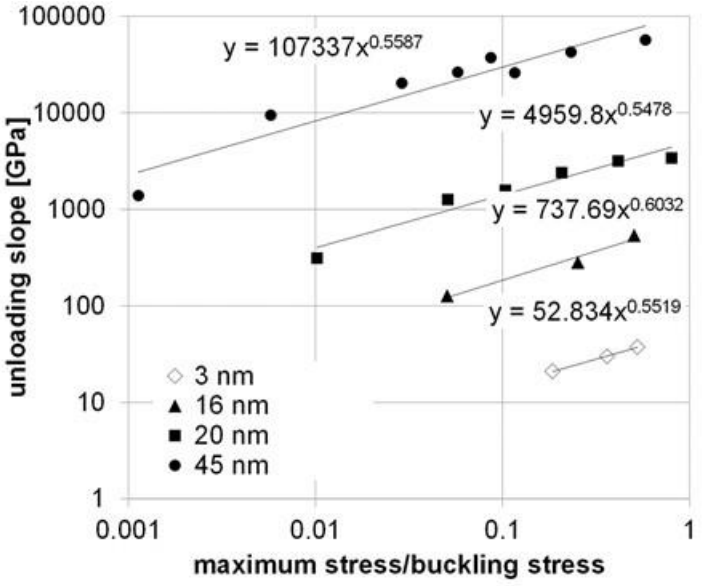

Figure 7.5. Unloading slope from Figure 7.4, plotted as a function of the corresponding maximum stress (normalized with buckling stress) for different HfB_2 coating thickness in CNT pillars.

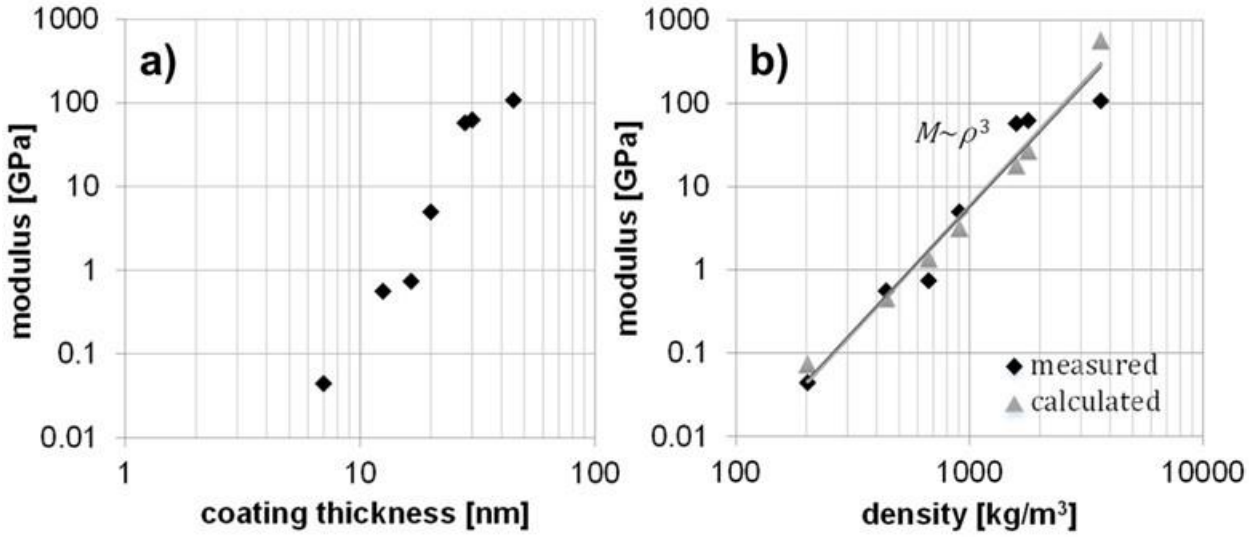

Figure 7.6. Modulus of HfB_2-CNT composites as function of coating thickness (a) and density (b). In (b) the measured values and their scaling are compared to the calculated measured values based on the mathematical model described in the manuscript.

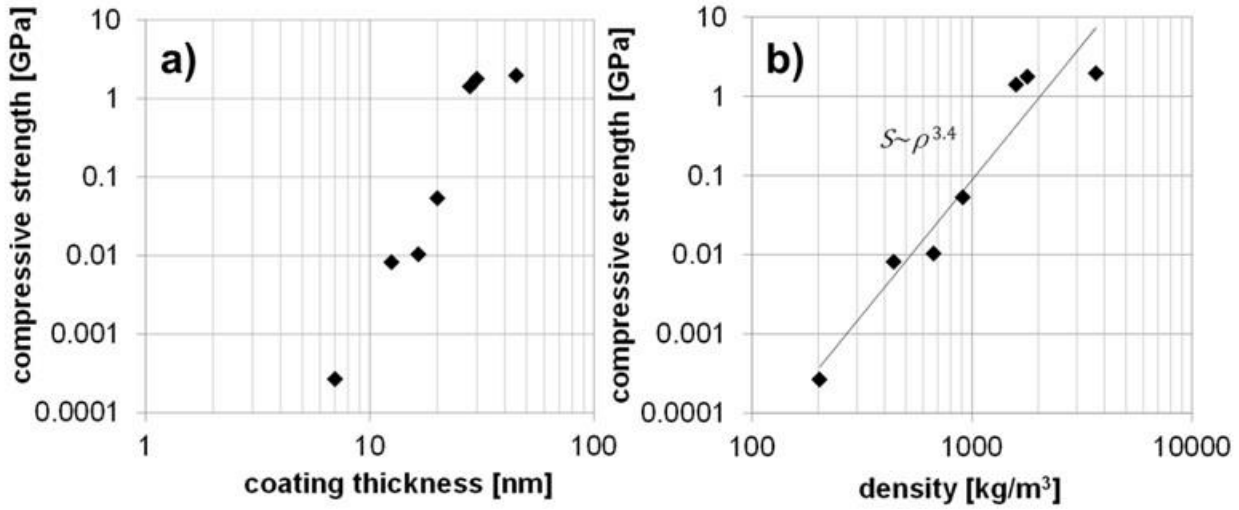

Figure 7.7. Compressive strength of HfB_2-CNT composites as function of coating thickness (a) and density (b)**.**

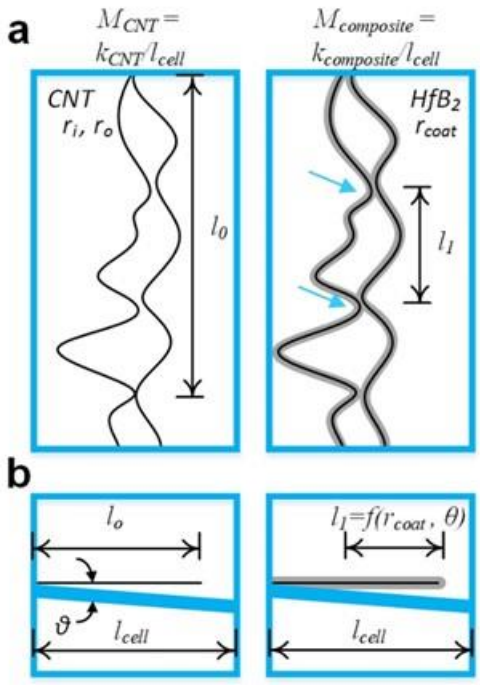

Figure 7.8. Schematics used to derive a minimalistic mathematical model for the mechanical behavior of the HfB_2-CNT composites. a) The schematics represent the CNT morphology observed in the SEM, which are considered as the unit cell of the HfB_2-CNT composite. b) Model of a CNT beam whose stiffness in bending governs the modulus of the HfB_2-CNT composite. The right panel in b) shows that for an increased coating thickness, the length of the CNT beam is effectively decreased

CHAPTER 8

FUTURE POSSIBILITIES AND PRELIMINARY RESULTS

8.1 Bottom-up Fill of Trenches with Forward-directed Fluxes

In Chapter 2, I demonstrated a new superconformal method for chemical vapor deposition (CVD) in trenches with HfO_2 films, which affords complete fill without any seam or void. The main requirement of this superconformal method is to operate in a kinetic regime, in which the film growth rate is proportional to the flux (pressure) of the rate limiting reactant, which is water in the case of HfO_2. With appropriate optimization of process conditions, (namely, substrate temperature and reactant partial pressure), such a kinetic regime can be obtained for many precursor-coreactant combinations (Table 8.1 and the references therein). Using this guideline, the superconformal method with forward-directed fluxes can be generalized to other dielectric or metallic materials for gap fill. Below, I briefly discuss the precursor-coreactant combinations for Al_2O_3 and SiO_2; a preliminary coating result for Al_2O_3 is presented.

8.1.1 Al_2O_3 film growth from trimethyl aluminum (TMA) and H_2O

TMA, $Al(CH_3)_3$, is a very well-studied Al source precursor for atomic layer deposition (ALD) of electronic quality Al_2O_3 films; it is highly reactive with H_2O as the oxygen source [1-3]. TMA has high volatility, with a vapor pressure of 12 Torr at room temperature [4], and can therefore be delivered to CVD reactor without the aid of a carrier gas. The high reactivity of TMA can, however, be moderated by using precursor rich growth conditions, such that the growth rate is then controlled by the water flux.

In preliminary experiments, I deposited Al_2O_3 films from TMA and water (forward-directed) by CVD. As a first step, an optimized kinetic regime was identified by performing film growth experiments on planar Si substrates (Figure 8.1). For a substrate temperature of 200 °C, there is a range of TMA and water partial pressures (0.07-0.20 mTorr for TMA and $\leq$ 0.1 mTorr for H_2O) within which the growth rate approximately saturates with TMA pressure and linearly

increases with water pressure; these partial pressures are suitable for superconformal coating in trenches with forward-directed water flux. The refractive index of an Al_2O_3 film, deposited with 0.19 mTorr TMA and 0.06 mTorr H_2O at 200 °C, is slightly lower than that of bulk Al_2O_3 (Figure 8.2); this is typically due to a reduced physical density of films grown at low temperature. Nonetheless, the refractive index of the CVD grown Al_2O_3 film compares very well with that of a film grown by ALD (marked with a black dot in Figure 8.2) [1].

Using the same conditions of Figure 8.2, Al_2O_3 coating in a rectangular trench with an aspect ratio of 3.5 provides a step coverage of 1.05 (Figure 8.3); the superconformal effect in this case is small and may not be sufficient to convert the trench to a V-shaped one with a V angle equal or greater than the critical value of 2° [5, 6] that was identified in Chapter 3 using a kinetic model. It was shown that to obtain a superconformal step coverage using the forward-directed flux method, the sticking probability of water needs to be low and the fraction of forward-directed water flux in the trench needs to be high. This information suggests that the relatively low step coverage in Figure 8.3 is due to a low fraction of forward-directed flux and/or a high sticking probability of water.

To enhance the fraction of forward-directed flux, a modification of the present reactor design is necessary; a conceptual new design was presented in Chapter 3. While reactor modification is a viable option, an easier alternative is to change the growth conditions to reduce the water sticking probability, such as decreasing the substrate temperature. Further experiments are needed to examine the effect of substrate temperature and reactant partial pressure.

8.1.2 SiO_2 film growth from tris(dimethylamino)silane (3DMAS) and H_2O_2

SiO_2 is a common dielectric material in the microelectronics device fabrication [7], and a chemical route to deposit SiO_2 at a low substrate temperature (< 400 °C) is of very high interest. Among the various Si source CVD or ALD precursors in current use, 3DMAS, $SiH(N(CH_3)_2)_3$, is reported to be one of the most highly reactive Si precursors at a low growth temperature [8, 9]. In addition, the vapor pressure of 3DMAS is quite high (16 Torr at 4 °C), making it easy to deliver to the CVD reactor without any carrier gas.

In Chapter 4, I experimentally showed (with *in situ* spectroscopic data) that under low-pressure process condition, 3DMAS does not react with H_2O on the growth surface at temperatures ≤ 300 °C. However, a stronger oxidant, such as hydrogen peroxide (H_2O_2) or ozone (O_3), can overcome the energy barrier to the surface reaction with 3DMAS to afford film growth at low temperature. In fact, ALD of SiO_2 film from 3DMAS and H_2O_2 at substrate temperatures of 150 to 550 °C is reported in reference [8]. Experiments using forward directed flux of H_2O_2 and a high saturation pressure of 3DMAS should be conducted in an attempt to achieve superconformal (or at least highly conformal) deposition of SiO_2 at substrate temperatures of ≤ 400 °C. Of course, detailed knowledge of the growth kinetics and film properties using planar Si substrates must be obtained first, in order to selecte a suitable kinetic regime for superconformal SiO_2 film growth.

8.2 Static CVD (SCVD) of Fe and $HfAl_xB_y$ alloy in CNT forest

In chapter 6, I demonstrated extremely conformal HfB_2 coating in CNT forests, with heights of ≤ 1.7 mm, to create mesoscale foam structures. Below, I describe a few technological interests for which SCVD can be employed to coat and infill complex and convoluted three-dimensional structures.

8.2.1 Fe nanoparticles on CNTs as catalyst

The CNT forests used in Chapters 6 and 7 consist of vertically aligned CNTs with microscopic randomness that causes the neighboring CNTs to touch each other. Conformal HfB_2 coating of these contact points (nodes) create weld-like strong joints, thereby significantly increases the stiffness and strength of the forest structure depending on the HfB_2 coating thickness. In chapter 7, we showed with a mathematical model that the mechanical behavior of the HfB_2-CNT composites strongly depends on the number of strongly bonded nodes. The stiffness of a coated forest is inversely proportional to the square of average distance between two nodes (i.e., the effective beam length). An increase in the number of nodes in the forest decreases the effective beam length in the foam structure, and thereby further enhances the stiffness of the forest.

A potential way to increase the number of nodes in the CNT forest scaffold is to create branching of the CNTs (Figure 8.4); the idea is to deposit nanoparticles of Fe catalyst on the

vertically aligned CNTs and then grow CNT branches starting on those Fe particles, causing a significant increase in the number of contact points. Later, this network of branched CNTs can be conformally coated with HfB_2 to create a modified foam structure with reduced beam length, thus a higher stiffness and strength compared with the existing results.

Fe nanoparticles can be deposited by CVD using a well-known Fe source precursor, iron pentacarbonyl, $Fe(CO)_5$, which has a very high vapor pressure of ~ 28 Torr at room temperature [10]. We previously studied CVD of Fe from $Fe(CO)_5$ in both SCVD and pumped CVD, where we demonstrated that the film morphology, smoothness and stoichiometry can be controlled by optimizing the growth conditions [11, 12].

As a proof-of-concept, I deposited Fe nanoparticles on CNTs with 20 Torr of $Fe(CO)_5$ pressure in SCVD at a substrate temperature of ≤ 200 °C (Figure 8.5a). In addition to the CNT forest of Figure 8.5a, a planar Si substrate (Figure 8.5b) and four other CNT forests were used in the same experiment (not shown) as a batch process; this resulted in a very high total growth surface area at temperature. Intentionally, the precursor pressure was not enough to make a blanket film; instead, Fe nanoparticles were obtained, which was the goal of this experiment. Note that blanket of Fe film is achievable using the same $Fe(CO)_5$ pressure but a lower total surface area of substrate.

A random distribution of Fe nanoparticles is observed both on the CNTs and on the planar Si substrate. A subsequent attempt to synthesize CNTs on these Fe particles at 775 °C resulted in collapse of the forest. In the same experiment, the sample of Figure 8.5b (on Si substrate) is also used; CNTs of average diameter ~ 30 nm grew on those Fe nanoparticles (Figure 8.6), which correlates well with the average Fe particle size in Figure 8.5b. The successful use of CVD-grown Fe nanoparticles suggests that a second level of branching within a CNT forest should be possible; I propose future experiments as follows. First, the CNT forest will be coated with a thin (< 5 nm) layer of HfB_2 to enhance the strength of the individual tubes; this will also improve the adhesion of the CNTs to the underlying Si substrate as reported in Chapter 6. Second, Fe nanoparticles will be deposited using growth conditions similar to those in Figure 8.5. Finally, the CNT forest decorated with Fe nanoparticles will be used to re-synthesize CNTs to create a branched network.

8.2.2 Fe infilling in porous Si

Infilling porous Si based template with a magnetic material to create one-dimensional nanowires are of great interest in the field of magneto-optical devices [13-16]. The magnetic behavior of Fe nanowires by infilling porous Si is worthwhile to investigate, given that we have an effective process to infill complex three-dimensional structure with Fe using $Fe(CO)_5$ precursor in SCVD. This motivation led to a collaborative effort with Prof. Paul Braun and his student Mr. Christian Ocier. Porous Si was synthesized by Mr. Ocier, and subsequent Fe infilling and film characterizations were done by myself.

In preliminary attempts, I used porous Si samples with ~ 5 µm pore height and 30-40 nm pore diameter and infilled them with Fe using 22 Torr $Fe(CO)_5$ at 150 °C by SCVD (Figure 8.7a). The effective aspect ratio of these pores is ≥ 125. The EDS elemental mapping in SEM shows that Fe infilling is achieved throughout the depth of the porous Si structure (Figure 8.7b). The analysis of magnetic anisotropy for these Fe nanowires is being carried out by Mr. Ocier. To confirm the capability of Fe infilling by SCVD, I used a companion microtrench substrate with the experiment of Figure 8.7. In this microtrench substrate, compete fill of Fe is observed in trenches with aspect ratio of ≤ 17 (Figure 8.8). This result agrees well with the Fe coating in porous Si (Figure 8.7).

8.2.3 Conformal coating of $HfAl_xB_y$ alloy in CNT forest

In Chapter 7, I showed that conformal coating of HfB_2 thin films in carbon nanotube forest significantly enhances the stiffness and modules of the structures. An important requirement for high temperature applications of such structures is the oxidation resistance of coating material. The low-temperature CVD grown HfB_2 films undergo crystallization when annealed at temperatures > 700 °C, causing cracks in the films due to volume shrinkage [17, 18]. Consequently, the films do not perform well for oxidation resistance at temperature > 700 °C.

A potential solution to the high temperature oxidization problem is to alloy the HfB_2 films with aluminum. When exposed to an oxidizing environment at high temperature, aluminum in the film is expected to form a protective Al_2O_3 layer (crust) at the surface, thereby protecting the bulk of the film. This is analogous to alloying of TiN coating with aluminum, commonly used to protect the surface of cutting tools [19-21].

In a separate project in our group, Mr. Zhejun Zhang (this project was originally started by a former group member, Dr. Elham Mohimi) is investigating $HfAl_xB_y$ alloy films by co-flowing Al source precursor, trimethylamine alane (TMAA), with $Hf(BH_4)_4$ in pumped CVD. In preliminary experiments, Mr. Zhang grew films with different concentration of Al, and subsequent annealing of these films in an O_2 containing environment at 800 °C resulted in a Al_2O_3 crust formation on the film surface. This is a highly promising result, and I believe that the knowledge from this research can be transferred to SCVD to coat CNT forest with $HfAl_xB_y$ alloy films. Since the simultaneous presence of two reactants with high partial pressures can results in the formation of intermediary products in gas phase reaction, experimental studies are necessary to understand the effect of growth temperature and partial pressures of the reactants in SCVD. Preferably, we need a source precursor for Al which does not react in the gas phase with $Hf(BH_4)_4$ at a growth temperature of $\leq$ 200 °C. In case such a precursor is not available, alternating thin layers of HfB_2 and Al can be deposited by SCVD cycles (only one reactant at a time); this is likely to afford films with enhanced oxidation resistance at high temperature.

8.3 Forward-directed Fluxes to Conformally Coat CNT Forest in Pumped CVD

In chapter 6, I demonstrated conformal HfO_2 coating in a CNT forest, deposited using forward-directed fluxes of TDMA-Hf precursor and water co-reactants in pumped CVD. In that work, the forward-directed ballistic fluxes were apparently able to penetrate all the way down to the bottom of the forest, affording a high degree of conformality before pinch-off at the opening near the top. Notably, the HfO_2 film was obtained from a two-reactant CVD system, which would not be possible in SCVD due to the gas phase reaction of TDMA-Hf and water.

In addition to HfO_2 film, the materials shown in Table 1 are suitable candidates as coating material for various thermo-mechanical and electrical applications. For example: conformal V_2O_5 coating of CNT is of high interest in gas sensing devices [22, 23] and as electrodes in new generation energy storage devices [24]; conformal coating of Al_2O_3, a refractory high-K dielectric, has applications in nanotube field effect transistors [25]; TiN is a benchmark material for tribological applications and has recently been used as a coating material on CNT for

electrochemical supercapacitors [26]; and TiO_2 coated CNTs are reported as filter for rapid and effective arsenic sorption [27].

Similar to HfO_2, CVD of the above materials needs co-flowing of two reactants (Table 1). Experimental investigations of conformal coating in CNT forests using forward-directed fluxes of these reactants (material system) may lead to fruitful composite structures.

8.4 Low Temperature Deposition of Conformal SiN_x Films

Silicon nitride (SiN_x) thin films have been subjected to extensive research and engineering studies [28, 29]. SiN_x films are used for many critical functions in microelectronic devices; such as dielectric layer, charge storage layer, stress liner, masking layer, diffusion barrier, and passivation layer [30, 31]. Low-pressure CVD (LPCVD) affords conformal SiN_x films, but the process requires a high temperature ($\geq$ 700 °C) that exceeds the thermal budget of these devices [32]. Current state-of-the-art technologies usually employ plasma enhanced CVD (PECVD) to grow SiN_x films at low temperature ($\leq$ 400 °C) [32], however, the conformality (step coverage) of SiN_x films deposited by PECVD are usually not as good as those deposited by LPCVD [33, 34].

I worked in a collaborative research with Prof. Gregory S. Girolami and his student Mr. Nels T. Anderson on low temperature CVD of SiN_x films. Prof. Girolami and Mr. Anderson have recently synthesized a single-source precursor, 1,1-diazido-silalcylopent-3-ene, as a candidate for SiN_x CVD growth; the synthesis of this chemical is known in the literature, but there is no report on using this for film growth. While the safe handling of this precursor in a turbo pumped CVD system is still being evaluated, Mr. Nels grew a few films using a Pyrex tube reactor which was evacuated by a roughing pump (base pressure ~ 10^{-2} Torr). I characterized the films for materials properties and conformality in deep trenches.

Film grown at 400 °C have dense and column-free microstructures with low surface roughness (Figure 8.9a). It contains a high amount of C and O (Figure 8.9b), likely due to the poor vacuum condition used during the deposition, which is inefficient to remove moisture and hydrocarbon impurities from the reactor. Because of the C and O contamination, we refer to this film material as $SiN_xC_yO_z$. Refractive index of the film of Figure 8.9a is slightly lower than that of bulk Si_3N_4 [35] and higher than that of bulk SiO_2 [35]. Considering the C incorporation into

film, this is a promising result. Film grown on microtrench substrate using the same condition of Figure 8.9 has nearly unity step coverage in trenches with aspect ratio of ≤ 7.

Future experiments using the 1,1-diazido-silalcylopent-3-ene precursor in a turbo pumped CVD reactor is necessary to minimize the C and O contaminations in the films. Further characterization, such as etch rate study, is also needed to verify the usefulness of these films for microelectronic device fabrication.

8.5 References

1. Groner, M.D., et al., *Low-temperature Al2O3 atomic layer deposition.* Chemistry of Materials, 2004. **16**(4): p. 639-645.

2. Groner, M.D., et al., *Electrical characterization of thin Al2O3 films grown by atomic layer deposition on silicon and various metal substrates.* Thin Solid Films, 2002. **413**(1-2): p. 186-197.

3. Tang, X., et al., *Room temperature atomic layer deposition of Al2O3 and replication of butterfly wings for photovoltaic application.* Journal of Vacuum Science & Technology A, 2012. **30**(1).

4. Mccullough, J.P., et al., *Trimethylaluminum - Thermodynamic Functions in Solid and Liquid States, 3-380 Degrees K - Vapor Pressure, Heat of Vaporization, and Entropy in Ideal Gas State.* Journal of Physical Chemistry, 1963. **67**(3): p. 677-&.

5. Talukdar, T.K., et al., *Superconformal Coating and Filling of Deep Trenches by Chemical Vapor Deposition with Forward-Directed Fluxes.* Manuscript in preparation, 2018.

6. Wang, W.B. and J.R. Abelson, *Filling high aspect ratio trenches by superconformal chemical vapor deposition: Predictive modeling and experiment.* Journal of Applied Physics, 2014. **116**(19).

7. Wolf, S. and R.N. Tauber, *Silicon Processing for the VLSI Era: Process technology*. 2000: Lattice Press.

8. Burton, B.B., et al., *SiO2 Atomic Layer Deposition Using Tris(dimethylamino)silane and Hydrogen Peroxide Studied by in Situ Transmission FTIR Spectroscopy.* Journal of Physical Chemistry C, 2009. **113**(19): p. 8249-8257.

9. Hirose, F., et al., *Low-temperature-atomic-layer-deposition of SiO2 with Tris(dimethylamino)silane (TDMAS) and Ozone using Temperature Controlled Water Vapor Treatment.* Silicon Nitride, Silicon Dioxide, and Emerging Dielectrics 10, 2009. **19**(2): p. 417-+.

10. Gilbert, A.G. and K.G. Sulzmann, *Vapor-Pressure of Iron Pentacarbonyl.* Journal of the Electrochemical Society, 1974. **121**(6): p. 832-834.

11. Zhang, P.Y., et al., *Iron CVD from iron pentacarbonyl: Growth inhibition by CO dissociation and use of ammonia to restore constant growth.* Journal of Vacuum Science & Technology A, 2016. **34**(5).

12. Cloud, A.N., *Ultraconformal chemical vpor deposition and synthesis of transition metal nitride films*, in *Materials Science and Engineering*. 2013, University of Illinois at Urbana-Champaign.

13. Granitzer, P. and K. Rumpf, *Porous Silicon-A Versatile Host Material.* Materials, 2010. **3**(2): p. 943-998.

14. Rusetskii, M.S., et al., *Magnetic Anisotropy of Nickel Nanowire Array in Porous Silicon.* Technical Physics Letters, 2011. **37**(5): p. 391-393.

15. Aravamudhan, S., et al., *Porous silicon templates for electrodeposition of nanostructures.* Applied Physics a-Materials Science & Processing, 2007. **87**(4): p. 773-780.

16. Gusev, S.A., et al., *Ferromagnetic Filaments Fabrication in Porous Si Matrix (Invited).* Journal of Applied Physics, 1994. **76**(10): p. 6671-6672.

17. Chatterjee, A., et al., *Nanoscratch and nanofriction behavior of hafnium diboride thin films.* Wear, 2008. **265**(5-6): p. 921-929.

18. Chatterjee, A., et al., *Tribological behavior of hafnium diboride thin films.* Surface & Coatings Technology, 2006. **201**(7): p. 4317-4322.

19. Kawate, M., A.K. Hashimoto, and T. Suzuki, *Oxidation resistance of Cr1-xAlxN and Ti1-xAlxN films.* Surface & Coatings Technology, 2003. **165**(2): p. 163-167.

20. Mo, J.L. and M.H. Zhu, *Tribological oxidation behaviour of PVD hard coatings.* Tribology International, 2009. **42**(11-12): p. 1758-1764.

21. PalDey, S. and S.C. Deevi, *Single layer and multilayer wear resistant coatings of (Ti,Al)N: a review.* Materials Science and Engineering a-Structural Materials Properties Microstructure and Processing, 2003. **342**(1-2): p. 58-79.

22. Willinger, M.G., et al., *The controlled deposition of metal oxides onto carbon nanotubes by atomic layer deposition: examples and a case study on the application of V2O4 coated nanotubes in gas sensing.* Physical Chemistry Chemical Physics, 2009. **11**(19): p. 3615-3622.

23. Willinger, M.G., et al., *Vanadium Oxide Sensing Layer Grown on Carbon Nanotubes by a New Atomic Layer Deposition Process.* Nano Letters, 2008. **8**(12): p. 4201-4204.

24. Boukhalfa, S., K. Evanoff, and G. Yushin, *Atomic layer deposition of vanadium oxide on carbon nanotubes for high-power supercapacitor electrodes.* Energy & Environmental Science, 2012. **5**(5): p. 6872-6879.

25. Baughman, R.H., A.A. Zakhidov, and W.A. de Heer, *Carbon nanotubes - the route toward applications.* Science, 2002. **297**(5582): p. 787-792.

26. Kao, E., et al., *Ald Titanium Nitride Coated Carbon Nanotube Electrodes for Electrochemical Supercapacitors.* 2015 Transducers - 2015 18th International Conference on Solid-State Sensors, Actuators and Microsystems (Transducers), 2015: p. 498-501.

27. Liu, H., K.C. Zuo, and C.D. Vecitis, *Titanium Dioxide-Coated Carbon Nanotube Network Filter for Rapid and Effective Arsenic Sorption.* Environmental Science & Technology, 2014. **48**(23): p. 13871-13879.

28. Kaloyeros, A.E., et al., *Review-Silicon Nitride and Silicon Nitride-Rich Thin Film Technologies: Trends in Deposition Techniques and Related Applications.* Ecs Journal of Solid State Science and Technology, 2017. **6**(10): p. P691-P714.

29. Meng, X., et al., *Atomic Layer Deposition of Silicon Nitride Thin Films: A Review of Recent Progress, Challenges, and Outlooks.* Materials, 2016. **9**(12).

30. Jang, W., et al., *The effect of plasma power on the properties of low-temperature silicon nitride deposited by RPALD for a gate spacer.* Physica Status Solidi a-Applications and Materials Science, 2015. **212**(12): p. 2785-2790.

31. Kern, W. and K.K. Schuegraf, *1 - Deposition Technologies and Applications: Introduction and Overview A2 - Seshan, Krisna*, in *Handbook of Thin Film Deposition Processes and Techniques (Second Edition)*. 2001, William Andrew Publishing: Norwich, NY. p. 11-43.

32. Nishi, Y. and R. Doering, *Handbook of Semiconductor Manufacturing Technology, Second Edition*. 2017: CRC Press.

33. Triyoso, D.H., et al., *Evaluation of Low Temperature Silicon Nitride Spacer for High-k Metal Gate Integration.* Ecs Journal of Solid State Science and Technology, 2013. **2**(11): p. N222-N227.

34. King, S.W., *Plasma enhanced atomic layer deposition of SiNx:H and SiO2.* Journal of Vacuum Science & Technology A, 2011. **29**(4).

35. *WVASE® Spectroscopic Ellipsometry Data Acquisition and Analysis Software*. 2012, J. A. Woollam Co., Inc.: Lincoln, NE 68508, USA.

36. Maruyama, T. and T. Shirai, *Silicon Dioxide Thin-Films Prepared by Chemical-Vapor-Deposition from Tetrakis (Dimethylamino)Silane and Ozone.* Applied Physics Letters, 1993. **63**(5): p. 611-613.

37. Juarez, H., et al., *Low temperature deposition: properties of SiO2 films from TEOS and ozone by APCVD system.* Xix Latin American Symposium on Solid State Physics (Slafes), 2009. **167**.

38. Maruyama, T. and S. Ohtani, *Silicon Dioxide Thin-Films Prepared by Chemical-Vapor-Deposition from Tetrakis(Diethylamino)Silane and Ozone.* Applied Physics Letters, 1994. **64**(21): p. 2800-2802.

39. Abendroth, B., et al., *Atomic layer deposition of TiO2 from tetrakis(dimethylamino) titanium and H2O.* Thin Solid Films, 2013. **545**: p. 176-182.

40. Wang, W.J.B., et al., *Chemical vapor deposition of TiO2 thin films from a new halogen-free precursor.* Journal of Vacuum Science & Technology A, 2014. **32**(6).

41. Wang, X.W., et al., *Atomic layer deposition of vanadium oxide thin films from tetrakis(dimethylamino)vanadium precursor.* Journal of Materials Research, 2017. **32**(1): p. 37-44.

42. Musschoot, J., et al., *Atomic layer deposition of titanium nitride from TDMAT precursor.* Microelectronic Engineering, 2009. **86**(1): p. 72-77.

43. Mohimi, E., *Co-Reactant Interactions with CVD Surfaces: Activation or Passivation of Growth*, in *Materials Science and Engineering*. 2017, University of Illinois at Urbana-Champaign.

8.6 Tables and Figures

Table 8.1. Potential precursor-coreactant combinations for bottom-up fill in trenches (or vias) using forward-directed fluxes

Film material	Metal Precursor	Co-reactant	Substrate temperate range (°C)	Reference
Al_2O_3	$Al(CH_3)_3$	H_2O	25–425	[1-3]
SiO_2	$SiH(N(CH_3)_2)_3$	H_2O_2 or O_3	150–550	[8, 9]
	$Si(N(CH_3)_2)_4$	O_3	100–400	[36]
	$Si(OCH_2CH_3)_4$	O_3	125–400	[37, 38]
TiO_2	$Ti(N(CH_3)_2)_4$	H_2O	50–330	[39]
	$Ti(H_3BNMe_2BH_3)_2$	H_2O	150–450	[40]
V_2O_5	$V(N(CH_3)_2)_4$	H_2O	50–200	[41]
TiN	$Ti(N(CH_3)_2)_4$	NH_3	150–300	[42]
VN	$V(N(CH_3)_2)_4$	NH_3	150–300	[43]

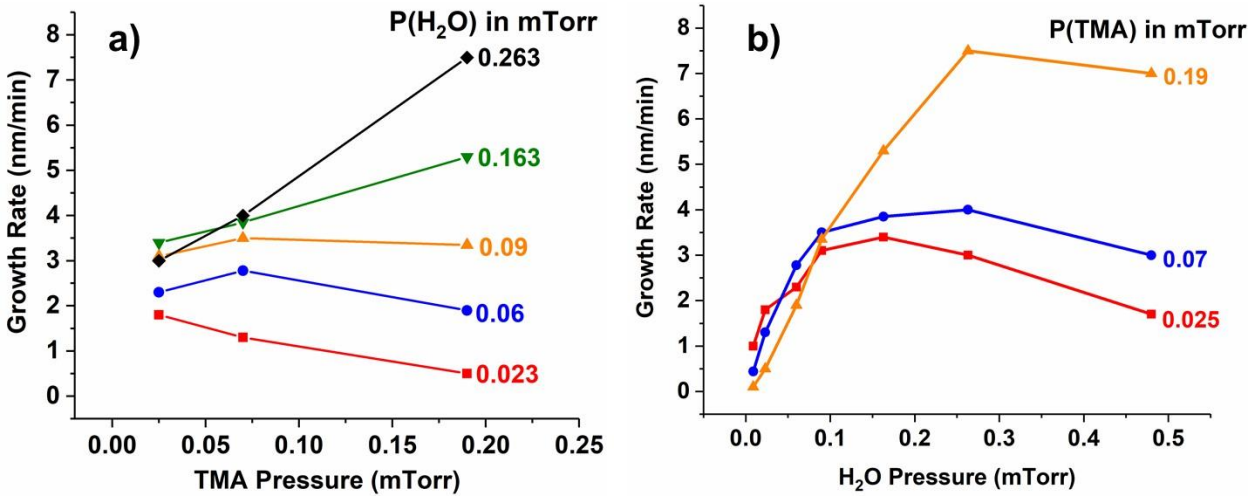

Figure 8.1. Al_2O_3 film growth rates on planar Si substrates as a function of TMA (a) and H_2O (b) partial pressures at a substrate temperature of 200 °C. Film growth rates are measured by *in situ* spectroscopic ellipsometry.

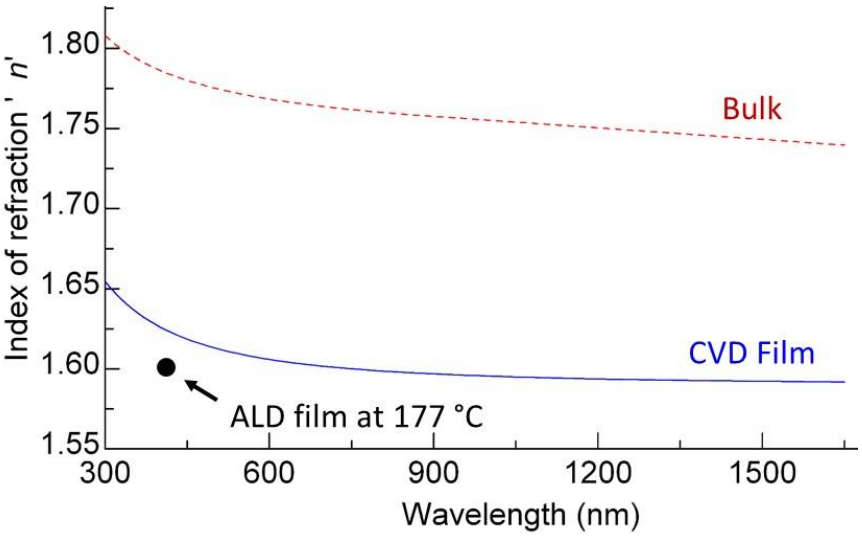

Figure 8.2. Index of refraction for CVD grown Al_2O_3 film, deposited with 0.19 mTorr TMA and 0.06 mTorr H_2O at 200 °C. The refractive index for bulk Al_2O_3 [35] and ALD grown Al_2O_3 film (black dot) [1] are shown for comparison.

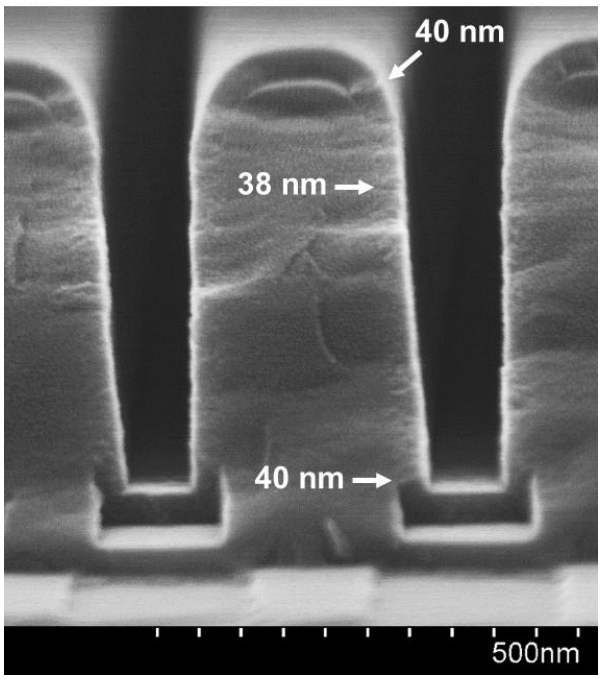

Figure 8.3. SEM image of trenches with aspect ratio of 3.5, coated using 0.19 mTorr TMA and 0.06 mTorr H_2O at 200 °C. The step coverage, below the slight bread-loaf at trench opening, is ~ 1.05 (slightly > 1).

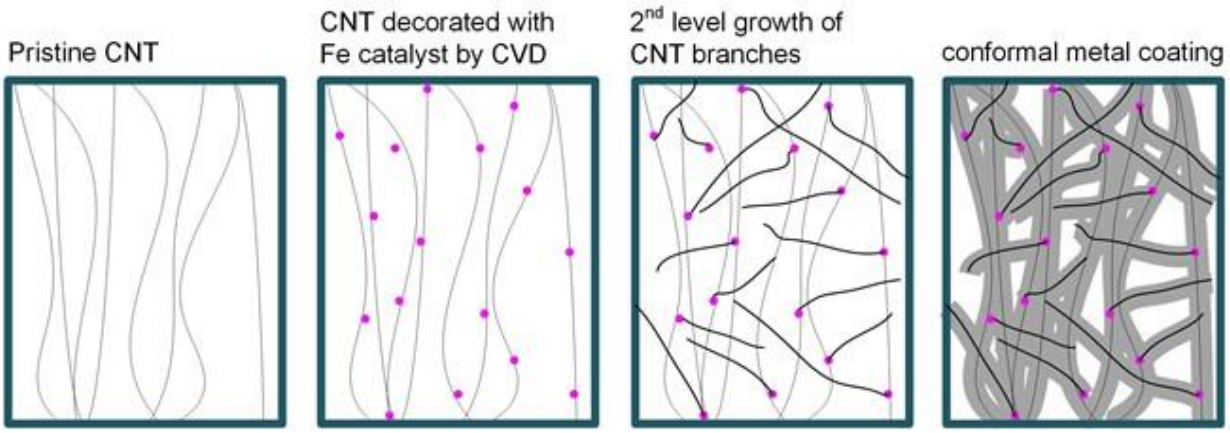

Figure 8.4. Schematic process flow of hierarchical CNT foams with a 2nd level branching and coating. Pristine CNTs are decorated with Fe particles by CVD; a 2nd growth of CNT branches is performed, followed by conformal coating (e.g., with HfB_2) to cross-link the hierarchical foam.

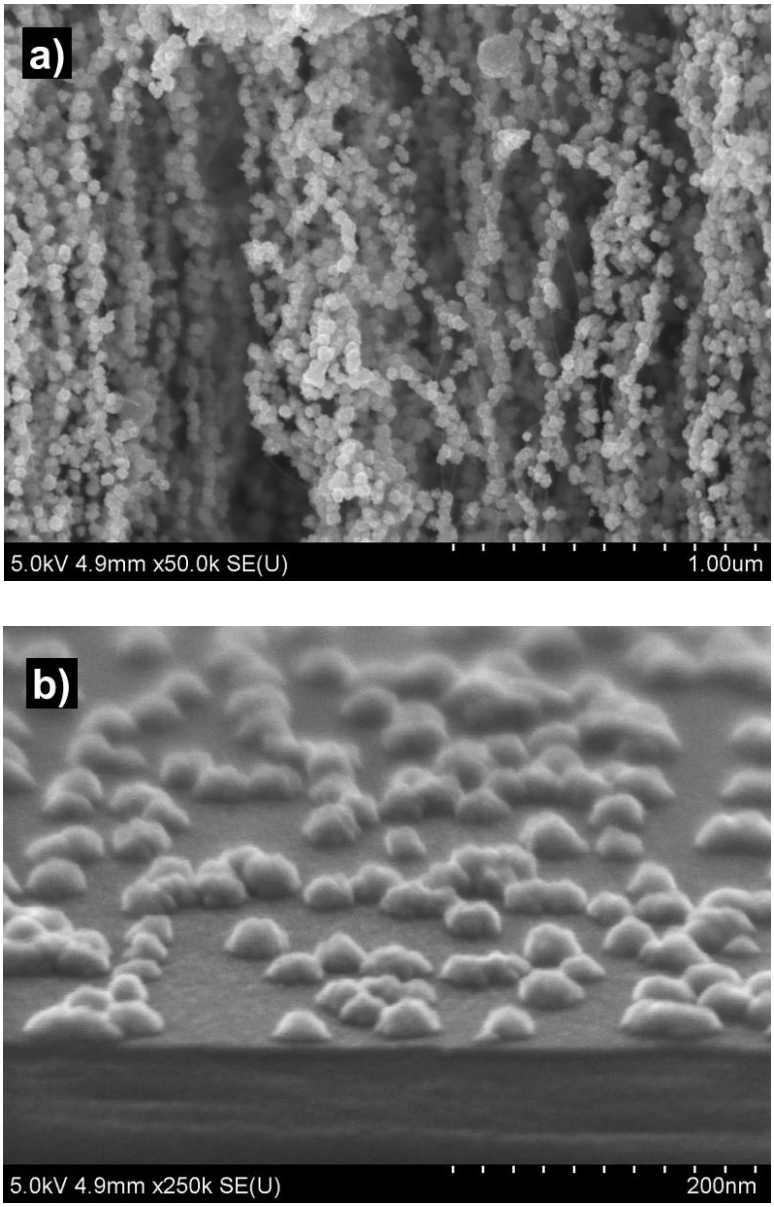

Figure 8.5. SEM images showing SCVD deposited Fe nanoparticles with 20 Torr of $Fe(CO)_5$ in a CNT forest of height 0.4 mm (a) and on a planar Si substrate (b). In addition to these two samples, four other CNT forests were used in the same experiment (not shown), resulting in a high total surface area.

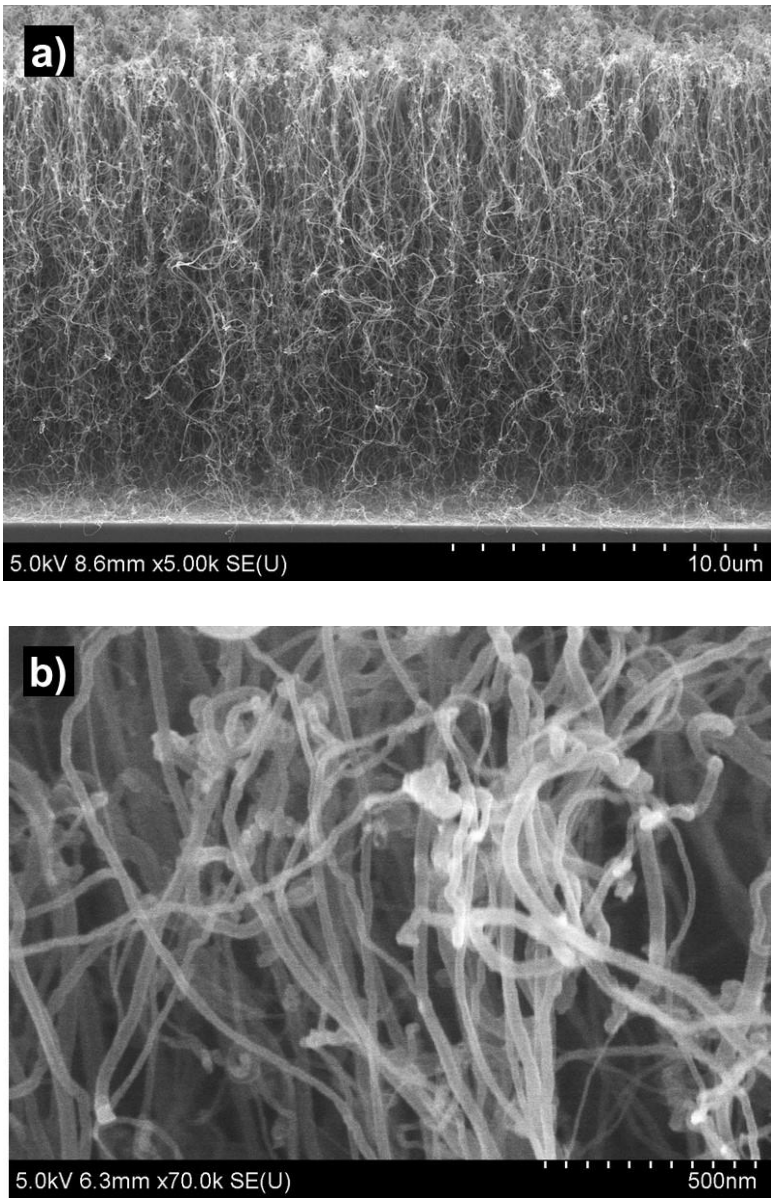

Figure 8.6. SEM images of CVD synthesized CNTs on the sample of Figure 8.5b. a) Low magnification image showing the full height of the synthesized CNT forest. b) Magnified image showing an average CNT outer diameter of 30 nm. Growth conditions: co-flow of C_2H_4, He and H_2 with flow rate ratio of 1:4:1 at 775 °C in Pyrex tube reactor.

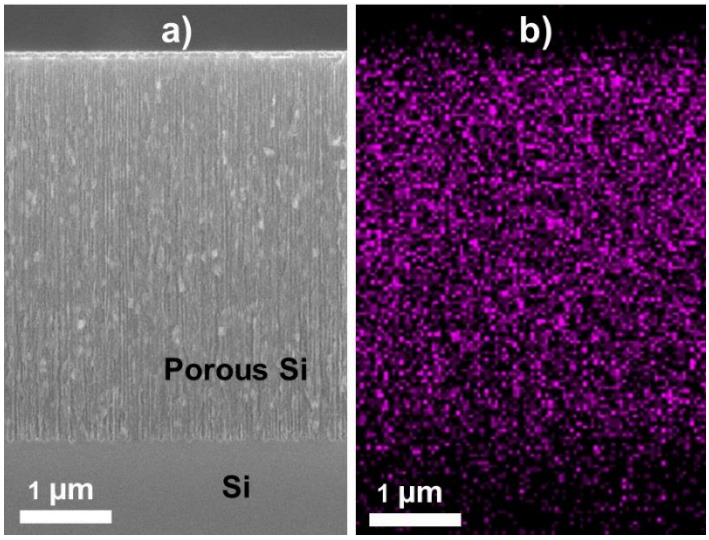

Figure 8.7. Fe infilling in porous Si using 22 Torr $Fe(CO)_5$ at 150 °C by SCVD. a) Cross-sectional SEM image showing the full height (thickness) of the porous Si structure on Si. The pores have a height of ~ 5 µm and diameter of 30-40 nm, and the corresponding aspect ratio is ≥ 125. b) EDS-SEM elemental map of the same cross section showing infilling of Fe all the way down to the bottom of the pores.

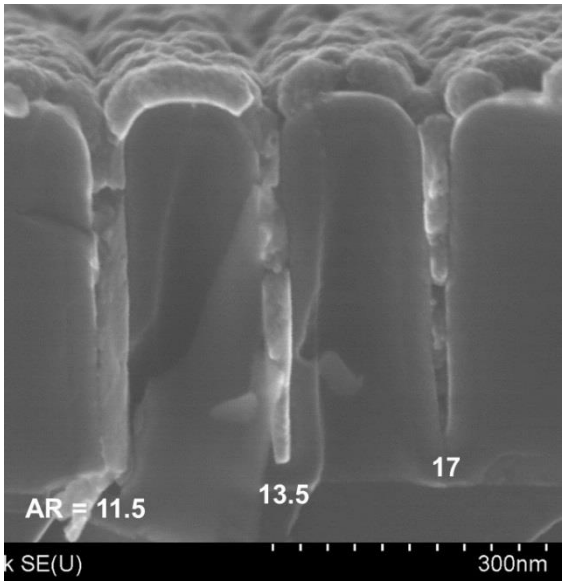

Figure 8.8. Complete Fe fill in trenches with aspect ratio of ≤ 17, coated in the same experiment of Figure 8.7 (a companion sample).

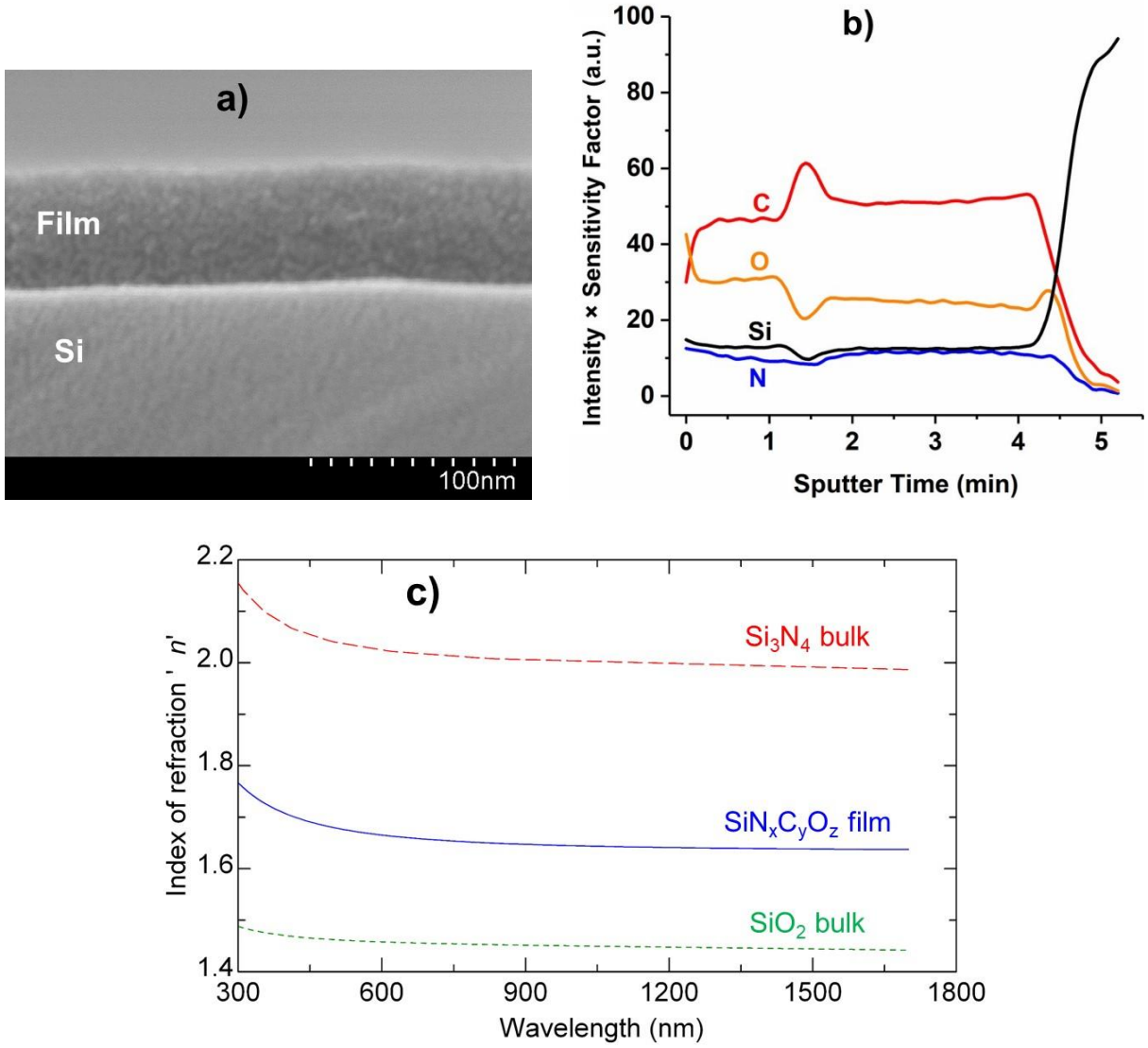

Figure 8.9. a) Cross-sectional SEM image showing ilm thickness of 60 nm, deposited with flowing 365 µL 1,1-diazido-silalcylopent-3-ene precursor at 400 °C for 5 hours in Pyrex tube reactor. The reactor tube is continuously pumped under a roughing vacuum (~ 10^{-2} Torr). b) Auger depth profile for the same sample. Due to charging effect on the film surface Auger data are interpreted qualitatively. c) Refractive index of the same film as a function of wavelength. Refractive indices of bulk Si_3N_4 [35] and bulk SiO_2 [35] are shown for comparison.

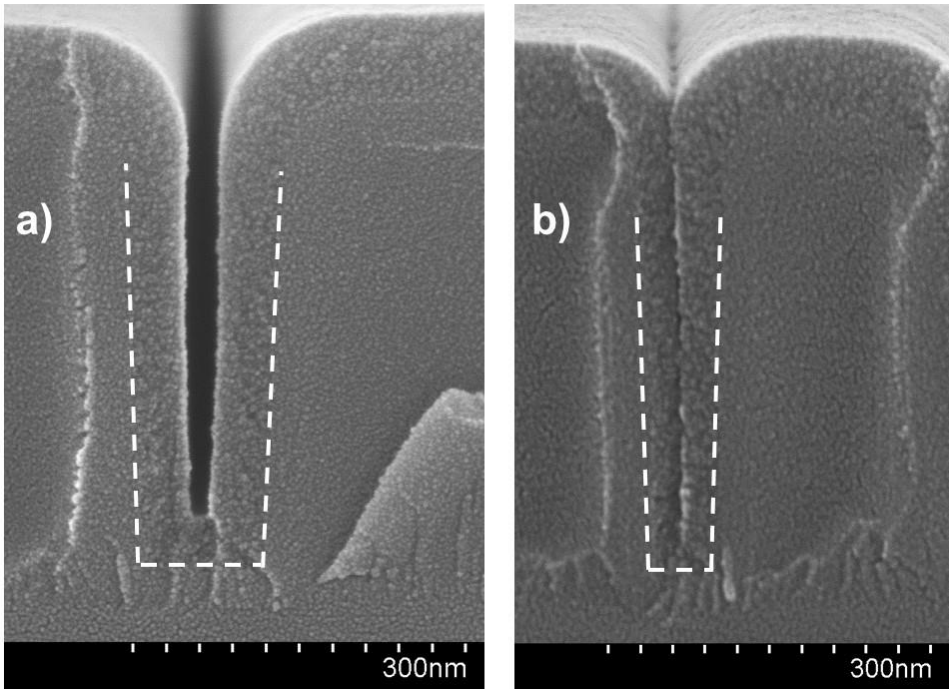

Figure 8.10. a) Cross-sectional SEM image of trenches with aspect ratio of 3.5 (a) and 7 (b), coated with $SiN_xC_yO_z$ film grown using the same conditions of Figure 8.9.